PhD

3rd CYCLE

FCUP
2024

U.PORTO

Derivation of M-Dwarf stellar parameters in the optical and near-infrared

Alexandros Antoniadis Karnavas

U.PORTO
FACULDADE DE CIÊNCIAS
UNIVERSIDADE DO PORTO

Derivation of M-Dwarf stellar parameters in the optical and near-infrared

Alexandros Antoniadis Karnavas
Doctoral Program in Astronomy
Department of Physics and Astronomy
Faculty of Sciences of the University of Porto

2024

U.PORTO
FACULDADE DE CIÊNCIAS
UNIVERSIDADE DO PORTO

Derivation of M-Dwarf stellar parameters in the optical and near-infrared

Alexandros Antoniadis Karnavas
Thesis carried out as part of the Doctoral Program in Astronomy
Department of Physics and Astronomy
2024

Supervisor
Sérgio António Gonçalves de Sousa, Researcher, Instituto de Astrofísica e Ciências do Espaço
Co-supervisor
Elisa Delgado Mena, Researcher, Instituto de Astrofísica e Ciências do Espaço

Acknowledgements

First of all, I would like to express my sincere gratitude to my supervisors Sergio Sousa and Elisa Delgado Mena for giving me the opportunity to conduct research on Astronomy. Their guidance, advice and encouragement were vitally supportive and motivative throughout the PhD program.

In addition, I would also like to thank the directors of the program, Nuno Santos and Mario Joao Monteiro, who provided me with important advices during the challenging journey of being a PhD student.

Furthermore, I would like to express my best wishes to all the collaborators, researchers and fellow students that I met during these years in Portugal. We shared knowledge and experience for which I am deeply grateful.

Warm greetings go to my few Greek friends in Porto, with whom I shared several pleasant moments, that made my stay more comfortable here.

Huge appreciation goes to my fiancee Eirini, who stood by me through all the ups and downs of these years, filling me with inner strength.

Of course, my deepest gratitude deserves to be attributed to my parents for their encouragement and unconditional love since I left Greece in order to chase my dreams in science and life.

Finally, I acknowledge the financial support from FCT in the form of the exploratory projects IF/00028/2014/CP1215/CT0002 and IF/00849/2015/CP1273/CT0003.

Resumo

Há grande interesse em determinar as propriedades das estrelas anãs M. Como são as estrelas mais comuns da nossa Galáxia, o conhecimento das suas características desempenha um papel crucial em várias áreas da Astronomia: desde a astrofísica estelar até à astronomia galáctica e com grande importancia na ciência exoplanetária. Estas estrelas são também as mais promissoras para a deteção de planetas menos massivos na zona habitável. Neste contexto, os dados espectroscopicos destas estrelas podem ser usados para revelar as suas composição química, assim como obter os paramêtros atmosféricos estelares mais relevantes para a sua caracterização, tal como a temperatura efectiva (T_{eff}), a metalicidade (expresso como [Fe/H]), gravidade de superfície ($\log g$), e a micro-turbulência (v_t). Paramêtros estelares são fundamentais para perceber a sua formação, evolução e influência nas propriedades dos planetas que se formem e orbitem em seu redor. A estimativa de paramêtros destas estrelas anãs frias do tipo M é noentanto muito complexa porque a análise espectroscópica tem que ultrapassar muitas dificuldades que não são encontradas para estrelas mais parecidas com o Sol.

Nesta tese, eu descrevo dois métodos que foram desenvolvidos para derivar paramêtros atmosféricos estelares de estrelas anãs do tipo M. Estes métodos são aplicados a regiões distintas dos espectros, um na região do óptico e o outro no infra-vermelho próximo. O primeiro método é uma ferramenta automática com recurso a técnicas de machine learning (ODUSSEAS) que opera no óptico e é baseado na medição das pseudo larguras equivalentes de mais de 4000 riscas de absorção espectral e na utilização do pacote de Python "scikit-learn" para prever temperatura effectiva (T_{eff}) e metalicidade ([Fe/H]). Estes parametros são previamente provenientes de calibrações fotométricas e espectroscópicas. ODUSSEAS foi aplicado para caracterizar estrelas, usando espectros obtidos por vários espectrógrafos. T_{eff} e [Fe/H] foram determinadas para 82 estrelas hospedeiras de planetas do base de dados SWEET-Cat. Os parâmeteros apresentados são precisos, com diferenças relativamente a outros estudos de -66 K e -0.11 dex para T_{eff} and [Fe/H], respectivamente. Para além disso, a correlação relativamente aos planetas de grande massa se formarem principalmente em torno de estrelas ricas em metais também foi confirmada para estrelas anãs do tipo M. O segundo método (MPIRA) utiliza medições de larguras equivalentes na construção de uma nova lista de riscas de absorção de ferro (FeI) e titanio (TiI) no domínio espectral do infravermelho próximo. São usados dados atómicos das riscas selecionadas e modelos de atmosferas estelares MARCS que são

introduzidas no software MOOG para calcular as respectivas abundancias. De seguida é aplicado um processo iterativo para determinar os melhores valores de T_{eff}, [Fe/H] e v_t. MPIRA foi testado em uma amostra de estrelas com espectros obtidos por SPIRou. Para obter resultados precisos, foram realizadas análises utilizando várias listas de riscas. Par as mesmas estrelas, a T_{eff} e a [Fe/H] determinados por MPIRA têm diferenças médias de apenas 73 K e 0.02 dex respectivamente, relativamente às determinados por ODUSSEAS.

Palavras-chave: estrelas, anãs M, paramêtros estelares, espectroscopia, óptico, infravermelho próximo

Abstract

There is great interest in determining the properties of M-dwarf stars. As they are the most common stars in our Galaxy, knowledge of their characteristics plays a crucial role in several areas of Astronomy: from stellar astrophysics to galactic astronomy and with great importance in exoplanetary science. These stars are also the most promising for detecting less massive planets in the habitable zone. In this context, the spectroscopic data of these stars can be used to reveal their chemical composition, as well as to obtain the most relevant stellar atmospheric parameters for their characterization, such as the effective temperature (T_{eff}), metallicity (expressed as [Fe/H]), surface gravity ($\log g$) and microturbulence (v_t). Stellar parameters are fundamental to understand the formation, evolution and influence on the properties of the planets that form and orbit around them. The parameter estimation of these cool M-type dwarf stars is, however, very complex, because the spectroscopic analysis has to overcome many difficulties which are not found for stars more similar to the Sun.

In this thesis, I describe two methods that were developed to derive stellar atmospheric parameters of M dwarfs. These methods are applied to distinct regions of the spectra, one in the optical and the other in the near-infrared region. The first method is an automatic tool using machine learning techniques (ODUSSEAS) which operates in the optical. It is based on measuring the pseudo equivalent widths of more than 4000 spectral absorption lines and using the Python package "scikit-learn" to predict T_{eff} and [Fe/H]. These parameters previously come from photometric and spectroscopic calibrations. ODUSSEAS was applied to characterize stars with spectra obtained from various spectrographs. T_{eff} and [Fe/H] were determined for 82 planet-host stars in SWEET-Cat database. The parameters presented are accurate, having mean differences compared to other studies within -66 K and -0.11 dex for T_{eff} and [Fe/H] respectively. Furthermore, the correlation regarding massive planets forming mainly around metal-rich stars was also confirmed for M dwarfs. The second method (MPIRA) uses measurements of equivalent widths to construct a new list of iron (FeI) and titanium (TiI) absorption lines in the near-infrared spectral domain. Atomic data of selected lines and MARCS stellar atmosphere models are used, which are introduced into the MOOG software to calculate their respective abundances. An iterative process is then applied to determine the best values of T_{eff}, [Fe/H] and v_t. MPIRA was tested on a sample of stars with spectra obtained from SPIRou. To achieve accurate results, analyses using various lists of spectral lines were carried out. For the same stars, T_{eff} and [Fe/H] determined by MPIRA have mean differences of only 73 K and 0.02 dex respectively, as compared to those determined by ODUSSEAS.

Keywords: stars, M dwarfs, stellar parameters, spectroscopy, optical, near-infrared

Table of Contents

List of Tables

List of Figures

1. Introduction

Stars are born by the gravitation collapse of gaseous nebulae, consisting mainly of hydrogen as well as helium and small amounts of heavier elements. A star in the main sequence, being a radiant spheroid of plasma, releases energy outwards by the thermonuclear fusion of hydrogen into helium inside its core. This process is counter-balanced by the gravity of the star, enabling it to sustain its structure. Stellar nucleosynthesis is the process that produces almost all naturally occurring chemical elements heavier than lithium. Stellar mass loss or supernova explosions return chemically enriched material to the interstellar medium, which is then recycled into new stars.

Stars can form orbital systems with other astronomical objects due to their gravitational interaction, such as planetary systems and stellar systems with two or more stars. They also form part of much larger structures, such as a star cluster or a galaxy.

Stellar properties like mass, chemical composition, effective temperature (T_{eff}), variability, distance, and motion are determined by a star's apparent brightness, spectrum, and changes in its position in the sky over time. Those characteristics vary significantly from star to star or even within the same star in the case of variable stars (in which T_{eff} and brightness can change significantly) and analysis of their light can help us distinguish them in groups according to their common physical properties.

When a spectrograph separates the stellar light into its component colors, a continuous band of colors can appear which includes narrow dark lines. These lines are created by atoms and ions in the outer layers of the stellar atmosphere. These layers absorb light at unique wavelengths for each type of atom or ion. Atomic physics predicts the positions and intensities of these absorption lines, based on the temperature, abundance, pressure and turbulence of the star. Thus, the morphology of these lines varies from star to star. Classification of stars by spectral features is based on the morphology of their spectra, as the appearance and disappearance of particular spectral features indicate the physical properties of the stars. The current system of spectral-type classification has its roots in the late 1800s at the Harvard Observatory. Astronomer Williamina Paton Stevens Fleming (1857–1911) (Murdin, 2000) initially classified 10351 stars using the letters of the alphabet in order to indicate the strength of their hydrogen absorption lines. So, letter A was used for the strongest, followed by B, C, etc. Back then, in 1890, there was no knowledge that these lines were forming due to hydrogen, but since they were visible in almost all stellar spectra, they provided a consistent way for the data to be categorized. Several years later, the classification was reordered in what is established nowadays to be the order of decreasing temperature. The seven main stellar types are O, B, A, F, G, K, M, so that they provide a smooth transition between the class boundaries. The scheme is based on lines which are mainly sensitive to stellar surface temperatures rather than actual differences in composition, gravity, or luminosity. This reordering was done primarily by astronomer Annie Jump Cannon (1863-1941) (Bok, 1941), also at the Harvard Observatory, while preparing the Henry Draper catalog of 225000 stars. Moreover, she subdivided each class into as many as ten subclasses, by adding the numbers 0 through 9 after the letter, to consider changes within a class. This method of spectral classification was formally adopted by the International Astronomical Union in 1922, and is still used today.

Initially, it was believed that the strength of the lines directly determined the amount of each element found in the star. However, stellar nature proved to be more complex than that. The theoretical background behind the ordering was discovered in 1925. Most stars have very similar compositions, so the strength of hydrogen and other lines in the spectrum is not a direct measure of the composition of the star. Actually, it is indicator of temperature, as a result of processes related to atomic physics occurring in the star. At relatively low temperatures, the gas in a stellar atmosphere contains many atoms, as well as molecules, and these produce the strongest absorption lines. At higher temperatures, molecules are destroyed and atoms begin losing electrons, so absorption lines of ions begin to appear. As the temperature increases the ionization becomes more intense, altering further the pattern of absorption lines. Thus, the smooth sequence of line patterns is actually a temperature sequence. These concepts of the physics that govern the stellar spectra are explained with detail in Chapter 2.

The early spectral catalogs mentioned above, included mostly stars with bright apparent magnitude, as instrumentation and technology were imposing restrictions to the boundaries of science conducted. Thus, most M stars therein, were giants rather than dwarfs. Hertzsprung in 1905 and Russell in 1914 independently created the diagram, which has taken their names eventually, showing the dominant number of giant stars detected.

A modern version of the Hertzsprung-Russell diagram is presented in Figure 1.1, in which more than four million stars within five thousand light-years from the Sun are plotted using information about their brightness, color and distance from the second data release from ESA's Gaia satellite (Gaia Collaboration et al., 2016). Plotting luminosities against temperatures of stars, a main sequence appears, with giant stars at the upper left edge and dwarfs at the lower right edge of the diagram.

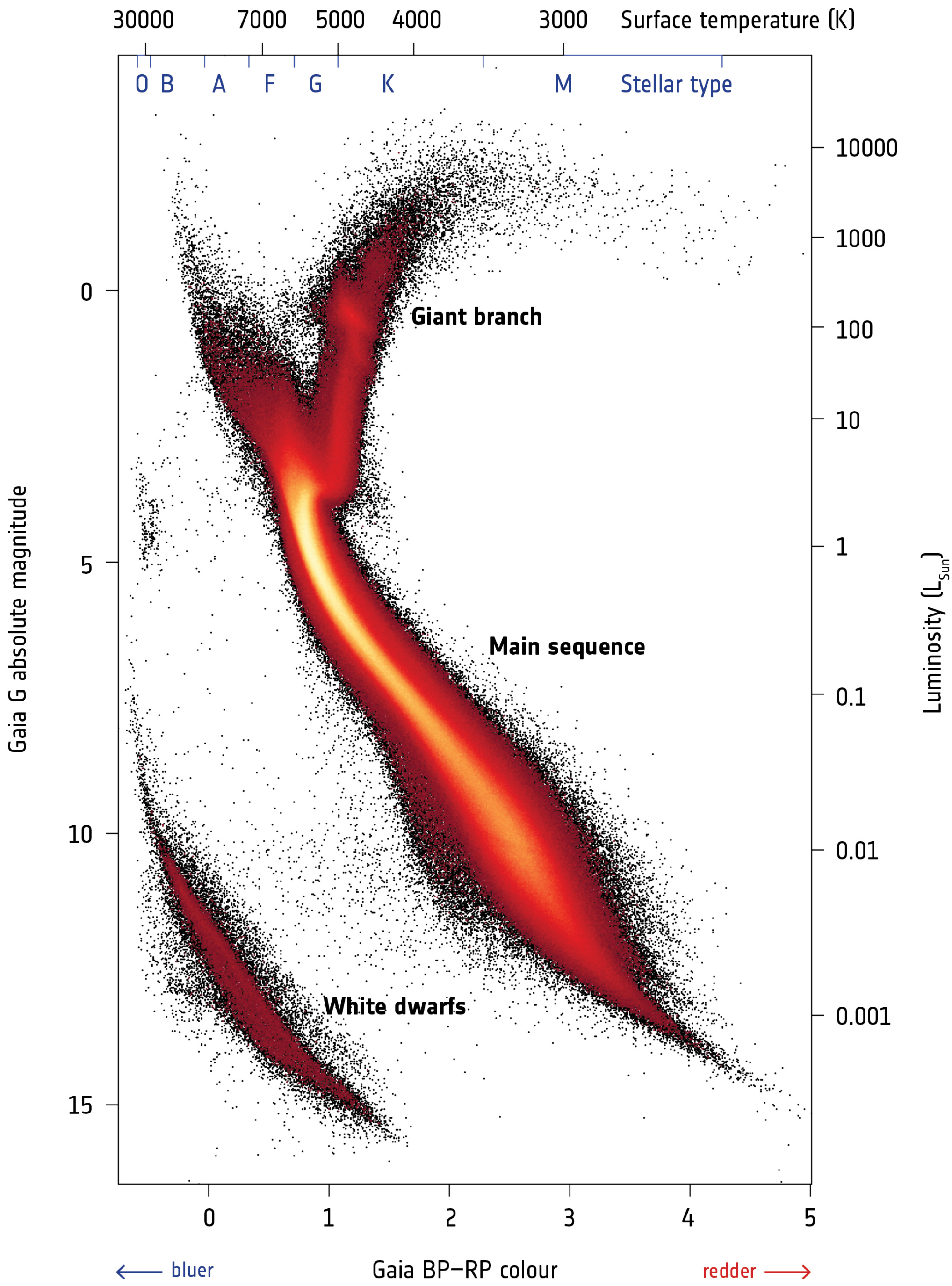

Figure 1.1: H-R diagram created with Gaia data. Source: Gaia Data Processing and Analysis Consortium (DPAC); Carine Babusiaux, IPAG – Université Grenoble Alpes, GEPI – Observatoire de Paris, France.

1.1. M-Dwarf stars

M dwarfs are small, cold and faint stars in the main sequence. They have radii between 0.08 to 0.62 $R_\odot$ and masses ranging from 0.08 to 0.60 $M_\odot$ (Baraffe & Chabrier, 1996). They are relatively cool with temperatures in the range of 2000 to 4000 K (Önehag et al., 2012). Their luminosities vary between 0.0001 and 0.08 $L_\odot$ (Mann et al., 2019).

M dwarfs have large convective envelope and small radiative core which, however, contains about 90% of the mass for a 0.55 $M_\odot$ star with spectral type M0. As the spectral type decreases to M3, this mass fraction becomes 70% for a 0.4 $M_\odot$ star while the mass in the envelope increases, and when reaching type M4 with mass 0.25 $M_\odot$, the star becomes fully convective (Reid & Hawley, 2005). This means that the star can burn a relatively higher amount of its fuel before leaving the main sequence, and thus have a much longer estimated lifespan than FGK stars. A M dwarf with mass 0.1 $M_\odot$ can continue burning hydrogen for up to hundreds of billion years. Their long-lasting life, as well as the fact that low-mass stars are more likely to form than massive ones, have a result M dwarfs being the most common stars in the Galaxy. It is estimated that 70% of stars in Milky Way are M dwarfs (Henry et al., 1994). Despite their abundant presence, M dwarfs can not be seen with naked eye from Earth, because there are none close by enough to be seen, and the closest ones have too low intrinsic brightness. Regarding their absolute visual magnitudes, M dwarfs have $V-$band absolute magnitudes between 7.5 and 20. The Sun, a G-type main-sequence star, has absolute magnitude of 4.83.

The spectral type of M dwarfs are indicated mainly by the presence of strong TiO lines, which dominate their optical spectra. The TiO bands saturate for later type M dwarfs, and other molecular bands, such as VO, are required for the spectral classification of late-type M dwarfs. Bessell (1991) have proposed these two molecular bands for spectral type calibrations. Due to their lower $T_{\rm eff}$ values (below 4000 K), M dwarf spectra have stronger molecular absorption bands than FGK stars (Gustafsson, 1989). Most dominantly, TiO, VO and metal hydrides molecular absorption bands are present at optical wavelengths, while H_2O and CO have wide absorption bands in the near-infrared (NIR) wavelength range. These molecules form billions of molecular lines which depress the spectral continuum and eventually it can be hardly identified in several spectral regions. Moreover, telluric absorption due to the atmosphere of Earth also limits the available wavelength ranges to be studied. M dwarfs are relatively much brighter in the NIR than in visible light. J and H bands in the regions of 10000 to 18000 Å are relatively free of both molecular bands and telluric lines, providing conditions for a better measurement of atomic lines (Önehag et al., 2012). Therefore, the proper selection of wavelength ranges with atomic lines that can be measured correctly, is a crucial step for the accurate characterization of M dwarfs.

Spectroscopic analysis of M dwarfs is still a difficult and challenging task. However, there is room for new and innovative methods both in the optical and NIR wavelength regions.

1.2. Motivation for M-dwarf analysis

The work of this thesis is driven by the need for the accurate determination of the M-dwarf stellar atmospheric parameters in the optical and in the NIR, developing methods able to overcome the obstacles that nature imposes in the M-dwarf spectra. The motivation to obtain knowledge for M dwarfs lies in several reasons. M-dwarf characterization plays an important role in multiple areas of astronomy: the research for exoplanets, the galactic astronomy, as well as stellar astronomy itself.

1.2.1 Exoplanet detection and characterization

Since the beginning of time, beings have turned their eyes upon the night sky, setting one fundamental existential question: are there other worlds out there? Nowadays, modern astronomy has the necessary scientific and technological tools to search for planets that could give a positive answer to this question. Wolszczan & Frail (1992) detected the first exoplanet in the early 90's. Until these lines are written, 5502 exoplanets* have been recorded, since better instrumentation nowadays make the detection common.

Planets can have different bulk compositions and be characterized as rocky, gaseous, iron or water ones (Thiabaud et al., 2014). Chemical composition of the host star is important for interior planetary structures, since stellar elemental abundances such as Fe, Si and Mg are main constraints to reduce degeneracy in interior structure models and to constrain mantle composition (Dorn et al., 2015).

The prime interest of the astronomical community is to find Earth-like planets, that could sustain life in the form we know it. As M dwarfs are the main stellar component of our Galaxy, they may be the biggest population of appropriate planetary hosts too (Lada, 2006). Indeed, the number of M dwarfs known to actually host exoplanets is increasing (Astudillo-Defru et al., 2017). Studies using observations taken by Kepler mission

*http://exoplanet.eu

(Borucki et al., 2010) indicate that rocky planets are common around M dwarfs having orbital periods of less than 50 days (Cassan et al., 2012). Specifically, M stars are prone to form rocky Earth-like planets rather than giant gaseous planets (Bonfils et al., 2013, Delfosse et al., 2013), so the efforts on this stellar population are on the right path.

With advances in astronomical instrumentation, the discoveries of exoplanets are becoming more and more frequent. Space-based transit missions such as TESS (Ricker et al., 2015) and PLATO (Rauer et al., 2014) are surveys dedicated to detect rocky planets around stars in the near galactic region, including M dwarfs. The small mass and radius of M dwarfs allow exoplanets to imprint larger signals on the observational data of the system that are relatively easier to be detected compared to planets around more massive and larger stars. It is only possible to obtain planetary global parameters such as its radius and mass if the stellar parameters are accurately known. Thus, it is crucial to characterize the host star, in order to characterize the exoplanet around it. Knowing the properties of the star is fundamental prerequisite, for deriving the planetary parameters which can only be obtained if the stellar parameters are determined accurately and precisely. When a possible exoplanet is detected, follow-up observations and analysis are required to confirm its existence and derive its properties. Besides mass and radius, full characterization of the new exoplanet would require derivation of its surface temperature, atmosphere composition, density and internal structure.

There are several methods that can be used to detect planets around other stars. Below, we describe how these methods work and what information can provide for the detected planets.

1.2.1.1 Transit method

The most successful method, in terms of number of exoplanets detected, is the transit method. During a planet passing in front of the host star, the total brightness observed decreases, as a small amount of stellar light is blocked by the transiting planet. This decrease of brightness appears periodically, every time the transit occurs. Figure 1.2 shows a representation of a transit of the planet and its impact on the light received. Transits occur when the planet crosses the face of the star from the observer's line of view, causing a small dip in the stellar brightness. Ingress starts at t_1 and by t_2 the planet is fully within the stellar disk from the observer's perspective. This is reversed for egress at t_3 and t_4 respectively. The curve in the transit is caused by the change of brightness from the stellar centre to its limb. The decrease of stellar brightness during the transit gives the measurement of the planet-to-star radius ratio according to the following relation:

$$\frac{\Delta L}{L} \sim \left(\frac{R_p}{R_s}\right)^2 \tag{1.1}$$

where L is the luminosity of the star, ΔL is the maximum luminosity variation, or else the transit depth, while R_s and R_p are the radius of star and planet respectively. Therefore, the stellar radius must be measured with the greatest accuracy possible, in order to calculate the planetary radius correctly.

Another factor defined for transits is the geometric probability, given as:

$$P \approx \frac{R_s}{a(1-e^2)} \tag{1.2}$$

where e is the eccentricity of the orbit, R_s is the radius of the star and a is the semi-major axis of the orbit, meaning the distance between the planet and the star. The probability of transit increases with the size of the star but decreases with distance to the star. In addition, this means that the transit method is most sensitive to exoplanets with large radius, and often in close orbit as these ones are more likely to be aligned with the observer's point of view to the host star.

The first transit was observed by Henry et al. (2000) and Charbonneau et al. (2000) around the star HD209458. The smallest planet discovered around a main-sequence star is Kepler-37b orbiting star Kepler-37 in the constellation Lyra, with a radius slightly greater than that of the Moon and slightly smaller than that of Mercury (Barclay et al., 2013). The vast majority of transit detections have come from Kepler (Borucki et al., 2008, 2010, 2011), a space-based mission for detecting Earth-size and smaller planets around solar-like stars. Besides Kepler, TESS (Ricker et al., 2015) has also announced discoveries of transiting planets (Gandolfi et al., 2018, Huang et al., 2018). CHEOPS (Broeg et al., 2013) is designed for transit follow-up of bright stars with known planets, providing high precision transit photometry, in order to obtain precise planetary radii. PLATO (Rauer et al., 2014) is another transit survey mission planned for launch in 2026. In contrast to Kepler it will focus on brighter nearby stars, with the goal to detect and accurately determine the planetary parameters of Earth-like planets. Apart from transit photometry done both with the space instruments mentioned above, and from instruments on earth like WASP (Pollacco et al., 2006) located at the Observatorio del Roque de los Muchachos on the island of La Palma in the Canary Islands and at the Sutherland Station of the South African Astronomical Observatory with aim to search for bright transiting exoplanet systems suitable for spectroscopic follow-up observations.

When a transiting planet crosses in front of the host star it blocks out light from the star. However, if the planet has a non-opaque atmosphere, a small portion of light passes through its atmosphere. The light that passes through the exoplanet atmosphere is partially absorbed, and is faintly imprinted with absorption lines. Transmission spectroscopy has been used to detect several elements and molecules in the atmosphere, revealing its chemical composition. Such studies are by Charbonneau et al. (2002) for Na, Tinetti et al. (2007) for H_2O, Brogi et al. (2014) for CO, Hoeijmakers et al. (2018) for Fe and Ti. The radius of the transiting exoplanet can also appear to change size when observed at wavelengths where there is strong opacity in the atmosphere (Burrows et al., 2000). Transits in different wavelength bands will have varying depths, dependant on the opacity of the atmosphere to each band. In planetary transits, there is degeneracy of the star-planet properties from the transit shape in a single band, for example systems of stars and planets with different sizes can have the same R_S/R_P ratio. By observing transits in multiple band-passes, degeneracy between the stellar radius and the orbital inclination can break as well as the stellar limb darkening can be determined (Jha et al., 2000).

The transit method has the highest false-positive rate per detections among the detection methods described below. To quantify this, Santerne et al. (2012) reported a false positive rate close to 35% for short period giant planets. Stellar activity is a main reason for detecting signs which mimic those of a transiting planet, since it causes an intrinsic variability in the luminosity of the star. A starspot is a cool region on the stellar surface that is caused by concentrated magnetic fields which reduce convection. This region has lower luminosity locally and as it rotates with the star, it creates quasi periodic variations of brightness, similarly to what a transiting planet would cause. Furthermore, starspots can influence the precision of the planet radius measured through the transit. An unidentified spot will appear to create a deeper transit, leading to a false determination of larger planetary radius. However, the presence of starspots on stellar surface can be observed during a planetary transit. If a planet passes in front of the spot, the luminosity decrease from the spot is temporarily hidden and a small bump occurs in the transit shape. Other astrophysical phenomena which can be interpreted wrongly as transiting exoplanet signals can be a binary system where a white-dwarf star transits its stellar companion. Follow-up radial-velocity (RV) observations are usually required, to confirm or not the actual existence of an exoplanet. On the other hand, the transit method complements RV measurements as the inclination i of the orbit can be determined from the transit. These determinations remove the $sini$ component found in the $M_p sini$ of RV detections, so the actual mass M_p of the exoplanet can be revealed.

In order to compare the relative decrease of stellar brightness for the Sun by the transit of Earth and the same effect for an M dwarf which hosts an exoplanet with radius equal to the radius of Earth, we adopt the following values for an average M3 dwarf: M_D = 0.37 $M_\odot$, R_D = 0.36 $R_\odot$ and L_D = 0.016 $L_\odot$ for its mass, radius and luminosity respectively (Pecaut & Mamajek, 2013). The radius of the Earth, and assuming the same value for the exoplanet, is equal to 0.00916 $R_\odot$. By applying Eq. 1.1 for the two cases, we obtain $\Delta L_\odot / L_\odot \sim$ 0.0084% for the Sun and $\Delta L_D / L_D \sim$ 0.065% for the M3 dwarf.

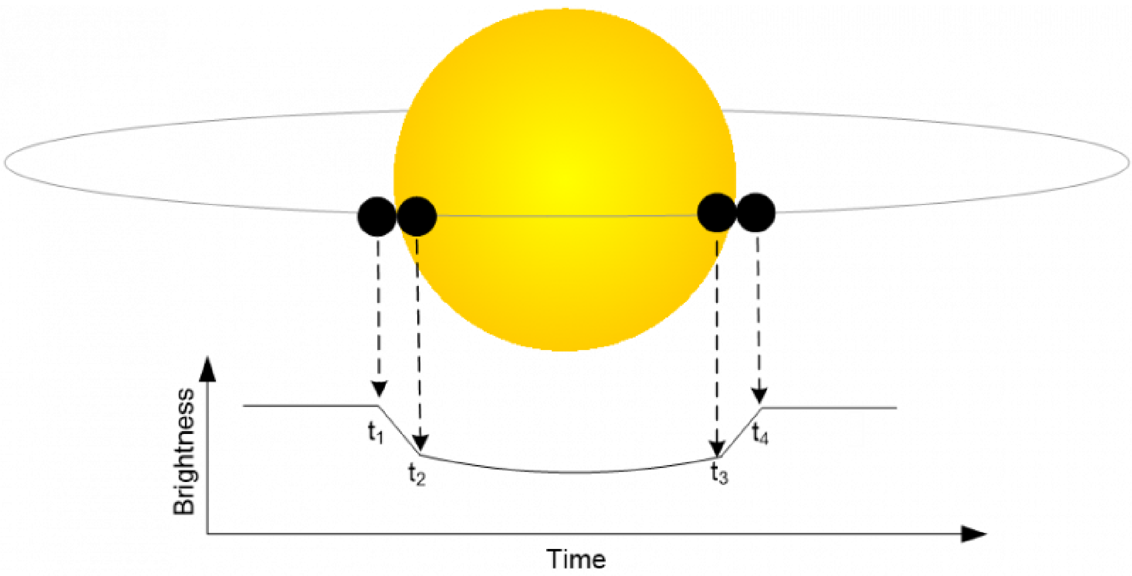

Figure 1.2: Illustration of planet transiting the host star and its impact on brightness. Image credit: `https://britastro.org`

1.2.1.2 Radial-velocity method

When an exoplanet orbits a star, they both orbit their common center of mass called barycenter. Since the star is more massive than the exoplanet, the center of mass is much closer to the star. The spectrum of the star periodically oscillates with the orbital period of the planet, due to the change in relative motion to the observer. This method measures the radial velocity (RV) of the star, meaning the velocity projected along line of sight, by analyzing the Doppler shift of its spectral lines, caused by the gravitational interaction with the exoplanet. Any radial motion towards and away from Earth will be observed as blueshift or redshift of the spectrum respectively, due to the Doppler effect. This spectral pattern is indicative of an orbiting planet. This phenomenon is illustrated in Fig. 1.3.

The variation of RV, directed along the line of sight, is given by the following relation:

$$RV = \gamma + K[\cos(\nu(t, P, T_0, e) + \omega) + e\cos(\omega)] \tag{1.3}$$

where γ is constant barycenter velocity of the system relative to the Sun (for which the barycenter motion of the Earth is known and removed), K is the velocity semi-amplitude, e the eccentricity, and ω the argument of periastron. The true anomaly ν, is a function of time t, orbital period P, the time of periastron passage T_0 and eccentricity.

The velocity semi-amplitude K of a star with mass M_S due to a companion planet with mass M_P with orbital period P, eccentricity e, and inclination i is as following:

$$K = \left(\frac{2\pi G}{P}\right)^{1/3} \frac{M_p \sin i}{(M_p + M_s)^{2/3}} \frac{1}{\sqrt{1-e^2}} \tag{1.4}$$

where G is the gravitational constant.

The RV method gave the detection of the first exoplanet around a solar-type star, the 51 Pegasi (Mayor & Queloz, 1995). Unlike to our Solar System structure, the first discoveries by this method revealed planets with masses similar to Jupiter in short-period orbits. For example, in the case of 51 Pegasi, the planet with mass 0.47 M_{jup} has orbit of 0.05 AU. Shortly after, more exoplanet discoveries followed and confirmed the existence of planets eventually known today as ”hot Jupiters” (Butler et al., 1997, Charbonneau et al., 2000).

The RV amplitudes of the first exoplanets detected were around 60 m/s. Advanced spectrographs such as HARPS (Mayor et al., 2003) and HARPS-N (Cosentino et al., 2012) provided a significantly better precision in RV measurements, bringing the detection limit to the level of 1 m/s. ESPRESSO (Pepe et al., 2014, 2021) is the cutting-edge, high precision optical spectrograph pushing the detection limit down to 10 cm/s.

Since the amplitude of RV signal is inversely proportional to the mass of the star as $K \propto M_s^{-2/3}$, instruments with configuration in the NIR have been developed specifically for M dwarfs, which are low-mass stars and with the majority of their flux emitted in the NIR. Such spectrographs are CARMENES (Quirrenbach et al., 2016), SPIRou (Artigau et al.,

2014) and NIRPS (Wildi et al., 2017).

In order to compare the velocity semi-amplitude K of the Sun-Earth system and the one for a system of an average M3 dwarf with an exoplanet of the same equilibrium temperature (T_{eq}) as Earth, we assume the following typical values as before: M_D = 0.37 $M_\odot$, R_D = 0.36 $R_\odot$ and T_{eff} = 3430 K for the mass, radius and effective temperature of the M3 dwarf (Pecaut & Mamajek, 2013). Regarding the exoplanet, we assume that it has the same T_{eq}, mass, albedo and inclination as Earth. In addition, the orbital period P, which is a parameter inside Eq. 1.4, is connected with the semi-major axis of the orbit as following:

$$P = 2\pi\sqrt{\frac{\alpha^3}{G(M_s + M_p)}} \tag{1.5}$$

where α is the semi-major axis, M_S is the stellar mass, M_P is the planetary mass and G is the gravitational constant.

The T_{eq} of a planet can be expressed as below:

$$T_{eq} = T_{eff}\sqrt{\frac{R_s}{2\alpha}}\,(1 - A_B)^{1/4} \tag{1.6}$$

where T_{eff} is the stellar effective temperature, R_S is the stellar radius, α is the semi-major axis and A_B is the Bond albedo of the planet.

If we combine Eq. 1.4 and Eq. 1.5, the fraction between the K parameters of the two systems can be expressed as:

$$\frac{K_D}{K_\odot} = \sqrt{\left(\frac{\alpha_\oplus}{\alpha_P}\right)\frac{(M_\oplus + M_\odot)}{(M_P + M_D)}} \tag{1.7}$$

where K_D and $K_\odot$ are the velocity semi-amplitudes of the M dwarf and the Sun respectively, while $\alpha_\oplus$ and α_P are the semi-major axes of the Earth and the planet respectively. The same subscripts are used for the masses M of the respective objects.

Assuming that this exoplanet has the same T_{eq} as Earth, the fraction of the semi-major axes can be expressed via Eq. 1.6 as:

$$\frac{a_\oplus}{a_P} = \frac{R_\odot}{R_D}\left(\frac{T_\odot}{T_D}\right)^2 \tag{1.8}$$

where $R_\odot$ and R_D are the radius of the Sun and the M dwarf respectively, while $T_\odot$ and T_D are the T_{eff} of the Sun and the M dwarf respectively.

Finally, by inserting Eq. 1.8 into Eq. 1.7, and by applying the values of all the parameters as adopted earlier, the velocity semi-amplitude of this M3 dwarf hosting an Earth-like exoplanet will be K_D = 21.3 $K_\odot$.

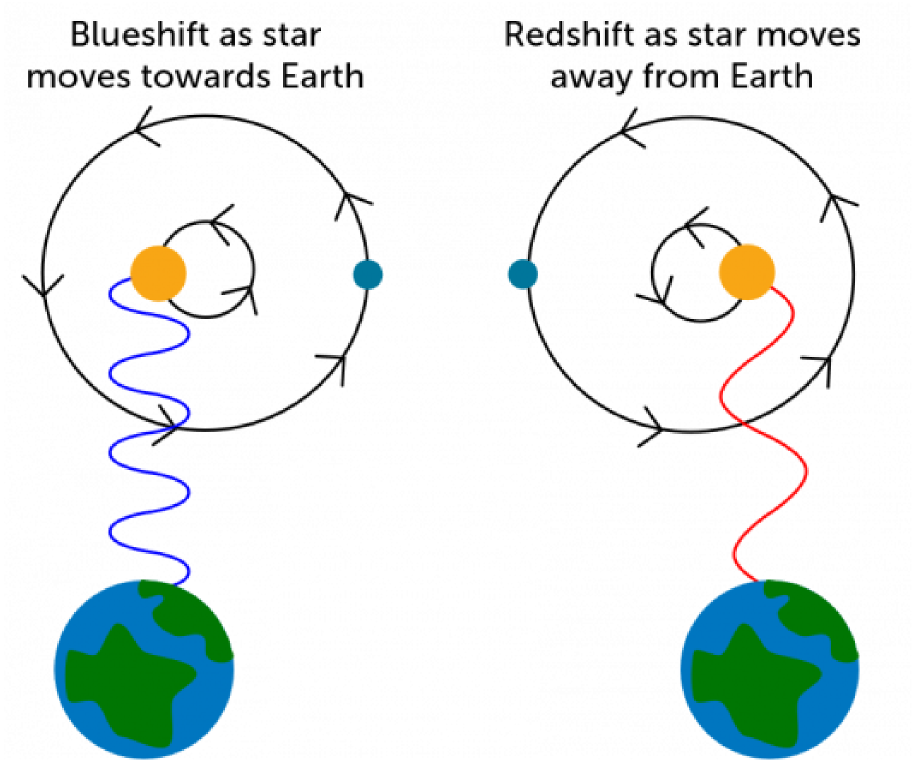

Figure 1.3: Illustration of star and planet orbiting the common center of mass. This motion can be detected as a blueshift and a redshift in the stellar spectrum due to the Doppler effect. Image credit: `https://www.princetoninstruments.com/`

1.2.1.3 Direct imaging

As the name of this method implies, direct imaging aims to gather an image of the exoplanet light separated from the light of its host star. The greatest challenge of obtaining a point source image of an exoplanet is the tiny ratio of the planet flux compared to the stellar flux. Direct imaging requires resolving the angular separation between the star and planet and is best performed to detect giant planets in orbits wider than 10 AU around nearby stars. Extremely young giants, which have higher thermal emissions, observed in the infrared are also potential candidates for detection with direct imaging.

The first planets were directly imaged applying adaptive optics with instrument NACO on the VLT (Chauvin et al., 2004). Other three planets around HR8799 were detected using angular differential imaging on the Keck and Gemini telescopes (Marois et al., 2008), and planet Fomalhaut-b using chronography on the HST (Kalas et al., 2008). Later, study by Marois et al. (2010) revealed a fourth planet in the system HR8799, which is shown in Fig. 1.4. High-contrast adaptive optics instruments, such as SPHERE at VLT (Beuzit et al., 2008) and GPI (Macintosh et al., 2008), are being used with several techniques to observe exoplanets, such as blocking or cancelling out the light from the star while retaining the planetary signal (Marois et al., 2005, Sirbu et al., 2017).

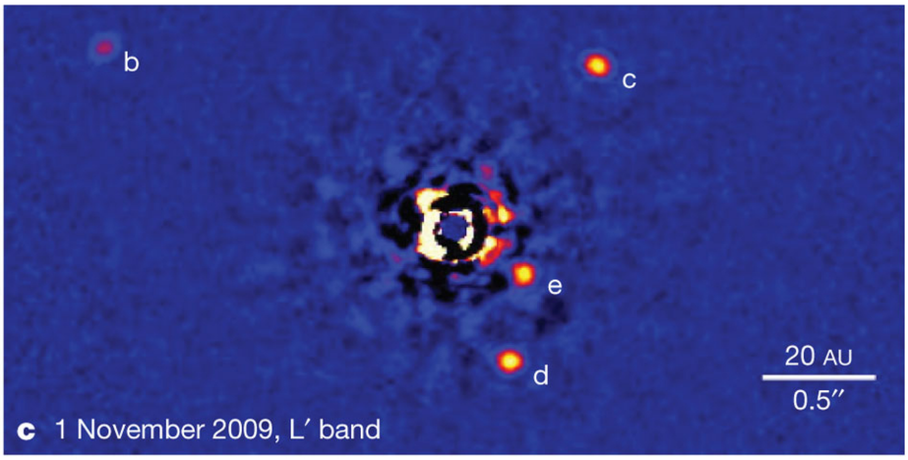

Figure 1.4: Detection by direct imaging of four exoplanets around HR8799. Taken by Marois et al. (2010).

1.2.1.4 Microlensing

Microlensing is an astronomical effect predicted by Einstein's General Theory of Relativity. The mass of an object bends spacetime which causes light to be deflected around objects of large mass. Microlensing is the method with which an observer looks at a star as another star in between the observer and the star passes through the line of sight. The intermediate star acts as a lens and increases the magnitude of the distant star. This increase of magnitude will reach its maximum when the two stars are most aligned as seen from the observer's point of view. Similarly, for the detection of an exoplanet, there must be an exoplanet orbiting the intermediate star. The exoplanet, acting as a microlens, will cause a secondary increase in magnitude. The amount of increase in magnitude is proportional to the mass of the exoplanet, as well as related to its configuration in the orbit around its host star. An example is shown in Fig. 1.5 where a lensing magnification is presented for OGLE2005-BLG-390 (Beaulieu et al., 2006). On the falling edge of the lensing event, a bump occurs due to the presence of a 5.5 Mjup companion. The first planet using this technique was found by Bond et al. (2004), a 2.6 Mjup planet, with a semi-major axis of about 4.3 AU, orbiting a K-dwarf star.

The difficulties of microlensing is that they require the alignment by chance between Earth, a nearby lens star, and a distance source star, which is unrepeatable. Unlike planets detected by other methods, which are associated with particular stars and can be observed repeatedly, planets detected by microlensing will never be observed again. Microlensing events are more probable towards the galactic bulge where there are more stars and thus a higher chance for the alignment to occur. The microlensing technique has been efficient in detecting exoplanets similar in size to Neptune. The precise stellar proper motions from the Gaia mission are being used to predict possible future alignments that could produce microlensing events (Klüter et al., 2018).

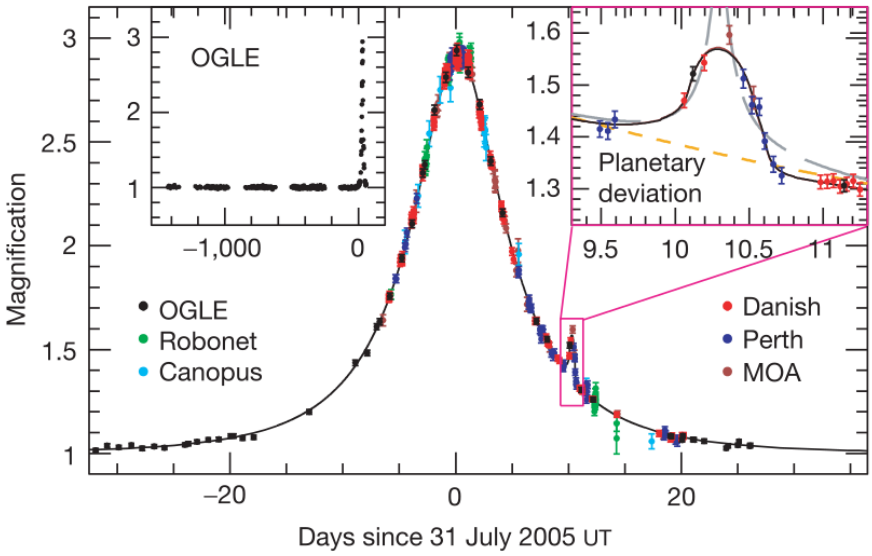

Figure 1.5: Microlensing event of OGLE2005-BLG-390 from Beaulieu et al. (2006). The presence of the planet causes the small bump shown in the upper right window.

1.2.1.5 Astrometry

Astrometry is the measurement of the position, i.e. the coordinates, of a star on the sky. These coordinates may change over time due to its relative motion compared to the Solar System. Moreover, an exoplanet might cause small changes in the coordinates due to the orbit of the star and exoplanet around the centre of mass. Using astrometry to detect exoplanets is very similar to the radial velocity method described above. ESA's Gaia mission (Gaia Collaboration et al., 2016) is devoted to provide precise results on astrometry, leading to exoplanet detections with this method (Perryman et al., 2014).

For a circular orbit the angle of the semi-major axis of the apparent orbital ellipse, the amplitude of the astrometric signature is given by:

$$\theta = \frac{M_p}{M_s + M_p}\frac{a}{d} \tag{1.9}$$

where M_P and M_S are the planet and stellar mass respectively, a is the semi-major axis in AU and d is the distance in parsec from the observer to the system.

From this relation we see that the astrometric signal is proportional to the planet/star mass ratio and to the orbital radius a. The amplitude of the astrometric signal decreases inversely with distance from the observer as the angle becomes smaller. This is in contrast to the RV and transit methods for which the amplitude is not affected by distance. Astrometry is complementary to the RV method, as it measures the orbital motion perpendicularly to the line of sight, allowing the determination of the three-dimensional orbit.

Astrometry has detected many binary stars (Gontcharov et al., 2000) and found several brown-dwarf companions (Sahlmann et al., 2011), however the exoplanets discovered are few. The first exoplanet detections based on data from Gaia were confirmed recently by Panahi et al. (2022).

The predicted astrometric variations for an exoplanet are at the level of sub milliarcseconds and thus are not achievable from the ground due to atmospheric turbulence. The most precise astrometric measurements come from space. These are performed using Gaia with the release of astrometric parameters for million sources (Gaia Collaboration et al., 2018) and reaching a precision of 0.04 mas for the brightest stars with magnitudes below 14.

In order to compare the $\theta_{S.E.}$ of the Sun - Earth system and the $\theta_{D.P.}$ of the adopted M dwarf - exoplanet system, we follow the previous assumptions of an M3 dwarf with M_D = 0.37 $M_\odot$ and a planet with mass and T_{eq} equal to that of Earth. Additionally, in this case, we assume that the two systems have the same distance from the observer. By applying to Eq. 1.6 the same T_{eq} in the two cases, the ratio $\alpha_\oplus/\alpha_P$ becomes equal to 7.88, adopting T_{eff} = 5777 K for the Sun and T_{eff} = 3430 K for the M3 dwarf, as well as the typical radius of R_D = 0.36 $R_\odot$. By applying to Eq. 1.9 this ratio and the respective masses of Sun, M3 dwarf and the mass of Earth in both cases, we get $\theta_{D.P.}$ = 0.343 $\theta_{S.E.}$.

1.2.1.6 Time transit variations

In this method, firstly a transiting exoplanet needs to be detected. In the case of a second (non-transiting) planet existing, its interaction with the transiting first planet, will cause variations in the occurrence of mid-transit. This interaction between the two planets will cause the mid-transit to happen earlier or later compared to the time it would occur if only one exoplanet would be present (Agol et al., 2005).

Due to the mass-radius degeneracy, the transit of a single planet can not determine directly the planetary mass. However, in multiple planet systems, the masses and sometimes the presence of other planets in the system can be determined from perturbations in the transit time and duration (Holman & Murray, 2005). A large number of systems have been detected that show transit timing variations (TTV) and transit duration variations (Holczer et al., 2016) due to the gravitational interaction between planets. Statistically, the confirmation of existence of multi-transiting planets is more straightforward than single planets, because the probability of having multiple false positives, being a product of the individual probabilities, is lower than having multiple planets in the system (Lissauer et al., 2012). Thus, multiple-planet systems are easier to be validated.

1.2.1.7 Modulations

Modulations caused by secondary transits and phase variations are an extension of the transit method. Planets with short periods and in close orbits around their stars will have reflected light variations because they will go through phases from full to new and back again, like the phases of Moon. In addition, these planets are heated as they receive much starlight, making thermal emissions potentially detectable. This method of detection requires higher precision to detect the reflection and thermal emission of the exoplanet. Since telescopes receive only the combined light, without the ability to resolve the planet from the star, the brightness of the host star seems to change over each orbit in a periodic way. The observed light curve is analyzed considering it has two components, not only light emitted from the star but also light from the planet, although at a much lower flux level. A transiting planet is shown in Fig. 1.6 at several positions of the orbit indicating the proportion of day side and night side in different phases observed. It shows the planet in orbit around a star, in which the planet also passes behind the star causing an occultation. Below the orbit, the diagram shows the changing flux variation as solid black line over time, following the orbit. If the orbital alignment is such that the planet will pass behind the star, it will cause an occultation of the planet. At this point the only light received will be only from the star, creating a baseline stellar measurement. The depth of the occultation, gives a direct measurement of the relative brightness of the planetary disk if the star-planet radius ratio is known (Winn, 2010). On the other hand, during the primary transit there is also a small thermal emission contribution from the night side of the planet, as well as it partially blocking the star. Throughout the orbit of the planet there is a variation in the planetary flux due to the alternating day-to-night side of the planet observed. The multiple components of the planetary flux, reflection and emission can be analyzed with multi-band phase curves (Esteves et al., 2013).

Optical phase curves will mostly show the reflected light from the day side of the planet, allowing modeling of the atmospheric albedo, which is the fraction of light reflected by the atmosphere, and can provide information on the atmospheric scattering (Madhusudhan & Burrows, 2012) and aerosol composition (Oreshenko et al., 2016). Thermal emission of the planet will provide stronger modulation of infrared phase curves and can provide insights into the atmospheres thermal structure and heat circulation (Koll & Abbot, 2016). When a planet has a high albedo and is situated around a relatively luminous star, its light variations are easier to detect in visible light while darker planets or planets around low-temperature stars are more easily detectable with infrared light with this method.

This method can find planets because the reflected light variation with orbital phase is largely independent of orbital inclination and does not require the planet to pass in front of the disk of the star compared to the main transit method. Spectra obtained during the occultation will have no planetary signal and can be used remove the stellar component from spectra obtained at other phases to obtain the planetary spectrum.

The first-ever direct detection of the spectrum of visible light reflected from an exoplanet was made by Martins et al. (2015), who developed a method which retrieved the signal from the reflected light of exoplanet 51 Pegasi b.

1.2.1.8 Disk kinematics

A protoplanetary disk is a rotating circumstellar disc of dense gas and dust, surrounding a young, newly formed star. The formation of extrasolar planetary systems that are so different from our own Solar System is still a research area not fully understood. However, the past few years there has been progress on analysis of the disks of gas and dust around young stars. Observations with the Atacama Large Millimeter/submillimeter

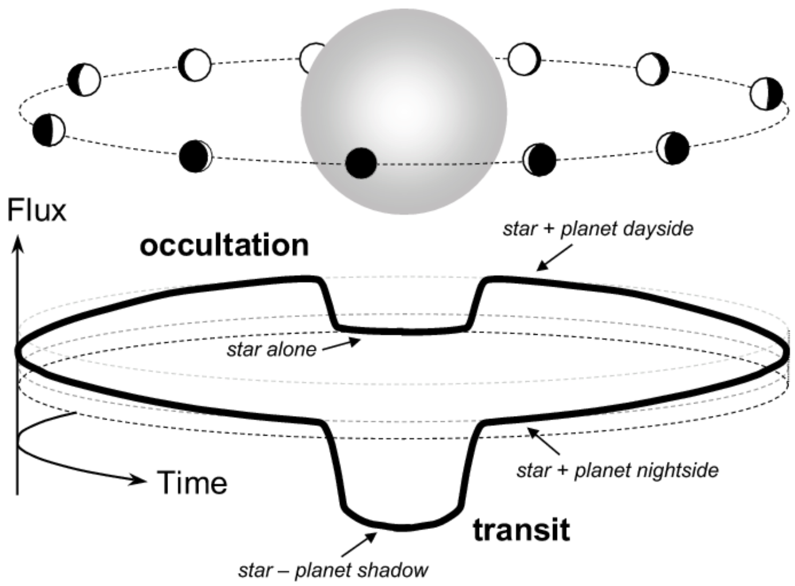

Figure 1.6: Flux from a star and planet in different phases during its orbit from Winn (2010).

Array (ALMA) and extreme adaptive-optics systems have revealed that most disks of gas and dust around young stars contain substructure, including rings and gaps, spirals and azimuthal dust concentrations. Recent ALMA surveys suggest that planets could indeed be responsible for carving out several of the observed gaps. The most straightforward explanation is that the gaps are the results of forming planets interacting with the disc (Dipierro et al., 2015). An embedded planet can explain both the disturbed Keplerian flow of the gas, detected in CO lines, and the gap detected in the dust disc at the same radius according to the same authors. Disc kinematics are dominated by Keplerian rotation. Embedded planets perturb the gas flow in their vicinity, creating spiral waves both inside and outside their orbit. The disturbed velocity pattern is detectable by high spectral and spatial resolution ALMA line observations (Perez et al., 2015). This technique was used to detect embedded planets in the disc surrounding HD163296 Pinte et al. (2018). Moreover, Pinte et al. (2019) reported the kinematic detection of a planet located in a gas and dust gap at 130 AU in the disc surrounding the young star HD97048. While gaps appear to be a common feature in protoplanetary disks, Long et al. (2018) presented a direct correspondence between a planet and a dust gap, indicating that at least some gaps are the result of planet-disk interactions.

1.2.1.9 Summary of detections and quest for an Earth-like exoplanet

The above mentioned techniques are used to find exoplanets. The contribution of each method cumulatively and compared to the others, can be seen in Figure 1.7 *. It is noticed that the transit method has grown rapidly, offering the majority of detections. The other significant method is the radial-velocity (RV) method, which achieves detections in a steady pace over the years. Especially, the two first techniques (transit and radial velocity method) are the ones finding the smallest exoplanets. Since the detection of the first exoplanet around a solar-type star (Mayor & Queloz, 1995), the astronomical community has been able to detect lower mass exoplanets as seen in Fig. 1.8†, which shows all detections of exoplanets during the years against their masses, having color-coded their radius. The regime of Earth-mass exoplanets, which corresponds to the level of 0.003 Mjup, have been reached since the previous decade. In addition, Fig. 1.9 shows the planetary masses against the masses of their host stars, having color-coded the stellar $T_{\rm eff}$ values. We notice that the planets with the smallest masses, have been detected around stars with sub-solar masses such as M dwarfs.

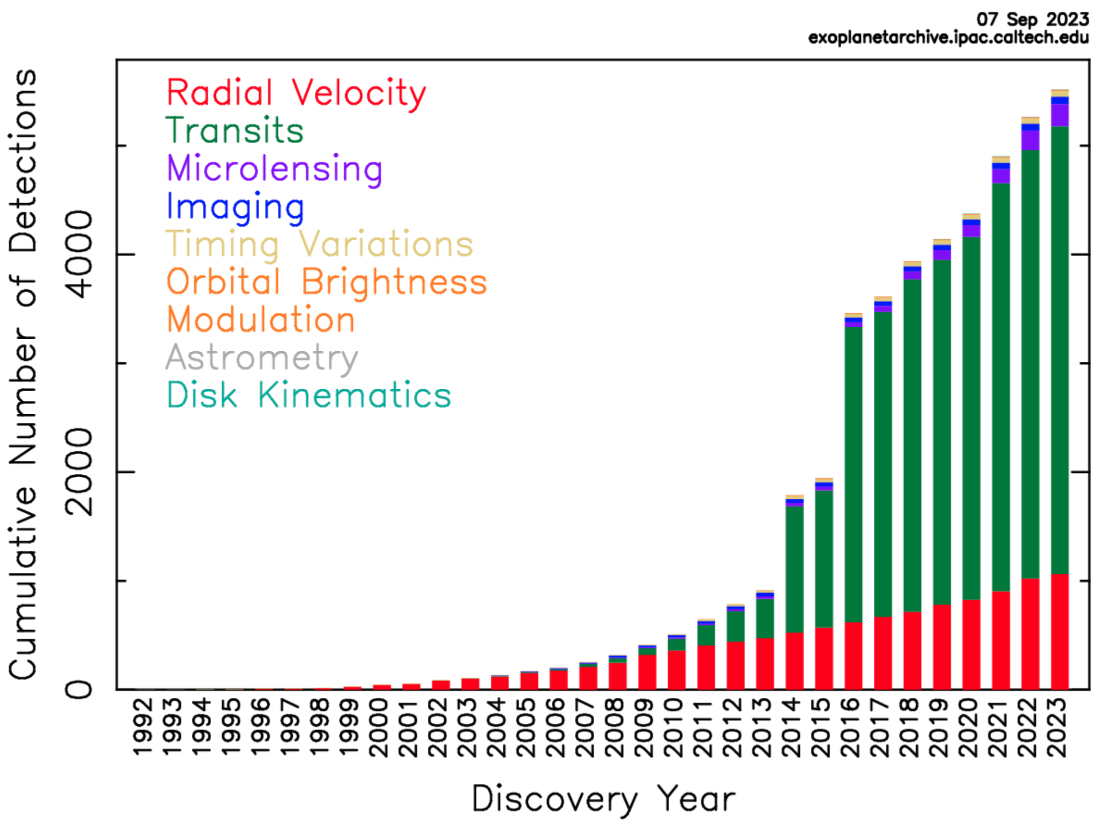

Figure 1.7: Cumulative detections of exoplanets, colored for each method.

*https://exoplanetarchive.ipac.caltech.edu/
†http://exoplanet.eu/

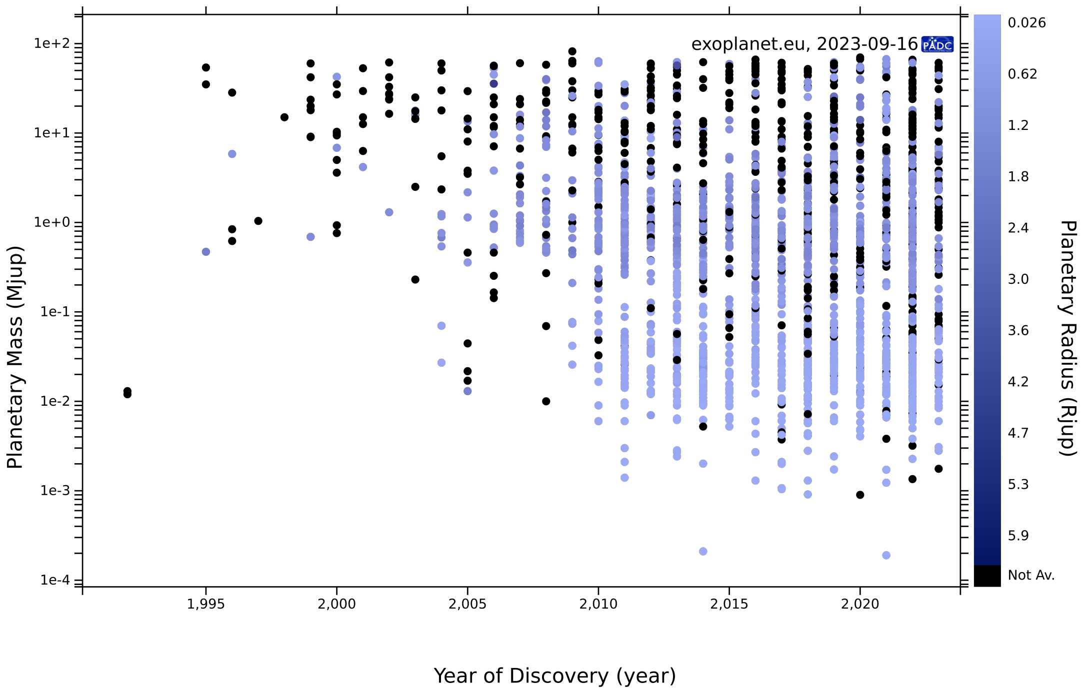

Figure 1.8: Distribution of mass of detected exoplanets during the years.

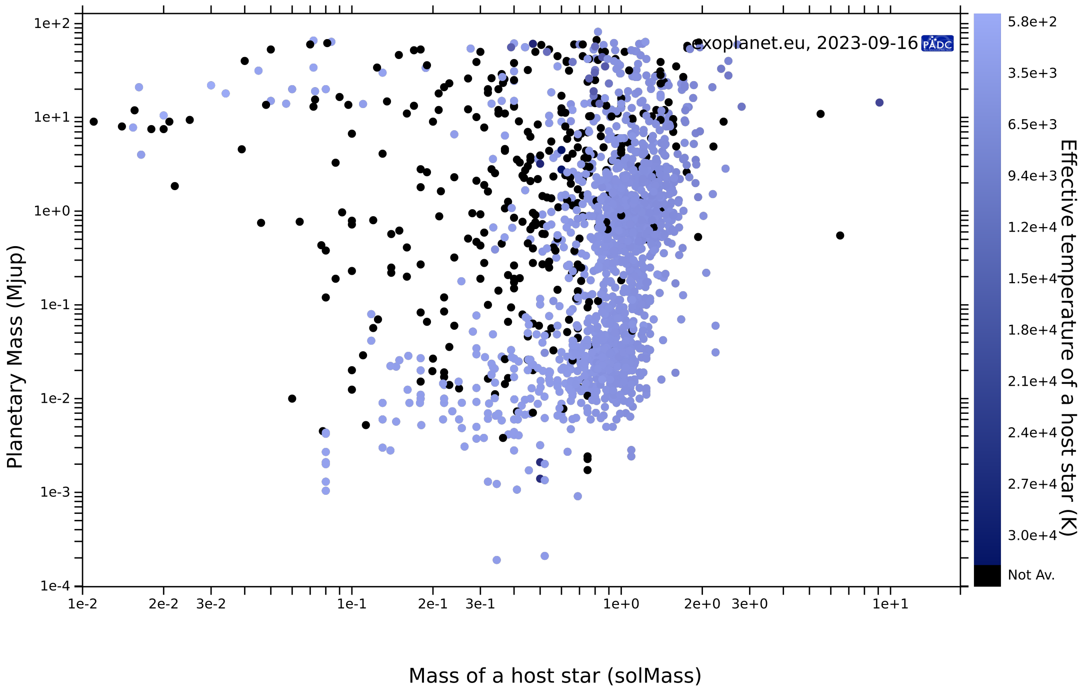

Figure 1.9: Distribution of mass of detected exoplanets against mass of their host stars.

Reasonably, from the variety of exoplanets potentially discovered, those which resemble Earth attract profoundly the scientific interest. However, detecting an Earth-like exoplanet around a star similar to the Sun (G-dwarf star) is quite difficult. The habitable zone is the distance interval from a star where liquid water can be found. This zone is not only dependent on stellar parameters, but also on the atmospheres of exoplanets since an exoplanet with a dense atmosphere can keep the heat, thus be further away from its host star and still have liquid water, compared to an exoplanet with a lighter atmosphere (Kopparapu et al., 2013). Due to the high surface temperature of solar-like stars, the habitable zone will be far from the host star (Kasting et al., 1993). Reasonably, the efforts have been concentrated towards detecting Earth-like planets around M dwarfs which are the lightest stars. M stars are also cooler, hence the habitable zone will be closer to them (Kasting, 1997), compared to more massive and hotter stars, and ultimately the period for habitable exoplanets will be shorter. The shorter period means that the surveys can be shorter for these exoplanets. Moreover, as explained already, since the host stars are smaller the signal from a transit will be easier to detect. Similarly, the RV signal will be larger for an Earth-like planet in the habitable zone of an M dwarf compared to a similar exoplanet around a G star. Thus, it is more efficient to focus on smaller and cooler stars, with potential planets orbiting in closer distances, where the possibilities of detecting habitable planets similar to Earth are greater.

1.2.2 Galactic Astronomy

M dwarfs are of great interest in the research field of Galactic archaeology. Their large numbers, as the 70% of the stars in our Galaxy consists of them, combined with their long lifetimes in the main sequence, which are greater than the Hubble time (Laughlin et al., 1997), make them important for studying the chemical and dynamical evolution of the Galaxy (Lépine et al., 2007).

The measurement of stellar parameters with spectroscopy revealed different kinds of galactic stellar populations. The stars in the universe are divided into three populations. During the 1940's, Baade (1944) identified the two first populations. Population I consist of relatively young and metal-rich stars, while population II consists of relatively old and metal-poor stars. Four decades later, Bond (1981) identified population III for massive old, hot stars with no metal content. Population I stars exist commonly in the spiral arms of our Galaxy. The Sun is an example of a metal-rich star in population I. These stars usually have regular elliptical orbits of the Galactic Center, with a low relative velocity. Their ages vary a lot, since the oldest ones were formed at around 10 billion years ago and new ones still are formed to the present epoch. They are metal-rich, as they were formed when iron and other elements were more abundant in the Galaxy, compared to the earlier stages of the universe. On the other hand, Population II stars have relatively few elements heavier than helium and hence they are metal-poor. These stars were born during an earlier time of the universe, more than 10 billions years ago. Intermediate population II stars are common in the bulge near the centre of our Galaxy, while the ones found in the galactic halo are older. Population II stars are also found massively in globular clusters. These stars are mostly M dwarfs stars since the more massive Population II stars have already ended their life in the main sequence and have already become white dwarfs, neutron stars or black holes. Population III stars are a potential population of extremely massive, luminous and hot stars with virtually no metals. Hypothetically, such stars may have existed at high redshifts in the very early universe and may have initiated the production of chemical elements heavier than hydrogen, which are needed for the later formation of planets. The existence of population III stars is implied by cosmology, but there is no direct detection of them, as they would have turned long ago to white dwarfs or black holes. Indirect evidence for their existence has been found in a gravitationally lensed galaxy in a very distant part of the universe (Fosbury et al., 2003). While the observations did not uniquely diagnosed the presence of Population III stars, they were all qualitatively consistent with the predictions of the models of such stars and their surrounding nebulae.

Furthermore, homogeneous derivation of stellar atmospheric parameters is needed for a proper chemical analysis of the Galaxy. If the parameters are derived with a consistent method, then the errors when comparing populations are minimized. Very precise abundances can unveil new populations within the Galaxy, as the high-α metal-rich population discovered in Adibekyan et al. (2011). In addition, Adibekyan et al. (2012) derived chemical abundances of refractory elements by analyzing spectra from 1111 FGK dwarf stars belonging to the HARPS GTO volume limited sample. As presented in this study, it is possible to separate different galactic populations (thin disk, thick disk, and the halo) by studying the chemical abundances of stars. Furthermore, a continuation of this work was done by Delgado Mena et al. (2017) using the same sample of stars and aiming for the derivation of chemical abundances of heavy elements. There are not many studies on galactic chemical evolution using M dwarfs, because precise abundances are not achieved yet in big samples, but the first steps towards this direction have already been done by Abia et al. (2020), Ishikawa et al. (2022) and Souto et al. (2022).

In the context of the Galactic structure, Reid et al. (1997) used broadband photometry and low-resolution spectra of a complete sample of late-K and M dwarfs brighter than I=22 in three fields at high galactic latitude, to study issues relating to galactic structure and large scale abundance gradients in the Galaxy. Results showed that the average abundance in the Galactic disk remains close to solar even at heights of more than 2 kpc above the Plane. Investigating galactic dynamics and magnetic activity, (West et al., 2006) presented a spectroscopic study and dynamical analysis of $\sim$2600 M7 dwarfs. They confirmed that the fraction of magnetically active stars decreases with vertical distance from the Galactic plane and demonstrated that the drop in the activity fraction of M7 dwarfs can be explained by thin disk dynamical heating. Studying the Galactic disk kinematics, Gizis et al. (2002) suggested that the thick disk component may provide an explanation for the surprisingly low velocity dispersions measured for a photometrically selected sample of ultra-cool dwarfs. If the thick disk is slightly metal-poor, the hydrogen burning limit could lie close to the M7 boundary of the ultra-cool sample.

In relation to the galactic mass and luminosity, Hawkins & Bessell (1988) examined the observed luminosity function comparing it with theoretical functions and worked on the connection between the galactic local missing mass and the presence of low-luminosity dwarfs. Moreover, Kirkpatrick et al. (1994) used data for the luminosity function together with an empirical derivation of the mass-luminosity relation to compute a mass function independent of theory. This mass function increased toward the end of the main sequence, but the observed density of M dwarfs was still insufficient to account for the missing mass. If the increases seen in the luminosity and mass functions are indicative of a large, unseen, sub-stellar population, brown dwarfs may yet add significantly to the mass of the Galaxy.

From all the above, it can be understood that deriving stellar properties for M dwarfs with high accuracy is of great importance for several aspects of Galactic research.

1.2.3 Stellar Astronomy

Theoretical stellar modeling over the last years have developed significantly, but there are still disagreements between the values predicted from current models and the observational data. Methods that rely on the correct determination of the spectral continuum only work well for the metal-poor and earliest types of M dwarfs (Woolf & Wallerstein, 2005). Methods using spectral synthesis have not achieved as precise results as in FGK cases because of the poor knowledge of many molecular line strengths. Recently, spectral synthesis in the NIR has lead to advances, as shown by several studies (Önehag et al., 2012, Lindgren et al., 2016, Rajpurohit et al., 2018, Passegger et al., 2019, Souto et al., 2020, Marfil et al., 2021, Cristofari et al., 2022). Regarding these limitations, most attempts at determining T_{eff} and metallicity use photometric calibrations (Bonfils et al., 2005, Johnson & Apps, 2009, Neves et al., 2012) or spectroscopic indices (Rojas-Ayala et al., 2010, 2012, Mann et al., 2013a). Uncertainties in metallicity range from 0.20 dex using photometric calibrations to 0.10 dex when using spectroscopic scales in the NIR (Rojas-Ayala et al., 2012). Regarding T_{eff}, precisions of 100 K are reported, but significant uncertainties and systematic errors are still present, ranging from 150 to 300 K, depending on the applied methods of determination (Casagrande et al., 2008, Rojas-Ayala et al., 2012).

Therefore, more accurate methods for determining M dwarf parameters could extend the knowledge and the input for the improvement on theoretical modeling of the stars, that in turn would lead to better understanding and progress in the stellar characterization. The field of stellar characterization, which is the topic of this thesis, is presented in detail throughout Chapter 2.

1.3. This thesis

This thesis focuses on deriving stellar atmospheric parameters for M-dwarf stars. This goal is accomplished using high resolution and high S/N spectra in the optical and NIR. For this purpose, two methods are developed: ODUSSEAS for the optical and MPIRA for the NIR.

Chapter 2 explains the theoretical background on stellar atmospheres. It describes the methodologies applied for the stellar atmospheric characterization and presents the concepts on which our tools are based. Furthermore, it includes a literature overview with the work done on the field of M-dwarf characterization, highlighting the achievements of science done among several studies. Chapter 3, describes the development of ODUSSEAS and analyzes the results obtained with this method in the optical. Similarly, Chapter 4 describes the development of MPIRA, presenting the process of its creation and the results obtained in the NIR. Finally, Chapter 5 summarizes the work developed and its main conclusions. It attempts to open a discussion about the future improvements that can evolve the work further.

2. Stellar characterization

In this chapter we describe the most important theoretical aspects that are required for our methodology. We describe the main concepts of physics about the stellar atmospheres and their dependence on stellar parameters, based on the book published by Gray (2005), where the reader should refer to for a more in-depth analysis. In addition, the main methods to derive spectroscopic parameters are described, based on which several works have been developed through the years. We provide a literature review on the research done in the field of M-dwarf characterization.

2.1. Physics of Stellar Atmospheres

Stellar atmosphere is the region that releases the energy produced within the star. The stellar atmosphere is not totally transparent to all light. Part of it, is absorbed or scattered in the atmosphere. In the case of absorption, the light will be emitted later in random direction. This is "printed" as an absorption line in the stellar spectrum. These lines correspond to electronic transitions among the different levels of atoms and molecules. The different elements at different stages of energy in the atmosphere is the reason for absorbing light at different wavelengths. The strength of the spectral lines is affected by the physical conditions in the stellar atmosphere. It depends on the $T_{\rm eff}$, the pressure or else gravity (expressed as $\log g$), the chemical abundances and the atomic characteristics of the transition making the absorption line. The most important aspect in the determination of the stellar parameters is the strength of the absorption line, that also depends on the number of absorbers that correspond to a certain electronic transition. The strength of a line depends on the fraction of atoms excited to the nth energy level, N_n, on which the electron producing the absorption, is. The ratio between the number of atoms in an energy level n and the total number of the atoms of that species is proportional to the statistical weight g_n and the Boltzmann factor. This fraction can be expressed through the Boltzmann equation as following:

$$\frac{N_n}{N} = \frac{g_n}{u(T)} 10^{-\theta(T)\chi_n} \tag{2.1}$$

where N is the total number of atoms per unit volume, T is the temperature, $u(T) = \Sigma g_i e^{-\chi_i/kT}$ is the partition function with k being Boltzmann's constant, $\theta(T)$ = 5040/T and χ_n is the excitation potential for the lower energy level. The statistical weight g_n of a set of quantum states, defined by a set of quantum numbers describing a system, is the total number of states possible with this set of quantum numbers.

While atoms can get excited according to Boltzmann's equation above, they can also get ionized. The ionization ratio for a collision-dominated gas is described by the Saha equation, which relates the ratio of atoms in state r to atoms in the excited state above for the same element, $r+1$, in the following way:

$$\frac{N_{r+1}}{N_r} = \frac{1}{P_e}\frac{(2\pi m_e)^{3/2}(kT)^{5/2}}{h^3}\frac{2u_{r+1}(T)}{u_r(T)}e^{-I/kT} = \frac{\Phi(T)}{P_e} \tag{2.2}$$

where m_e is the electron mass, h is Planck's constant, I is the ionization potential of the neutral atom, and $\Phi(T)$ is all not related to the electron pressure P_e.

For the above, there has been the assumption of Local Thermodynamic Equilibrium (LTE). Thermodynamic equilibrium is achieved when the temperature, pressure and chemical potential of a system are constant. In LTE, these thermodynamic parameters are varying in space and time but this variation is slow enough, so it can be assumed that in the local region of each point, thermodynamic equilibrium exists. LTE is obtained in stellar atmospheres, when the length scale of the changes in temperature is larger than the mean free path. It is a reasonable approximation in dwarf stars because they have small mean free path, compared to the larger mean free path of evolved stars, where LTE is no longer valid. When LTE occurs, each point is considered to behave like a black body of temperature T. It is assumed when the ratio of collision to radiation induced transitions is large, as it is the case for photospheres of FGKM dwarfs.

The atomic lines have properties based on quantum mechanics, that needs to be known for the spectroscopic analysis. The ionization state, of iron as example, FeI describes an element in its atomic form, while FeII describes iron in its first ionized form. The excitation potential χ is the excitation energy level of the lower state in the transition. A atomic line with a high χ is formed in the deeper layers of the atmosphere, since the higher temperatures there can excite the element. On the contrary, atomic lines with lower χ are formed higher in the atmosphere at lower temperatures. The oscillator strength, $\log(gf)$, describes the atomic transition probability. The damping coefficients Γ are caused by the uncertainty of lifetime in an energy level according to Heisenberg's uncertainty principle. For this uncertainty, a natural broadening is introduced. These properties need to be measured from theoretical calculations or experimental atomic physics.

2.2. Effect of stellar parameters on spectrum

2.2.1 The Equivalent Width

The measurement of Equivalent Width (EW) of spectral lines is important in analysis of stellar spectra. The EW is the way to measure the strength of the line. It depends on the atmospheric conditions such as $T_{\rm eff}$, $\log g$, abundance (e.g. [Fe/H]), and microturbulence (v_t). The EW is mathematically described as the integration over the absorption line, by converting its area to a rectangle with its side to the normalized continuum flux (F_c) having this value as width. It is calculated by the following equation:

$$EW = \int_0^\infty \frac{F_c - F(\lambda)}{F_c} d\lambda \tag{2.3}$$

where λ is the wavelength. In the integral, it is assumed that there is one single line, so the integral is over all wavelength. In practice, the integral is calculated in small windows around a spectral line. The EW is illustrated in Fig. 2.1.

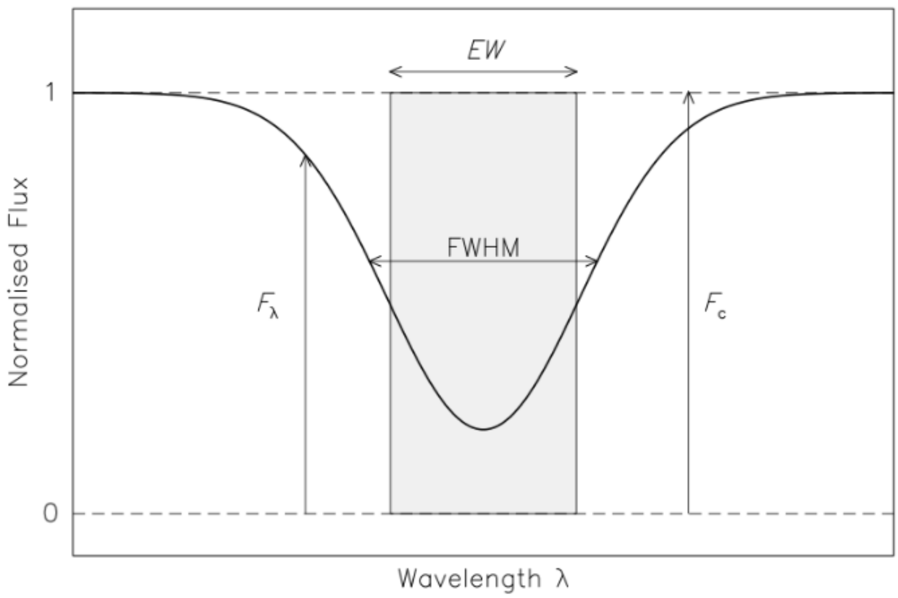

Figure 2.1: The EW of an absorption line is defined as the width of a rectangle that has an area equal to the line, as illustrated in grey. Illustration taken by Carroll & Ostlie (1996).

2.2.2 Temperature

As mentioned above, the EW depends on the atmospheric parameters. Temperature is the most important variable in determining the line strength. This significant dependence results from transition probabilities of the excitation and ionization process equations as presented earlier.

Four different cases are shown, which are illustrated in Fig. 2.2 where the EW of two Fe lines, one neutral and one ionized, are plotted against T_{eff}. At low T_{eff} neutral elements, such as FeI, are the strongest lines as the number of ionized atoms are too small to contribute significantly to the EW. This is the result of the Saha equation. As T_{eff} increases, FeI is converted into ionized FeII. As the number of FeI decreases so does the EW, and likewise as the number of ion FeII increases so does the EW. This continues until second ionized atoms, FeIII, are formed and the same condition emerges. Their behaviour can be explained mathematically with four cases, as described below. The complete analysis and derivation of the following equations can be found in chapter 13 of Gray (2005). In what follows, R is the line strength, i.e. the ratio of line to continuous absorption, T is the temperature, χ is the excitation potential, I is the ionization energy and Ω can be considered a constant as it slightly depends on pressure.

The first case is a weak line of a neutral species with the element mostly neutral.

This case is described by the equation:

$$\frac{1}{R}\frac{dR}{dT} = \frac{2.5}{T} + \frac{\chi + 0.75}{kT^2} - \Omega \quad (2.4)$$

The second case is a weak line of a neutral species with the element mostly ionized, described by the equation:

$$\frac{1}{R}\frac{dR}{dT} = \frac{\chi + 0.75 - I}{kT^2} \quad (2.5)$$

The third case is a weak line of an ion species with the element mostly neutral, described by the equation:

$$\frac{1}{R}\frac{dR}{dT} = \frac{5}{T} + \frac{\chi + 0.75 + I}{kT^2} - 2\Omega \quad (2.6)$$

And finally, the fourth case is a weak line of an ion species with the element mostly ionized, for which the equation is:

$$\frac{1}{R}\frac{dR}{dT} = \frac{2.5}{T} + \frac{\chi + 0.75}{kT^2} - \Omega \tag{2.7}$$

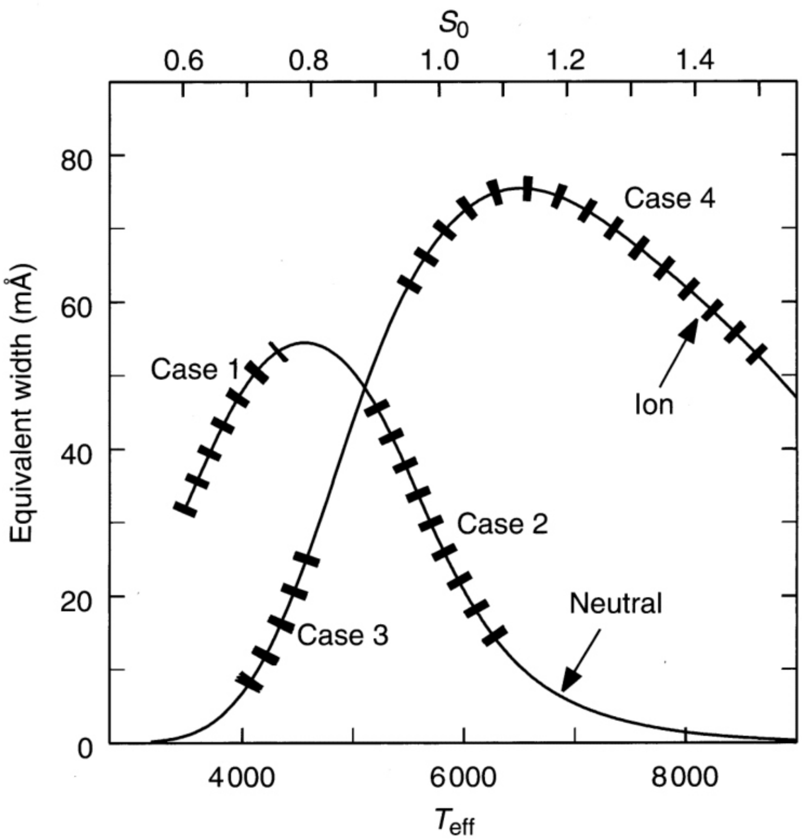

Figure 2.2: Plot of the behaviour of the EW of weak metal lines with T_{eff}. The cases discussed in the text are shown. Taken from Gray (2005).

2.2.3 Pressure

Pressure dependence in the stellar atmosphere is related to the gravity dependence. The effects of pressure on the spectrum can be seen as a change in the ratio of line absorbers to the continuous opacity, as a sensitivity of the damping constant for strong lines and as a dependence on the linear Stark broadening in hydrogen (Gray, 2005). The first effect translates into a $\kappa_\nu \approx$ constant P_e. By comparing two stages of ionization for the same element, it is possible to obtain $\log g$ using weak lines. This is a common method for FGK stars, using measurements for FeI and FeII lines.

To account for pressure effects we must consider gas pressure P_g and electron pressure P_e. In cool stars, the gas pressure can be approximated by

$$P_g \approx \text{constant}\, g^{2/3} \tag{2.8}$$

while the electron pressure is in turn given by

$$P_e \approx \text{constant}'\, g^{1/3} \tag{2.9}$$

where g is the stellar surface gravity.

In this case, pressure changes can be translated into approximately gravity dependencies. We can see such dependence illustrated in Fig. 2.3.

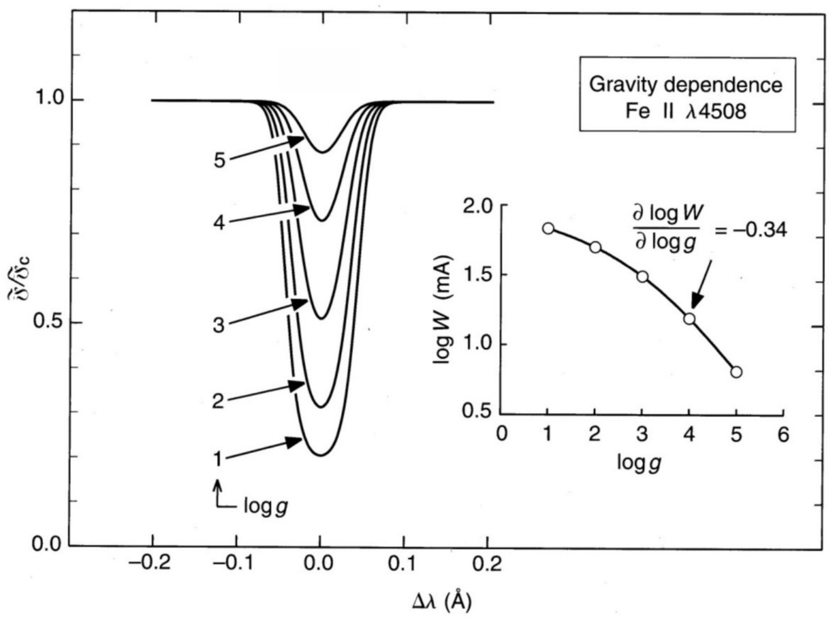

Figure 2.3: Profiles of FeII λ 4508 Å shown for several values of $\log g$. The inset graph shows a log-log plot of the change in EW with surface gravity. Taken from Gray (2005).

Pressure effects in stellar spectra are much weaker than $\mathrm{T_{eff}}$ effects. For weak metal lines in cool stars, based on Eq.2.2 (Saha Equation), we can distinguish the following cases:

1. weak lines formed where most of the element is in the next higher ionization stage are insensitive to pressure changes.

2. weak lines formed where most of the element is in that same ionization stage are pressure sensitive, thus lower pressure causes greater line strength.

3. weak lines formed where most of the element is in the next lower ionization stage are very pressure sensitive.

Using Eq.2.2 for case 1, it must be noted that the number of the atoms in the highest state is roughly equal to the total number of atoms of that element, $N_{r+1} \approx N$. Thus,

$$N_r \approx \text{constant } P_e \tag{2.10}$$

which gives the line absorption coefficient as

$$l_\nu \approx \text{constant } N_r \approx \text{constant } P_e. \tag{2.11}$$

The strength of a weak line, R, is proportional to the ratio of the line to the continuous absorption coefficient κ_ν:

$$R = \frac{F_c - F_\lambda}{F_c} = \text{constant } \frac{l_\nu}{\kappa_\nu}. \tag{2.12}$$

When negative hydrogen dominates κ_ν which is the case here it is proportional to the electron pressure, $\kappa_\nu \propto P_e$ which means the line strength is not proportional to electron pressure:

$$R = \frac{l_\nu}{\kappa_\nu} \approx \text{constant}. \tag{2.13}$$

For case 2, in a similar way, $N_r \approx N_{r+1} \approx N = \text{constant}$. This leads to $l_\nu \approx \text{constant}$, thus giving:

$$R = \frac{l_\nu}{\kappa_\nu} \approx \frac{\text{constant}}{P_e} \approx \text{constant } g^{-1/3}. \tag{2.14}$$

For case 3 we can show that $N_r \approx N = \text{constant}$, and $N_{r+2} \approx \text{constant}$ / ${P_e}^2$. The relation of line strength can be written as:

$$R = \frac{l_\nu}{\kappa_\nu} \approx \frac{\text{constant}}{P_e^3} \approx \text{constant } g^{-1}. \tag{2.15}$$

Regarding solar-type stars, where most metals are ionized, cases 1 and 2 are more common. For the cooler M dwarfs, cases 1 and 2 are also the most common ones, but the spectral analysis is more complicated due to the line absorption that depress the continuum. If the surface gravity is unknown, it can be determined by adjusting its value so that the ion and neutral lines will give the same abundance, since the former are pressure dependent and the latter are insensitive to pressure changes. Otherwise, if the ionized lines are too weak and blended to be measured accurately, the parameter $\log g$ can be kept fixed to a common value during the process of parameter determination.

2.2.4 Abundance

The abundance of an element affects the EW of a line. As the abundance increases, more photons can be absorbed, so the line strength also increases. In general though, the EW does not change linearly with abundance, as we can see in Fig. 2.4. A plot like the upper panel of Fig. 2.4, which depicts the change in EW according to abundance, is called a curve of growth. Instead of EW, it is common to use the reduced EW, expressed as log(EW/λ), because it normalizes Doppler-dependent phenomena such as microturbulence and thermal broadening by including the wavelength in the expression. The lower panel of Fig. 2.4 shows the line-profile change with the chemical abundance of the absorbing species.

There are three different cases seen in Fig. 2.4. The first one corresponds to the behaviour of weak lines, for which their EW is linearly proportional to the abundance. The second phase begins when the central depth approaches its maximum value and the line saturates. In this case, the EW increases slowly until the absorption broadens the wings of the line. At that point, the third phase starts as the optical depth of the wings becomes significant compared to the absorption of the continuum. The dependence of the EW becomes again proportional to the abundance. However, for these strong lines the profile is no longer Gaussian. We are only interested in the first phase, where the behaviour of the curve is linear. Every spectral line shows a similar behaviour. The details of its growth with abundance will depend on the continuous absorption at the position of the line, the temperature, the surface gravity, and the atomic constants for the line.

2.2.5 Microturbulence

Small-scale motion, which is motion of material at length scales smaller than the unit optical depth, is called microturbulence (v_t). These velocities produce Doppler shifts that are similar to those arising from thermal motions. Thus, microturbulence adds an absorption coefficient to the spectral lines. It is a broadening parameter that is incorporated into stellar parameter analysis to explain the EWs of saturated lines when they are measured to be greater than predicted by 1D models based on thermal and damping broadening alone. To obtain the correct value of microturbulence, one has to change its value in the atmospheric models until all spectral lines of an element give the same abundance, independently of the EWs. Fig. 2.5 shows its effect on the curve of growth. As we can

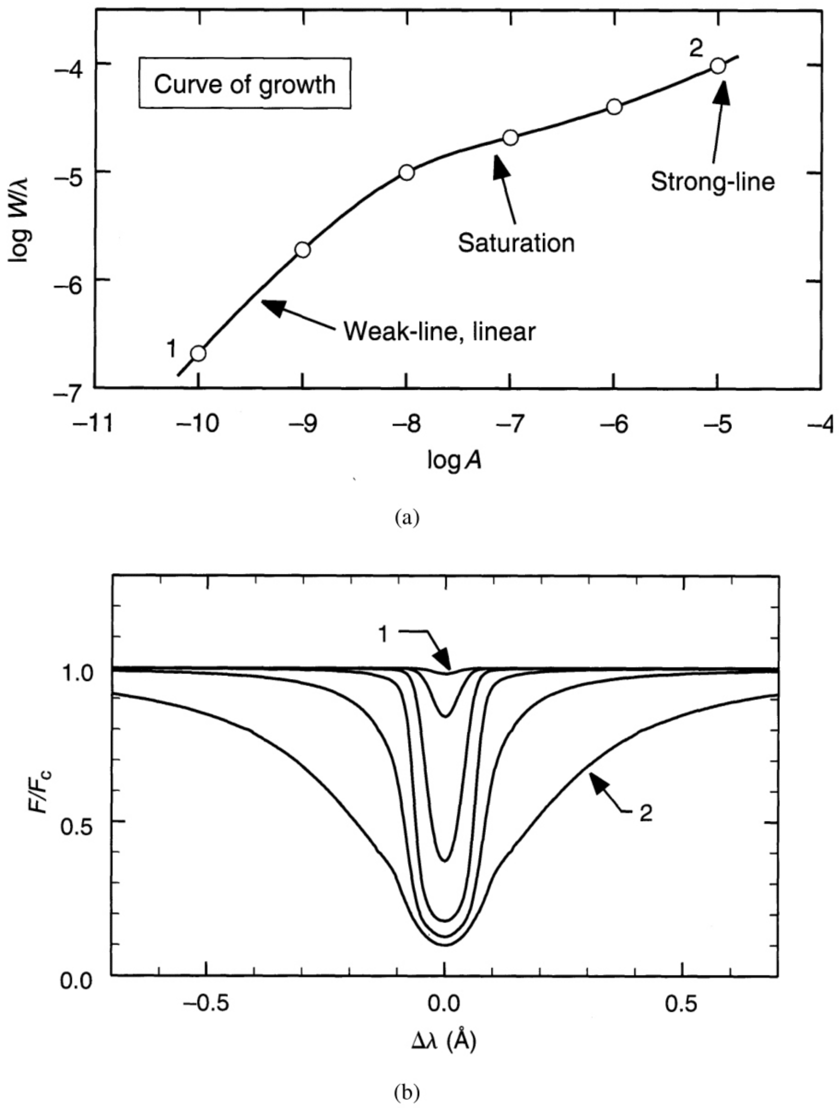

Figure 2.4: Upper panel: Typical curve of growth from a model photosphere: logarithmic plot of the reduced EW (W/λ) with abundance (A). Lower panel: Line profile change with chemical abundance of the absorbing species. The dots in the upper panel correspond to the different line profiles in the lower panel. Taken from Gray (2005).

see, changes in microturbulence can change the shape of the curve and consequently the measured abundance. As it increases, so does the EW and hence the measured abundance. Also, Fig. 2.5 depicts how microturbulence delays saturation. In these calculations, one postulates an isotropic Gaussian velocity distribution of dispersion ξ km/s.

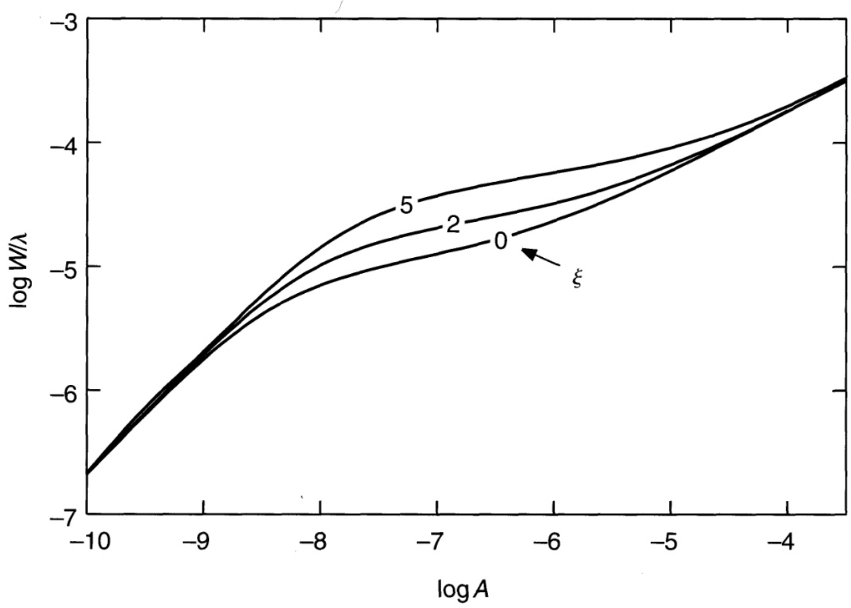

Figure 2.5: The presence of microturbulence delays saturation by spreading the line absorption over a slightly wider spectral band. The values of velocity dispersion ξ for an assumed Gaussian velocity distribution of microturbulence are in km/s. Taken from Gray (2005).

2.3. Radiative-trasfer software

Many different codes exist that solve the radiative transfer equations. In this thesis, we used the MOOG* code developed by Sneden (1973). MOOG, provided publicly by Sneden et al. (2012), is one of the most widely used codes for generating and studying synthetic spectra. Typically, the use of MOOG contributes to the determination of the chemical composition of a star. It is written in FORTRAN and it can perform several tasks of line analysis and spectral synthesis, assuming Local Thermodynamic Equilibrium (LTE) in plane-parallel 1D stellar atmosphere. MOOG includes different drivers for executing different tasks. It can derive abundances of lines from measured EWs for a given model atmosphere. It can derive the theoretical EWs of lines for a given star, from a model atmosphere with a given set of atmospheric parameters. It can compute a synthetic spectrum for a given model atmosphere and atomic line list. Furthermore, it has the ability to plot spectra and perform visual analysis. In this work, we have used MOOG for the derivation of abundances by providing measured EWs and the synthesis of selected lines as well as their respective continuum alone above them in order to compare with the observed spectra, as explained in detail throughout Chapter 4.

*http://www.as.utexas.edu/~chris/moog.html

Spectroscopy Made Easy (SME) computes synthetic spectra and adjusts the stellar parameters based on comparison with observational spectra. SME solver consists of the IDL routines for preparing spectral synthesis and performing optimization, as well as an external library (synth code) for synthetic spectrum calculations. Synth code is written in C++ and Fortran. SME was first developed by Valenti & Piskunov (1996) and has been updated by Piskunov & Valenti (2017). Most recently, a python version of it has been developed, called PySME (Wehrhahn et al., 2023).

Synth3 (Kochukhov, 2007) is a Fortran code which calculates spectra emerging from static, 1D model atmosphere, under the assumption of LTE. Practically, the code is used to model stars of spectral classes from early B to late M. It also includes the option to calculate spectra emergent from stellar atmospheres with a depth-dependent chemical composition and microturbulent velocity. In the standard mode, Synth3 computes intensity by solving numerically the scalar radiative transfer equation for a set of seven limb angles. Next, an external routine is used to produce disk-integrated flux spectrum from Synth3 intensity spectra for specified radial-tangential macroturbulent and projected rotational velocities, assuming spherically symmetric star.

BinMag (Kochukhov, 2007) is an IDL code designed to examine theoretical stellar spectra computed with Synth3 and produce graphical comparison between the observed and computed spectra. BinMag applies radial velocity shift and broadening to the theoretical spectra to account for the effects of stellar rotation, radial-tangential macroturbulence, instrumental smearing. The code can also simulate spectra of spectroscopic binary stars and can be used to measure EW, fit line profile shapes, and automatically determine radial velocity and broadening parameters.

SIU (Reetz, 1991) is a Fortran code built into IDL environment. All stellar atmospheric parameters, wavelength region and spectral resolution are specified inside the IDL environment. Unlike MOOG, it does not work without IDL. SIU calculates the emergent specific intensity or disk-integrated flux from plane-parallel 1D stellar atmosphere both in LTE and NLTE approximations.

SYNTHE was developed by Sbordone et al. (2004) with the goal to create synthetic spectra for the models of ATLAS code (Kurucz, 1970). ATLAS is used for the production of LTE 1D atmosphere models of stars.

Finally, Turbospectrum is a FORTRAN-based code for spectral synthesis, assuming LTE, developed by Plez (2012). It can synthesize 600 different molecules and uses the treatment of line broadening described by Barklem & O'Mara (1998).

2.4. Atmosphere modeling

The codes described previously need a set of stellar models and a proper line list to function correctly so that they can provide synthetic spectra which match the stellar observations. Therefore, the creation and selection of stellar models is a fundamental step for accurate determinations of stellar parameters.

The main categories of stellar models are the plane-parallel and the spherical ones. A plane-parallel model is based on the assumption that the stellar atmosphere can be approximated as parallel planes from the bottom of the atmosphere to its surface. This means that physical variables depend on one space coordinate only, which is the vertical depth. For most stars, this is justified because the extension of the atmosphere is negligibly small compared to the stellar radius. These models are more often used for dwarf stars. On the other hand, a spherical model takes into consideration the shape of the star as a whole, simulating it as a series of concentric layers. These models are often used for giant stars. Due to the thickness of their atmosphere, the shape of the star becomes relevant and geometry effects have to be taken into account (Heiter & Eriksson, 2006).

Stellar models have values for the temperature, pressure, density, sound speed, and opacity for these layers or planes, based on astrophysical equations that describe the interior of stars. These models are based on spectroscopic parameters for the star, so that the $T_{\rm eff}$, metallicity and $\log g$ at the stellar atmosphere correspond to the values measured when observing the stellar spectrum.

The ATLAS code was originally created by Kurucz (1970) using the assumption of LTE and hydrostatic, plane parallel atmospheres. Nowadays, the source code is publicly available and it has been developed by different people several times over the years, thus existing in many versions. Notable improvements were done by Mould (1976), Mould & Wyckoff (1978), who modified the initial ATLAS code (Kurucz, 1970) by including convection and a much bigger list of atomic and molecular lines, including the TiO molecule, founded as temperature sensitive. There are both plane parallel and spherical versions as well as those using opacity sampling or opacity distribution functions. Recent ATLAS models (Kurucz, 2005) include large parameter ranges, with $T_{\rm eff}$ values from 3500 to 50000 K, $\log g$ from 0.0 to 5.0 dex, and several different metallicities.

The MARCS (Model Atmospheres in Radiative and Convective Scheme) code was originally presented in 1975 by Gustafsson et al. (1975). The MARCS models used assume plane-parallel 1D stratification, hydrostatic equilibrium, mixing-length convection, and LTE. The evolution of the code since then, has offered better modeling of the line opacity, spherical modeling and including an increasing number of physical data. Nowadays, a large grid of different models is available online. The MARCS site* contains about 52000 stellar atmospheric models of spectral types F, G, K and M, as well as flux sample files indicating rough surface fluxes (Gustafsson et al., 2008). The model T_{eff} ranges from 2500 to 8000 K, with steps of 100 K for 2500 to 4000 K and steps of 250 K for 4000 to 8000 K. The $\log g$ ranges between -1.0 and 5.5 in steps of 0.5 (cgs units). Overall metallicities relative to the Sun are between -5.0 and +1.0 in variable steps. The reference solar abundance mixture that is used in the model metallicity is from Grevesse et al. (2007). Models with different values of v_t are also available.

The PHOENIX code was developed by Allard & Hauschildt (1995) and has been regularly updated throughout the years. The first PHOENIX library consisted of 700 stellar model atmospheres for M dwarf stars (Allard & Hauschildt, 1995), calculated under the assumption of LTE. The next improvement was made with the NextGen models (Hauschildt et al., 1999) with more line lists and opacity treatment for all molecules and all atmospheres ranging from 3000 to 10000 K. PHOENIX models can be produced in two different spatial configuration modes: the 1D mode assuming spherical symmetry and the 3D mode (Hauschildt & Baron, 2009). PHOENIX is a code that can calculate atmospheres and spectra for many different objects including main sequence stars, giants, white dwarfs, supernovae, brown dwarfs and extrasolar giant planets (Baron et al., 2010). Apart from the stellar model atmospheres, PHOENIX also provides computed synthetic spectra (Husser et al., 2013) which cover a wavelength range from 500 to 50000 Å with resolution R = 500000 in the optical and R = 100000 in the infrared. The parameter space covers the range from 2300 to 12000 K for T_{eff}, from 0.0 to 6.0 dex for $\log g$, and from -4.0 to +1.0 dex for [Fe/H].

2.5. Photometry

The surface T_{eff} of stars can be determined by combining the luminosity L with measurements of stellar radius R, through equation:

*https://marcs.astro.uu.se/

$$L = 4\pi R^2 \sigma\ T_{eff}^4 \tag{2.16}$$

where σ is the Stefan-Boltzmann constant.

A method for the estimation of temperature is the black-body method. This is based on the measurement of flux emitted by the star across multiple photometric bands, and matching them to black-body curves using Planck's law:

$$E(\lambda, T) = \frac{2hc^2}{\lambda^5} \frac{1}{e^{\frac{hc}{\lambda kT}} - 1} \tag{2.17}$$

where h is Planck's constant, c is the speed of light, λ is the wavelength in meters, k is the Boltzmann constant and T is the temperature in Kelvin.

The first study to apply this method was by Greenstein et al. (1970). More publications followed in the next decades and later, using photometry up to the K band (Reid & Gilmore, 1984, Berriman et al., 1992). Furthermore, the L band was included in the work by Tinney et al. (1993) as well.

A significant work for the derivation of T_{eff} and metallicity of M dwarfs through photometry was presented by Casagrande et al. (2008). Casagrande et al. (2008) created a technique to determine T_{eff} and metallicity of for M dwarfs, based on their previous study of FGK stars (Casagrande et al., 2006) when they applied the infrared flux method (IRFM). IRFM uses multiple photometry bands to derive T_{eff}, bolometric luminosities and angular diameters. It is based on the comparison of the ratio between the bolometric flux and the infrared monochromatic flux both measured on Earth, to the ratio between the surface bolometric flux and the surface infrared monochromatic flux for a model of the star. To adapt this method to M dwarfs, Casagrande et al. (2008) added optical bands, creating the Multiple Optical and Infrared Technique (MOITE). This method provided sensitive indicators of both temperature and metallicity. The calibrations had an internal precision ranging from 17 to 85 K. The total error budget was reported equal to 100 K and comparisons with literature showed systematics between 100 and 200 K. In addition, they obtained metallicities by computing the T_{eff} of the star for each color band for several trial metallicities, between -2.1 and 0.4 in steps of 0.1 dex, and by selecting the metallicity that minimizes the scatter among the six trial T_{eff} values. They estimated that their total metallicity uncertainty was 0.2 to 0.3 dex.

Another way of estimating parameters for M dwarfs based on photometry, is the use of empirical color-magnitude diagrams. The significant work by Bonfils et al. (2005) was a breakthrough in the field, creating a photometric calibration based on the metallicity effect of the $V-K$ color in a M_K vs $(V-K)$ diagram. This study was initiated by the observation that metallicity affects luminosity through a given photometric filter in two ways. First, higher metallicity decreases the bolometric luminosity for a given mass. Second, it shifts flux from the visible range to the NIR through higher line-blanketing by TiO and VO molecular bands. These mechanisms combined, decrease the luminosity of the more metal-rich stars through visible filters (Delfosse et al., 2000). Bonfils et al. (2005) used 20 FGK+M binary systems as calibrators, where the metallicity from the primary was calculated via the EW method following the work by Santos et al. (2004) and the metallicity of the secondary was assumed to be equal. Moreover, spectroscopic measurements of early-type, metal-poor M dwarfs by Woolf & Wallerstein (2005) were also added to the calibration sample. The polynomial relation between $V-K$ color and M_K finally provided metallicity estimates with uncertainty of 0.20 dex.

In the next years, Johnson & Apps (2009) argued that the calibration by Bonfils et al. (2005) systematically underestimated the metallicity of their high-metallicity M dwarfs by 0.32 dex. They derived a new photometric metallicity calibration from the metallicities of only six metal-rich M dwarfs in systems with FGK primaries. They showed that M dwarfs with planets appear to be systematically metal rich, a result consistent with the metallicity distribution of FGK dwarfs with planets.

Furthermore, Schlaufman & Laughlin (2010) presented a new improved calibration, showing that previous empirical photometric calibrations by Bonfils et al. (2005) and Johnson & Apps (2009) systematically underestimated or overestimated metallicity respectively. They derived a physically-motivated model that explained an order of magnitude more of the variance in the calibration sample than the other two studies.

Thereafter, Neves et al. (2012) published a comparative study of the three photometric calibrations above. They compared these calibrations using a sample of 23 M dwarfs and found that the calibration by Schlaufman & Laughlin (2010) had the lowest offsets and residuals against the sample. Neves et al. (2012) used improved statistics to marginally refine that calibration, providing the tightest dispersion of the fit, equal to 0.17 dex. In that paper, the reader can see alltogether the equations of the different calibrations, along with their calculated uncertainties.

Regarding stellar parameters such as T_{eff}, radius and luminosity, that are derived based on interferometric angular diameter measurements, an important work was executed by Boyajian et al. (2012). This study presented 21 interferometrically determined radii of nearby K and M dwarfs. They developed empirical relations of the broadband color indices as functions of T_{eff}, radii and luminosities of the stars. They added metallicity as an additional parameter to properly constrain the fits, where the data showed an effect on the color indices due to metallicity among the K stars, becoming strong in the M stars. Relations between temperature and radius, temperature and luminosity, and mass and radius, were found to be independent of metallicity though. Comparisons between single and binary star properties on temperature–radius plane, showed that for given stellar radius, binary-star T_{eff} estimates in the literature were systematically lower than the interferometrically determined values of single stars by 200–300 K.

Equations and relations established in the work by Mann et al. (2015) were used to directly estimate T_{eff}, luminosities, radii and metallicities for 183 nearby M dwarfs from photometric colors. Accurate spectro-photometric calibrations were applied to derive T_{eff}, [Fe/H] and bolometric flux and hence radius using the Stefan–Boltzmann relation. Their method of measuring T_{eff} was calibrated using stars with determinations from interferometry. Using masses derived from the empirical mass–M_{Ks} relation of Delfosse et al. (2000), resulted to a consistent mass–radius relation for the stars. [Fe/H] were calibrated with spectroscopically determined metallicities of solar-type FGK companions.

Rabus et al. (2019) provided 13 new high-precision measurements of stellar diameters for low-mass dwarfs obtained by means of NIR long-baseline interferometry with PIONIER at the Very Large Telescope Interferometer. Together with accurate parallaxes, these measurements led to precise estimates for their linear radii, T_{eff}, masses, and luminosities. Thus, they refined the T_{eff} scale towards the coolest M dwarfs. They measured for late-type stars with enhanced metallicity slightly inflated radii, whereas for stars with decreased metallicity, they measured smaller radii. They derived an empirical M_G-T_{eff} relation that is better suited for M dwarfs with T_{eff} between 2600 and 4000 K. Furthermore, they identified observationally a discontinuity in the T_{eff}-radius plane, which is likely due to the transition from partially convective M dwarfs to the fully convective regime. The transition was found to happen between 3200 and 3340 K, or equivalently for stellar masses around 0.23 $M_{\odot}$. In this region the stellar radii were in the range from 0.18 to 0.42 $R_{\odot}$ for similar T_{eff}.

2.6. Spectroscopy

2.6.1 Equivalent Width Method

The EW can be estimated through the fitting of a Gaussian curve across the absorption line of the spectrum and by using the parameters of the Gaussian to estimate the area of the rectangle. The amount of light absorbed by the stellar atmosphere, that creates such line, can be calculated by transforming each line to a single value, as described in Sect. 2.2.1. Then, these EW values can be used to estimate the abundance of a given element, given a set of spectroscopic stellar parameters. This method of parameter determination is based on the ionization and excitation balance. Commonly, it is referred as the Equivalent Width method.

Firstly, a list of lines must be constructed, for an element that has several neutral and ionized lines in the wavelength region of interest and optimally with a wide excitation potential range to be more sensitive to T_{eff}. Such element can be iron (Fe) or titanium (Ti). The elemental lines and their atomic data can be extracted from the Vienna Atomic Line Data Base (VALD) online* (Piskunov et al., 1995). A stellar atmospheric model is needed, as described in Sect. 2.4. Finally, a software is needed to compute abundances from a given atmospheric model built with a set of parameters, and measured EWs of the selected lines, for example MOOG as described in Sect. 2.3.

The classical determination of atmospheric parameters for solar-type stars follows the methodology below (Santos et al., 2004). The first step is the measurement of the EWs for the list of lines of the chosen element. The second step is the computation of a stellar model atmosphere from initial values of T_{eff}, [Fe/H], $\log g$ and v_t. Those initial values can be the solar values or from other reference star, by interpolating on a grid of model atmospheres. As third step, both the measured EWs and the computed stellar atmosphere are used to calculate the abundance of the element for each line by using a radiative tranfer code. At this point, T_{eff} is determined by looking at the slope of abundances of the lines versus their excitation potential values. If the slope is not zero, the process starts again from the second step, changing the values of the stellar atmosphere model, until the slope reaches zero. In a similar way, v_t is determined by looking at the slope of the abundances of the lines versus the reduced EW (log EW/λ). If the slope is not close to zero, the process goes back to second step, adapting the model parameters accordingly. Regarding the determination of $\log g$, it can be done by comparing the abundance derived

*`http://vald.astro.uu.se/`

from the neutral and ionized lines of the element. If the abundances are not the same, the process starts again with new parameter value. At this stage, the value of [Fe/H] has already converged. In practice, the iterations are made by changing all the parameters at the same time, because the parameters are not independent and also to speed up the process.

The EW method can be quite precise when the spectrum is of high-resolution and has well defined continuum, resulting in separated and properly-shaped lines, as usually happens in FGK stars. However, it becomes less accurate and precise for spectra with blended lines and poorly defined continuum, which are common conditions for cooler stars such as M dwarfs. Our modified version of this method is presented in Chapter 4.

2.6.2 Synthesis method

The other approach for the spectroscopic derivation of stellar parameters is the spectral synthesis method, which is based on comparing the observed spectrum to synthetic spectra created. Spectra can be reproduced with accurate stellar model atmospheres and proper line lists for a given spectral type and wavelength range, by means of a radiative trasfer code. The determination of stellar parameters can be done by synthesizing either the whole observed spectrum or particular spectral regions of interest.

In the case of using the entire observational spectrum, pre-calculated grid of synthetic spectra can be compared to it (Rajpurohit et al., 2018). As the full spectrum is created from scratch and includes all lines theoretically existing in the stellar one, blended lines are less problematic for this method. However, it requires significant computing power, as well as both an accurate stellar atmosphere model and a complete line list. By masking specific wavelength regions, one can also exclude troublesome features, such as telluric lines, parts of bad data reduction, or spectral features with currently unreliable atomic or molecular data such as the oscillator strength $\log(gf)$. In the alternative case of synthesizing particular spectral regions, the synthetic fitting can be done for selected small windows around sensitive spectral features (Bean et al., 2006b). This way is a compromise between fitting the entire spectral range and calculating the synthetic spectra on the fly which requires more time than using already existing grid of spectra.

Iterative algorithms generate new synthetic spectra, reaching closer to the observed one, and minimize the difference between the synthetic and the observed spectra, using for example a χ^2 fitting procedure. The synthetic spectrum which is the closest one to match with the observed one, setting a specific threshold of convergence, is eventually created with the parameters that should also be closest to the ones of the observed star.

Results from spectral synthesis are affected by the different approaches above, as well as by different atmosphere models which can be used, the radiative transfer code which is chosen for the calculation of the synthetic spectra, atomic data and whether their values have been calibrated, and the minimization process applied.

2.6.3 Spectroscopic studies of M dwarfs in the optical

Spectroscopic research on M dwarfs dates back in the 1970s, when Mould (1976) worked on their spectral features of TiO and CaH. TiO bands were found sensitive to metallicity and temperature, while the CaH ones sensitive to surface gravity. It initiated the creation of spectral indices for spectroscopic identification (Stauffer & Hartmann, 1986), as well as the development of better models of M dwarf photospheres (Allard & Hauschildt, 1995).

Bessell (1982) studied the properties of more than 150 high proper-motion dwarfs, revealing features of strong hydride bands and strong lines of FeI, CaI, NaI, KI, and examining the relation between those spectral features and the stellar metallicity.

Woolf & Wallerstein (2005) reported the first survey of chemical abundances in M and K dwarf stars using atomic absorption lines in spectra with resolution of 33000. They measured Fe and Ti abundances in 35 M and K dwarf stars using EWs and NextGen model atmosphere grid (Hauschildt et al., 1999). This study was a step towards the observational calibration of procedures to estimate the metallicity of low-mass dwarf stars using photometric and low-resolution spectral indices. The analyzed stars had reported errors up to 220 K for T_{eff}, and up to 0.18 dex for their [Fe/H] measurements.

Bean et al. (2006a) presented the spectroscopic metallicity of three M dwarfs with known or candidate planetary-mass companions. This study was made using high resolution of 60000 in the optical and is one of the first to analyze M dwarf spectra with this resolution. The analysis was based on spectral synthesis of atomic and molecular features. The technique allowed measurements of metallicity with precision errors of 0.12 dex.

Lépine et al. (2007) proposed the revision of the classification system based on empirical calibration of the TiO/CaH ratio for stars of near-solar metallicity. They introduced the parameter $\zeta_{TiO/CaH}$, which quantifies the weakening of TiO band strength due to metallicity effect, with values ranging from ζ = 1 for stars of near-solar metallicity to ζ = 0 for the most metal-poor and TiO depleted subdwarfs. This index was calibrated by Woolf et al. (2009) to give the actual metallicity [M/H] of a star based on its value for low-metallicity stars. This was an important step in parameter determination of M dwarfs, as an easily measured index was related to a fundamental stellar parameter.

Gaidos et al. (2014) published a catalog of optical spectra with resolution of 1000 for 2970 nearby (d < 50 pc) and bright (J < 9) late K and early M dwarfs, for which they estimated optical spectroscopic parameters. An initial list of stars was selected from the SUPERBLINK proper motion catalog, based on their properties. The T_{eff} of stars were estimated by least-squares fitting of spectra to model predictions, calibrated by fits to stars with established bolometric temperatures. Then, radius, luminosity and mass were estimated using empirical relations. Their estimated errors were around 100 K for T_{eff} and 0.12 dex for [Fe/H].

Neves et al. (2014) developed a technique to determine T_{eff} and [Fe/H] by measuring the pseudo EWs of 4104 absorption lines in the optical part of the spectrum within the range from 530 to 690 nm, setting a pseudo continuum for each line. T_{eff} and [Fe/H] of 110 M dwarfs, observed in the HARPS GTO M dwarf program, were derived by applying least-squares fit based on photometric reference T_{eff} and [Fe/H] scales that exist for 65 of them from Casagrande et al. (2008) and Neves et al. (2012) respectively. The dispersion around the applied calibration, calculated as the root mean square error, were 91 K for T_{eff} and 0.08 dex for [Fe/H], without taking into account though the intrinsic uncertainties of the original determinations of the reference parameters.

Maldonado et al. (2015) aimed to calibrate empirical relations in order to determine accurate stellar parameters for M dwarfs, using ratios of pseudo EWs of spectral features as a temperature diagnostic, a technique frequently used in solar-type stars. 21 stars with T_{eff} obtained from interferometric estimates of their radii (Boyajian et al., 2012) were used as calibrators. 112 temperature-sensitive ratios were identified and calibrated, providing T_{eff} with typical estimated uncertainties of about 70 K. Combinations of features and ratios of features were used to derive calibrations for the stellar metallicity, using 47 stars as calibrators by applying the photometric calibration provided by Neves et al. (2012). 696 combinations of the pseudo EWs of individual features and temperature-sensitive ratios for the stellar metallicity were calibrated, with estimated uncertainties ranging from 0.07 to 0.10 dex as lower limits, since they did not take into account possible systematic errors in the underlying calibration by Neves et al. (2012).

Passegger et al. (2016) used synthetic spectra based on the PHOENIX grid with the ACES description for the equation of state, to derive atmospheric parameters. To test the model accuracy, they compared the models to four benchmark stars using their UVES high-resolution optical spectra, with atmospheric parameters for which independent information from interferometric radius measurements were available. They used χ^2-based methods to determine parameters from the observations. Their inherent uncertainties were 35 K for T_{eff}, 0.11 dex for [Fe/H] and 0.14 dex for $\log g$. Their analysis indicated that there has been a large uncertainty in the accuracy of M-dwarf metallicity estimates, possibly due to systematic errors in earlier determinations for cool stars, since significant differences were noticed compared to other values from literature comparison.

Passegger et al. (2018) adapted the method described in Passegger et al. (2016), with new PHOENIX-ACES model grid which was especially designed for modeling spectra of cool dwarfs, having a new equation of state to improve the calculations of molecule formation in cool stellar atmospheres. Moreover, they modified their algorithm and line selection especially for M dwarfs. They derived the stellar parameters for a total of 300 stars analyzing their optical spectra obtained mainly from CARMENES. They estimated errors by adding Poisson noise to model spectra with random parameter distributions to simulate S/N of 100 and applied their algorithm to recover the input parameters. Using this method, the derived uncertainties were 51 K for T_{eff}, 0.16 dex for [Fe/H] and 0.07 dex for $\log g$.

Rajpurohit et al. (2018) focused on matching BT-Settl model spectra to CARMENES simultaneous observations in the optical and NIR for 292 M dwarf spectra. Since this work determined parameters by matching observed spectra to a grid of computed models, using the least-squares minimization technique, the reported uncertainties corresponded to the size of the grid, 100 K for T_{eff} and 0.30 dex for metallicity and $\log g$.

Passegger et al. (2019) published parameters for 282 M dwarfs by fitting updated PHOENIX models to high-resolution CARMENES spectra in both the optical and NIR wavelength ranges. The showed the importance of selecting magnetically insensitive lines for fitting to avoid effects of stellar activity in the line profiles. This work compared stellar parameters derived from multi-wavelength range spectra of the same star observed simultaneously, using homogeneous and consistent methods in both cases. Compared to literature, they concluded that fundamental parameters derived from optical spectra as well as optical and NIR spectra combined, are in better agreement than those derived from the same spectra in the NIR alone. Their reported uncertainties were from 54 to 134 K for $T_{\rm eff}$, from 0.19 to 0.40 dex for [Fe/H] and from 0.04 to 0.12 dex for $\log g$, when determined with the combination of optical and NIR region.

Recently, Khata et al. (2021) estimated $T_{\rm eff}$, stellar radius, and luminosity for a sample of 271 M dwarfs (M0V-M7V) observed by CARMENES. They used the simultaneously observed spectra in the optical and NIR bands, to derive empirical calibration relationships for estimating the fundamental parameters of these low-mass stars. A sample of nearby and bright M dwarfs were selected as calibrators for which the physical parameters were acquired from high-precision interferometric measurements. They inspected a range of spectral features and assessed them for reliable correlations, in order to identify the most suitable indicators of $T_{\rm eff}$, radius, and luminosity (log $L/L_{\odot}$). They preformed multivariate linear regression and found that the combination of pseudo EWs and EW ratios of the CaII at 0.854 μm and CaII at 0.866 μm lines in the optical and the MgI line at 1.57 μm in the NIR give the best fitting linear functional relations for the stellar parameters with root mean square error of 99 K for $T_{\rm eff}$.

2.6.4 Spectroscopic studies of M dwarfs in the near-infrared

Research in near-infrared (NIR) domain was initiated by Rojas-Ayala et al. (2010). $K-$band spectra with resolution of 2700 for 17 M dwarfs, belonging to binary pairs, with resolution of 2700 were obtained with metallicity estimates derived from their FGK companions. Analysis of these spectra and inspection of theoretical synthetic spectra, revealed that the M-dwarf metallicity can be inferred from the EWs of their NaI doublet (2.206 μm and 2.209 μm) and CaI triplet (2.261 μm, 2.263 μm, and 2.265 μm) absorption lines. These features were used, as well as a temperature-sensitive water index (H_2O-K) to construct an empirical metallicity indicator applicable for M dwarfs with near-solar metallicities (-0.5 < [Fe/H] < +0.5). This indicator had an accuracy of ±0.15 dex, comparable to that of existing techniques for estimating M-dwarf metallicities, but was more observationally accessible, requiring only a low resolution $K-$band spectrum. Applying this method to eight known M-dwarf planet hosts, they estimated metallicities ([Fe/H]) in excess of the mean metallicity of M dwarfs in the solar neighborhood, consistent with the metallicity distribution of FGK planet hosts.

Rojas-Ayala et al. (2012) improved the technique above, as they re-calibrated the [Fe/H] and [M/H] relations using a new water index, H_2O-K_2, as an indicator of the spectral type and T_{eff}. This paper studied 133 M dwarfs, including 18 stars with reliable metallicity estimates (from their FGK companions) and 11 M-dwarf planet hosts. These results were obtained from measuring both the EWs of the CaI and NaI lines mentioned in the previous paragraph and the spectral index quantifying the absorption due to H_2O opacity (the H_2O-K_2 index). The reported uncertainies were 0.14 dex. Apart from confirming the previous work with a larger sample of stars, this work also provided estimates for T_{eff} and spectral types, based on water absorption. Their metallicity estimates reproduced expected correlations with Galactic space motions and Hα emission line strengths, and returned statistically identical metallicities for M dwarfs within a common multiple system. Comparisons to model atmosphere revealed an overall offset between the atomic line strengths predicted by models as compared to actual observations. Finally, they found systematic residuals between the H_2O-based spectral types and those derived from optical spectral features with previously known sensitivity to stellar metallicity, such as TiO.

Önehag et al. (2012) presented a study of CRIRES spectra with resolution of 50000 observed in the J band and provided metallicities for a sample of eight M dwarfs and three wide-binary systems. The authors derived metallicities based on the best fit of synthetic spectra to the observed spectra. To verify the accuracy of the applied atmospheric models and test their synthetic spectrum approach, three binary systems with a K-dwarf primary and an M-dwarf companion were observed and analysed along with the single M dwarfs. Their sample had narrow range of T_{eff} (from 3200 to 3400 K, with a single star of T_{eff}=3900 K) and metallicity (from -0.1 dex to +0.2 dex). They obtained good agreement between the metallicities derived for the primaries and secondaries of the test binaries, thus confirming the reliability of their method in the J band. The method was consistent with previous studies for the analyzed stars, but the small sample size made the comparison limited.

Mann et al. (2013a) published new methods and improved calibrations of existing methods, to determine late-K and M-dwarf metallicities from low resolution (1300 < R < 2000) optical and infrared spectra. 112 wide binary systems containing a late-type and a solar-type star were analyzed, of which 62 ones with previously published metallicities and 50 ones with metallicities derived by the methods presented in the paper. The sample was used to empirically determine which features in the spectrum of the companion are best correlated with the metallicity of the primary. 120 features were detected in the spectra of K and M dwarfs, considered useful for predicting metallicities. The authors derived metallicity calibrations for different wavelength ranges, and showed that it is possible to get metallicities reliable within 0.10 dex using either visible, $J-$, $H-$, or $K-$band spectra. They found that the most accurate metallicities derived from visible spectra require the use of different calibrations for early-type (K5.5-M2) and late-type (M2-M6) dwarfs. Lastly, they used the sample of wide binaries to test and refine existing calibrations for the determination of M dwarf metallicities. They concluded that the ζ parameter, which measures the TiO/CaH ratio of bands, is correlated with [Fe/H] for super-solar metallicities, and ζ does not always correctly identify metal-poor M dwarfs.

Terrien et al. (2015) published a large survey, providing a catalog of 886 M dwarfs in the full NIR region (from 0.8 to 2.4 μm). The spectra used had a resolution of about 2000 and S/N > 100, and the survey focused on measuring the stellar abundances ([Fe/H] and [M/H]), using spectroscopic calibrations from different previous publications. Their results had an uncertainty of about 0.11 dex. The T_{eff} of those stars was estimated using H_2O indices, and their reported precisions were 110 K for J band, 170 K for H band, and 78 K for K_s band. It was finally concluded that the best method for [Fe/H] determination in M1-M5 stars was using the K_s-band spectra.

Lindgren et al. (2016) analyzed M dwarfs in four binary systems with FGK dwarf companions. Determination of parameters was done with the software package Spectroscopy Made Easy (SME). Synthetic spectra were computed on the fly, based on a grid of MARCS model atmospheres and a list of atomic and molecular data. The metallicity determination was based on spectra taken in the J band with CRIRES spectrograph and lines of several atomic species were used for that. The results agreed within 0.04 dex between the two stars of the binaries and also with literature values. They noted that a S/N above 50 was required to achieve uncertainties below 0.10 dex. Furthermore, they proposed a way to determine the T_{eff} of later-than-M2 M dwarfs through synthetic spectral fitting of the FeH lines in their observed spectra. This work was further improved in Lindgren & Heiter (2017), expanding the parameter range of both metallicity and T_{eff}. A total of 16 targets were analyzed and their estimated uncertainties were 100 K for T_{eff}, 0.03 to 0.07 dex for metallicity and 0.10 dex for $\log g$.

Veyette et al. (2017) presented an empirical calibration of synthetic M-dwarf spectra that can be used to infer T_{eff}, Fe abundance and Ti abundance. They obtained spectra with resolution 25000 for 29 M dwarfs with NIRSPEC. Using the PHOENIX stellar atmosphere modeling code, they generated a grid of synthetic spectra covering a range of temperatures, metallicities and alpha-enhancements. From their observed and synthetic spectra, they measured the EWs of multiple FeI and TiI lines and a temperature-sensitive index based on the FeH band head. They used abundances measured from widely separated solar-type companions to empirically calibrate transformations to the observed indices and EWs that force agreement with the models. Their calibration achieved precision of 60 K for T_{eff}, 0.10 dex for[Fe/H] and 0.05 dex for [Ti/Fe].

Two studies by Souto et al. (2017, 2018) used APOGEE spectra with resolution of 22500, in order to perform chemical analysis and determine spectroscopic parameters of three M dwarfs. In the former publication, the derived results were obtained by doing spectral synthesis using the code Turbospectrum and MARCS model atmospheres, while in the later publication both MARCS and PHOENIX model atmospheres were adopted. The stellar parameters and chemical abundances derived from the different models did not show significant offsets. The uncertainties were around 100 K for T_{eff} and 0.09 dex for [Fe/H]. The analysis was expanded to a larger M dwarf sample (Souto et al., 2020) with the characterization of 21 M dwarfs. The atmospheric parameters were derived from spectral synthesis with MARCS models and the APOGEE atomic/molecular line list, together with H_2O and FeH molecular line lists.

Sarmento et al. (2021) aimed to develop an alternative method for deriving stellar parameters of M dwarfs using the $H-$band spectra provided by APOGEE. Synthetic spectra were generated with iSpec (Blanco-Cuaresma et al., 2014), Turbospectrum and MARCS model atmospheres, along with a custom line list that includes over one million water lines, and were compared to APOGEE observational spectra. T_{eff}, [M/H], $\log g$ and v_t were determined through χ^2 minimization for 313 M dwarfs. The impact of the spectra normalization on the results was analyzed too. The overall errors reported for this method were around 100 K for T_{eff}, 0.10 dex for [M/H] and 0.20 dex for $\log g$.

Marfil et al. (2021) determined T_{eff}, [Fe/H] and $\log g$ for a sample of 343 M dwarfs observed with CARMENES. In this study, SteParSyn was employed. It is a Bayesian spectral synthesis implementation, designed to infer the stellar atmospheric parameters of late-type stars following a Markov Chain Monte Carlo approach, which was described in detail by Tabernero et al. (2022). They made use of the BT-Settl model atmospheres and the radiative transfer code Turbospectrum to compute a grid of synthetic spectra around 75 FeI and TiI lines, as well as the TiO γ and ϵ bands. Their T_{eff} scale was in good agreement with the literature, but large discrepancies were noticed in the [Fe/H] scales, which might arise from the different methodologies and sets of lines considered. However, there was excellent agreement in the [Fe/H] between the components in the wide physical FGK+M and M+M systems included in their sample.

Olander et al. (2021) did line-formation calculations based on modern model atmosphere grid appropriate for M dwarfs along with a synthetic spectrum synthesis code that treats formation of atomic and molecular lines in cool-star atmospheres including non-LTE. They used NIR spectra collected with the CRIRES instrument as reference observational data. They found that $T_{\rm eff}$ obtained with spectroscopic techniques in different studies mostly agree to better than 100 K and are mostly consistent with $T_{\rm eff}$ derived from interferometric radii and bolometric fluxes. At the same time, much worse agreement in the surface gravities and metallicities was evident. Significant discrepancies in the latter parameters appeared when results of the studies based on the optical and NIR observations were intercompared. They showed that non-LTE effects are negligible for FeI in M-dwarf atmospheres but are important for KI, which has a number of strong lines in the NIR spectra of these stars. They concluded that these effects, leading to potassium abundance and metallicity corrections on the order of 0.20 dex, may be responsible for some of the discrepancies in the published analyses.

Most recently, Cristofari et al. (2022) derived parameters comparing spectra acquired with the NIR spectro-polarimeter SPIRou to synthetic spectra computed from MARCS model atmospheres, in order to derive the $T_{\rm eff}$, $\log g$, metallicity ([M/H]) and alpha-enhancement ([α/Fe]) of 44 M dwarfs. Relying on 12 of these stars, they calibrated their method by refining their selection of well modelled stellar lines, and adjusted the line list parameters to improve the fit when necessary. The retrieved $T_{\rm eff}$, [M/H] and $\log g$ were in good agreement with literature values, having dispersions of the order of 50 K for $T_{\rm eff}$ and 0.10 dex for metallicity and $\log g$.

3. ODUSSEAS - Deriving stellar parameters in the optical

3.1. Overview of our method in optical

One of the most popular methods to derive stellar atmospheric parameters for FGK stars is by measuring the EWs of many metal lines of the spectrum (Sousa et al., 2008, 2015). The continuum position is quite clear in FGK stars, thus the EWs can be measured confidently. In M dwarfs, the presence of billions of molecular lines makes the continuum identification a challenging and even impossible task. Consequently, the determination of abundances and stellar parameters in the optical, following the traditional approach of the EW method, can not be applied. Therefore, a way to overcome the need of true continuum placement, is the use of pseudo EW by fitting a pseudo continuum from peak to peak for each line of interest. Then, those values can be associated via calibration with the corresponding stellar atmospheric parameters. Neves et al. (2014) used their MCAL code to measure pseudo EWs in the optical part of the spectrum for 110 M dwarfs observed in the HARPS GTO M-dwarf program by setting a pseudo continuum for each line. In that study, T_{eff} and [Fe/H] of these stars were derived by applying a calibration based on photometric reference T_{eff} and [Fe/H] scales that exist for 65 of them from Casagrande et al. (2008) and Neves et al. (2012), respectively. In the first case, the reference T_{eff} is the average value of the $V-J$, $V-H$, and $V-K$ photometric scales as seen in Casagrande et al. (2008), while for [Fe/H] the calculation of its reference values was done using stellar parallaxes, and V and K_s magnitudes as described in Neves et al. (2012) under the assumption that the measured metallicities of FGK stars in binary stellar systems are the same with their M-dwarf companions.

Machine learning is a widely used tool in astronomy nowadays. An overall review of the applications of machine learning to astrophysical problems can be found in Ball & Brunner (2010), Ivezić et al. (2014) and Rodríguez et al. (2022). The interest for machine learning algorithms and automatic processes is emerging from the increasing volume of survey data (Howard, 2017). These algorithms receive input data, which are used for training and testing the models, and by applying statistical methods they determine the output values. They can be accurate in predicting outcomes without the need for the user to explicitly create a specific model to the problem at hand. Such tools can be applied to a wide range of studies, with the input attributes being, the photometric or spectroscopic properties of the sources.

For example, in the field of stellar astronomy, Akras et al. (2019) used machine learning algorithms such as classification tree, linear discriminant analysis, and K-nearest neighbour in order to seek color indices in the infrared for identifying and distinguishing symbiotic stars. Das & Sanders (2019) used Bayesian artificial neural network in order to determine the mass, age and distance of red-giant stars. The training input was a combination of photometric, spectroscopic and astrometric data. More recently, Passegger et al. (2020) presented a deep neural network architecture to analyze high-resolution stellar spectra and predict stellar atmospheric parameters. The convolutional network was trained on synthetic PHOENIX-ACES spectra in different optical and NIR wavelength regions. In the field of galaxies and cosmology, Rau et al. (2019) developed the code GAME (GAlaxy Machine learning for Emission lines) which determines important physical properties of the galaxies, i.e. metallicity, density, column density and ionization parameter, from their emission-line spectra. Ucci et al. (2019) applied machine learning to derive a mapping between light-curve features of variable stars with long periods and their magnitude. The goal was to extend the traditional period-luminosity relation of variable stars, which provides accurate distance measurements to nearby galaxies and are therefore a vital tool for cosmology.

Given the utility of machine learning techniques and the difficulty of obtaining parameters for M dwarfs, we decided to develop a machine learning method useful for this kind of stars. This is the code ODUSSEAS* (Observing Dwarfs Using Stellar Spectroscopic Energy-Absorption Shapes), which follows the pseudo-EW approach. It is based on a supervised machine learning algorithm, meaning that it is provided with both input and expected output and uses these to create a model. It makes use of the machine learning "scikit learn" package of Python and offers a quick automatic derivation of $T_{\rm eff}$ and [Fe/H] for M dwarf stars using their 1D spectra and resolutions as input.

The input to the machine learning function are the values of the pseudo EWs for a set of HARPS GTO spectra and the expected output are the values of their reference $T_{\rm eff}$ and [Fe/H] from selected literature studies, respectively. In the original version of the tool (Antoniadis-Karnavas et al., 2020), the reference values of $T_{\rm eff}$ and [Fe/H] come from Casagrande et al. (2008) and Neves et al. (2012) respectively, for a dataset of 65 stars.

*https://github.com/AlexandrosAntoniadis/ODUSSEAS

In the upgraded version (Antoniadis-Karnavas et al, paper submitted) a new reference dataset of 47 stars has been created with interferometry-based Teff values (Khata et al., 2021, Rabus et al., 2019) and [Fe/H] values derived by applying the method of Neves et al. (2012) using updated values of parallaxes from Gaia DR3 archive (Gaia Collaboration, 2020). Eventually, the user can select in the options of the tool which reference dataset to be applied for the determinations of parameters.

After training with a part of the reference data, the algorithm produces a model and tests it on the rest of the reference data; it predicts their values and compares them with the reference ones given as expected output. Thus, it examines the accuracy and the precision of the model using several regression metrics described below. Finally, it applies the model to unknown spectra and estimates their stellar parameters and corresponding uncertainties.

In Sect. 3.2 we describe how ODUSSEAS computes the pseudo EWs. In Sect. 3.3 we provide in more detail the data flow of the code ODUSSEAS. We explain the characteristics of the machine learning function and its efficiency regarding different regression types, resolutions, and wavelength areas. In Sect. 3.4 we present the application of the tool to spectra obtained from several spectrographs of different resolutions and we examine the results. In Sect. 3.5 we discuss about the original reference parameter values and we compare the results with other methods, that eventually motivated us for creating a new reference dataset. In Sect. 3.6 we describe the last update of the tool, which is based on the new reference dataset with T_{eff} values being derived based on interferometry. Then, in Sect. 3.7 we determine stellar parameters for 82 planet-host stars in SWEET-Cat, collecting their spectra from the public archives. We apply both reference scales and we compare the results between them. Furthermore, in Sect. 3.8 we compare our results to those of other methods with which we share a sufficient number of common stars. In Sect. 3.9 we present our results for M dwarfs of the ESPRESSO GTO program, which spectra became available to us and for which there are no public data. Finally, in Sect. 3.10 we present the correlations between metallicity of the M dwarfs in SWEET-Cat and planetary mass of their exoplanets, comparing the distributions.

3.2. Pseudo-EW measurements

Since the identification of the continuum is very difficult in the spectra of M dwarfs, a pseudo continuum is set in each absorption line. The method is based on measurements of the pseudo EWs of absorption lines and blended lines in the range between 530 and

690 nm. Parts where activity-sensitive Na doublet and Hα lines and strong telluric lines exist, are excluded from the line list. These wavelength areas, which have been removed, are from 588 to 590.5 nm, from 656.1 to 656.4 nm and from 686 to 690 nm respectively. The line list consists of 4104 absorption features, which are given in the form of left and right boundaries, between which these features are supposed to be created. This method, based on pseudo EWs and the specific line list, was used by Neves et al. (2014) too.

We created our own Python version of the method to compute the pseudo EWs. The code reads the line list and the 1D fits files of the stellar spectra. The important keywords of the spectral file format that the code reads are the CRVAL1, CDELT1 and NAXIS1. The directory where the fits files must be stored and other technical details for ODUSSEAS to run properly, are explained in the README section of the github page of the tool*. The code has an option to perform automatic radial-velocity correction of the input spectra, in case they are shifted. This is implemented in the code using the cross-correlation function "crosscorrRV" of "pyAstronomy" (`https://pyastronomy.readthedocs.io/en/latest/pyaslDoc/aslDoc/crosscorr.html`) and a mask of 14 lines within the range from 5371.50 Å to 6122.22 Å. For each line, the code identifies the position of the minimum flux of the feature, which is the central absorption wavelength. Starting from this position, the code identifies the maximum on each side of this absorption feature, which has a range to search for, defined by the respective boundaries provided in the line list. Eventually, the code fits the pseudo continuum along the edges of the absorption feature with a straight line and obtains the pseudo EW by calculating the area between the pseudo continuum and the flux. Mathematically, the pseudo EW is defined as follows, where F_{pp} is the value of the flux between the peaks of the feature (i.e., the pseudo continuum) and F_λ is the flux of the line at each integration step:

$$\text{pseudoEW} = \Sigma \frac{(F_{pp} - F_\lambda)}{F_{pp}} \Delta\lambda \tag{3.1}$$

Figure 3.1 shows an example of pseudo EW, using the star Gl176 and an absorption line at the region around 6531 Å.

For the evaluation of our pseudo-EW measurements, we calculated the pseudo EWs of all the 4104 lines for 110 stars of the HARPS GTO M-dwarf sample (Bonfils et al., 2013). These values were compared to the ones calculated with the MCAL code. In

*`https://github.com/AlexandrosAntoniadis/ODUSSEAS`

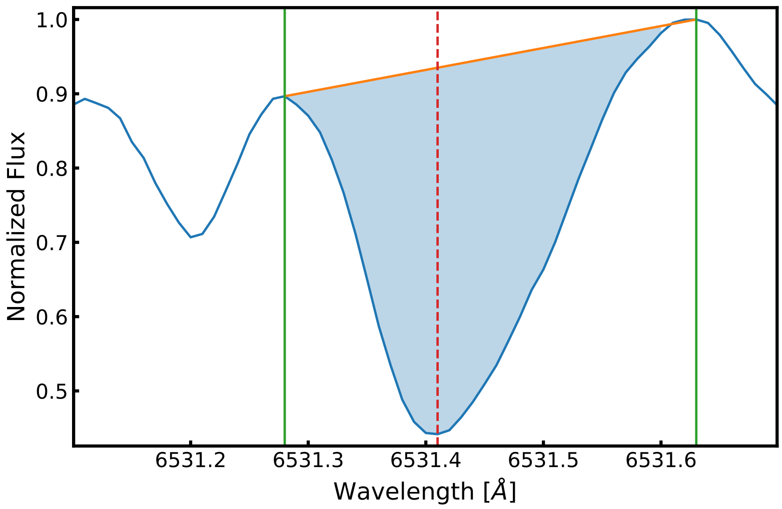

Figure 3.1: Area fitting for the calculation of pseudo EW for a line with central λ = 6531.4 Å. The position of the pseudo continuum is adjusted accordingly. This pseudo EW is equal to 87 mÅ.

the upper panel of Fig. 3.2, we present the comparison of all the pseudo-EW values for the star Gl176 as an example. Inside the plots, AA stands for measurements of this work and VN stands for the measurements by Neves et al. (2014). The slope in the diagrams of most stars is almost identical with the identity line, with only a few pseudo EWs having considerably different values. In the lower panel of Fig. 3.2 we show the relative difference (the percentage) of the values against values of this work. A scatter appears for the pseudo-EW values smaller than 30 mÅ, which is normal, as the relative difference for these narrow lines is greater. In contrast, nearly all lines broader than 50 mÅ are measured with significant agreement.

The quality test for measuring the pseudo EWs comes from the following comparison. We plot the mean differences and mean relative differences between our method and the code by Neves et al. (2014), for each line averaged over all the stars, in order to see how all the lines are measured. The result is very good as can be seen in Fig. 3.3, with only 184 lines out of 4104 showing a mean relative difference greater than $\pm$15%.

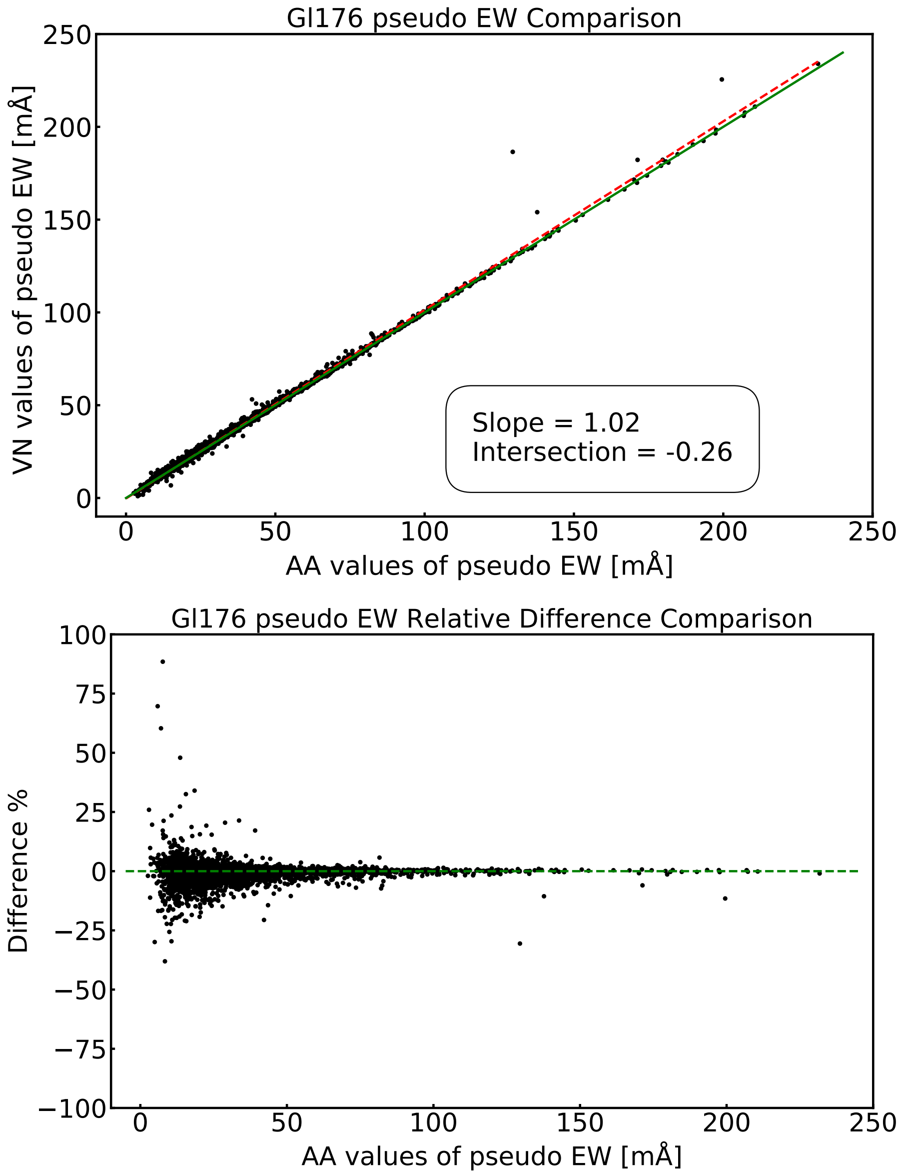

Figure 3.2: Upper panel: Comparison between the pseudo-EW values measured by our tool and the MCAL code by Neves et al. (2014). Lower panel: Percentage difference of the pseudo-EW values plotted against our values.

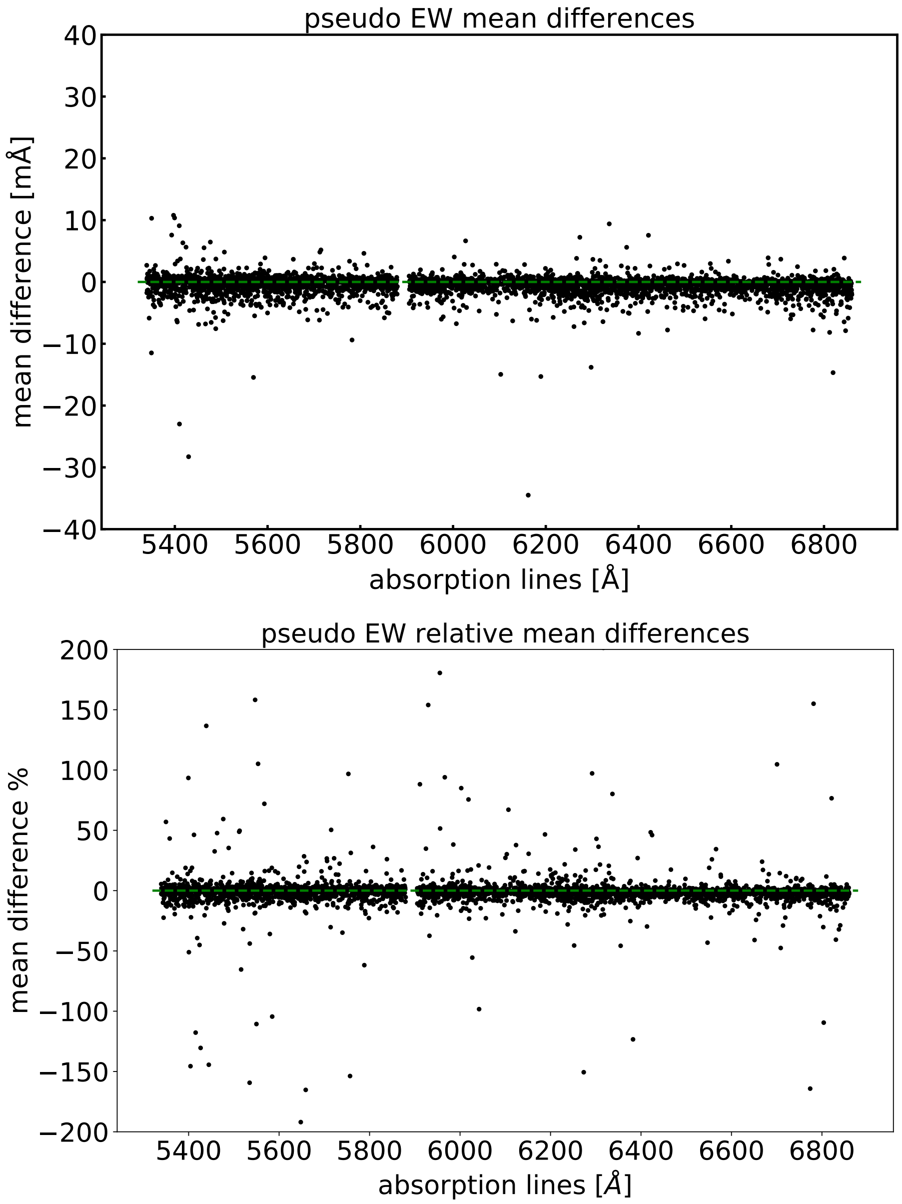

Figure 3.3: Upper panel: Difference of each line as averaged over the measurements of all stars. Lower panel: Percentage difference of each line as averaged over the measurements of all stars.

3.3. Machine learning on M dwarfs

”ODUSSEAS.py” measures the pseudo EWs of new stellar spectra and derives their unknown T_{eff} and [Fe/H] via machine learning. Prior to that, there is a preliminary code, ”HARPS_dataset.py”, with which we have created the databases that contain pseudo-EW measurements in different resolutions and the reference stellar parameters. Below, there is a detailed description of their structure, their input parameters and how to use the codes.

3.3.1 The HARPS dataset

When we run the code ”HARPS_dataset.py”, the outcome is a file which is used later as input to the machine learning algorithm when running ”ODUSSEAS.py” for training the machine and testing the generated model. It contains the names of reference stars of the HARPS M dwarf sample, the central wavelengths of the 4104 absorption features from 530 to 690 nm, their pseudo-EW values according to the resolution at which we convolve the spectra, and their reference values of T_{eff} and [Fe/H]. The reason for creating different reference databases of HARPS spectra convolved to the resolutions of spectra we want to analyze, is explained in Sect. 3.4.1. The 65 spectra used as the initial reference dataset, have a signal-to-noise ratio (S/N) of more than 100, as reported by Neves et al. (2014). The stars and their reference parameters are presented in Table A.1. The range of the reference stellar parameters is presented in Fig 3.4. Their photometric derivations have uncertainties of 100 K for T_{eff} and 0.17 dex for [Fe/H], as reported by Casagrande et al. (2008) and Neves et al. (2012) respectively.

The convolution function used is the ”instrBroadGaussFast” of ”pyAstronomy”, which applies Gaussian instrumental broadening. The width of the kernel is determined by the resolution; a description of it can be found at `https://pyastronomy.readthedocs.io/en/latest/pyaslDoc/aslDoc/broad.html`.

Since the HARPS spectra have a specific finite resolution, the code calculates the actual resolution to which they need to be convolved by the function in order to obtain spectra at the final resolution required, that is defined as input parameter. This calculation is done considering the following relation:

$$\sigma_{conv} = \sqrt{\sigma_{final}^2 - \sigma_{orig}^2} \tag{3.2}$$

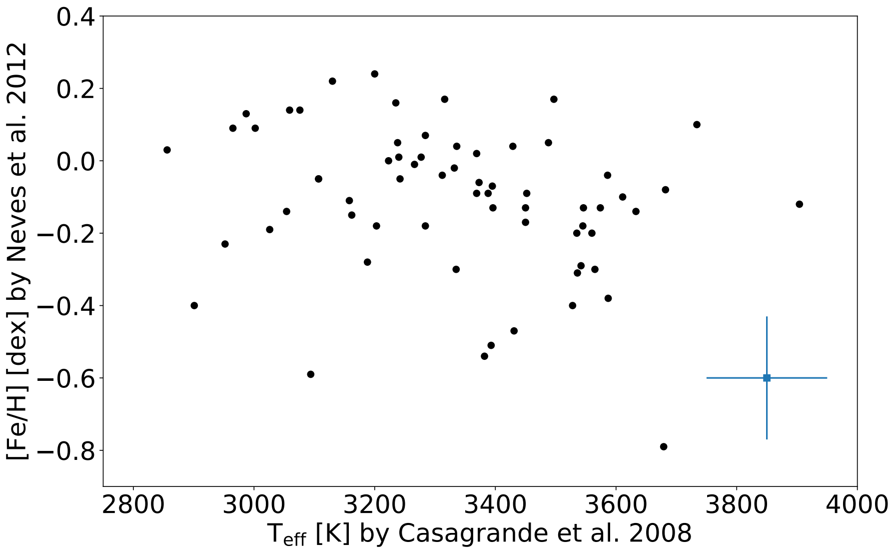

Figure 3.4: Distribution of reference T_{eff} and [Fe/H] of the initial 65-star dataset used to train and test the machine learning models. The cross symbol represents their uncertainties, which are 100 K and 0.17 dex respectively.

where σ_{conv} corresponds to the resolution to which a spectrum with an original resolution of σ_{orig} needs to be convolved, in order to obtain a final resolution of σ_{final}.

It is reminded that $\sigma \equiv \Delta v$ is related with resolution R via the relation below :

$$\frac{1}{R} = \frac{\Delta\lambda}{\lambda} = \frac{\Delta v}{c} \tag{3.3}$$

Two settings are input by the user. First, one chooses whether or not to convolve the reference HARPS spectra to the spectral resolution of the new data. We provide pre-computed pseudo EWs of the reference dataset for a range of spectral resolutions in widely used spectrographs. Namely, we have already created the reference databases for resolutions of 115000 for HARPS* (Mayor et al., 2003), 110000 for UVES† (Dekker et al., 2000), 94600 for CARMENES‡ (Quirrenbach et al., 2016), 75000 for SOPHIE§ (Perruchot et al., 2008) and 48000 for FEROS¶ (Kaufer et al., 1999). In these cases, there is no need to convolve the spectra again and recalculate the pseudo EWs. Second, the user must define the resolution of the data being analyzed. The "HARPS_dataset.py" is presented schematically in Fig. 3.5.

*https://www.eso.org/sci/facilities/lasilla/instruments/harps.html
†https://www.eso.org/sci/facilities/paranal/instruments/uves.html
‡https://carmenes.caha.es/ext/instrument/index.html
§http://www.obs-hp.fr/guide/sophie/sophie-eng.shtml
¶https://www.eso.org/sci/facilities/lasilla/instruments/feros.html

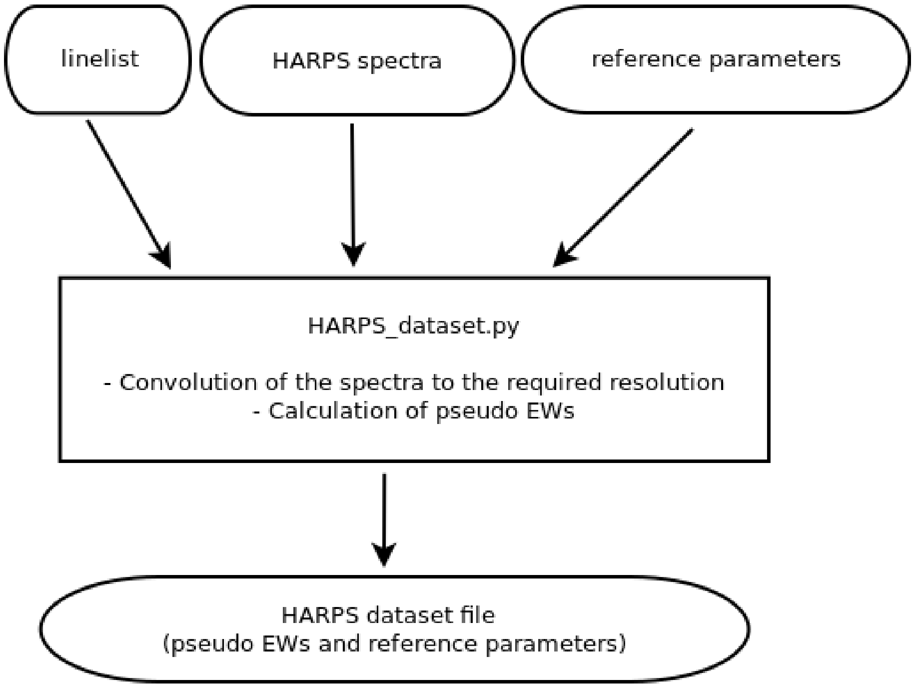

Figure 3.5: Workflow of HARPS_dataset.py.

3.3.2 ODUSSEAS tool

ODUSSEAS.py makes use of two algorithms we developed: the New_data.py algorithm for measuring the pseudo EWs of new spectra to analyze, and the MachineLearning.py algorithm for deriving their $T_{\rm eff}$ and [Fe/H]. The innovative aspect of this tool is the simultaneous predictions for spectra of different resolutions and wavelength ranges, while giving the opportunity for the determination to be based on reference parameters derived by different methods.

The user has the option to select which reference dataset to be applied: the initial 65-star one with photometric $T_{\rm eff}$ values from Casagrande et al. (2008) and [Fe/H] values from Neves et al. (2012), or the new 47-star one with $T_{\rm eff}$ values based on interferometry (Khata et al., 2021, Rabus et al., 2019) and [Fe/H] values calculated following the method by Neves et al. (2012) using updated values of parallax from Gaia Early Data Release 3. In addition, the user can set the regression type to be used by the machine learning process. The ”ridge” is recommended, but also ”ridgeCV” and ”linear” work at a similar level of efficiency as well. Section 3.3.4 presents the efficiency of all the regression types used.

The workflow of ”New_data.py” is similar to that of ”HARPS_dataset.py”; it reads the files and resolutions of new spectra and, if needed, it calculates and corrects their radial velocity shift. In addition, if the original step of a spectrum is not 0.010, i.e. equal to that of the HARPS dataset, it is changed with linear interpolation to this value. Thus, the pseudo EWs are measured in a consistent way. The files containing the pseudo-EW measurements of each spectrum are then used during the operation of ”MachineLearning.py”, which returns the values of T_{eff} and [Fe/H] along with the regression metrics of the models that predicted them. The diagram of ”ODUSSEAS.py” is presented in Fig. 3.6 showing its inputs, operations, and output in a concise manner.

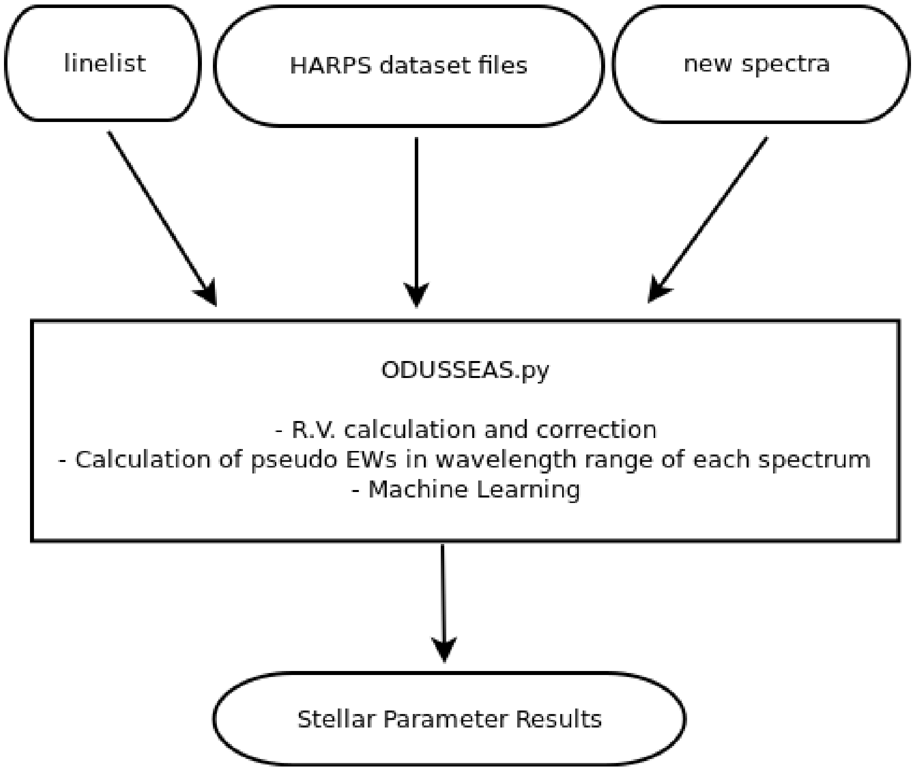

Figure 3.6: Workflow of ODUSSEAS.py.

3.3.3 Machine learning function

Here the machine learning function is presented in more detail. The machine learning algorithm operates in a loop for each star to analyze separately, as each star may have a different wavelength range and resolution. For each star in the file list, the algorithm automatically loads two files: the HARPS dataset of the respective resolution, for training and testing the model, and the pseudo EWs of the star for which we want to derive T_{eff} and [Fe/H], in order to apply the model and return the stellar parameters. Based on the wavelength range of each spectrum, a mask is applied to the HARPS dataset in order to consider the absorption lines in common between spectra.

We set the tool to split the HARPS reference stars randomly into training groups consisting of 70% of the sample (45 stars) and testing groups consisting of the remaining 30% of the population (20 stars). With these numbers selected, the machine learning model can be both trained accurately with a big percentage of the reference sample and tested on a sufficient number of stars. Moreover, after each run, the tool saves a group of plots with the reference and the predicted parameters of model testing, as well as their differences, as a visualization of the model accuracy. An example is presented in Fig. 3.7.

The algorithm is provided with different regression types to be used: the ”linear”, the ”ridge”, the ”ridgeCV”, the ”multi-task Lasso”, and the ”multi-task Elastic Net”. All these kinds of models provide an output value by fitting a linear regression to the input values. The relation between the predicted value *y* (the stellar parameter), the input variables *x* (the pseudo EWs), and the coefficients *w* is expressed as

$$y(w, x) = w_o + w_1 x_1 + ... + w_p x_p \tag{3.4}$$

The ”linear regression” fits a linear model with coefficients to minimize the residual sum of squares between the observed responses in the data set and the responses predicted by the linear approximation. A disadvantage of this model is that the ordinary least squares that it uses, rely on the independence of the model terms. When terms are correlated, the least-squares estimate becomes highly sensitive to random errors in the observed response, producing a large variance. The solution to this case is given by the ”ridge regression”. Ridge model imposes a penalty on the size of coefficients. The ridge coefficients minimize a penalized residual sum of squares. The ridge regression makes the coefficients become more robust to collinearity. Another version of this model, is the ”ridgeCV”, which has a built-in cross validation function. In short, this process divides the training set in smaller subsets (folds) and the performance is then the average of the values computed in the loop. ”Multi-task Lasso” is a linear model that estimates sparse coefficients for multiple regression problems jointly. It is useful in some cases due to its tendency to prefer solutions with fewer parameter values, effectively reducing the number of variables upon which the given solution is dependent. ”Multi-task Elastic Net” is a linear model trained to learn a sparse model where few of the weights are non-zero like Lasso, while still maintaining the regularization properties of Ridge. It is useful when there are multiple features that are correlated with one another. Lasso is likely to pick one of these at random, while elastic-net is likely to pick both. A practical advantage of trading-off between Lasso and Ridge is that it allows Elastic-Net to inherit some of Ridge’s stability under rotation. The mathematical details of each regression type are described in the official online documentation at `https://scikit-learn.org/stable/modules/linear_model.html`.

The performance of machine learning is indicated by the following three kinds of returned regression metrics. The mean absolute error is computed as the model is applied to the test dataset. This corresponds to the expected value of the absolute error loss in the predictions. In addition, the "explained variance" (E.V.) score is computed. The best possible value of this score is 1. Variance is the expectation of the squared deviation of a random variable from its mean. It measures how far a set of numbers spread out from their average value. Furthermore, the "r2" score computes the coefficient of determination, defined as R^2. The best possible score is 1 too. The coefficient of determination is the proportion of the variance in the dependent variable that is predictable from the independent variables. This score provides a measure of how well future samples are likely to be predicted by the model. A constant model that always predicts the expected value, disregarding the input features, would get a score of 0. In the case of multi-output, the resulting E.V. and r2 scores are by default the averages with uniform weight of the respective scores for T_{eff} and [Fe/H]. The mathematical types of those regression metrics are described in the official online documentation at `https://scikit-learn.org/stable/modules/model_evaluation.html#regression-metrics`.

For each star, the tool makes 100 determinations by randomly splitting the training and testing groups each time. After these determinations, it returns the average values of T_{eff} and [Fe/H], the dispersion these results (measured as the standard deviation), the average values of the mean absolute errors of the models, and the average scores of machine learning. This iterative process minimizes the possible dependence of the resulting parameters on how the stars from the HARPS dataset are split for training and testing in one single measurement. As there are not many stars in the reference datasets (65 stars in the original reference dataset and 47 stars in the new reference dataset), the results of the measurements could be significantly affected by the selection of stars that end up in the training set. Similarly, the machine learning errors could be significantly affected by the selection of stars in the testing set. This is why multiple runs are performed, shuffling and splitting the reference stars into different training and testing groups each time; then the average values and the uncertainties are calculated to give the final results. The final results are automatically saved in the file named "Parameter_Results.dat".

3.3.4 Machine learning efficiency

First, the regression models were tested to find the best one. We used the 65-star HARPS dataset with the photometric reference values, at their real resolution of 115000. For 100

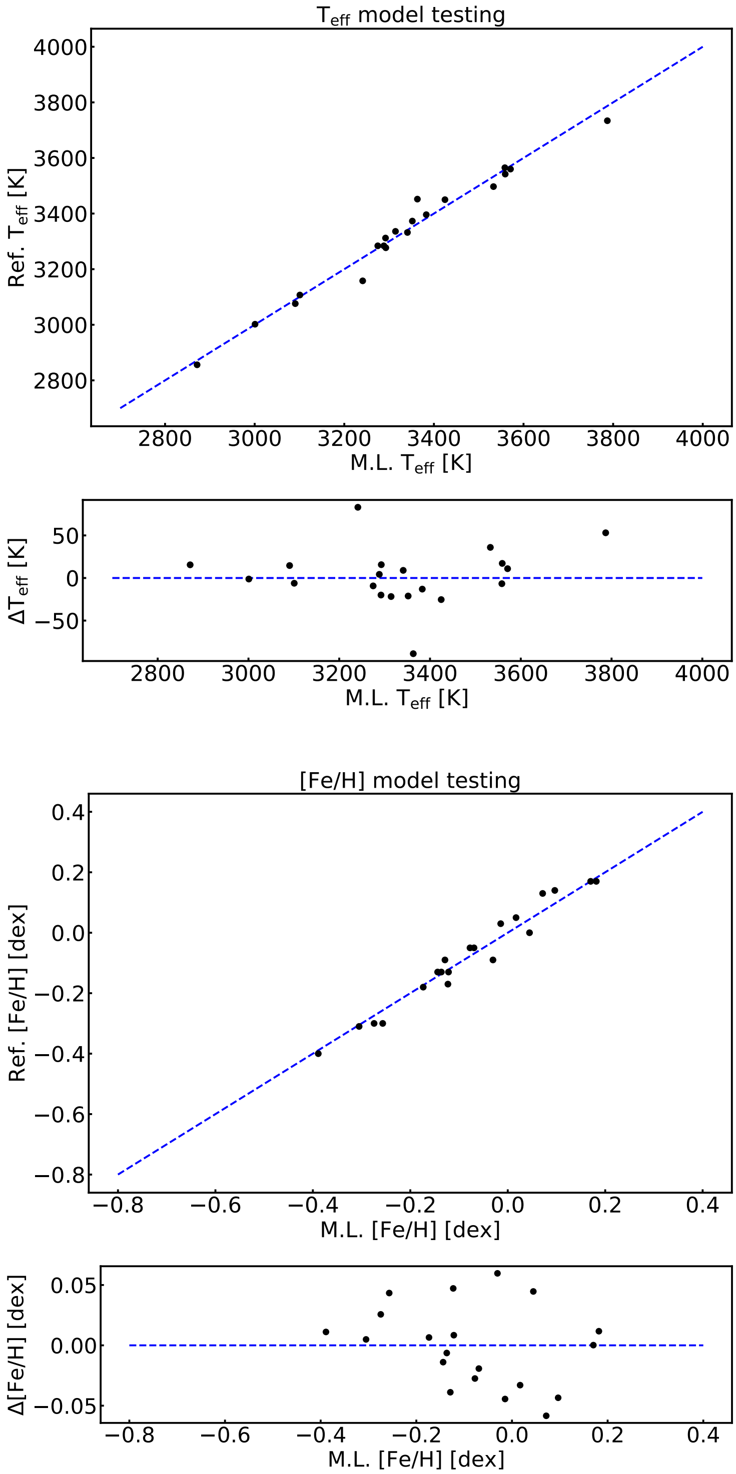

Figure 3.7: Demonstration of predictions applying ridge regression. Upper panel: T_{eff} values expected (Ref.) and predicted (M.L.) on the test dataset, along with their differences. Lower panel: [Fe/H] values expected (Ref.) and predicted (M.L.) on the test dataset, along with their differences.

runs with each regression type, the scores and the absolute mean errors of the stellar parameters on the test set were measured. The average values around which each model tends to result are reported in Table 3.1. The linear, ridge, and ridgeCV models work very well in general, giving r2 and E.V. scores with average values of around 0.93 and 0.94 respectively. The range of these scores from the 100 runs is usually from 0.87 to 0.99. The average uncertainties of those regression types are $\sim$27 K for $T_{\rm eff}$ and $\sim$0.04 for [Fe/H]. The ridge model leads to slightly greater scores than the linear one. The ridgeCV model, which has a built-in cross validation function that applies "leave-one-out" or "k-fold" strategies, does not seem to work better than the classic ridge one, at least for this sample of M dwarf measurements. In any case, the 100-run iteration of the algorithm, provides the intrinsic function of the ridgeCV model, even when the normal ridge one is applied. Furthermore, multi-task Elastic Net and multi-task Lasso give considerably lower scores and higher mean absolute errors. Therefore, the use of ridge regression is advocated, as it operates best on the spectral values of the M dwarfs.

Second, the E.V. and r2 scores, as well as the mean absolute errors of the algorithm were evaluated for different resolutions of the spectra. We did this for the 65-star HARPS dataset at its actual resolution of 115000 and we repeated this process for convolved datasets at resolutions of the other broadly used spectrographs. This was done to examine the level of machine learning precision towards lower resolutions. The average values from 100 measurements of each case are presented in Table 3.2.

To further test the reliability of the method, the efficiency of the machine learning was examined in different wavelength ranges of the spectrum. The line list, which is from 530 to 690 nm, was divided in four spectral regions and we measured the respective scores and mean absolute errors. This test was done to analyze whether machine learning works better when using the full range or a specific part of the wavelengths. For this test, we used the case of the convolved data at the resolution of 110000. The machine learning operates at its best while using the full range of the initial line list. In addition, regarding the divided areas, we notice that using the bluer part of the wavelength range leads to higher scores and lower mean absolute errors. In general, the results show that we can obtain highly precise predictions for stars observed at any part of the 530 to 690 nm spectrum. These results are presented in Table 3.3.

Table 3.1: Average values of the scores and the mean absolute errors (M.A.E.) for T_{eff} and [Fe/H] of the test dataset after 100 runs with each regression type

Regression	r2 score	E.V. score	M.A.E. T_{eff} [K]	M.A.E. [Fe/H] [dex]
Ridge	0.93	0.94	27	0.037
RidgeCV	0.93	0.94	27	0.038
Linear	0.93	0.93	27	0.039
Multi-task Elastic Net	0.91	0.92	35	0.045
Multi-task Lasso	0.88	0.89	41	0.056

Table 3.2: Average values of the scores and the mean absolute errors (M.A.E.) for T_{eff} and [Fe/H] of the test dataset after 100 runs at each resolution (using the ”ridge” regression)

Resolution	r2 score	E.V. score	M.A.E. T_{eff} [K]	M.A.E. [Fe/H] [dex]
real 115000	0.93	0.94	27	0.037
conv. 110000	0.93	0.94	28	0.038
conv. 94600	0.93	0.93	28	0.039
conv. 75000	0.93	0.93	29	0.041
conv. 48000	0.92	0.93	30	0.043

Table 3.3: Average values of the scores and the mean absolute errors (M.A.E.) for T_{eff} and [Fe/H] of the convolved-to-110000 dataset after 100 runs with different wavelength ranges of the line list.

Wavelength range (nm)	Number of lines	r2 score	E.V. score	M.A.E. T_{eff} [K]	M.A.E. [Fe/H] [dex]
530 - 690	4104	0.93	0.94	28	0.038
530 - 580	1300	0.92	0.93	31	0.039
580 - 630	1300	0.91	0.91	48	0.044
630 - 690	1504	0.89	0.90	56	0.048

3.4. Determination of stellar parameters

The tool has been applied to spectra taken from the public data archives of the several instruments mentioned earlier. To test the efficiency of our tool on spectra obtained using instruments other than HARPS, we used spectra from stars in common with the 65-star HARPS dataset, so that we could compare our results with the photometric reference parameters of the respective HARPS spectra. To further validate the accuracy of our tool, we proceeded to perform comparison for different datasets of stars.

3.4.1 Resolution and spectral shape

We examined the spectral change of M dwarfs according to lower resolutions. This is illustrated in Fig. 3.8 where spectral lines of Gl176 are shown in detail, both for the original HARPS spectrum and the convolved ones to several resolutions. These lines were measured and their pseudo-EW values are reported in Table 3.4. All the differences confirm that lower resolution always leads to lower pseudo-EW values. This happens because in lower resolutions the absorption lines broaden and become more shallow, thus the positions of their peaks that are used to set the pseudo continuum also change, leading to lower pseudo-EW measurements.

This is why we need to convolve the HARPS spectra to the respective resolutions of the new spectra. Consequently, machine learning compares the pseudo EWs of the same resolution and accurately predicts the stellar parameters. Figure 3.9 shows the spectral shapes of Gl674 for three different cases: the original HARPS spectrum with resolution 115000, the convolved HARPS spectrum to the resolution of FEROS (48000), and the original FEROS spectrum, which is the lowest resolution we examine. The convolved HARPS spectrum follows the shape of the FEROS one in a consistent way.

Figure 3.10 shows the comparison of the pseudo EWs of the SOPHIE spectrum for Gl908 and the spectrum of the same star by HARPS before and after its convolution. The SOPHIE spectrum, which is of a lower resolution, has consistently lower pseudo-EW values than the HARPS one, as expected. After the convolution of the HARPS spectrum to the resolution of SOPHIE, the overall trend of their pseudo-EW values become highly compatible.

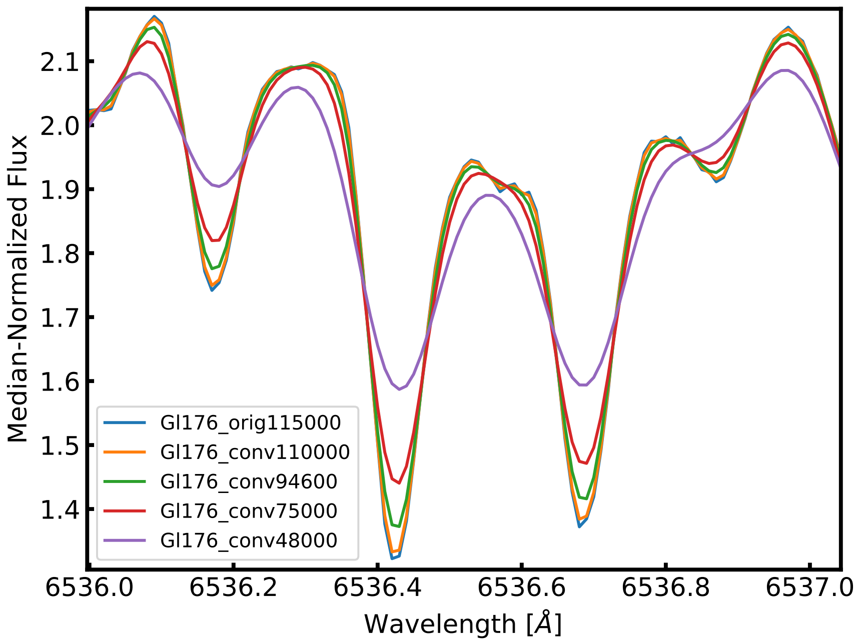

Figure 3.8: Shape of the HARPS original spectrum for Gl176 and convolved in different resolutions. The lower the resolution the swallower the absorption lines.

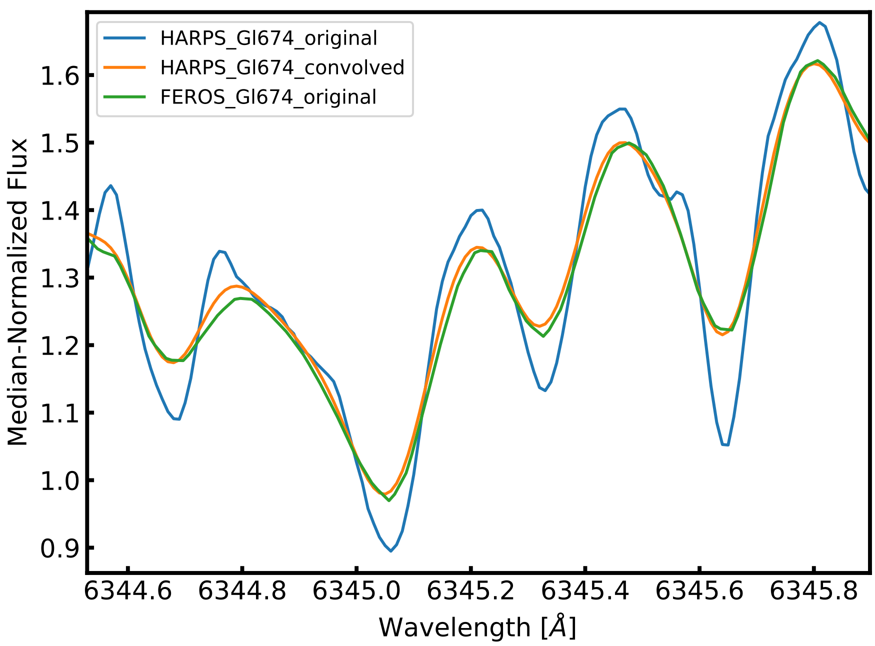

Figure 3.9: Shape of spectra for Gl674 at the original HARPS resolution (blue), at the FEROS resolution (green), and at the HARPS convolved to FEROS resolution (orange).

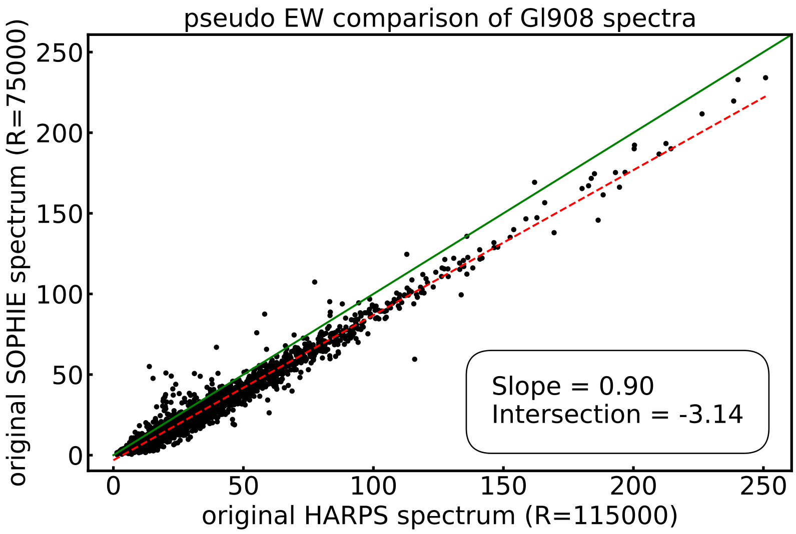

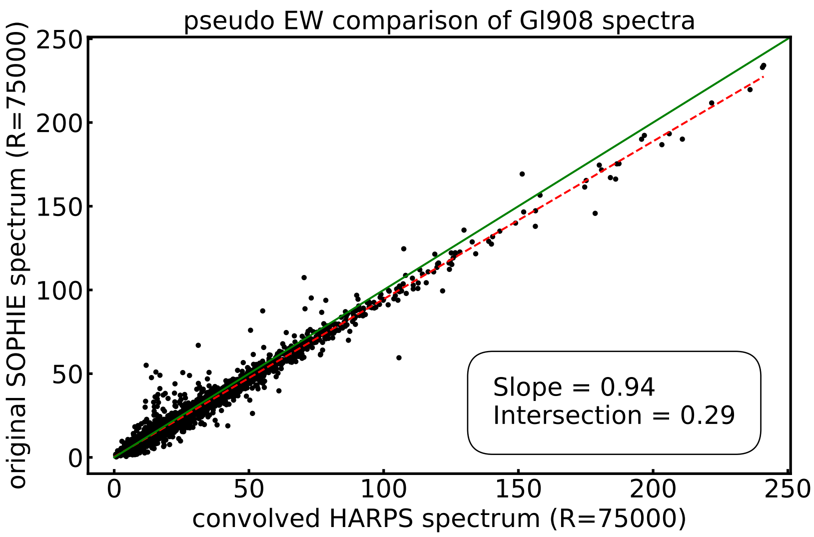

Figure 3.10: Upper panel: Pseudo-EW values of the original Gl908 spectra for HARPS and SOPHIE. Lower panel: Pseudo-EW values of Gl908 after the convolution of HARPS to the resolution of SOPHIE. The units of pseudo EWs are mÅ. After the convolution, there is agreement between the identity line (solid green) and the slope (dashed red), with the intersection being close to zero.

Table 3.4: Pseudo EWs of three absorption lines for HARPS spectrum Gl176 at different resolutions. The lower the resolution, the smaller the pseudo EW.

Resolution	p.EW of λ 6536.18 [mÅ]	p.EW of λ 6536.41 [mÅ]	p.EW of λ 6536.67 [mÅ]
original 115000	14.19	29.08	27.31
convolved 110000	14.04	28.89	26.98
convolved 94600	13.39	28.27	26.35
convolved 75000	11.99	27.45	25.08
convolved 48000	7.50	22.50	20.04

3.4.2 Measurements on different spectrographs

The performance of our tool was examined in new spectra. We show the accuracy of the predicted stellar parameters and the precision for each resolution by presenting the mean absolute errors of the models and the dispersion of the results, as calculated after 100 determinations for each spectrum.

For the case of HARPS, we used a spectrum of Gl643 with S/N = 83, which is not part of the HARPS dataset used in the machine learning. As reference values for this star, we consider its parameters reported by Neves et al. (2014). For the cases of the other instruments, we used a UVES spectrum of Gl846 with S/N = 149, a CARMENES spectrum of Gl514 with S/N = 191, a SOPHIE spectrum of Gl908 with S/N = 90 and a FEROS spectrum of Gl674 with S/N = 61. As reference $T_{\rm eff}$ and [Fe/H] to those spectra, we considered the values by Casagrande et al. (2008) and Neves et al. (2012) respectively in the HARPS dataset.

The results of $T_{\rm eff}$ and [Fe/H] are presented in Table 3.5. The parameters of the new spectra are very close to the respective reference values. The differences in $T_{\rm eff}$ vary up to $\sim$50 K and the differences in [Fe/H] vary up to 0.03 dex. The mean absolute errors of models and the dispersion of values increase slightly with decreasing resolution. Thus, measurements of FEROS spectra are reasonably the least precise compared to the other cases.

Table 3.5: Machine learning (M.L.) results of $T_{\rm eff}$ and [Fe/H], their dispersion (Disp.), the mean absolute errors (M.A.E.) of the models, and the reference values (Ref.)

Star	Spec.	Ref. $T_{\rm eff}$ [K]	M.L. $T_{\rm eff}$ [K]	M.A.E. $T_{\rm eff}$ [K]	Disp. $T_{\rm eff}$ [K]	Ref. [Fe/H] [dex]	M.L. [Fe/H] [dex]	M.A.E. [Fe/H] [dex]	Disp. [Fe/H] [dex]
Gl643	HARPS	3102	3113	27	10	-0.26	-0.28	0.04	0.01
Gl846	UVES	3682	3691	28	13	-0.08	-0.05	0.04	0.02
Gl514	CARMENES	3574	3547	28	17	-0.13	-0.13	0.04	0.03
Gl908	SOPHIE	3587	3580	28	18	-0.38	-0.35	0.04	0.03
Gl674	FEROS	3284	3338	30	24	-0.18	-0.16	0.04	0.03

3.4.3 Measurements at different S/N

As next step, we examined the possible variation of the results regarding different S/N for a given spectrum. The spectrum Gl514 of CARMENES was selected for this task, which has the highest S/N of those we examined (equal to 191, as reported in the CARMENES data archive). We injected amounts of noise with the normal distribution function of python, which correspond to the lower S/N values that we set. Since the final noise is the quadratic sum of the initial noise and the injected noise, the final S/N values were calculated using the relation below.

$$(\frac{1}{SNR})^2_{final} = (\frac{1}{SNR})^2_{initial} + (\frac{1}{SNR})^2_{injected} \tag{3.5}$$

New spectra were created with final S/N values ranging from 9 to 100. For each spectrum, we measured the stellar parameters and their dispersion. Figure 3.11 illustrates the measurements of the CARMENES spectrum while degrading its S/N. Overall, the results are similar to those for the original spectrum and the differences are kept roughly constant with respect to the original values. For S/N values down to 20, the dispersions are between 17 and 27 K for T_{eff} and between 0.03 and 0.04 dex for [Fe/H], i.e., at similar levels to those for the original spectrum. For S/N values below 20, the dispersions start to increase up to $\sim$50 K and up to $\sim$0.07 dex respectively. Moreover, there is a slight decrease of the order of 30 K in T_{eff} and a slight increase of the order of 0.02 dex in [Fe/H] for the spectra with S/N below 20. However, these changes are similar to the precision errors of the tool. Therefore, we conclude that our tool works consistently for spectra with S/N above 20. Below this S/N, the errors increase significantly.

3.4.4 Comparison of results between our tool and Neves et al. (2014)

We proceeded to an overall comparison of our results on a group of HARPS spectra with the ones presented by Neves et al. (2014). For this purpose, we measured 30 HARPS spectra from the total 110-star GTO sample, which are not part of the photometric reference dataset. Based on the information from Neves et al. (2014), we excluded very active stars and stars with S/N lower than 25, below which the method of these latter authors does not apply. Both methods were tested and shown to not work properly for very active or young stars, since the pseudo EWs of such spectra are affected and their parameters cannot be determined accurately with the pseudo-EW approach we follow. Subsequently, we compared the results we obtained using our tool with the results presented by Neves et al. (2014).

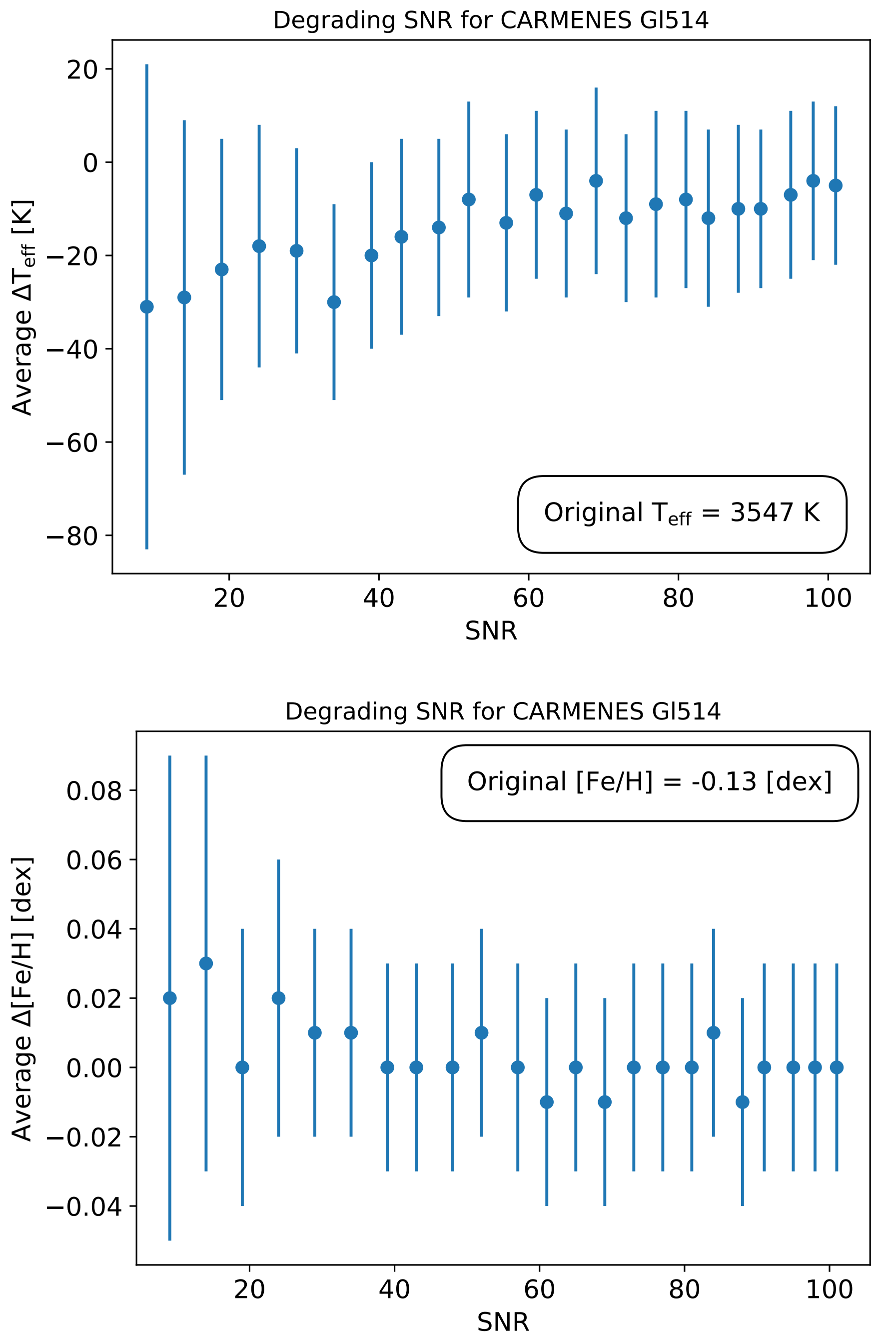

Figure 3.11: Average differences and the dispersion of T_{eff} (upper panel) and [Fe/H] (lower panel) for CARMENES Gl514 spectrum with different values of S/N.

The errors of the stellar parameters derived using our tool are 27 K for T_{eff} and 0.04 dex for [Fe/H], as the mean absolute errors are measured when the machine learning model is applied on the test dataset. The errors of the calibration by Neves et al. (2014), which are quantified from the root mean squared error (RMSE) in that work, are equal to 91 K and 0.08 dex respectively. Both determinations are tied to the same initial systematic uncertainties of the photometric reference parameters used, which are 100 K for T_{eff} and 0.17 dex for [Fe/H]. The results and their differences are presented in Table 3.6 and Fig. 3.12. The mean and median difference in T_{eff} is 11 and 22 K respectively, with a standard deviation of 101 K. Regarding [Fe/H], the mean and median difference is -0.04 dex, with a standard deviation of 0.06 dex.

The work by Neves et al. (2014) follows a traditional approach, using a least-squares weighted fit to determine parameters. The regression of our tool reduces those errors of T_{eff} and [Fe/H] from 91 to 27 K and from 0.08 to 0.04 dex respectively. Therefore, our machine learning approach significantly increases the precision of parameter determinations. In terms of speed, the determination of T_{eff} and [Fe/H] for a star using machine learning, including multiple runs, shuffling and splitting the training and test samples each time, requires only a few seconds.

3.4.5 Estimating total uncertainties

Intrinsic uncertainties exist in the T_{eff} and [Fe/H] reference values of the HARPS dataset, because their initial photometric derivations have average uncertainties of 100 K and 0.17 dex respectively. Since these parameters are used as the training values for the machine learning process, we decided to inject these uncertainties by perturbing their values accordingly in order to see how the final results of the predictions vary.

To this end, we created Gaussian distributions on the parameters for each HARPS training dataset, increasing the dispersion of distribution of the reference parameters each time in steps of 10 K and 0.02 dex until reaching uncertainties of 100 K and 0.17 dex. This added different training values to the machine learning algorithm each time. For each step, we created 100 Gaussian-distributed training datasets. After these runs of machine learning, we calculated the average values of predicted parameters and their dispersion. In Fig. 3.13, we present the variations for spectra from the highest resolution (HARPS), the lowest resolution (FEROS), and an intermediate resolution (CARMENES).

Table 3.6: Stellar parameters of 30 HARPS spectra as calculated by our tool (AA) and Neves et al. (2014), both applying the same photometric reference scale. The S/Ns of those stars are between 28 and 97, as reported by Neves et al. (2014).

Star	T_{eff} (AA) [$\pm$27 K]	T_{eff} (Ne14) [$\pm$91 K]	T_{eff} Diff. [K]	[Fe/H] (AA) [$\pm$0.04 dex]	[Fe/H] (Ne14) [$\pm$0.08 dex]	[Fe/H] Diff. [dex]
CD-44-836A	3104	3032	72	-0.07	-0.07	0.00
G108-21	3214	3186	28	-0.02	-0.02	0.00
Gl1057	2926	2916	10	-0.11	-0.10	-0.01
Gl1061	2772	2882	-110	-0.25	-0.09	-0.16
Gl1065	3106	3082	24	-0.32	-0.23	-0.09
Gl1123	2971	2779	192	-0.02	0.15	-0.17
Gl1129	3037	3017	20	-0.02	0.05	-0.07
Gl1236	3225	3280	-55	-0.44	-0.47	0.03
Gl1256	2964	2853	111	-0.02	0.06	-0.08
Gl1265	3020	2941	79	-0.28	-0.20	-0.08
Gl12	3245	3239	6	-0.31	-0.29	-0.02
Gl145	3297	3270	27	-0.27	-0.28	0.01
Gl203	3174	3138	36	-0.31	-0.22	-0.09
Gl299	3078	3373	-295	-0.53	-0.53	0.00
Gl402	3052	2943	109	0.00	0.03	-0.03
Gl480.1	3214	3211	3	-0.48	-0.48	0.00
Gl486	3096	2941	155	-0.02	0.03	-0.05
Gl643	3113	3102	11	-0.29	-0.26	-0.03
Gl754	2988	3005	-17	-0.23	-0.14	-0.09
L707-74	3250	3353	-103	-0.39	-0.38	-0.01
LHS1134	3007	2950	57	-0.20	-0.13	-0.07
LHS1481	3342	3510	-168	-0.66	-0.76	0.10
LHS1723	3031	3167	-136	-0.29	-0.24	-0.05
LHS1731	3229	3273	-44	-0.22	-0.19	0.03
LHS1935	3222	3181	41	-0.20	-0.22	0.02
LHS337	3003	3007	-4	-0.33	-0.27	-0.06
LHS3583	3205	3236	-31	-0.13	-0.22	0.09
LHS3746	3111	3013	98	-0.17	-0.13	-0.04
LHS543	3042	2872	170	0.17	0.23	-0.06
LP816-60	3030	2960	70	-0.11	-0.07	-0.04

The datapoints represent the average difference between the resulting parameters after being calculated with the 100 different datasets and the reference values. The error bars show the dispersion of the difference. We notice that the average differences from the reference values are almost the same among different Gaussian distributions, regardless of the amount of uncertainty injected to the Gaussian distribution.

The average results of T_{eff} and [Fe/H] for the spectra from all the instruments are presented in Table 3.7. We report their maximum errors after considering the maximum

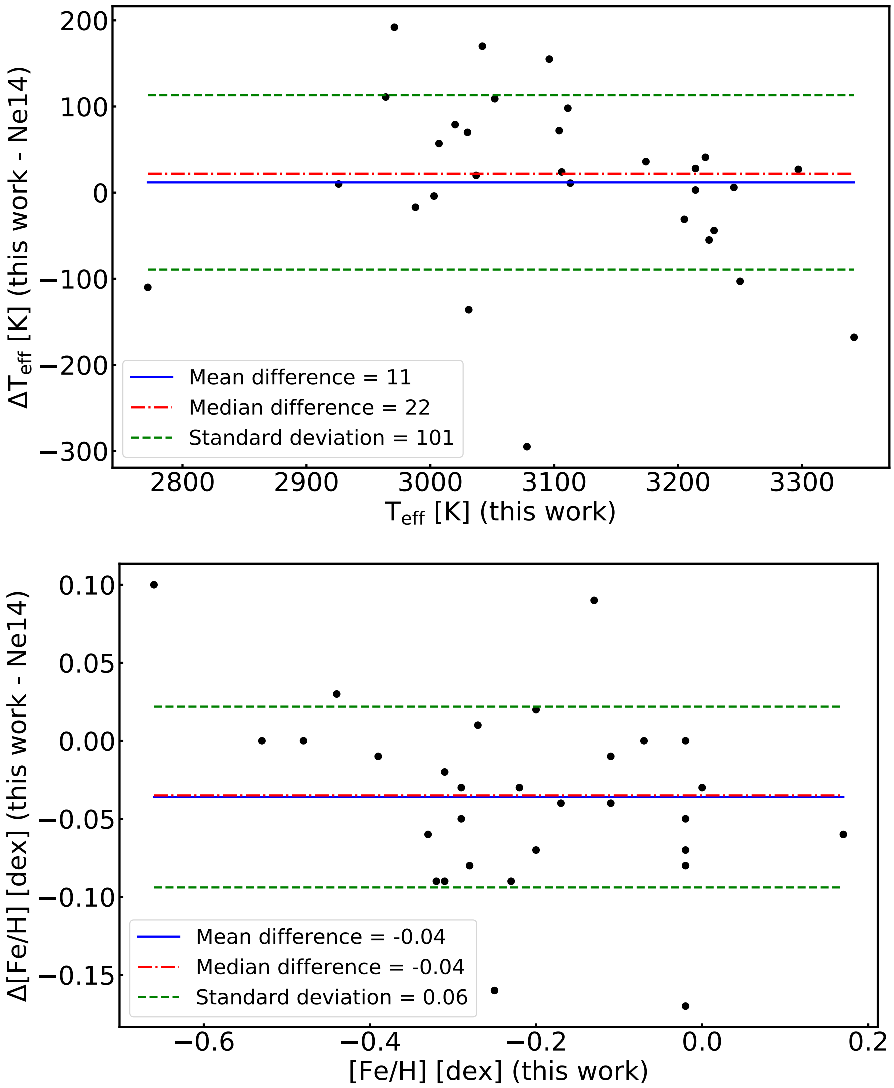

Figure 3.12: T_{eff} comparison (upper panel) and [Fe/H] comparison (lower panel) between this work and Neves et al. (2014), applying the same photometric reference scale.

Gaussian distribution with 100 K and 0.17 dex. Overall, the average values of the parameters remain roughly the same as those calculated with no Gaussian distribution at all. The mean absolute errors of the machine learning models have grown to values of between 65 and 80 K for T_{eff} and between 0.10 and 0.13 dex for [Fe/H], depending on the resolution of the HARPS dataset. The dispersion of the derived parameters grows as the resolution of the spectra decreases. Specifically, the dispersion is smaller than the injected uncertainties for the HARPS spectrum (∼60 K and ∼0.10 dex), while for the spectra from other instruments, it is slightly higher than the uncertainties injected (∼110 to ∼130 K and ∼0.18 to ∼0.22 dex respectively). However, in all cases the resulting average values are very close to their expected ones. Differences in T_{eff} are up to ∼40 K and in [Fe/H] are up to 0.03 dex, with respect to the expected values.

Table 3.7: Machine learning (M.L.) results of T_{eff} and [Fe/H] after injecting uncertainties with Gaussian distributions of 100 K and 0.17 dex in the parameters of the training HARPS datasets, their dispersion (Disp.), the mean absolute errors (M.A.E.) of the models, and the reference values (Ref.) for comparison.

Star	Spec.	Ref. T_{eff} [K]	M.L. T_{eff} [K]	M.A.E. T_{eff} [K]	Disp. T_{eff} [K]	Ref. [Fe/H] [dex]	M.L. [Fe/H] [dex]	M.A.E. [Fe/H] [dex]	Disp. [Fe/H] [dex]
Gl643	HARPS	3102	3126	65	60	-0.26	-0.29	0.10	0.10
Gl846	UVES	3682	3678	68	109	-0.08	-0.06	0.10	0.18
Gl514	CARMENES	3574	3545	77	113	-0.13	-0.13	0.12	0.19
Gl908	SOPHIE	3587	3585	78	120	-0.38	-0.36	0.13	0.21
Gl674	FEROS	3284	3324	80	138	-0.18	-0.15	0.13	0.22

3.4.6 Validation of [Fe/H] determinations by measuring binary systems

[Fe/H] was determined in binary systems containing M dwarfs which are not part of the photometric reference sample used for machine learning. Thus, we validated our method of [Fe/H] prediction in an independent way. We determined [Fe/H] both in FGK+M and in M+M systems for an even more intrinsic test of [Fe/H] agreement. The [Fe/H] determinations of eight FGK+M binary systems with spectra obtained from UVES and FEROS spectrographs are presented in Table 3.8. Regarding the FGK stars, their [Fe/H] and respective uncertainties were derived using the method described in Sousa et al. (2008) and Santos et al. (2013). It measures the EWs of FeI and FeII lines and assumes ionization and excitation equilibrium. It makes use of the radiative transfer code MOOG (Sneden, 1973) and a grid of Kurucz model atmospheres (Kurucz, 1993). The [Fe/H] values of the respective M dwarf secondaries, derived by ODUSSEAS using the photometric reference dataset, are presented along with the total uncertainties of our tool at the resolutions of UVES (0.10 dex) and FEROS (0.13 dex). All binaries have differences within the uncertainties of the methods. We proceeded to [Fe/H] determinations of stars in five M+M binary systems, measuring the pseudo EWs of their spectra from the CARMENES public archive. In Table 3.9, we present these results along with their own dispersions, since both were estimated by our tool with the same initial uncertainties. We notice agreement between the respective members of all the M+M binaries, within the dispersions of their [Fe/H] determinations. This is a validation that our tool predicts [Fe/H] in a consistent and accurate way. The differences of [Fe/H] values between both FGK+M and M+M binaries, are shown in Fig. 3.14. The mean difference of the secondary star compared to the primary one is -0.02 dex with a standard deviation of 0.07 dex.

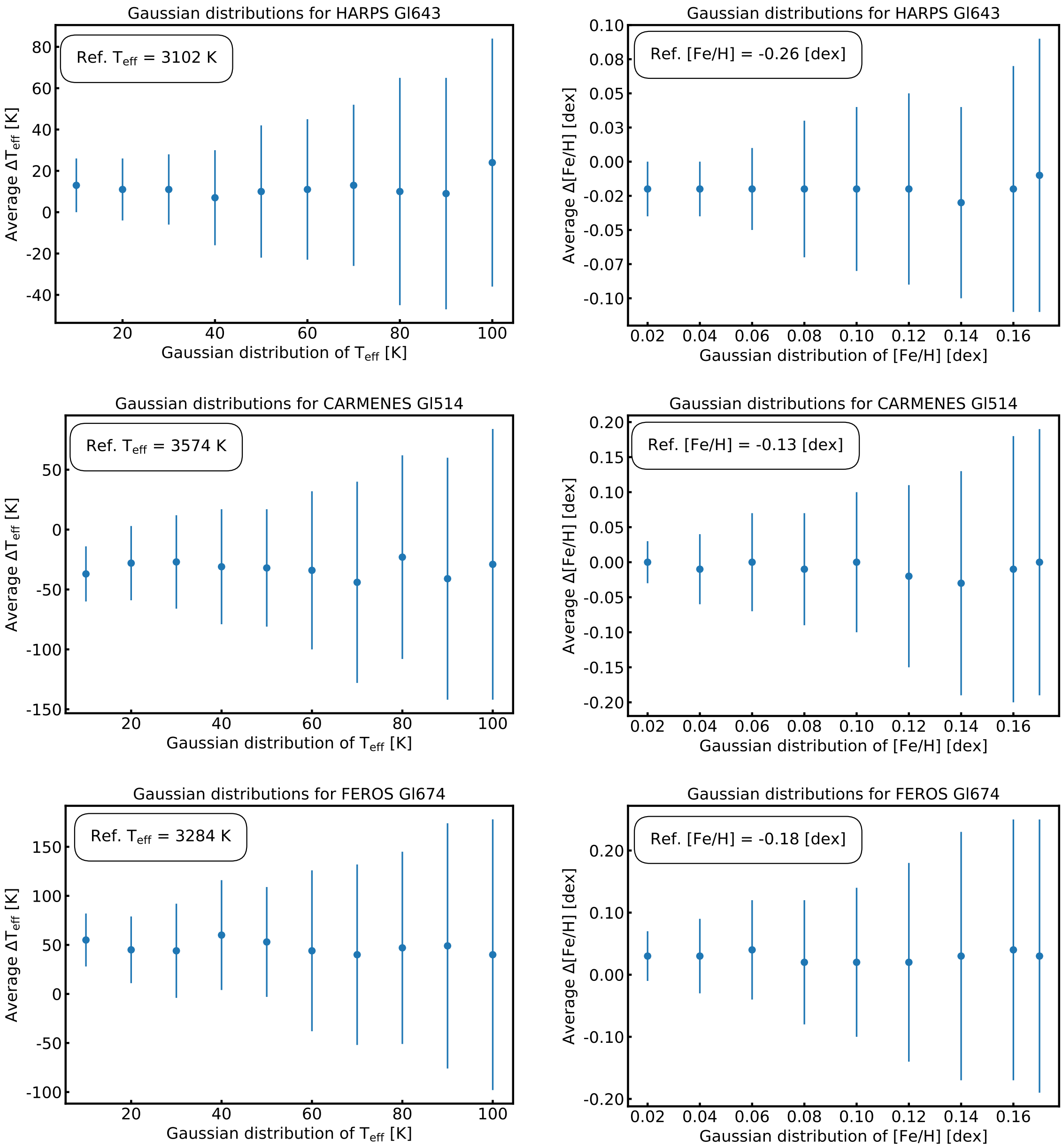

Figure 3.13: Average differences and dispersions of results for several amounts of Gaussian distribution injected to the reference parameters of the training HARPS datasets. The result of each step is the average outcome from 100 different distributed datasets.

3.4.7 Application to ESPRESSO data of highest resolution

After the analysis of the efficiency towards lower resolutions and the successful application to the spectrographs mentioned above, the tool has been also applied successfully on spectra from ESPRESSO* (Pepe et al., 2021) spectrograph that became available to us. This case is special because the resolution (R = 140000) of ESPRESSO spectra is higher than the resolution (R = 115000) of the HARPS reference spectra. For these very high resolutions of ESPRESSO and HARPS, the results derived by ODUSSEAS

*https://www.eso.org/sci/facilities/paranal/instruments/espresso.html

Table 3.8: Metallicity comparison between members of FGK+M binary systems.

Primary	[Fe/H] [dex]	σ[Fe/H] [dex]	Secondary	[Fe/H] [dex]	σ[Fe/H] [dex]	[Fe/H] Difference [dex]
Gl100A	-0.29	0.05	Gl100C	-0.29	0.13	0.00
Gl118.1A	0.02	0.05	Gl118.1B	0.05	0.10	0.03
Gl173.1A	-0.37	0.03	Gl173.1B	-0.29	0.10	0.08
Gl157A	-0.08	0.04	Gl157B	0.02	0.13	0.10
NLTT19073	0.08	0.03	NLTT19072	-0.07	0.13	-0.15
NLTT29534	0.00	0.03	NLTT29540	-0.03	0.10	-0.03
NLTT34137	-0.12	0.05	NLTT34150	-0.13	0.10	-0.01
NLTT34353	-0.10	0.03	NLTT34357	-0.11	0.10	-0.01

Table 3.9: Metallicity comparison between members of M+M binary systems.

Primary	[Fe/H] [dex]	Disp. [dex]	Secondary	[Fe/H] [dex]	Disp. [dex]	[Fe/H] Difference [dex]
Gl553	-0.07	0.06	Gl553.1	-0.10	0.07	-0.03
Gl875	-0.15	0.05	Gl875.1	-0.17	0.06	-0.02
Gl617A	0.04	0.04	Gl617B	-0.08	0.08	-0.12
Gl745A	-0.48	0.04	Gl745B	-0.53	0.06	-0.05
Gl752A	0.01	0.03	Gl752B	-0.07	0.08	-0.08

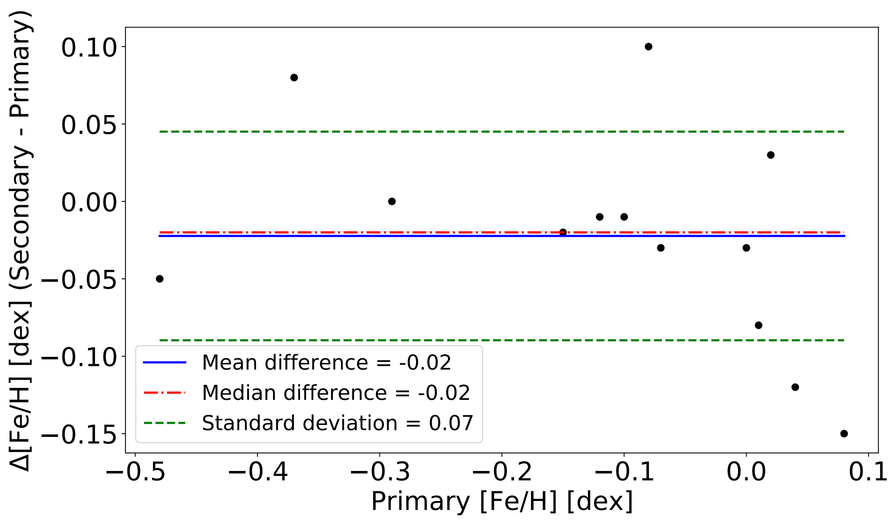

Figure 3.14: Difference of metallicity between members of binary systems.

are essentially the same, either by using directly the original highest-resolution spectra of ESPRESSO to be determined according to the HARPS reference spectra (first way), or by degrading them first to the slightly lower -but still high- resolution of HARPS (second way). Between an ESPRESSO spectrum being analyzed according to the HARPS reference dataset and the same spectrum downgraded in the HARPS resolution before being analyzed by ODUSSEAS, the differences in the resulting parameters are smaller than the precision errors of the machine learning model themselves, so essentially there is no difference. Typical differences below 0.02 dex and 10 K that were noticed in the determinations of parameters for ESPRESSO spectra following the two ways, are even smaller than the precision errors that our machine learning models can provide. However, there is difference in terms of speed. Measuring the spectra the first way, takes one minute per star, while the computational process for degradation before measuring, needs ten minutes per spectrum (from R = 140000 to R = 115000). Therefore, we can follow the first way as it is less time-consuming and still able to determine parameters with highest accuracy and precision for ESPRESSO data. Studies which have applied ODUSSEAS tool on ESPRESSO spectra have been already published for the planetary systems of M dwarfs LHS1140 (Lillo-Box et al., 2020), L98-59A (Demangeon et al., 2021), TOI-3235 (Hobson et al., 2023) and TOI-244 (Castro-González et al., 2023).

3.5. Discussion on the reference parameter scales

Since supervised machine learning determines the parameters based on reference values given to it, their systematics will also apply to the results of new stars. So far, we used as references the photometric T_{eff} and [Fe/H] scales by Casagrande et al. (2008) and Neves et al. (2012) respectively, as they were derived in a homogeneous way for a sufficiently large number of spectra available to us.

3.5.1 Comparison of reference parameters with Mann et al. (2015)

We compared these reference parameters with determinations by Mann et al. (2015) and the differences are reported in Table 3.10. These differences are illustrated in Fig. 3.15.

Regarding T_{eff}, the photometric reference values have an average underestimation of 182 K with a standard deviation of 70 K. This systematic difference originates from the different methods of derivation used. Work by Casagrande et al. (2008) is based on the multiple optical-infrared technique (MOITE) for M dwarfs, which is an extension of the infrared flux method (IRFM) as described in Casagrande et al. (2006). On the other hand, determinations by Mann et al. (2015) were made by comparing the optical spectra with the CFIST suite of the BT-SETTL version of the PHOENIX atmosphere models (Allard et al., 2013). A detailed description of this method can be found in Mann et al. (2013b). Regarding [Fe/H], we notice no significant systematic difference in parameter values resulting from the methods of calibration by Neves et al. (2012) and Mann et al. (2015). The average difference is 0.06 dex lower for ODUSSEAS, with a standard deviation of 0.11 dex for the sample of stars in common.

Table 3.10: Stellar parameters of 26 reference stars in common with Mann et al. (2015) and their differences.

Star	T_{eff} (Ref.) [$\pm$100 K]	T_{eff} (Mann15) [$\pm$60 K]	T_{eff} Diff. [K]	[Fe/H] (Ref.) [$\pm$0.17 dex]	[Fe/H] (Mann15) [$\pm$0.08 dex]	[Fe/H] Diff. [dex]
Gl54.1	2901	3056	-155	-0.40	-0.26	-0.14
Gl87	3565	3638	-73	-0.30	-0.36	0.06
Gl105B	3054	3284	-230	-0.14	-0.12	-0.02
Gl176	3369	3680	-311	0.02	0.14	-0.12
Gl205	3497	3801	-304	0.17	0.49	-0.32
G213	3026	3250	-224	-0.19	-0.22	-0.03
Gl250B	3369	3481	-112	-0.09	0.14	-0.25
Gl273	3107	3317	-210	-0.05	-0.11	0.06
Gl382	3429	3623	-194	0.04	0.13	-0.09
Gl393	3396	3548	-154	-0.13	-0.18	0.05
Gl436	3277	3479	-202	0.01	0.01	0.00
Gl447	2952	3192	-240	-0.23	-0.02	-0.21
Gl514	3574	3727	-153	-0.13	-0.09	-0.04
Gl526	3545	3649	-104	-0.18	-0.31	0.13
Gl555	2987	3211	-224	0.13	0.17	-0.04
Gl581	3203	3395	-192	-0.18	-0.15	-0.03
Gl686	3542	3657	-115	-0.29	-0.25	-0.04
Gl699	3094	3228	-134	-0.59	-0.40	-0.19
Gl701	3535	3614	-79	-0.20	-0.22	0.02
Gl752A	3336	3558	-222	0.04	0.10	-0.06
Gl846	3682	3848	-166	-0.08	0.02	-0.10
Gl849	3200	3530	-330	0.24	0.37	-0.13
Gl876	3059	3247	-188	0.14	0.17	-0.03
Gl880	3488	3720	-232	0.05	0.21	-0.16
Gl887	3560	3688	-128	-0.20	-0.06	-0.14
Gl908	3587	3646	-59	-0.38	-0.45	-0.07

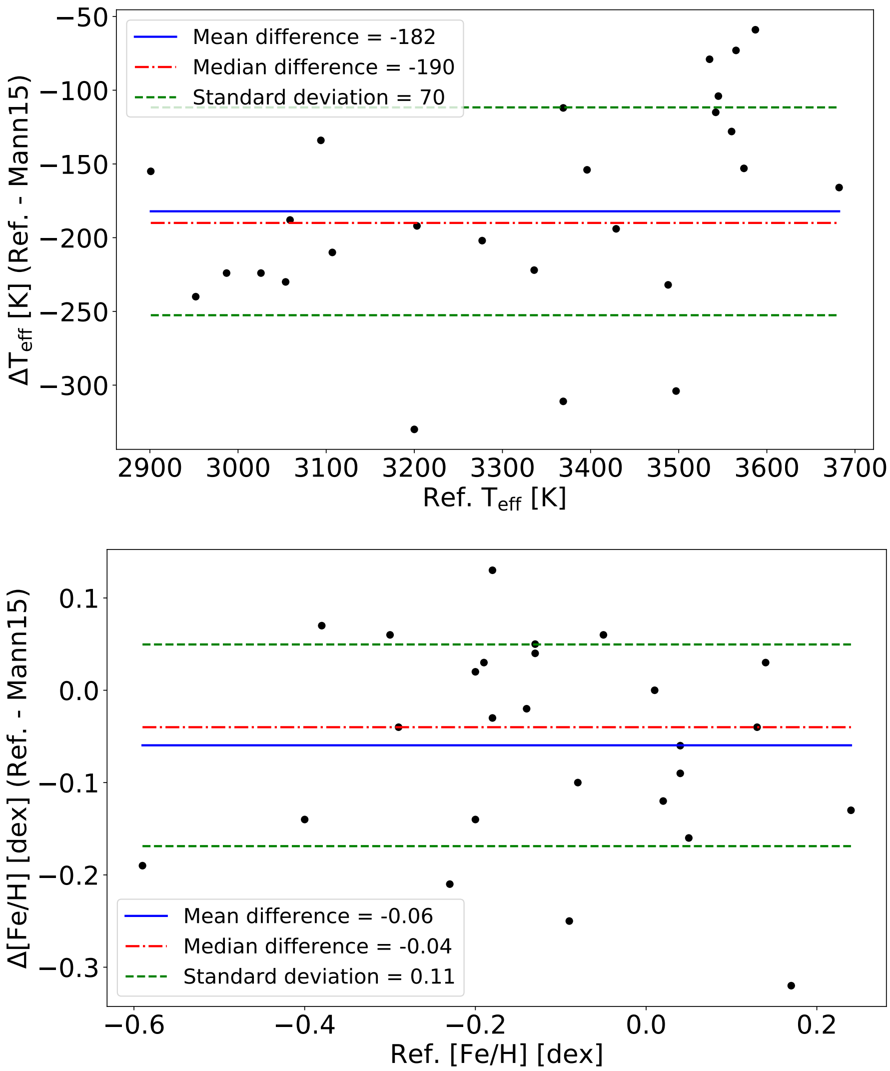

Figure 3.15: T_{eff} comparison (upper panel) and [Fe/H] comparison (lower panel) between the photometric reference parameters and Mann et al. (2015) for 26 stars in common.

3.5.2 Investigating different determination techniques

After the publication of the tool, a collaboration emerged as co-author in the published work by Passegger et al. (2022). In that study, we determined stellar atmospheric parameters of 18 well-studied M dwarfs observed with the CARMENES spectrograph following different approaches. Four methods were applied to the spectra. Two of them (Pass-19 code and SteparSyn) are based on synthetic spectra fitting, while the other two (Deep Learning and ODUSSEAS) are based on the machine learning concept. Pass-19 code uses a downhill simplex method with a χ^2 minimization to find the synthetic model spectrum that best fits the observed spectrum by fitting several wavelength ranges in the visual and NIR simultaneously. It incorporates PHOENIX-ACES model spectra grid (Husser et al., 2013). The method is fully described in Passegger et al. (2018, 2019).

The SteParSyn code (Tabernero et al., 2022) is a Bayesian implementation of the spectral synthesis technique that determines the probability distributions of the stellar atmospheric parameters from a Markov Chain Monte Carlo approach. In general terms, the code compares a grid of synthetic spectra, pre-computed around certain spectral features of interest. The Deep Learning method is described in Passegger et al. (2020). For each stellar parameter, a convolutional deep neural network with several hidden layers is built. In order to learn features from the input spectrum, the networks are trained with PHOENIX-ACES synthetic models.

We analyzed the discrepancies in the derived stellar parameters in several analysis runs. Our goal was to minimize these discrepancies and find stellar parameters that are more consistent with the literature value. Similarly to the comparison of reference T_{eff} with values by Mann et al. (2015), we noticed that the photometric reference scale of ODUSSEAS gave results underestimated, compared to the other three methods, as well as to the literature values. In Table 3.11, these differences are presented, when calculating the parameters with each method free of specific restrictions. The mean differences of the ODUSSEAS results to the literature median was -86 K, to interferometric literature values -123 K, to Pass-18 code -178 K, to SteparSyn -132 K and to Deep Learning -176 K respectively. From these comparisons, it was clear that the IRFM/MOITE-based photometric reference scale was consistently underestimating T_{eff} values for M dwarfs, so we examined the possibility of replacing our photometric reference dataset, with reference values from interferometry as a potential improvement of our determinations.

Table 3.11: T_{eff} average difference of ODUSSEAS results using the photometric reference scale, compared to other methods and literature

Method	T_{eff} Difference [K]
literature median	-86
interferometric literature	-123
Pass-18 code	-178
SteparSyn	-132
Deep Learning	-176

3.6. Upgrade with new reference scale

After the publications of the tool and the comparative study of parameter-determination methods, we searched the literature to find a sufficient number of stars among the 110 ones for which we had HARPS spectra, that they had T_{eff} based on interferometry.

One year after our publication, Khata et al. (2021) presented a sample of 23 target stars with high precision long-baseline interferometric measurements of radii (Boyajian et al., 2012, Mann et al., 2015, Rabus et al., 2019) for the calibration of stellar parameters. 13 calibrators were chosen from Newton et al. (2015) where the bolometric luminosity was measured from multicolor photometry (Boyajian et al., 2012) and T_{eff} was calculated using the interferometric radius and bolometric flux (Mann et al., 2013b). This calibration sample was supplemented with 6 M dwarfs taken from Mann et al. (2015), where the bolometric flux was calculated by integrating over the radiative flux density and T_{eff} was calculated by fitting the optical spectra with the PHOENIX (BT-Settl) models (Allard et al., 2013). The remaining 4 calibrators were selected from Rabus et al. (2019), where they estimated the bolometric flux using PHOENIX models (Husser et al., 2013) along with photometric observations and T_{eff} using the Stefan-Boltzmann law. Khata et al. (2021) proceeded to a calibration, deriving stellar parameters for 271 stars. For 43 of those 271 stars, we had HARPS GTO spectra available. We also added 4 more stars from the HARPS GTO sample with values derived by Rabus et al. (2019) to our new reference dataset. Rabus et al. (2019) reported on 13 new high-precision measurements of stellar diameters for low-mass dwarfs obtained by means of NIR long-baseline interferometry with PIONIER at the Very Large Telescope Interferometer. Together with accurate parallaxes from Gaia DR2, these measurements provided precise estimates for their linear radii, T_{eff}, masses, and luminosities. Thus, ODUSSEAS was upgraded by adding a new reference dataset of 47 stars with T_{eff} based on interferometry (Khata et al., 2021, Rabus et al., 2019).

For these 47 stars, [Fe/H] values were derived using the same method as in the original reference dataset, applying the following relation by Neves et al. (2012):

$$[Fe/H] = 0.57\Delta(V - K_s) - 0.17 \tag{3.6}$$

where $\Delta(V - K_s)$ = $(V - K_s)_{obs} - (V - K_s)_{iso}$, in which $(V - K_s)_{obs}$ is the observed $V - K$ color and $(V - K_s)_{iso}$ is a fifth order polynomial function of the absolute magnitude M_{Ks} with the coefficients being in increasing order: (51.1413, -39.3756, 12.2862, -1.83916, 0.134266, -0.00382023). As input values to the equation, we have used V and K magnitudes reported in Simbad* and the updated values of parallaxes from Gaia eDR3 for the calculation of M_{Ks}.

*http://simbad.cds.unistra.fr/simbad/

This new reference dataset is presented in Table A.2. The range of the new reference stellar parameters is presented in Fig 3.16. The methods of derivation for these reference values have intrinsic uncertainties of 99 K for T_{eff} and 0.17 dex for [Fe/H], by Khata et al. (2021) and Neves et al. (2012) respectively.

Among the 37 stars in common in the two reference datasets, the average difference between the new reference and the old reference scale is 151 K for T_{eff} and -0.01 dex for [Fe/H]. As we present and discuss later, in Sect. 3.7 and Sect. 3.9, these average differences between the reference datasets translate to average differences of the same order in the determinations for several samples of stars.

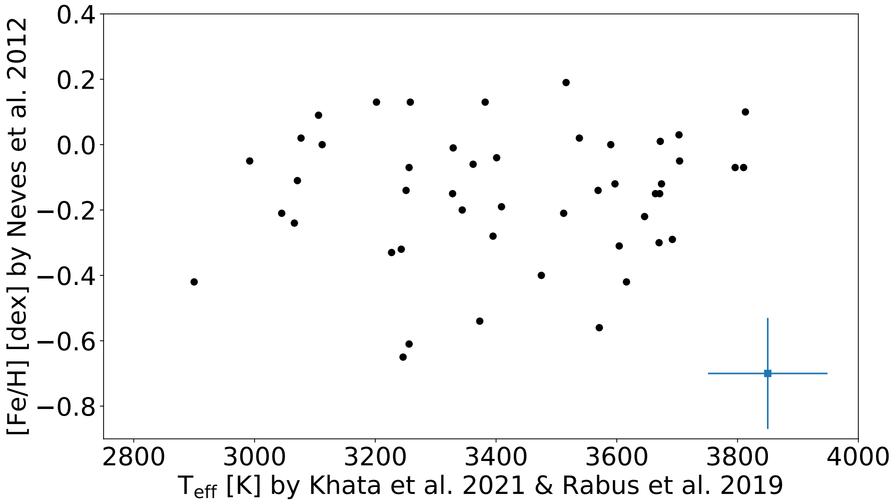

Figure 3.16: Distribution of reference T_{eff} and [Fe/H] of the new 47-star dataset used to train and test the machine learning models. The cross symbol represents their uncertainties, which are 99 K and 0.17 dex respectively.

The same steps as those applied to the initial 65-star reference dataset, were followed again, in order to check the machine learning efficiency, accuracy and precision with this new 47-star reference dataset. Since our new reference dataset consists of less stars (47) than the original one (65), we decided to increase the percentage of stars in the training group from 70% to 80%, in order to include relatively more stars in the process of building the machine learning models, while still keeping a sufficient number of stars (10) for testing and measuring the mean absolute errors of the new models. The E.V. score varies mostly between 0.89 and 0.90, while the r2 score is between 0.88 and 0.89. These values are slightly lower than the respective scores between 0.92 and 0.94 of the original reference dataset, because the new population of reference stars is smaller than the initial one (47 compared to 65 stars). Still, the new scores are quite high for making predictions with sufficient accuracy and precision regarding M dwarfs. The mean absolute errors of the machine learning models are around 65 K for T_{eff} and 0.04 dex for [Fe/H] for all resolutions. The determinations of parameters for the stars with spectra of different spectrographs are presented in Table 3.12, together with their new reference values as defined by the new reference dataset. The predictions of ODUSSEAS had differences varying from 5 to 64 K for T_{eff} and from 0.00 to 0.05 dex for [Fe/H] compared to the expected values. We also injected the intrinsic uncertainties of our new reference values to the new training datasets, similarly as before. These are 99 K for T_{eff} and 0.17 dex for [Fe/H], as reported by Khata et al. (2021) and Neves et al. (2012) respectively. They lead to machine learning model errors varying from 90 to 99 K for T_{eff} and from 0.11 to 0.13 dex for [Fe/H], as the resolution of the spectra becomes lower. The predictions of the parameters remained within these error ranges compared to the expected reference values. These results are presented in Table 3.13.

Table 3.12: Machine learning (M.L.) results of T_{eff} and [Fe/H], their dispersion (Disp.), the mean absolute errors (M.A.E.) of the models, and the reference values (Ref.) applying the new 47-star reference scale.

Star	Spec.	Ref. T_{eff} [K]	M.L. T_{eff} [K]	M.A.E. T_{eff} [K]	Disp. T_{eff} [K]	Ref. [Fe/H] [dex]	M.L. [Fe/H] [dex]	M.A.E. [Fe/H] [dex]	Disp. [Fe/H] [dex]
Gl643	HARPS	3243	3238	65	11	-0.32	-0.31	0.04	0.01
Gl846	UVES	3810	3802	65	21	-0.07	-0.06	0.04	0.02
Gl514	CARMENES	3671	3624	65	33	-0.15	-0.15	0.04	0.03
Gl908	SOPHIE	3475	3507	65	53	-0.40	-0.36	0.04	0.03
Gl674	FEROS	3409	3473	65	42	-0.19	-0.14	0.04	0.03

Table 3.13: Machine learning (M.L.) results of T_{eff} and [Fe/H] after injecting uncertainties with Gaussian distributions of 99 K and 0.17 dex in the parameters of the new training HARPS datasets, their dispersion (Disp.), the mean absolute errors (M.A.E.) of the models, and the reference values (Ref.) for comparison.

Star	Spec.	Ref. T_{eff} [K]	M.L. T_{eff} [K]	M.A.E. T_{eff} [K]	Disp. T_{eff} [K]	Ref. [Fe/H] [dex]	M.L. [Fe/H] [dex]	M.A.E. [Fe/H] [dex]	Disp. [Fe/H] [dex]
Gl643	HARPS	3243	3227	90	95	-0.32	-0.31	0.11	0.13
Gl846	UVES	3810	3794	92	107	-0.07	-0.11	0.11	0.18
Gl514	CARMENES	3671	3625	95	127	-0.15	-0.12	0.12	0.23
Gl908	SOPHIE	3475	3502	97	130	-0.40	-0.37	0.13	0.23
Gl674	FEROS	3409	3481	99	149	-0.19	-0.16	0.13	0.24

3.7. Determination of parameters for 82 planet-hosts in SWEET-Cat

We determined T_{eff} and [Fe/H] in 82 stars of SWEET-Cat, a catalogue of Stars With ExoplanETs, which was originally introduced in 2013 (Santos et al., 2013). Since then, many more exoplanets were confirmed increasing significantly the number of host stars listed there (Sousa et al., 2021). SWEET-Cat contains planet-host stars and their parameters. As explained in the introduction, a crucial step for a comprehensive analysis of the exoplanets is the accurate and precise characterization of their host stars. Stellar parameters derived from high-resolution and high-S/N spectra, along with new results from Gaia eDR3, can provide updated and precise parameters for the discovered planets. Statistical studies of exoplanets and their host stars require consistent measurements in order to avoid different systematics affecting the results. SWEET-Cat aims for determining stellar parameters in a consistent and homogeneous way, by analysis of high quality spectra which are assembled for stars hosting planets.

Among the planet-host stars in the current SWEET-Cat archive, we searched for the stars with T_{eff} lower than 4000 K and G magnitude brighter than 13. The ESO archive* is the main source of reduced spectral public data for SWEET-Cat. We searched the required data in the ESO archive using the "astroquery.eso" module and we downloaded data by HARPS, ESPRESSO, UVES and FEROS spectrographs. In most cases we downloaded more than one spectrum per star to achieve a higher S/N by combining them. We discarded spectra with S/N below 20, due to their bad quality. The total number of files downloaded varies per star, until it reaches a maximum S/N of 2000 for the combined spectrum. We obtained the final combined spectrum for each star for a given instrument by shifting all spectra to the same wavelength reference before the flux combination, using a cross-correlation function with the highest S/N individual spectrum taken as the mask. We used a sigma clipping to remove unusual peaks. We saved the final spectra in 1D fits-file format, which contain the S/N information both of the combined spectra themselves, as well as the S/N of the individual spectra that were combined. In addition, we combined in a similar way as above, individual spectra for more planet-host M dwarfs in SWEET-Cat, observed by HARPS-N spectrograph (and archived in the IA2†, Italian Center for Astronomical Archive) and by SOPHIE‡ spectrograph. We constructed these final spectra in the same way as for the ones obtained from ESO. Furthermore, we searched and

*http://archive.eso.org/wdb/wdb/adp/phase3_main/form
†http://archives.ia2.inaf.it/tng/
‡http://atlas.obs-hp.fr/sophie/

obtained spectra in the public archive of CARMENES* spectrograph so to increase our sample of planet-host M dwarfs with available spectra. For stars with spectra obtained by multiple instruments, we measured the combined spectra from the instruments of the higher resolution available, as well as their spectra from other instruments, presenting multiple results in several cases, in order to evaluate the overall consistency among determinations using spectra from different sources. For the next steps of our work, we selected those parameter values with the lowest estimated errors, instead of the average values, because the average can still be significantly affected by the presence of lower-quality spectra.

The stars and their parameters, determined both with the new and the old reference datasets, are reported in Table 3.14. The total budgets of parameter uncertainties are reported for each star individually. These are derived automatically by adding quadratically the dispersion of the resulting stellar parameters and the maximum uncertainties of the machine learning models at the respective resolution of each spectrum, after having taken into consideration the intrinsic uncertainties of the reference dataset parameters during the machine learning process. In Fig. 3.17 we show the differences of the derived parameters for spectra of the same stars observed with different instruments. The differences are calculated compared to the average value from the multiple spectra. The values are quite consistent when ODUSSEAS is applied to different instruments. The standard deviation of the parameters, relative to the average values, is 30 K for T_{eff} and 0.03 dex for [Fe/H]. There are very few large individual differences, but they are within the uncertainties reported.

The distribution of S/N values for the spectra with the selected parameters and their correlation with the G magnitudes of the stars are presented in Fig. 3.18.

The comparisons of selected determinations by the two reference datasets are presented in Fig. 3.19. There is an average difference of 138 K with standard deviation of 68 K between measurements occurring from the new and the old reference dataset, which is what we optimally expect, based on the differences reported in the comparative study of different methods (Passegger et al., 2022). Thus, the new interferometry-based T_{eff} scale compensates the underestimation of the order of 140 K that was noticed and explained in Sect. 3.5.2. It seems to provide indeed more accurate values compared to the ones as predicted by the initial reference scale.

*http://carmenes.cab.inta-csic.es/gto/jsp/reinersetal2017.jsp

Regarding the [Fe/H] results, a small trend in differences is noticed for the metal-poor stars, which have slightly lower values with the new reference dataset. On the other hand, stars with [Fe/H] results close to solar values and above, appear to have higher or lower values with the new reference dataset. These differences may occur due to the different samples of reference stars between the two datasets. Another reason may be the updated parallax values that are used to derive the reference [Fe/H] in the new scale, which originate from Gaia eDR3, compared to the parallax values from Hipparchos that were used in the calculation of [Fe/H] by Neves et al. (2012) in the initial reference dataset. Among the common stars in the two reference datasets, the new reference [Fe/H] scale has an average difference of -0.01 dex compared to the old one. The average difference in our results is 0.00 dex with standard deviation of 0.05 dex. Having color-coded the datapoints of each panel with the values of the other parameter, looking at the upper panel of T_{eff} differences, we notice that metal-poor stars tend to have comparatively smaller differences between the two reference scales (from 50 K to 150 K difference), rather than the stars with [Fe/H] close to solar values and above, for which the differences are mainly from 150 K up to 300 K. We also notice that these metal-poor stars of the sample, all have T_{eff} values below 3700 K. The distribution of resulting parameters with the new reference dataset among the 82 M dwarfs is presented in Fig. 3.20. In any case, the user can set which reference dataset prefers to be applied.

Table 3.14: Determination of parameters and total error budgets for 82 stars in SWEET-Cat applying the new and old reference datasets.

Star	Spec.	T_{eff} (New) [K]	[Fe/H] (New) [dex]	T_{eff} (Old) [K]	[Fe/H] (Old) [dex]
CD Cet	CARMENES	3091±115	-0.11±0.13	3113±98	-0.23±0.14
G264-012	CARMENES	3339±104	-0.06±0.13	3237±87	-0.12±0.13
Gl15A	HARPS-N	3602±91	-0.45±0.11	3546±65	-0.39±0.10
Gl15A	CARMENES	3656±107	-0.33±0.13	3604±83	-0.29±0.12
Gl15A	SOPHIE	3602±100	-0.33±0.13	3484±78	-0.30±0.13
Gl27.1	HARPS	3715±90	-0.14±0.11	3566±66	-0.09±0.10
Gl27.1	UVES	3713±94	-0.11±0.11	3597±69	-0.08±0.10

continued

Star	Spec.	T_{eff} (New) [K]	[Fe/H] (New) [dex]	T_{eff} (Old) [K]	[Fe/H] (Old) [dex]
Gl27.1	FEROS	3703±107	-0.07±0.13	3622±87	-0.06±0.13
Gl49	HARPS-N	3726±91	0.00±0.11	3485±65	0.04±0.10
Gl49	CARMENES	3670±100	0.03±0.12	3522±79	0.02±0.12
Gl49	SOPHIE	3788±102	0.02±0.13	3438±80	0.12±0.13
Gl96	CARMENES	3821±100	-0.05±0.12	3680±80	-0.04±0.13
Gl96	SOPHIE	3830±100	0.00±0.13	3656±80	-0.01±0.13
Gl163	HARPS	3431±93	0.01±0.11	3217±65	0.01±0.10
Gl163	FEROS	3507±108	0.03±0.13	3275±85	0.02±0.13
Gl176	HARPS	3623±90	-0.02±0.11	3390±65	0.01±0.10
Gl176	CARMENES	3426±109	-0.04±0.13	3389±90	-0.13±0.13
Gl176	SOPHIE	3628±102	-0.03±0.13	3382±80	0.05±0.13
Gl179	CARMENES	3420±103	0.13±0.12	3263±81	0.02±0.13
Gl179	SOPHIE	3405±108	0.10±0.14	3140±81	0.08±0.13
Gl179	FEROS	3386±116	0.06±0.13	3188±90	0.07±0.13
Gl180	HARPS	3544±90	-0.31±0.11	3423±65	-0.26±0.10
Gl180	UVES	3580±95	-0.28±0.11	3485±71	-0.28±0.10
Gl180	CARMENES	3567±101	-0.31±0.12	3501±80	-0.27±0.12
Gl180	FEROS	3585±105	-0.24±0.13	3474±85	-0.21±0.13
Gl229	HARPS	3782±90	-0.06±0.11	3577±65	-0.01±0.10
Gl229	ESPRESSO	3751±92	-0.05±0.11	3555±66	-0.02±0.10
Gl229	UVES	3801±97	-0.02±0.11	3622±71	-0.04±0.10
Gl229	CARMENES	3738±101	-0.07±0.13	3605±79	-0.05±0.12
Gl251	SOPHIE	3397±100	-0.05±0.13	3221±79	-0.07±0.13
Gl273	HARPS	3282±92	-0.12±0.11	3103±65	-0.09±0.10
Gl273	HARPS-N	3297±93	-0.15±0.11	3120±66	-0.13±0.10
Gl273	CARMENES	3237±107	-0.19±0.13	3188±83	-0.14±0.12
Gl273	SOPHIE	3244±103	-0.03±0.13	3153±80	-0.08±0.13
Gl273	FEROS	3344±137	-0.20±0.14	3219±96	-0.17±0.14

continued

Star	Spec.	T_{eff} (New) [K]	[Fe/H] (New) [dex]	T_{eff} (Old) [K]	[Fe/H] (Old) [dex]
Gl317	HARPS	3354±94	0.12±0.11	3143±66	0.14±0.10
Gl317	FEROS	3497±122	0.12±0.14	3232±92	0.12±0.14
Gl328	UVES	3925±98	0.06±0.11	3854±73	-0.01±0.11
Gl328	SOPHIE	3929±106	0.10±0.14	3829±84	-0.01±0.14
Gl328	FEROS	3924±112	0.15±0.14	3876±87	-0.01±0.14
Gl357	HARPS	3458±90	-0.35±0.11	3342±65	-0.30±0.10
Gl357	HARPS-N	3473±94	-0.37±0.11	3388±67	-0.34±0.10
Gl357	UVES	3474±94	-0.29±0.11	3400±70	-0.27±0.10
Gl357	FEROS	3532±129	-0.26±0.14	3426±100	-0.24±0.14
Gl367	FEROS	3651±108	-0.03±0.13	3424±86	-0.03±0.13
Gl378	SOPHIE	3758±101	0.02±0.13	3613±80	-0.01±0.13
Gl393	HARPS	3549±92	-0.20±0.11	3411±65	-0.17±0.10
Gl393	ESPRESSO	3530±92	-0.22±0.11	3425±65	-0.19±0.10
Gl393	CARMENES	3561±102	-0.18±0.12	3501±80	-0.19±0.12
Gl393	SOPHIE	3500±101	-0.13±0.13	3419±80	-0.15±0.13
Gl393	FEROS	3628±106	-0.15±0.13	3462±87	-0.16±0.13
Gl422	HARPS	3459±95	-0.17±0.11	3259±66	-0.16±0.10
Gl422	UVES	3458±102	-0.18±0.11	3308±73	-0.20±0.11
Gl422	FEROS	3527±118	-0.15±0.13	3317±88	-0.15±0.14
Gl433	HARPS	3630±90	-0.18±0.11	3468±65	-0.14±0.10
Gl433	UVES	3637±94	-0.19±0.11	3521±67	-0.19±0.10
Gl436	HARPS	3478±91	-0.08±0.11	3289±65	-0.04±0.10
Gl436	HARPS-N	3458±96	-0.13±0.11	3326±67	-0.12±0.10
Gl436	CARMENES	3476±103	-0.03±0.12	3418±84	-0.09±0.12
Gl436	SOPHIE	3422±100	-0.01±0.13	3318±80	-0.04±0.13
Gl436	FEROS	3531±107	-0.01±0.13	3347±84	-0.04±0.13
Gl463	HARPS-N	3532±95	0.05±0.11	3324±66	0.05±0.10
Gl463	CARMENES	3582±109	0.02±0.13	3505±91	-0.05±0.13

continued

Star	Spec.	T_{eff} (New) [K]	[Fe/H] (New) [dex]	T_{eff} (Old) [K]	[Fe/H] (Old) [dex]
Gl463	SOPHIE	3577±132	0.04±0.14	3339±96	0.06±0.14
Gl486	HARPS	3246±93	-0.06±0.11	3105±68	-0.06±0.10
Gl486	ESPRESSO	3231±112	0.06±0.13	3151±77	0.01±0.13
Gl486	UVES	3340±97	-0.06±0.11	3183±71	-0.06±0.11
Gl486	FEROS	3395±107	-0.01±0.13	3173±85	-0.06±0.13
Gl536	HARPS	3694±90	-0.16±0.11	3559±65	-0.13±0.10
Gl536	HARPS-N	3707±90	-0.16±0.11	3583±65	-0.16±0.10
Gl536	CARMENES	3698±104	-0.14±0.12	3634±80	-0.17±0.12
Gl536	FEROS	3706±124	-0.10±0.14	3581±89	-0.11±0.14
Gl581	HARPS	3367±91	-0.25±0.11	3224±65	-0.21±0.10
Gl581	CARMENES	3426±100	-0.20±0.12	3359±85	-0.19±0.12
Gl581	FEROS	3468±115	-0.17±0.13	3305±90	-0.21±0.14
Gl625	HARPS-N	3509±92	-0.51±0.11	3459±66	-0.47±0.10
Gl625	CARMENES	3530±106	-0.45±0.12	3487±80	-0.42±0.12
Gl625	SOPHIE	3548±102	-0.41±0.13	3419±84	-0.36±0.13
Gl649	HARPS	3720±90	-0.09±0.11	3546±65	-0.04±0.10
Gl649	CARMENES	3671±102	-0.06±0.12	3577±69	-0.06±0.12
Gl649	SOPHIE	3708±100	-0.05±0.13	3512±80	-0.04±0.13
Gl674	HARPS	3425±91	-0.26±0.11	3304±65	-0.22±0.10
Gl674	ESPRESSO	3417±92	-0.29±0.11	3292±66	-0.24±0.10
Gl674	FEROS	3484±108	-0.16±0.13	3344±84	-0.17±0.13
Gl676A	HARPS	3978±92	0.08±0.11	3732±67	0.08±0.11
Gl676A	FEROS	3982±114	0.12±0.14	3775±88	0.08±0.14
Gl680	HARPS	3572±90	-0.22±0.11	3431±65	-0.17±0.10
Gl680	FEROS	3603±109	-0.24±0.13	3473±87	-0.13±0.14
Gl682	UVES	3202±101	-0.02±0.11	3108±73	-0.06±0.10
Gl682	ESPRESSO	3232±106	0.08±0.12	3102±74	0.05±0.11
Gl682	FEROS	3324±112	0.01±0.14	3100±92	0.01±0.14

continued

Star	Spec.	T_{eff} (New) [K]	[Fe/H] (New) [dex]	T_{eff} (Old) [K]	[Fe/H] (Old) [dex]
Gl685	HARPS-N	3787±91	-0.08±0.11	3635±65	-0.04±0.10
Gl685	CARMENES	3721±103	-0.05±0.12	3642±80	-0.04±0.12
Gl685	SOPHIE	3754±101	-0.05±0.13	3614±81	-0.01±0.13
Gl686	HARPS	3632±91	-0.35±0.11	3566±65	-0.31±0.10
Gl686	CARMENES	3633±103	-0.26±0.13	3563±82	-0.29±0.13
Gl686	SOPHIE	3657±101	-0.28±0.13	3577±79	-0.27±0.13
Gl686	FEROS	3652±108	-0.22±0.13	3612±88	-0.24±0.14
Gl687	HARPS-N	3453±94	-0.03±0.11	3273±66	-0.03±0.10
Gl687	SOPHIE	3453±104	0.03±0.13	3288±82	0.00±0.13
Gl699	HARPS	3226±91	-0.62±0.11	3113±68	-0.58±0.10
Gl699	HARPS-N	3258±93	-0.62±0.11	3160±68	-0.59±0.10
Gl699	UVES	3300±97	-0.57±0.11	3191±75	-0.56±0.11
Gl699	CARMENES	3228±114	-0.53±0.13	3161±87	-0.58±0.13
Gl699	SOPHIE	3199±103	-0.52±0.13	3161±82	-0.53±0.13
Gl720A	HARPS-N	3832±92	-0.07±0.11	3759±66	-0.12±0.10
Gl720A	CARMENES	3778±106	-0.06±0.13	3773±81	-0.12±0.13
Gl720A	SOPHIE	3774±103	0.05±0.13	3716±81	-0.04±0.13
Gl740	HARPS	3832±91	-0.04±0.11	3663±66	-0.02±0.10
Gl740	HARPS-N	3837±91	-0.06±0.11	3691±66	-0.04±0.10
Gl740	CARMENES	3779±103	-0.01±0.13	3721±82	-0.05±0.13
Gl740	SOPHIE	3824±102	-0.02±0.13	3717±84	-0.05±0.13
Gl740	FEROS	3808±102	0.02±0.13	3673±82	-0.01±0.13
Gl752A	HARPS	3554±91	0.02±0.11	3337±65	0.05±0.10
Gl752A	CARMENES	3540±100	0.01±0.12	3384±78	0.02±0.12
Gl752A	SOPHIE	3580±99	0.09±0.13	3349±80	0.05±0.13
Gl832	HARPS	3587±90	-0.18±0.11	3459±65	-0.14±0.10
Gl832	FEROS	3563±103	-0.11±0.13	3466±82	-0.11±0.13
Gl849	HARPS	3486±95	0.16±0.11	3208±66	0.20±0.10

continued

Star	Spec.	T_{eff} (New) [K]	[Fe/H] (New) [dex]	T_{eff} (Old) [K]	[Fe/H] (Old) [dex]
Gl849	CARMENES	3471±106	0.20±0.12	3333±89	0.12±0.12
Gl876	FEROS	3265±108	0.07±0.13	3102±84	0.08±0.13
Gl887	HARPS	3679±90	-0.23±0.11	3578±65	-0.19±0.10
Gl887	FEROS	3701±112	-0.17±0.14	3584±84	-0.14±0.13
Gl1214	UVES	3109±129	-0.12±0.12	3005±80	-0.06±0.12
Gl1214	FEROS	3115±129	-0.04±0.14	3022±95	-0.09±0.14
Gl3082	HARPS	3645±90	-0.23±0.11	3508±65	-0.18±0.10
Gl3082	UVES	3674±95	-0.19±0.11	3570±69	-0.17±0.10
Gl3082	FEROS	3681±108	-0.14±0.13	3550±83	-0.12±0.13
Gl3090	HARPS	3701±91	-0.02±0.11	3509±67	0.01±0.10
Gl3090	FEROS	3737±104	0.04±0.13	3536±83	0.02±0.13
Gl3138	HARPS	3884±92	0.02±0.11	3797±69	-0.05±0.11
Gl3323	FEROS	3195±114	-0.34±0.14	3092±89	-0.33±0.14
Gl3341	HARPS	3455±100	0.08±0.12	3433±74	-0.02±0.12
Gl3470	UVES	3620±106	0.03±0.11	3385±76	0.09±0.11
Gl3634	HARPS	3535±92	-0.08±0.11	3347±65	-0.02±0.10
Gl3942	HARPS-N	3823±90	-0.04±0.11	3680±66	-0.04±0.10
Gl3998	HARPS	3729±91	-0.13±0.11	3557±65	-0.09±0.10
Gl3998	HARPS-N	3720±91	-0.13±0.11	3557±65	-0.07±0.10
Gl3998	FEROS	3712±102	-0.03±0.13	3546±83	-0.03±0.13
Gl9066	CARMENES	3317±114	-0.20±0.13	3232±102	-0.35±0.14
Gl9689	HARPS	3832±94	0.08±0.11	3674±66	0.05±0.10
Gl9689	HARPS-N	3850±94	0.01±0.11	3692±66	0.00±0.10
HD238090	CARMENES	3812±107	-0.03±0.13	3800±83	-0.11±0.13
HD260655	ESPRESSO	3639±103	-0.21±0.12	3632±69	-0.22±0.11
HD260655	CARMENES	3671±116	-0.21±0.14	3750±82	-0.28±0.13
HIP4845	HARPS	3915±98	0.10±0.12	3900±76	-0.06±0.13
HIP36985	HARPS	3809±95	-0.01±0.11	3634±72	-0.01±0.11

continued

Star	Spec.	T_{eff} (New) [K]	[Fe/H] (New) [dex]	T_{eff} (Old) [K]	[Fe/H] (Old) [dex]
HIP36985	CARMENES	3800±105	0.03±0.13	3667±87	-0.05±0.13
HIP36985	FEROS	3834±110	0.05±0.14	3643±93	0.01±0.14
HIP38594	HARPS	3903±97	0.03±0.11	3874±72	-0.10±0.12
HIP57050	CARMENES	3305±102	0.06±0.12	3161±80	0.02±0.12
HIP57050	SOPHIE	3348±104	0.03±0.13	3134±82	0.01±0.13
HIP79431	FEROS	3488±124	0.10±0.13	3281±89	0.20±0.13
K2-3	HARPS	3788±96	-0.11±0.12	3815±69	-0.19±0.11
K2-3	HARPS-N	3752±96	-0.09±0.12	3773±70	-0.16±0.11
K2-3	FEROS	3748±117	-0.04±0.14	3836±94	-0.16±0.14
K2-18	CARMENES	3587±113	-0.09±0.13	3534±112	-0.19±0.15
K2-122	HARPS-N	3906±94	0.05±0.11	3668±66	0.03±0.10
L98-59	HARPS	3420±92	-0.34±0.11	3297±66	-0.31±0.10
L168-9	HARPS	3872±91	0.05±0.11	3634±65	0.06±0.10
L168-9	FEROS	3842±103	0.11±0.13	3645±84	0.10±0.13
Lalande21185	UVES	3529±115	-0.26±0.12	3467±76	-0.23±0.11
Lalande21185	CARMENES	3518±121	-0.32±0.12	3557±81	-0.35±0.12
LHS1678	HARPS	3549±94	-0.45±0.11	3456±65	-0.42±0.10
LHS1815	HARPS	3678±92	0.05±0.11	3458±66	0.05±0.10
LP714-47	ESPRESSO	3860±92	0.06±0.11	3606±66	0.08±0.10
LSPMJ2116+0234	FEROS	3590±108	-0.03±0.13	3302±86	-0.01±0.13
LTT1445A	HARPS	3374±92	-0.36±0.11	3240±68	-0.35±0.10
LTT1445A	ESPRESSO	3330±92	-0.42±0.11	3242±68	-0.39±0.10
Proxima Centauri	HARPS	2756±112	-0.18±0.11	2702±69	-0.12±0.10
Proxima Centauri	UVES	2804±113	-0.21±0.11	2833±78	-0.23±0.11
Ross128	HARPS	3114±93	-0.30±0.11	2983±66	-0.26±0.10
Ross128	FEROS	3166±111	-0.30±0.13	3085±90	-0.28±0.14
TOI-270	HARPS	3539±92	-0.31±0.11	3422±66	-0.29±0.10
TOI-270	ESPRESSO	3465±93	-0.38±0.11	3407±66	-0.33±0.10

continued

Star	Spec.	T_{eff} (New) [K]	[Fe/H] (New) [dex]	T_{eff} (Old) [K]	[Fe/H] (Old) [dex]
TOI-776	HARPS	3765±90	-0.11±0.11	3634±66	-0.10±0.10
TOI-776	ESPRESSO	3730±91	-0.13±0.11	3621±66	-0.12±0.10
TOI-1235	HARPS-N	3925±94	0.03±0.11	3824±68	-0.04±0.11
TOI-1266	HARPS-N	3614±92	-0.32±0.11	3521±66	-0.28±0.10
TOI-1801	HARPS-N	3797±91	-0.07±0.11	3698±69	-0.09±0.11
TYC-2187-512-1	CARMENES	3682±102	-0.16±0.13	3620±80	-0.14±0.13
TYC-2187-512-1	FEROS	3678±105	-0.16±0.13	3615±84	-0.14±0.13
Wolf1061	HARPS	3307±92	-0.12±0.11	3103±66	-0.08±0.10
Wolf1061	CARMENES	3315±100	-0.03±0.12	3211±81	-0.07±0.12
Wolf1061	FEROS	3357±132	-0.10±0.14	3207±99	-0.10±0.14

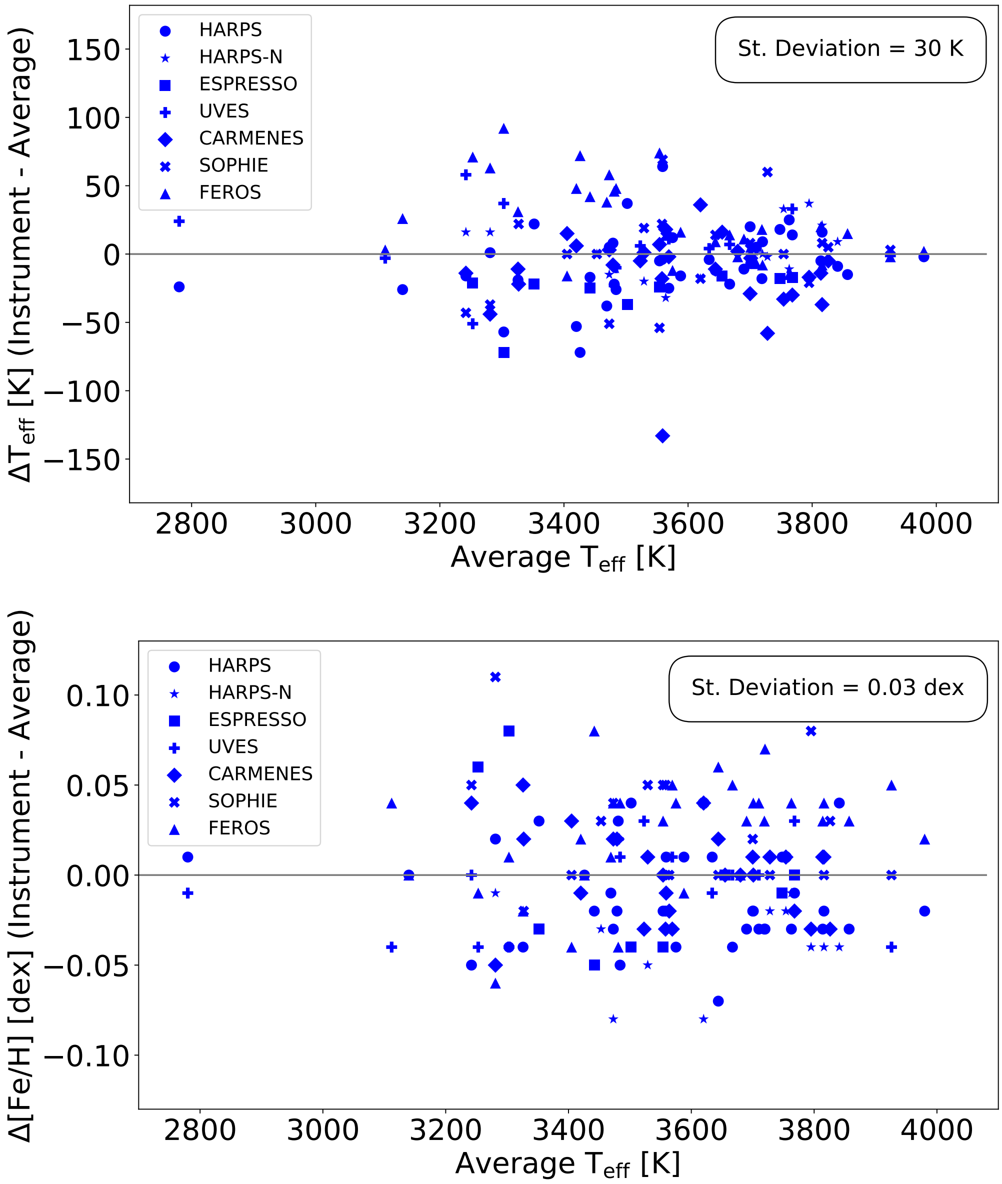

Figure 3.17: Comparison of determinations for stars with spectra from different instruments. The differences are relative to the average values of T_{eff} (upper panel) and [Fe/H] (lower panel).

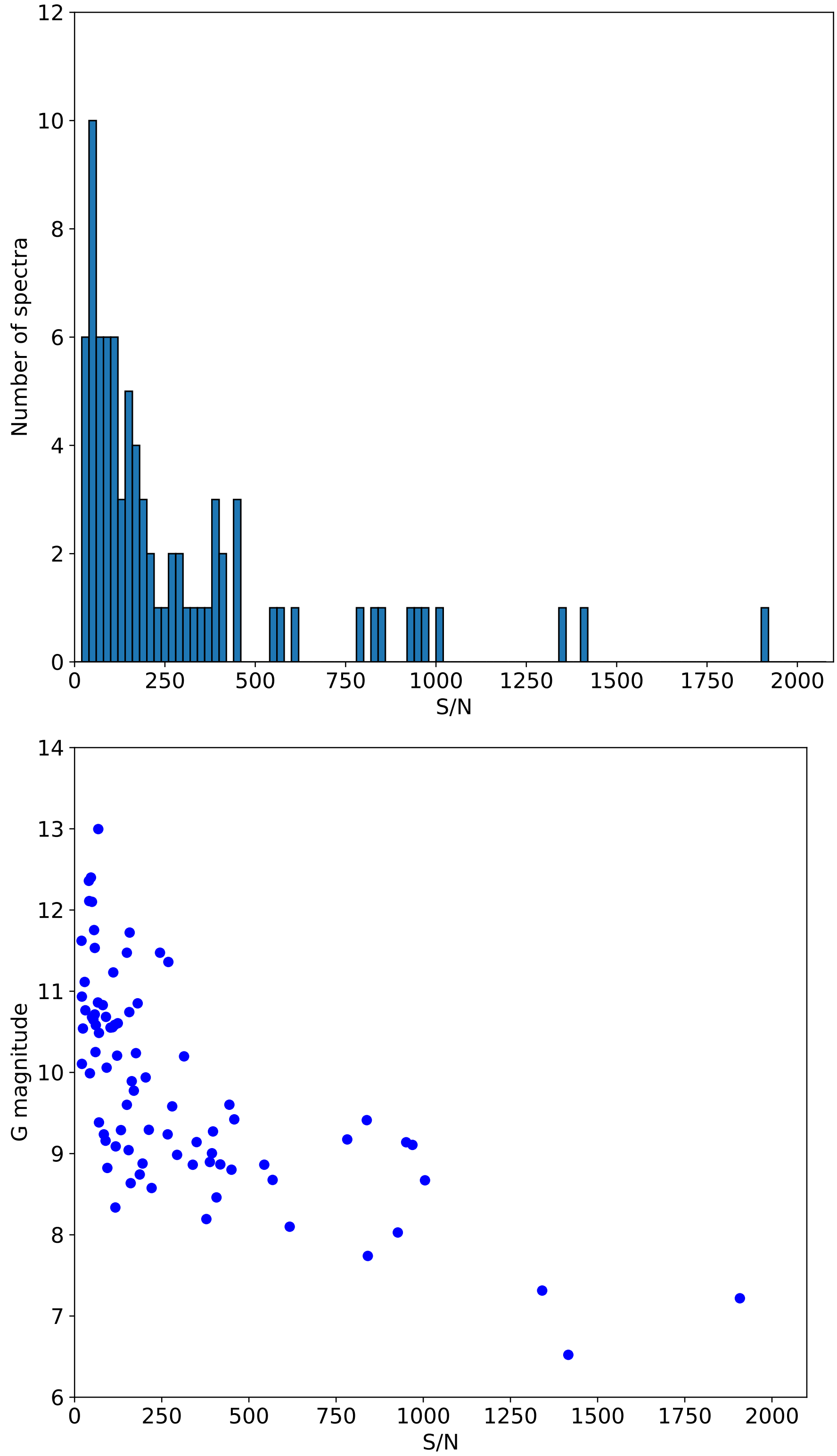

Figure 3.18: Distribution of S/N values (upper panel) and their relation to the G magnitude (lower panel) for spectra of the 82 stars in SWEET-Cat.

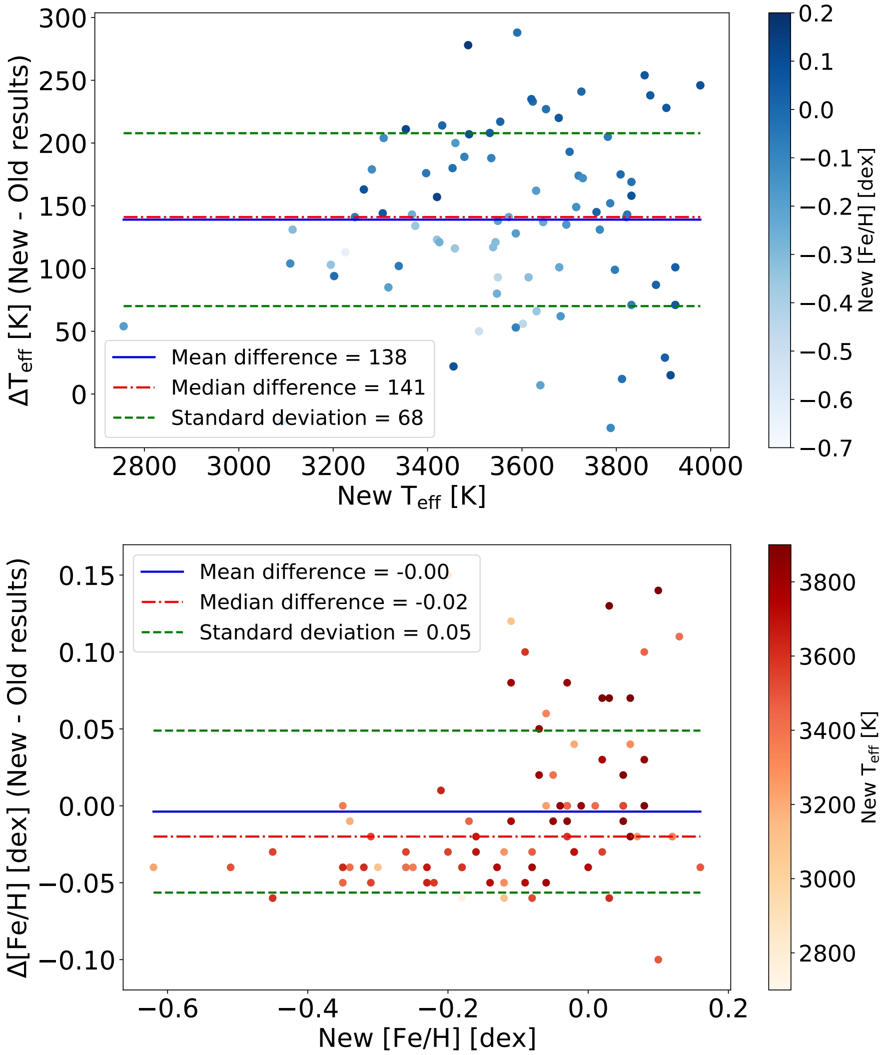

Figure 3.19: T_{eff} comparison (upper panel) and [Fe/H] comparison (lower panel) for 82 stars in SWEET-Cat by applying the new and the old reference datasets.

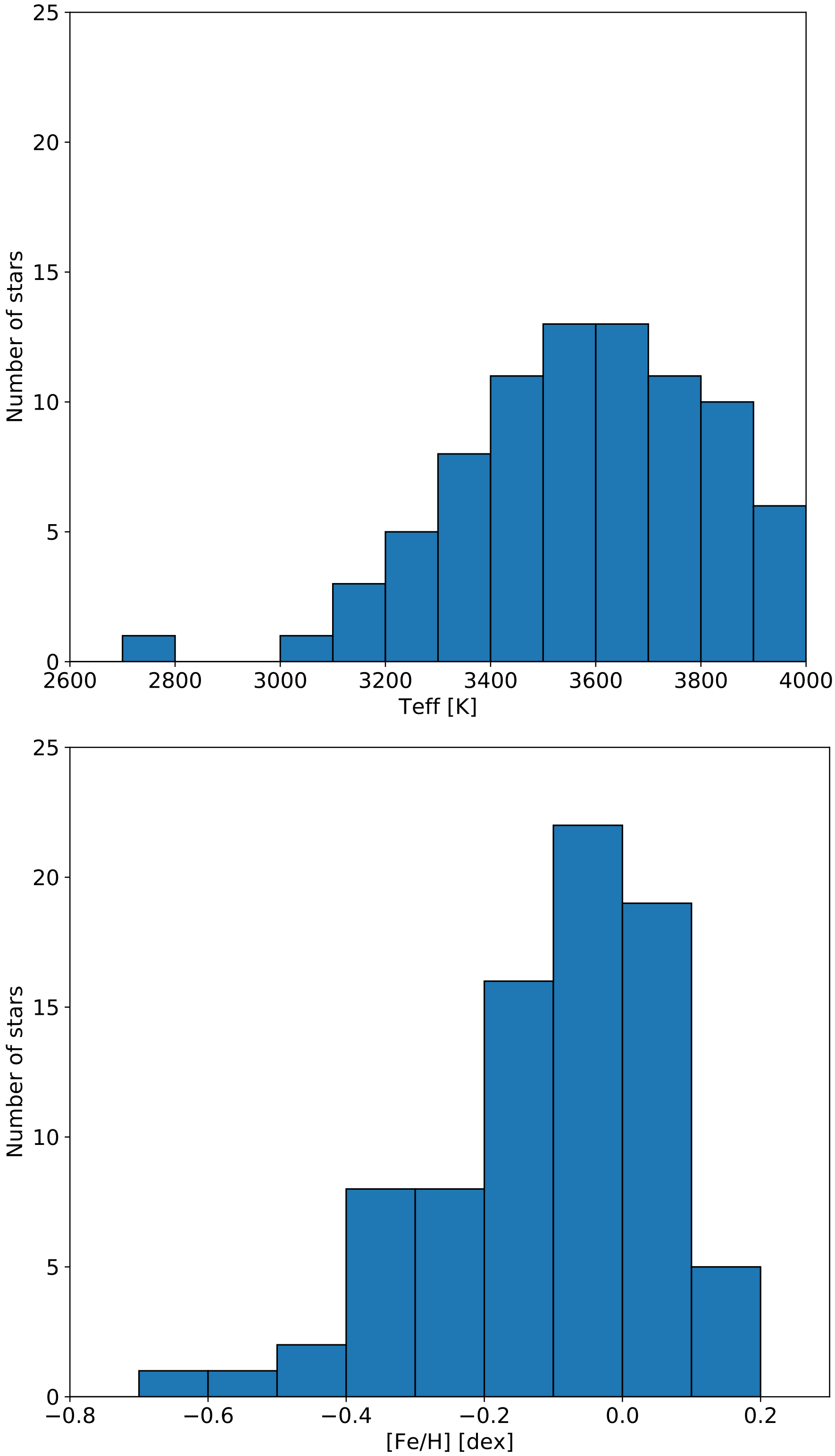

Figure 3.20: Distribution of T_{eff} (upper panel) and [Fe/H] (lower panel) determinations for 82 stars in SWEET-Cat by applying the new reference dataset.

3.8. Comparison of results with literature studies

Having our determinations for the 82 M dwarfs, we proceeded in a comparison of our results (derived with the new reference dataset) with studies in the literature, with which we shared a sufficient amount of common stars (at least 15% of our sample), so that the overall differences could have statistical significance. Thus, we selected four publications, with at least 13 stars in common each of them, in order to compare the determinations of T_{eff} and [Fe/H]. Maldonado et al. (2015) and Rojas-Ayala et al. (2012) have derived the stellar parameters applying the concept of pseudo EWs, while Passegger et al. (2018) and Mann et al. (2015) have used spectral synthesis with PHOENIX models.

Maldonado et al. (2015) used 112 ratios of pseudo EWs of spectral features as a temperature diagnostic. The sample of 21 M dwarfs from Boyajian et al. (2012), with T_{eff} obtained from interferometric estimates of their radii, were used as calibrators. Combinations of features and ratios of features were used to derive calibrations for the determination of [Fe/H]. They assembled a list of 47 metallicity calibrators with available HARPS spectra, known parallaxes and magnitudes by using the photometric calibration provided by Neves et al. (2012). The differences of parameters for 17 stars in common, are presented in Fig. 3.21. Regarding T_{eff}, the mean and median differences are -22 K and 0 K respectively, with a standard deviation of 58 K. There seems to be a trend, as for cooler stars our determinations give lower T_{eff} values. [Fe/H] mean and median differences are small too, reasonably since both methods have used the relation by Neves et al. (2012) in their respective calibration processes for the determination of [Fe/H]. They are equal to -0.04 and -0.05 respectively, with a standard deviation of 0.05 dex.

Rojas-Ayala et al. (2012) measured EWs of the Ca and Na lines, and a spectral index quantifying the absorption due to H_2O opacity (the H_2O–K2 index). They set pseudo continuum for each feature, which is estimated from a linear fit to the median flux within 0.003 m wide regions centered on the continuum points. Using empirical spectral type standards and synthetic models, they calibrated the H_2O–K2 index as an indicator of M dwarf spectral type and T_{eff}. They also presented a relationship that estimates the [Fe/H] and [M/H] metallicities of M dwarfs from their NaI, CaI, and H_2O–K2 measurements. The differences of parameters for 13 stars in common, are presented in Fig. 3.22. Regarding T_{eff}, the mean and median differences are -66 K and -40 K respectively, with a standard deviation of 97 K. [Fe/H] mean and median differences are -0.11 and -0.12 dex respectively, similar to the typical uncertainty range of our measurements as reported in Table 3.14.

The standard deviation of the [Fe/H] difference is 0.12 dex.

Passegger et al. (2018) adapted the method described in Passegger et al. (2016), which determined T_{eff}, $\log g$, and [Fe/H] using the grid of PHOENIX model spectra presented by Husser et al. (2013). The PHOENIX-ACES model grid that they used, was especially designed for modeling spectra of cool dwarfs, because it uses a new equation of state to improve the calculations of molecule formation in cool stellar atmospheres. They applied a χ^2 method to derive the stellar parameters by fitting the models to high-resolution spectroscopic data. Our differences with Passegger et al. (2018) for 26 stars in common, are presented in Fig. 3.23. Regarding T_{eff}, the mean and median differences are -50 K and -45 K respectively, with a standard deviation of 48 K. [Fe/H] mean and median differences are -0.09 and -0.12 dex respectively, similar to the typical uncertainty range of our measurements. The standard deviation of the [Fe/H] difference is 0.12 dex.

Mann et al. (2015) calculated T_{eff} by comparing optical spectra with the CFIST suite of the BT-SETTL version of the PHOENIX atmosphere models (Allard et al., 2013). Metallicities were calculated from the NIR spectra using the empirical relations from Mann et al. (2013a) for K7–M4.5 dwarfs and from Mann et al. (2014) for M4.5–M7 dwarfs. These studies provide relations between the EWs of atomic features like Na and Ca in NIR spectra and the metallicity of the star, calibrated using wide binaries with an FGK primary and an M dwarf companion. The differences of parameters for 21 stars in common, are presented in Fig. 3.24. Regarding T_{eff}, the mean and median differences are only -11 and -4 K respectively, with a small standard deviation of 31 K. [Fe/H] mean and median differences are -0.11 and -0.10 dex respectively, similar to the typical uncertainty range of our measurements. The standard deviation of the [Fe/H] difference is 0.07 dex.

In all four cases, our T_{eff} values are slightly lower with average differences much smaller than the error range of our determinations, which is mostly slightly above 90 K. Regarding [Fe/H], the difference with Maldonado et al. (2015) is considerably small since both methods use as calibration scale the relation by Neves et al. (2012), although applied to different set of reference stars and with different values of parallax. Comparing our [Fe/H] results with the other three methods, we notice that our determinations are on average around -0.11 dex lower, as much as the common error range of our determinations after having taken into account the intrinsic reference uncertainties in our final error estimation.

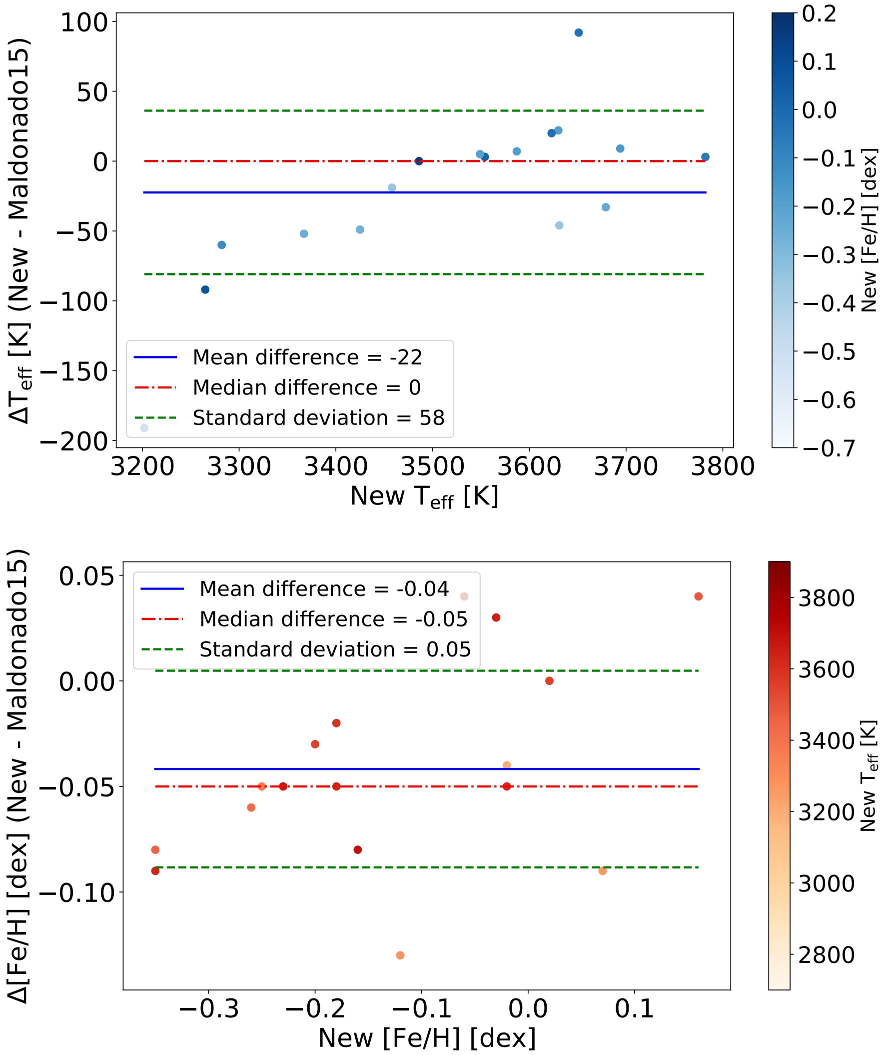

Figure 3.21: T_{eff} comparison (upper panel) and [Fe/H] comparison (lower panel) between our results and Maldonado et al. (2015) for 17 stars in common.

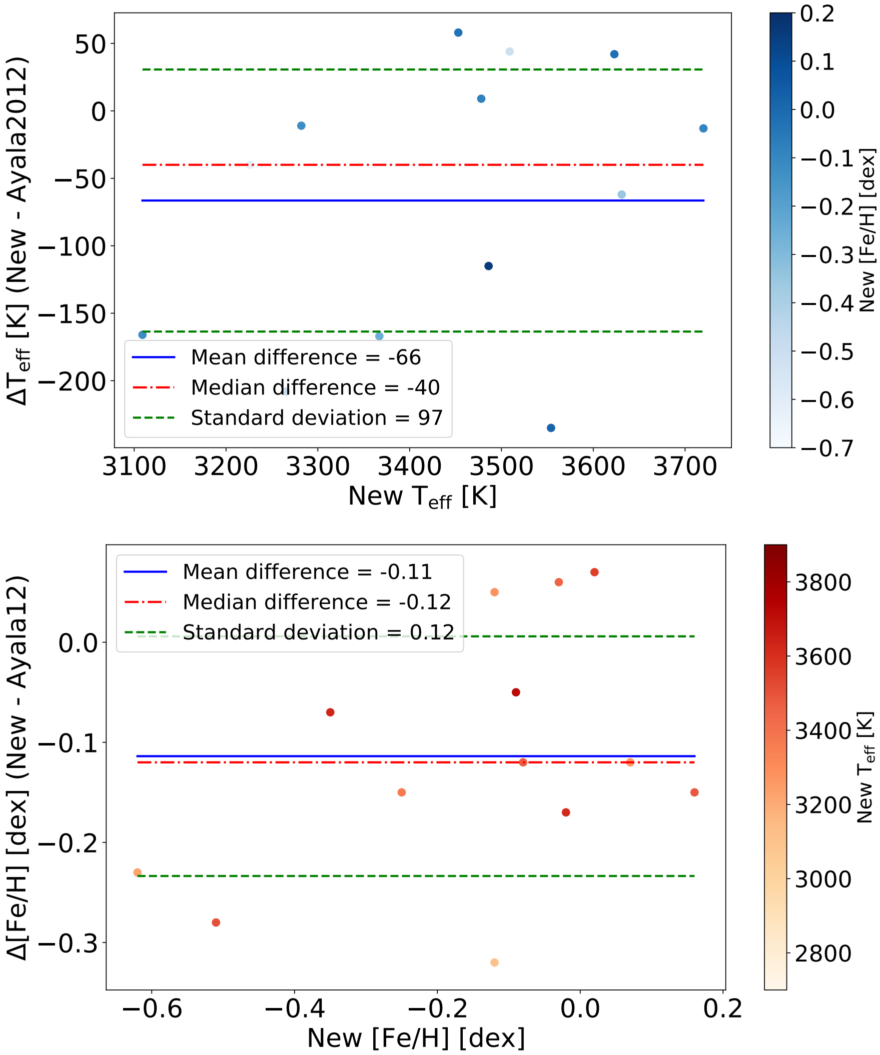

Figure 3.22: $T_{\rm eff}$ comparison (upper panel) and [Fe/H] comparison (lower panel) between our results and Rojas-Ayala et al. (2012) for 13 stars in common.

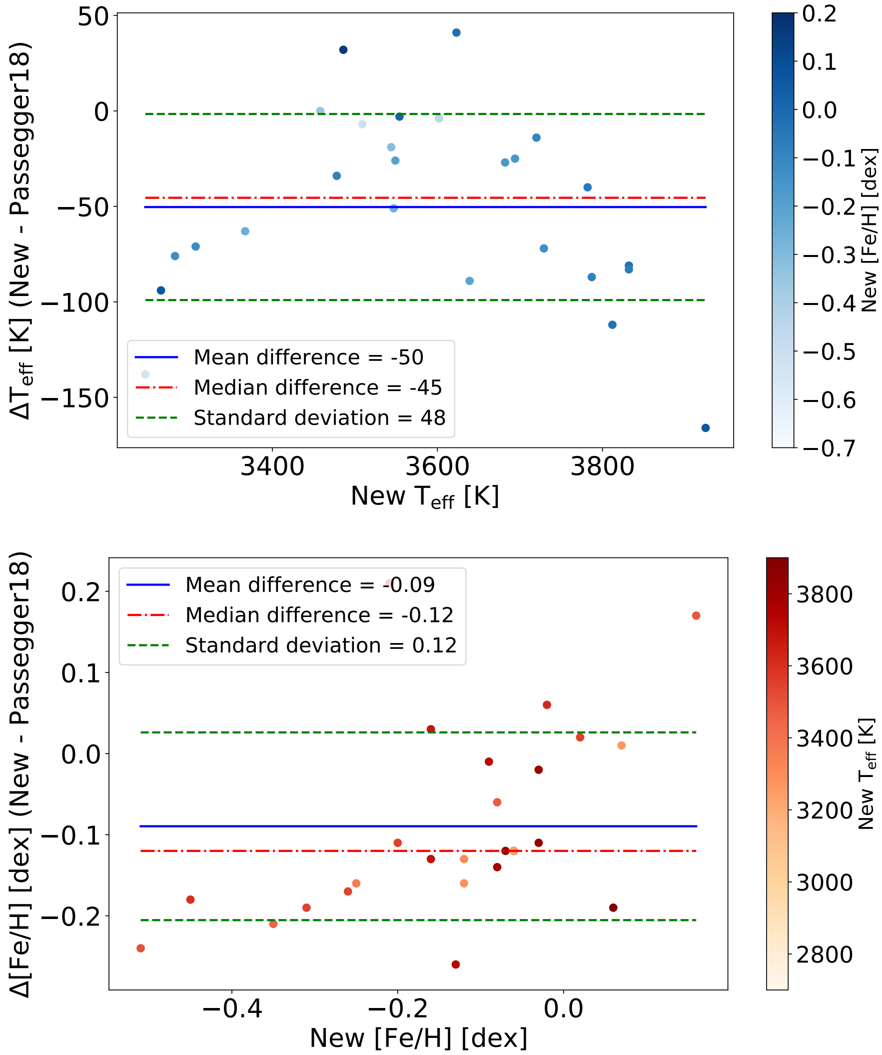

Figure 3.23: T_{eff} comparison (upper panel) and [Fe/H] comparison (lower panel) between our results and Passegger et al. (2018) for 26 stars in common.

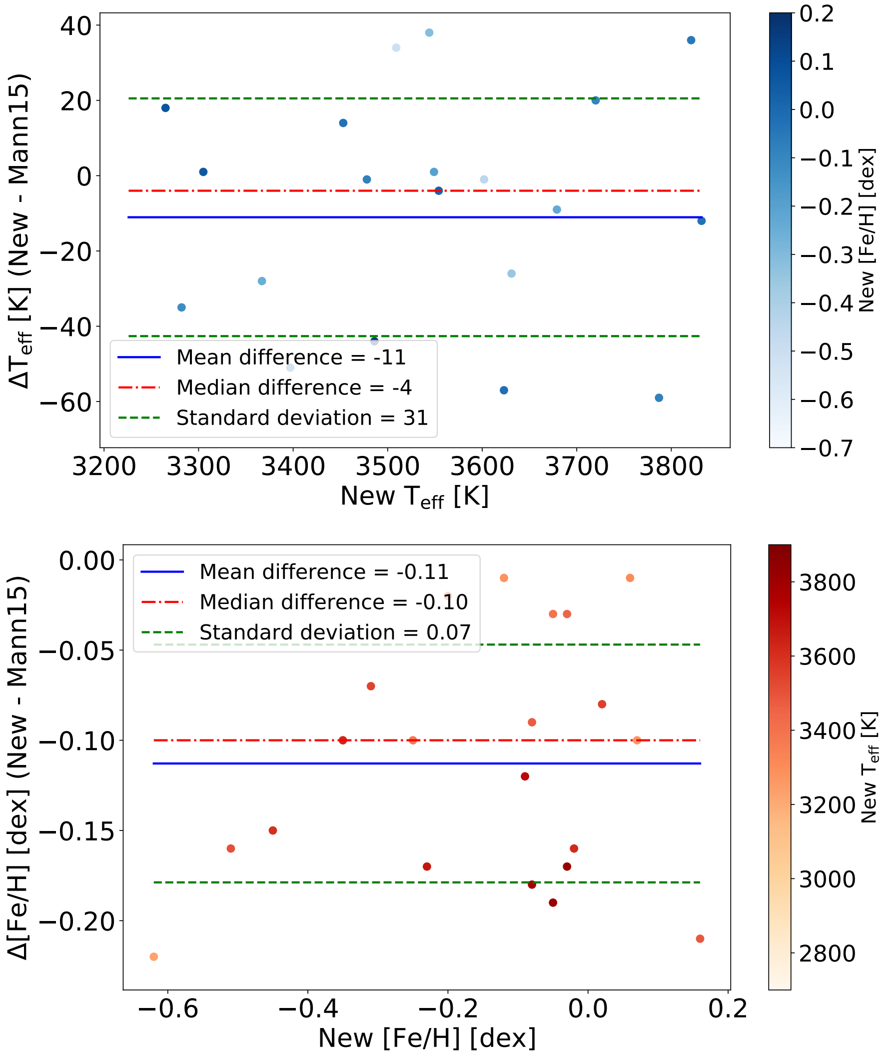

Figure 3.24: T_{eff} comparison (upper panel) and [Fe/H] comparison (lower panel) between our results and Mann et al. (2015) for 21 stars in common.

3.9. Results of ESPRESSO GTO sample

In Table 3.15 we present our results for ESPRESSO GTO sample of M dwarfs which were made available to us and are not part of the public or the reference datasets. We applied the new reference scale as well as the original one and we report the respective differences in the parameters. These differences are presented in Fig. 3.25. For this selection of stars, the average differences of T_{eff} and [Fe/H] are 101 K and -0.01 dex respectively. The distribution of parameters for the ESPRESSO spectra, derived with the new reference dataset, are presented in Fig. 3.26.

Table 3.15: Determination of parameters for ESPRESSO GTO sample of M dwarfs.

Star	T_{eff} (New) [K]	[Fe/H] (New) [dex]	T_{eff} (Old) [K]	[Fe/H] (Old) [dex]	T_{eff} Diff. [K]	[Fe/H] Diff. [dex]
BD-012447	3543±92	-0.23±0.11	3423±66	-0.21±0.10	120	-0.02
BD+101857	3790±99	-0.12±0.11	3857±65	-0.16±0.11	-67	0.04
BD+156290	3263±93	0.05±0.11	3049±66	0.07±0.10	214	-0.02
BD+202465	3338±109	0.02±0.12	3122±99	0.09±0.13	216	-0.07
G68-8	3269±94	0.18±0.11	3026±66	0.17±0.10	243	0.01
G158-50	3315±94	-0.53±0.11	3218±69	-0.52±0.10	97	-0.01
Gl1002	2765±112	-0.50±0.12	2700±73	-0.47±0.11	65	-0.03
Gl1061	2784±114	-0.37±0.12	2714±70	-0.37±0.11	70	0.00
Gl3618	2823±117	-0.82±0.12	2753±74	-0.79±0.12	70	-0.03
HD191849	3794±91	-0.12±0.11	3749±66	-0.15±0.10	45	0.03
K2-129	3372±92	-0.13±0.11	3205±66	-0.14±0.10	167	0.01
TOI-134	3847±91	-0.01±0.11	3625±65	0.01±0.10	222	-0.02
TOI-175	3379±92	-0.38±0.11	3281±66	-0.35±0.10	98	-0.03
TOI-198	3645±95	-0.41±0.13	3693±67	-0.40±0.10	-48	-0.01
TOI-455	3335±91	-0.39±0.11	3229±67	-0.40±0.10	106	0.01
VAX Mic	3859±95	-0.05±0.11	3830±70	-0.13±0.11	29	0.08
VYZ Cet	2961±108	-0.49±0.11	2891±69	-0.46±0.10	70	-0.03

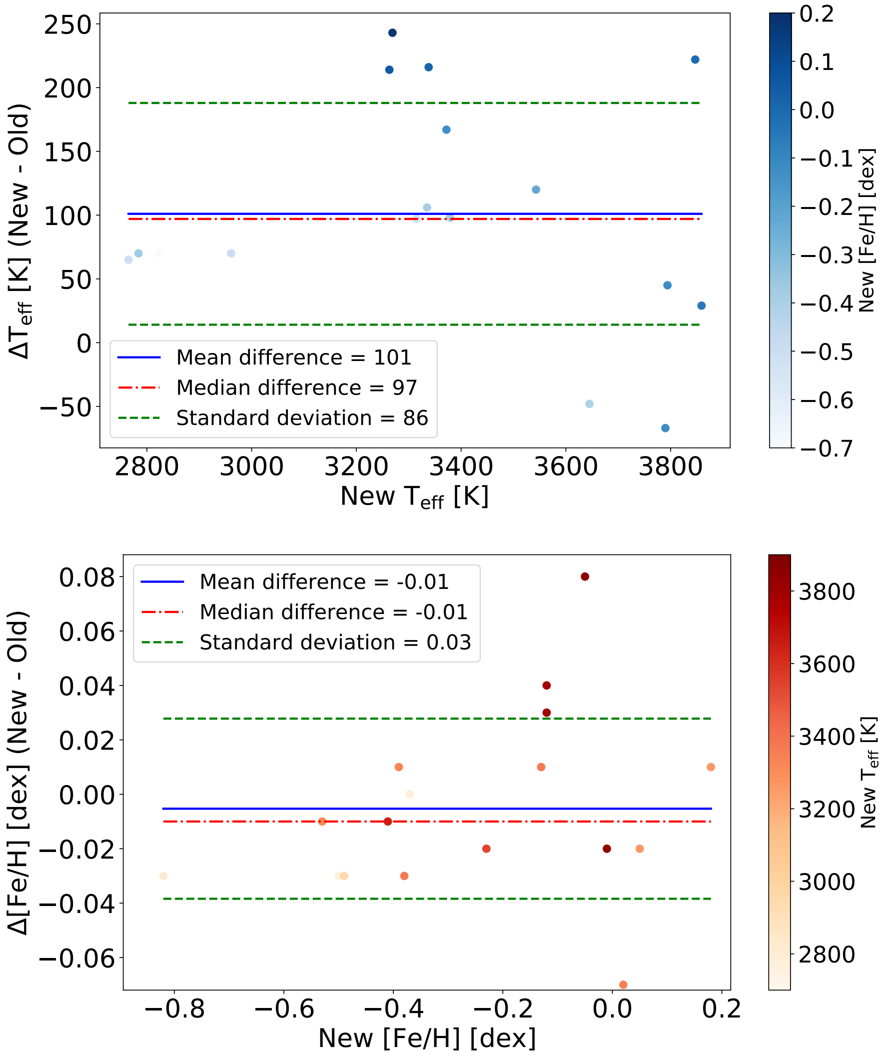

Figure 3.25: T_{eff} comparison (upper panel) and [Fe/H] comparison (lower panel) for ESPRESSO GTO sample of stars by applying the new and the old reference datasets.

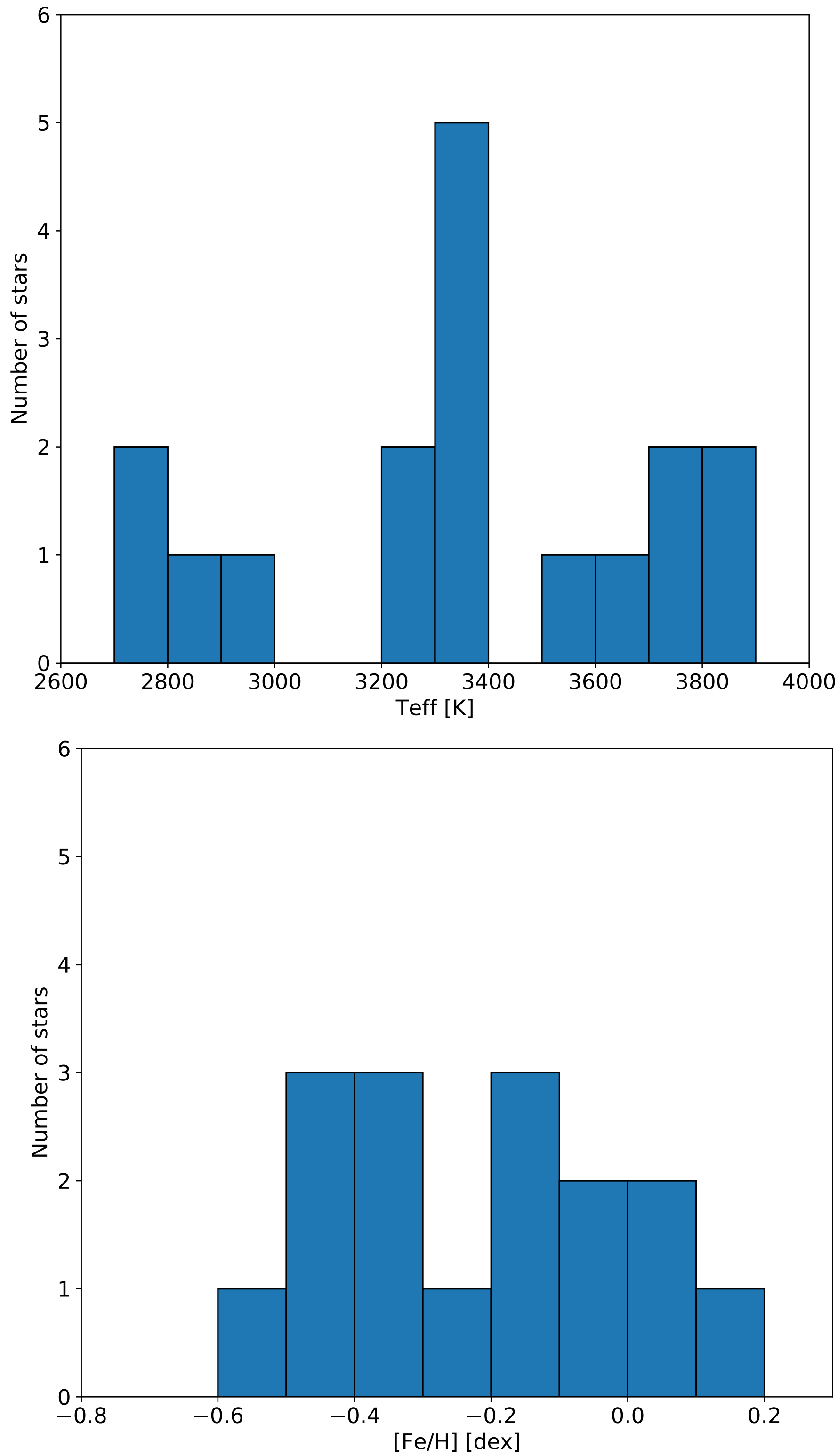

Figure 3.26: Distribution of T_{eff} (upper panel) and [Fe/H] (lower panel) determinations for ESPRESSO GTO sample of stars by applying the new reference dataset.

3.10. Planetary mass - stellar metallicity correlation

Theory of planet formation suggests correlation between the presence of giant planets and the high metallicity of their host stars (Laughlin, 2000, Gonzalez et al., 2001). Santos et al. (2003, 2004) confirmed that the frequency of planets is a rising function of the stellar metallicity, at least for stars with [Fe/H] > 0. Fischer & Valenti (2005) also concluded that above solar metallicity, there is a smooth and rapid rise in the fraction of stars with giant planets. Furthermore, in that study, high stellar metallicity appears to be correlated with the presence of multiple-planet systems and with the total detected planet mass. The first planets found were massive and giants, because of the observational biases from the planet detection methods. Later, the correlation was tested for lower-mass planets, where the correlation was not observed (Udry et al., 2006, Sousa et al., 2008, 2011, Buchhave et al., 2012, Wang & Fischer, 2015). Observational works for M-dwarf samples specifically, have been in agreement with the correlation of giant-planet occurrence with high stellar metallicity (Bonfils et al., 2007, Johnson & Apps, 2009, Schlaufman & Laughlin, 2010, Rojas-Ayala et al., 2012, Terrien et al., 2012, Neves et al., 2013, Maldonado et al., 2020).

We used our planet-host M dwarfs from SWEET-Cat to examine the correlation between planetary mass and stellar metallicity. The masses of exoplanets were obtained from NASA Exoplanet Archive*. 78 stars are included in our analysis, the ones measured for SWEET-Cat except Gl699, HIP36985, TOI-1801 and K2-122, which they were not included in the NASA Exoplanet Archive. The total number of planets orbiting those stars are 125. The low-mass planets (lower than 30 $M_{\oplus}$) are 102, while the high-mass planets (greater than 30 $M_{\oplus}$) are 23. We chose this division because the location of the gap in the distribution of planetary mass is 30 $M_{\oplus}$, as presented in Mayor et al. (2011). Thus, we keep this threshold to be consistent with similar works in M dwarfs too, such as Neves et al. (2013), Maldonado et al. (2020). There are 60 low-mass planet host stars (LMPH) and 18 high-mass planet host stars (HMPH). In Fig. 3.27, the mass distributions for the low-mass planets and the high-mass planets are presented. We notice that most of the low-mass planets have masses below 15 $M_{\oplus}$, while the masses of the high-mass planets are more widely scattered. In Fig. 3.28, the left panels show the relative frequencies of planets (upper left) and planet-host stars (lower left) against the metallicity distribution of stars as derived by the new version of ODUSSEAS, separated by the two planet

*https://exoplanetarchive.ipac.caltech.edu/

populations. As relative frequency, we consider the way the planets and the host stars respectively, are distributed based on the metallicity inside their own population defined by the mass division. For example, in these panels, the low-mass (yellow) values of relative frequencies all sum up to 1 and the high-mass (red) values all sum up to 1 accordingly. The right panels present the absolute numbers of planets (upper right) and stars (lower right). The metallicity of the host star appears multiple times for systems with multiple planets. The planet with the highest mass is considered for multiplanet systems, in order to characterize the star as LMP host or HMP host. We notice a correlation of high-mass planets increasing at high stellar metallicity. In order to compare the distributions, we applied Kolmogorov-Smirnov tests for low-mass planets versus high-mass planets and LMP hosts versus HMP hosts. The closer the K-S statistic number is to 0, the more likely it is that the two samples are drawn from the same distribution, while the closer the value is to 1, the more significant is the difference of the two samples. If the p-value is very close to 0 then the distributions are statistically different, while for higher p-values the distributions are similar. For the low-mass planets (LMP) versus high-mass planets (HMP) comparison we get a K-S statistic = 0.58 and a p-value = $2.07 \cdot 10^{-6}$, while for the low-mass planet hosts (LMPH) versus the high-mass planet hosts (HMPH) comparison we get a K-S statistic = 0.49 and a p-value = $1.33 \cdot 10^{-3}$. These values imply that the difference is statistically significant between the samples of low-mass planets and high-mass planets in relation to metallicity of the host stars.

Furthermore, in order to examine the planetary-mass correlation regarding more stellar characteristics apart from the metallicity, we created similar distributions as before, having divided the host stars in three categories based on their T_{eff}, as indicator of their luminosity and mass. The colder ones with T_{eff} below 3400 K are presented in Fig. 3.29. The intermediate ones with T_{eff} between 3400 and 3700 K are presented in Fig. 3.30. The hotter ones with T_{eff} above 3700 K are presented in Fig. 3.31. In the same way, we applied Kolmogorov–Smirnov tests for each group of distributions. All the results are presented in Table 3.16. The numbers of planets and stars totally, as well as for each group separately, are presented in parenthesis next to each group of objects. Regarding the separate groups based on T_{eff}, we notice a significant difference for the distributions of planets around the cooler stars. In this case, the K-S statistic has the highest value of all, equal to 0.77, and the p-value is low enough, equal to 0.001, one order of magnitude lower than the cases about intermediate and hotter stars. The fact that the distributions of low-mass planets and high-mass planets in the cooler stellar range appear significantly different may be the outcome of the trend that, as noticed in the lower panel of Fig. 3.19, the cooler metal-poor stars are measured with our new reference dataset more consistently (at least they have consistent differences from the values measured with the old reference dataset), compared to hotter metal-rich stars which appear more scattered when comparing their values to those derived by the old reference dataset. Thus, potential systematic uncertainties in the [Fe/H] values attributed to hotter stars may not make possible for similar significant differences to appear in the distributions of their planets according to stellar [Fe/H].

From the comparison of distributions for our overall sample of M dwarfs and planets, we confirm that the known correlation between the presence of giant planets and the high metallicity of their host stars, appears in the case of M-dwarf systems too. A bigger sample of M-dwarf planet hosts with spectroscopic data available, would make this conclusion even stronger. This result supports the core-accretion scenario (Pollack et al., 1996) against the disk-instability model (Boss, 2000), as being the main mechanism of giant-planetary formation in the case of M dwarfs too. According to Boss (2002), the formation of a giant planet as a result of disk instabilities is almost independent of the metallicity. On the other hand, the core-accretion scenario suggests that the higher the metallicity (and thus the dust density of the disk), the higher might be the probability of forming a core (and eventually massive core) before the disk dissipates (Pollack et al., 1996, Kokubo & Ida, 2002).

Table 3.16: Kolmogorov–Smirnov tests comparing the LMP vs HMP and LMPH vs HMPH distributions for the whole sample and for different groups of stellar T_{eff}. In parenthesis, we report the numbers of the objects for each case.

Samples	T_{eff} range	K-S statistic	K-S p-value
LMP (102) vs HMP (23)	all	0.58	$2.07 \cdot 10^{-6}$
LMPH (60) vs HMPH (18)	all	0.49	$1.33 \cdot 10^{-3}$
LMP (24) vs HMP (7)	T_{eff} < 3400	0.77	$1.01 \cdot 10^{-3}$
LMPH (13) vs HMPH (4)	T_{eff} < 3400	0.75	$3.78 \cdot 10^{-2}$
LMP (49) vs HMP (10)	3400 < T_{eff} < 3700	0.46	$3.71 \cdot 10^{-2}$
LMPH (28) vs HMPH (9)	3400 < T_{eff} < 3700	0.37	$2.41 \cdot 10^{-1}$
LMP (29) vs HMP (6)	T_{eff} > 3700	0.59	$3.73 \cdot 10^{-2}$
LMPH (19) vs HMPH (5)	T_{eff} > 3700	0.59	$8.21 \cdot 10^{-2}$

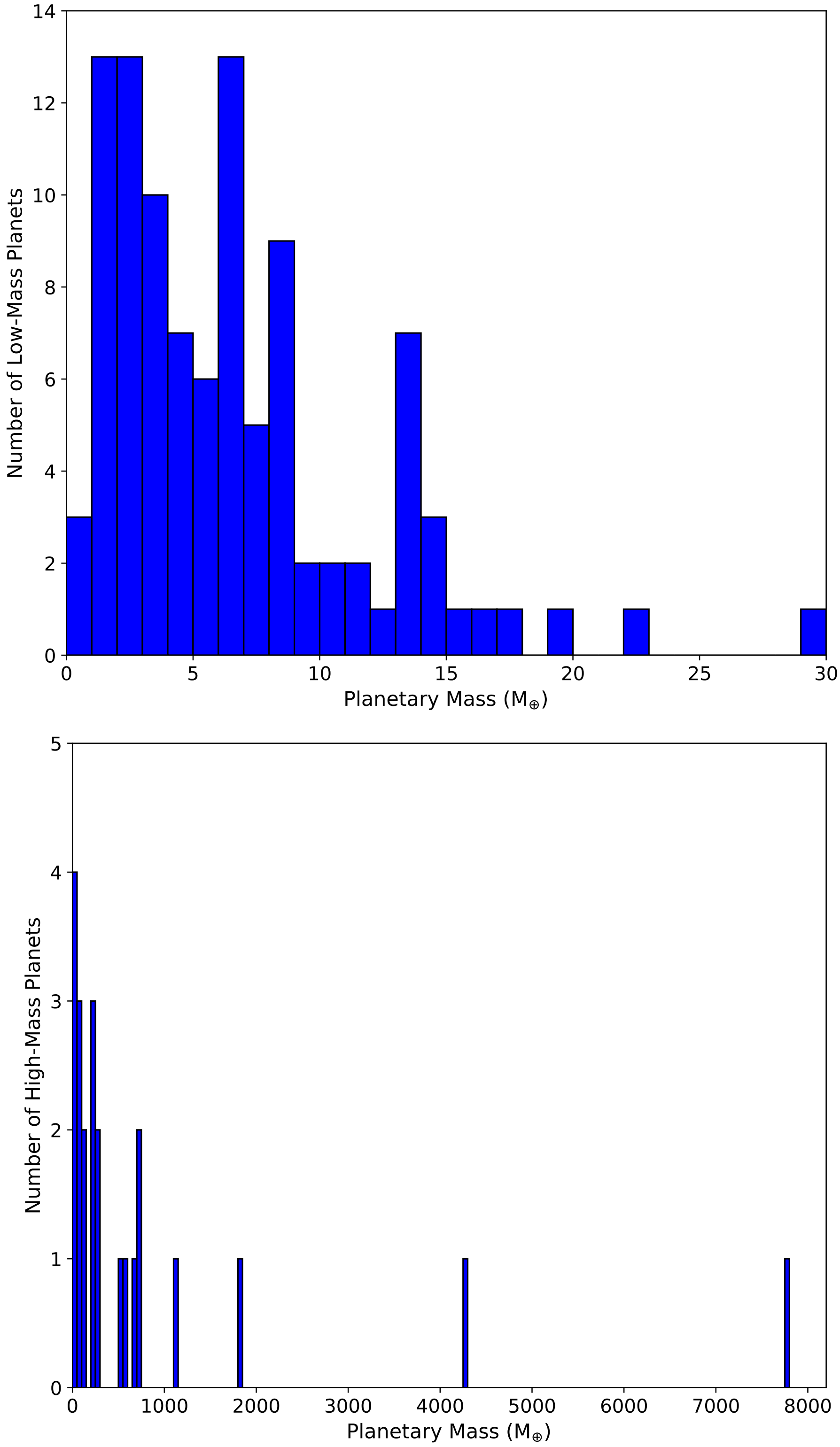

Figure 3.27: Upper panel: Distribution of mass for the low-mass planets. Lower panel: Distribution of mass for the high-mass planets.

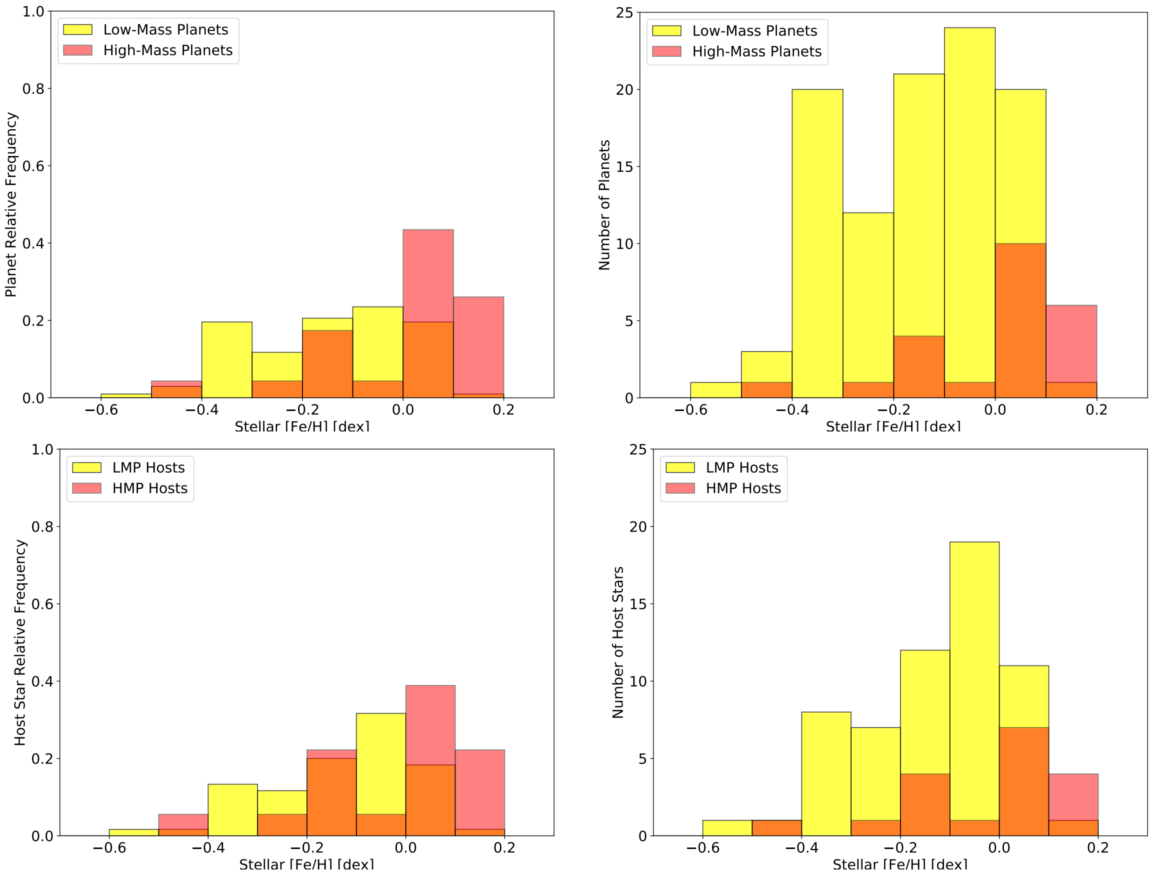

Figure 3.28: Upper left panel: The planet relative frequency distributions for the LMP and HMP populations. Upper right panel: The absolute number of planets. Lower left panel: The host-star relative frequency for hosting LMP or HMP. Lower right panel: The host star absolute numbers.

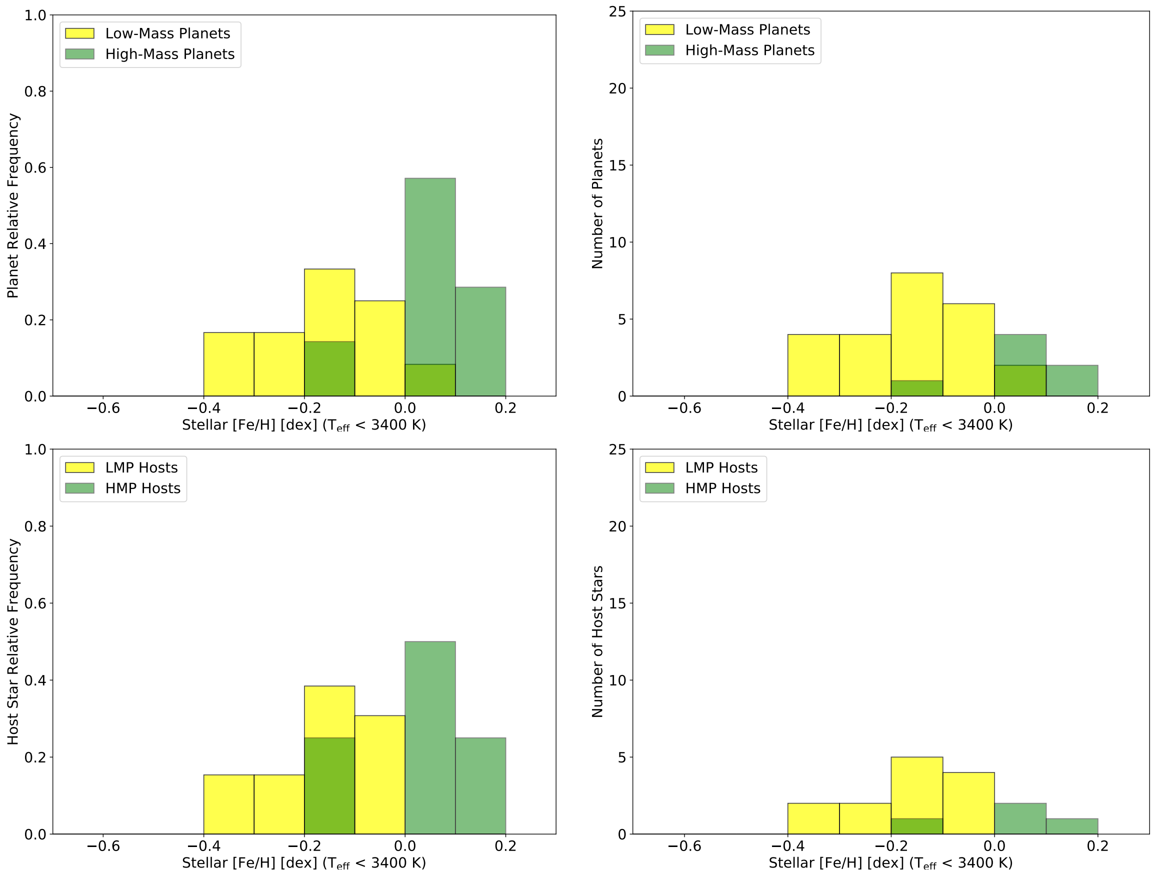

Figure 3.29: Upper left panel: The planet relative frequency distributions for the LMP and HMP populations. Upper right panel: The absolute number of planets. Lower left panel: The host-star relative frequency for hosting LMP or HMP. Lower right panel: The host star absolute numbers. T_{eff} < 3400 K.

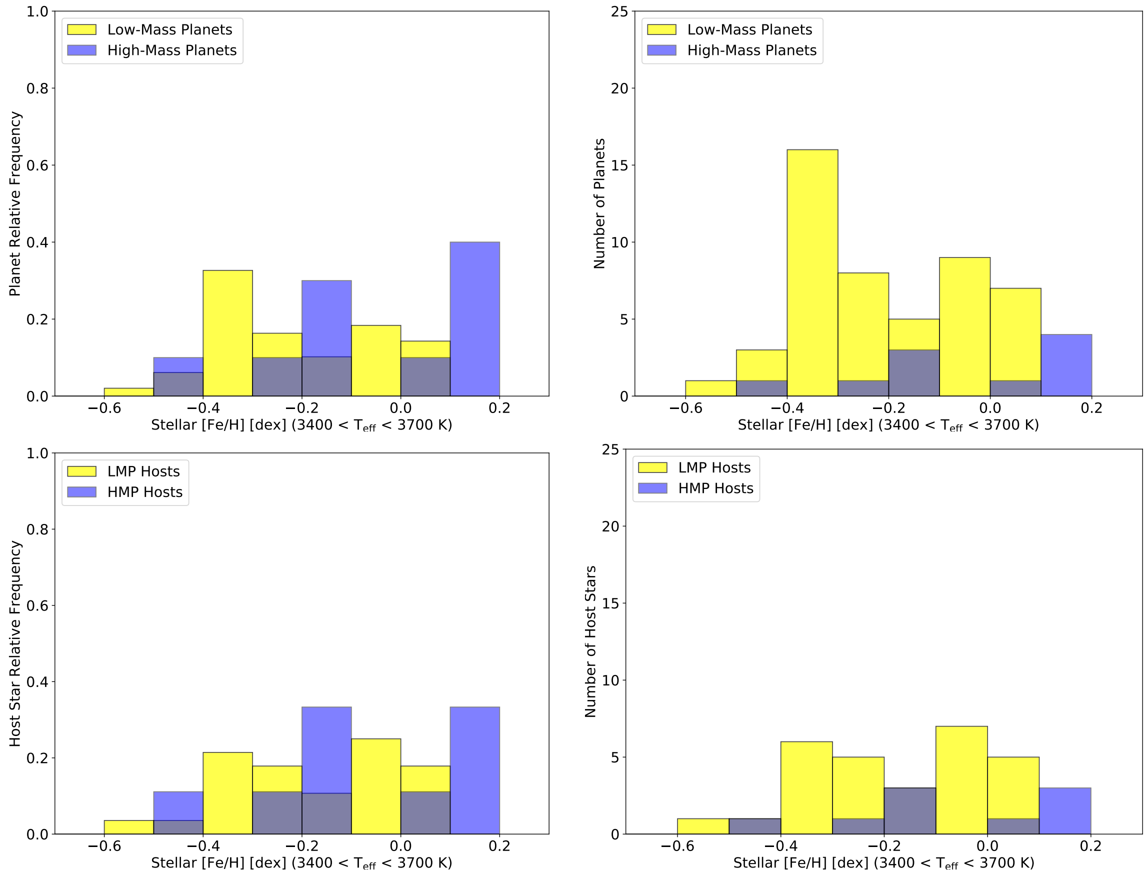

Figure 3.30: Upper left panel: The planet relative frequency distributions for the LMP and HMP populations. Upper right panel: The absolute number of planets. Lower left panel: The host-star relative frequency for hosting LMP or HMP. Lower right panel: The host star absolute numbers. 3400 < T_{eff} < 3700 K.

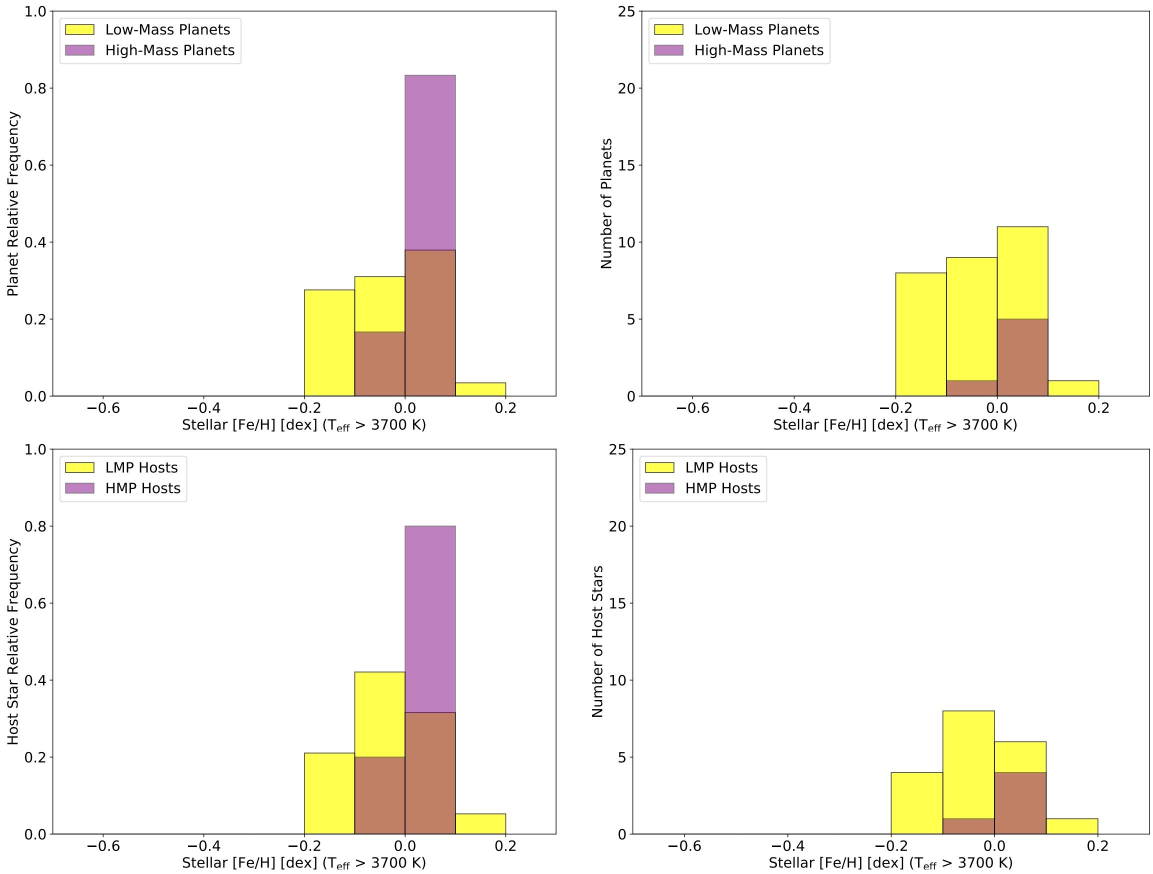

Figure 3.31: Upper left panel: The planet relative frequency distributions for the LMP and HMP populations. Upper right panel: The absolute number of planets. Lower left panel: The host-star relative frequency for hosting LMP or HMP. Lower right panel: The host star absolute numbers. T_{eff} > 3700 K.

4. MPIRA - Deriving stellar parameters in the near-infrared

4.1. Overview of our method in the NIR

M dwarfs are intrinsically faint stars. They emit more light in the NIR than in the optical. Thus, by studying those stars in the NIR, a large fraction of the flux can be obtained for analysis. An advantage of the NIR spectral region compared to the optical one, when dealing with cool stars such as M dwarfs, is that the continuum is less depressed and the blend of lines is less strong (Önehag et al., 2012). This can be noticed in Fig. 4.1, where regions of optical and NIR spectra are presented for the same M dwarf Gl846. The optical spectrum of these stars suffers significantly by contamination of molecular absorption lines and depression of the continuum, which are problems we managed to overcome by following the pseudo-EW approach, together with applying convolution and machine-learning modeling in our optical method. NIR seems to be the most promising wavelength region for examining M dwarfs and determining their stellar atmospheric parameters.

In order to derive abundances and eventually the stellar atmospheric parameters, two main things are needed: a radiative transfer code and a stellar atmosphere model. MOOG* software (Sneden, 1973) solves the radiative transfer equations, assuming local thermodynamical equilibrium (LTE). It derives line abundances from measured equivalent widths or spectral synthesis for a given model atmosphere. MARCS model atmospheres (Gustafsson et al., 2008) are provided as a pre-calculated grid in the parameter space. A specific atmosphere model is then obtained from the grid by interpolating from nearest parameter values, in order to give the requested combination of stellar parameters.

The configuration file of MOOG contains the location path with the interpolated MARCS model atmosphere and the file of the line list including the measured EWs, the atomic numbers, the excitation-potential values and the $\log(gf)$ values. These files are formatted in a proper way for the operation of MOOG.

The EWs of absorption lines, can be measured either manually or automatically. Throughout the work, both ways were examined. An advantage of measuring EWs manually is that we can control the process on spot and try to measure lines with different ways of

*http://www.as.utexas.edu/~chris/moog.html

fitting if there are nearby blended features and decide for an accurate placement of the continuum. The drawbacks of the manual approach are the time needed in case of a big line list and the subjective way of choosing the surrounding continuum and the features to fit, that may lead to systematic errors depending on the person doing the measurements. On the other hand, applying an automatic process to measure the EWs saves time, but the way the code will set the continuum and apply the fittings is something that must be visually examined and tested before it can be trusted.

The most crucial step is to determine a proper line list that will lead successfully from the measurement of the EWs, to the computation of the abundances with a radiative transfer code by applying stellar atmospheric modeling, and finally to the determination of the stellar parameters. The lines must be carefully selected, with no blending and with continuum placement being as accurate as possible, when measuring the EWs. Although the continuum depression is less severe in the NIR, the precise continuum identification remains a challenge (Sarmento et al., 2021).

This chapter describes our method developed in the NIR for the determination of T_{eff}, metallicity (expressed as [Fe/H]) and microturbulence (v_t) of M dwarf stars. Thereafter, this method is called MPIRA (Measuring Parameters in InfraRed Astronomy).

In Sect. 4.2 we describe the construction of our initial line list. In Sect. 4.3 we examine the obtained lines by doing synthesis to them and to their respective surrounding region without the target line, in order to refine the line selection. In Sect. 4.4 we examine different ways of measuring the EWs and we compare the resulting abundances. In Sect. 4.5 we describe the computational process of MPIRA, including the evaluation of the impact of different $\log(gf)$ values for the spectral lines, in our attempt to reach more accurate and precise parameter determinations. We refine our line list further and we present the final stellar atmospheric parameters, as well as their individual uncertainties, for our NIR sample of stars. Finally, we compare our results in the NIR analyzed by MPIRA with our results for the same stars both in the optical analyzed by ODUSSEAS.

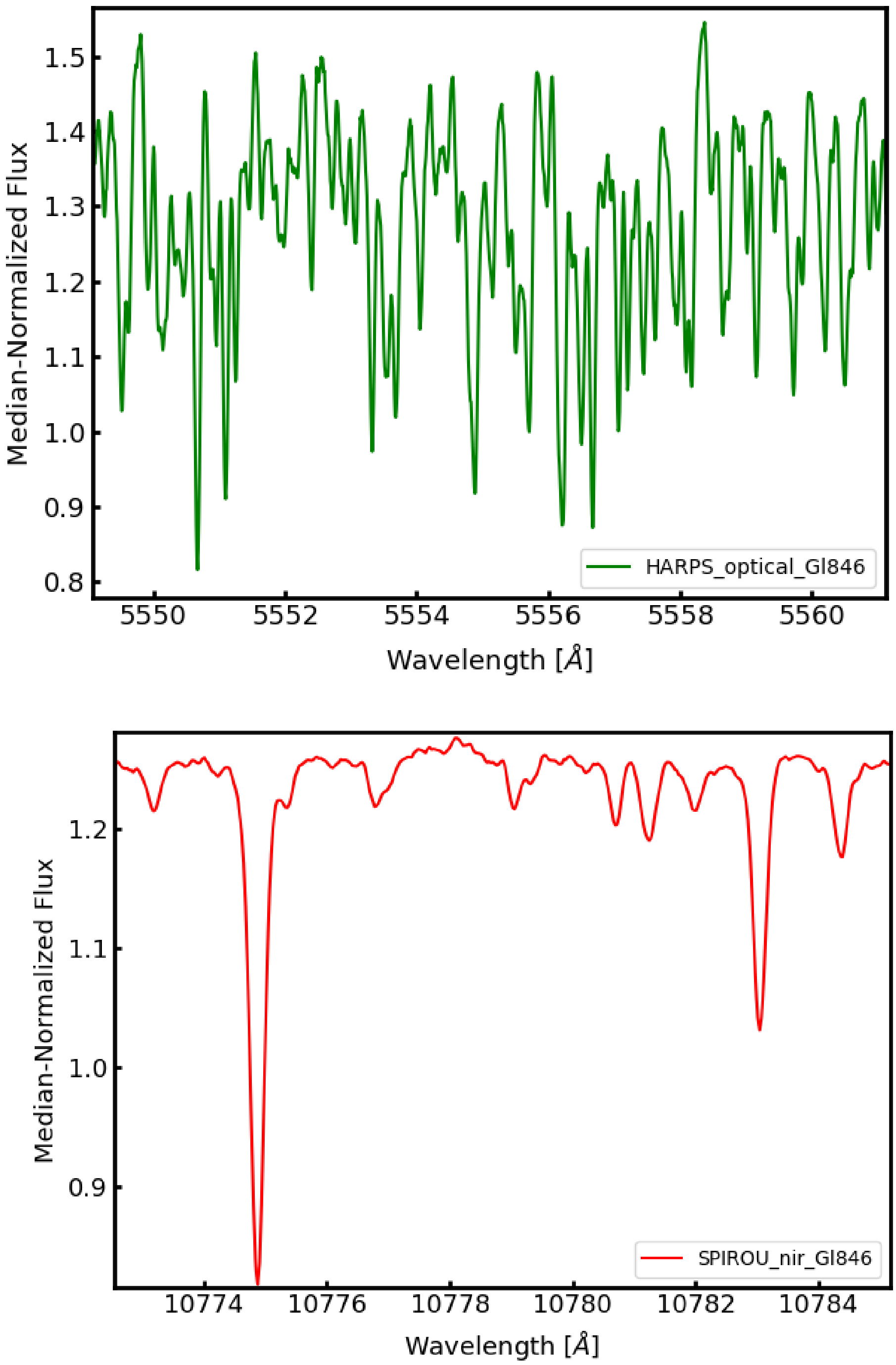

Figure 4.1: Upper panel: Spectral region in the optical of HARPS spectrum for star Gl846. Lower panel: Spectral region in the NIR of SPIRou spectrum for star Gl846.

4.2. Investigation for a proper line list in NIR

4.2.1 Identification of spectral lines in NIR stellar spectra

In the NIR, a reliable line list is needed. As a starting point, we applied a refined version of a NIR line list by Andreasen et al. (2016), which was constructed and tested upon K stars with the perspective to be used also for M dwarf stars. The list consists of 86 Fe lines spanning from 10065.05 to 23308.48 Å. The initial line list was created after downloading from the Vienna Atomic Line Database (VALD) a list of all Fe lines in the NIR region from 10000 to 25000 Å and examining a solar spectrum of highest resolution and S/N possible. VALD is a collection of atomic and molecular transition parameters of astronomical interest. It offers options for selecting subsets of lines for typical astrophysical applications, such as line identification.

At first, we had available four SPIRou spectra for the stars HD189733, Gl15A, Gl699 and Gl1002 of types K2, M2, M4 and M5.5 respectively, covering a wavelength range from 9700 to 24000 Å. The data were kindly provided to us by the SPIRou team. We applied the automatic tool ARES (Sousa et al., 2015) to them measuring the EWs of the given lines, in order to examine the quality of the line shapes and the respective fittings of ARES. ARES is a code that computes automatically the EWs of absorption lines in stellar spectra. Its inputs are the 1D spectrum, a list of lines to measure and a file that contains the parameters necessary for the computation. The code takes a region around each line, where it defines the position of the continuum. Then, it identifies the number and the position of the lines needed to fit at the local spectrum. It uses multi Gaussian fits, as Gaussian fit is a very good approximation for weak lines. The fitting parameters are used to calculate the EW of each line. Since this code was initially designed for measuring lines in FGK stars, we needed to adjust its settings, in order to perform as good as possible for the M dwarf spectra, where the continuum can not be precisely determined and the lines suffer from blending. We examined different values of parameters, so to find those which properly fit most lines. We ended up on the following settings:

”smoothder” = 8. This is a parameter for the calibration of search of lines. It is noise smoother for the derivatives.

”space” = 5. It is the interval in Å for the computation around each line.

”lineresol” = 0.1. This sets the line resolution of the input spectra. If the code finds two lines closer than the value set for it, then it takes the two lines as one line alone.

”miniline” = 2. This is the weakest line strength in mÅ to be printed in the output file.

”rejt” is an important parameter for the calibration of the continuum position and it is related with the S/N of the spectrum. Thus, this parameter was adjusted for each spectrum individually, as we adapted ARES to measure the S/N on three spectral regions with no significant contamination of lines and the median S/N value was chosen. These regions are 10098 to 10104 Å, 11122 to 11132 Å and 11262 to 11270 Å. In the cases of the four spectra examined, its applied values ranged from 0.992 to 0.999.

The lines used for ARES to correct automatically the radial-velocity shift of the spectra are the following three strong lines of Aluminium: 16718.957 Å, 16750.564 Å and 16763.360 Å.

After ARES returned the output of all the lines measured for each spectrum, we had to visually investigate in each spectrum, to see whether those Gaussian fits were matching with the lines and whether those lines were properly shaped or blended. ARES provides an option which stores all the plots of the fits in the lines.

In Fig. 4.2, we show examples of a properly-shaped line which is successfully fitted by ARES and a line which is blended and thus the resulting EW of the fit can not be trusted.

In Table 4.1, we present the efficiency of ARES on the four NIR spectra. We notice that there is significant difference between the properly-shaped lines of the K star and the M stars. Among the M stars, we notice that the latter spectral types have fewer well-shaped lines and thus fewer trustful fits for measuring their EWs.

Table 4.1: Examination of the initial lines measured by ARES. The latter the spectral type, the fewer the well-shaped lines with trustful EW measurements.

Star	Spectral Type	S/N	rejt	Well-shaped Lines	Blended Lines	Non-measured
HD189733	K2	1580	0.999	58	24	4
Gl15A	M2	3569	0.999	16	40	30
Gl699	M4	1417	0.999	7	43	36
Gl1002	M5.5	123	0.992	4	41	41

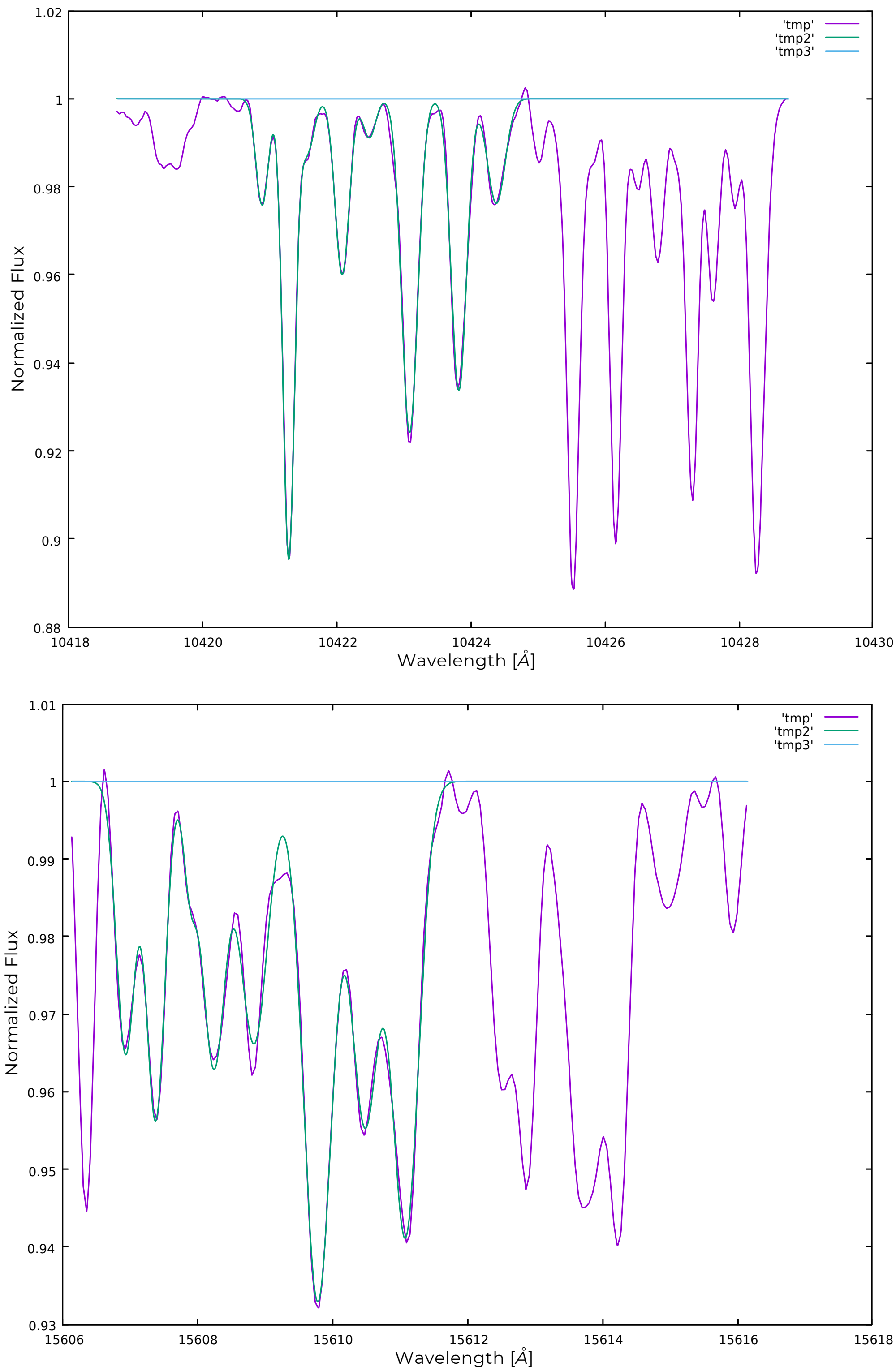

Figure 4.2: Upper panel: example of successful fit by ARES in a well-shaped FeI line at 10423.03 Å of Gl15A. Lower panel: example of a blended FeI line at 15611.15 Å of Gl15A. The y-axis of plots is the normalized flux and the x-axis is the wavelength in Å.

4.2.2 Construction of an M-dwarf line list in NIR

The full sample of the stellar spectra with resolution of 75000 that we eventually received from SPIRou team, their spectral types and their S/N values measured by ARES as explained above, are presented in Table 4.2. As noticed, more stars have been added to the starting sample of four stars (in which we measured the initial line list with ARES), covering spectral types between M0 and M5.5. The initial spectra had their wavelength values in vacuum. We converted the wavelength to air, applying the following equation from the IAU standard for the vacuum to air corrections (Edlén, 1953):

$$\frac{\lambda_o - \lambda}{\lambda} = a + \frac{b1}{c1 - 1/\lambda_o^2} + \frac{b2}{c2 - 1/\lambda_o^2} \tag{4.1}$$

where λ_o is the vacuum wavelength in m, λ is the air wavelength and the constant values were adopted by Ciddor (1996) as α = 0, b1 = 0.05792105, b2 = 0.00167917, c1 = 238.0185, c2 = 57.362.

As examined, the initial line list based on K stars does not operate correctly in its majority for M dwarfs. We had to identify proper lines in M-dwarf spectra by eye. Thus, we constructed a new line list for M dwarfs by doing a detailed visual examination of the lines between 9700 and 17000 Å in our spectra. Since M-dwarf spectra do not offer many properly shaped lines with a well-defined continuum, we included in our search both FeI lines and TiI lines from VALD, which are numerous and prominent in M dwarfs. We decided to modify the standard ARES+MOOG method, which follows the process described in Sect. 2.6.1, by using the abundance differences of Fe and Ti lines from their average elemental abundance in the stars, instead of their absolute values, so we can include both elements in the process of our tool MPIRA, as explained in detail throughout Sect. 4.5.

We used the option “Extract Stellar” of VALD, which extracts all spectral lines producing significant absorption for specific stellar atmospheric conditions. Those conditions were chosen as for a typical M2 dwarf with $T_{\rm eff}$ = 3500 K, $\log g$ = 4.8 dex, v_t = 1 km/s and wavelength region from 9000 to 17000 Å. The detection threshold was set to 0.10 mÅ, in order to get lines with significant central depth. Therefore, a total of 260 lines (171 FeI and 89 TiI lines) were identified by VALD and we visually inspected their shapes for the SPIRou spectra of types K2 to M5.5. Figure 4.3 illustrates how an absorption line becomes gradually less well-defined, due to line blending, as we observe it from earlier to later spectral types. Such lines with broken symmetry according to vertical axis and obvious blends in their shapes, were discarded from our selection.

Finally, from the 260 lines examined, we selected a total of 56 lines (18 FeI lines and 38 TiI lines) which seemed well shaped in spectral types from M0 to at least M3.5. Most of the lines were blended in the spectrum of Gl1002, which is star of type M5.5, so we excluded it (and any such late M types) from the further steps of our method. Our selected lines are presented in Table B.1, along with indicators on whether they are finally applied to our method or not, based on criteria explained throughout the later sections.

Moreover, we searched for FeII and TiII lines by identifying 750 absorption features in the spectra and crossmatching those with the respective element line lists provided by “Extract Element” of VALD. As explained in Chapter 2, ionized lines are needed for the calculation of $\log g$ in standard EW methods. However, in our M-dwarf spectra those lines have severe blending in similar wavelengths, along with very weak line depths, preventing us yet from including some of them in our line list. Therefore, due to the absence of trusted ionized lines, we kept $\log g$ parameter fixed to the common value of 4.8 dex (Rajpurohit et al., 2018, Sarmento et al., 2021) throughout our determinations of T_{eff}, [Fe/H] and v_t. It is known that a change of $\pm$0.5 dex in the assumed $\log g$ value implies only minor differences in the derived parameters (Berger et al., 2006, Casagrande et al., 2008). We also show later in Fig. 4.5 that among values of 4.5, 4.8 and 5.1 for $\log g$, the changes in absorption lines are minor. Although fixing the value is not ideal, it is a way to overcome the issue of severely blended ionized lines that can not be used in our method. Setting $\log g$ to a fixed value during the process, is another adaptation in our method compared to the standard ARES+MOOG method.

Table 4.2: Full sample of our SPIRou spectra in the NIR with R = 75000.

Star	Spectral Type	S/N
HD189733	K2	1580
Gl846	M0	1530
Gl514	M1	1333
Gl382	M2	1139
Gl15A	M2	3569
Gl436	M3	1534
Gl876	M3.5	936
Gl699	M4	1417
Gl1002	M5.5	123

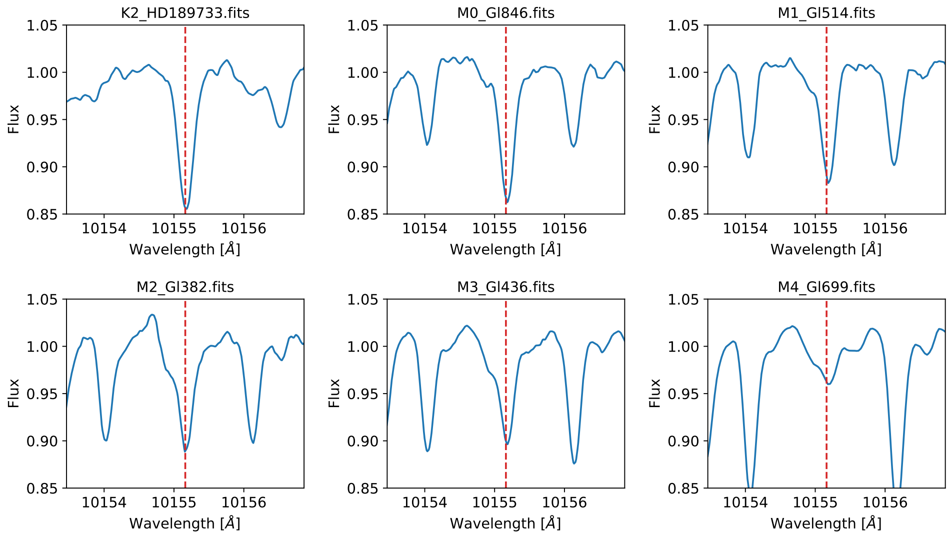

Figure 4.3: Gradual changes in shape of line according to the spectral type. The FeI line presented is at 10155.16 Å.

4.2.3 Application of adapted ARES+MOOG with 56-line list

We started by applying the adapted ARES+MOOG method with the 56 lines selected, on the SPIRou spectra of Table 4.2 except the one for Gl1002 of type M5.5 as mentioned earlier. As first step, we calculated the EWs of the stars by using the ARES software (Sousa et al., 2015) with the settings mentioned before. For each M dwarf, the MARCS model atmospheres were generated by the initial input reference $T_{\rm eff}$ and metallicity that we adopted by Mann et al. (2015) and we report in Table 4.3, and by typical values of $\log g$ = 4.80 dex and v_t = 1 km/s. For the K star, we adopted reference input values reported by Sousa et al. (2018): $T_{\rm eff}$ = 4969 K, [Fe/H] = -0.07 dex, v_t = 0.76 km/s, $\log g$ = 4.31 dex. The adopted solar abundance for Fe is 7.47. Regarding the reference Ti abundance of a star, we consider as such, the input Ti abundance value that MOOG reports when we give as input metallicity the reference value by Mann et al. (2015).

The abundances of those 56 lines and the average elemental abundance of the stars were calculated, while keeping the input parameters for modeling fixed to their reference values. These results are presented in Table 4.3. The goal of this first application was to check if these 56 lines measured by ARES give reasonable values of abundances and overall [Fe/H].

Although the K star had a reasonable difference of -0.07 dex compared to its reference value, there was a significant underestimation of metallicity for all M dwarfs, having differences between -0.19 to -0.36 dex compared to their reference values, with the mean underestimation being -0.28 dex. In addition, there was big dispersion (as standard deviation) for both FeI and TiI abundances, varying from 0.15 to 0.52 dex and being of the same order of magnitude as the difference, as can be seen in Table 4.3.

We repeated the process setting values of v_t smaller than 1, adopting common v_t values for M dwarfs (Wende et al., 2009, Lindgren & Heiter, 2017) based on their reference T_{eff}, but the overall abundances remained underestimated at similar levels.

We also ran the process excluding those lines that appeared as outliers with an individual abundance difference above 0.20 dex from the average in at least half of our stars, as a first rough try of refining the line list. Even though the dispersion of FeI and TiI was reduced in most stars, the total [Fe/H] of all the M dwarfs remained significantly underestimated as compared to the reference values from literature.

Furthermore, we repeated the process setting different fixed ”rejt” values from 0.991 to 0.999 for measuring the EWs, but there was no improvement related to it, so we continued applying the ”rejt” option of continuum adjustment based on the S/N ratio measured in spectral regions. In addition, changing the values of other ARES settings did not provide reasonable results for the M dwarfs.

Table 4.3: Attempt of abundance calculation with ARES+MOOG using the 56 lines. ”STD” stands for standard deviation and ”Diff.” for difference compared to the reference value (”Ref.”). The [Fe/H] is severely underestimated when compared to the reference values of all M dwarfs. Only the K star has a compatible value.

Star	Ref.T_{eff} [K]	Ref.[Fe/H] [dex]	Ab.FeI [dex]	STD FeI [dex]	FeI Diff. [dex]	Ab.TiI [dex]	STD TiI [dex]	TiI Diff. [dex]
HD189733	4969	-0.07	7.33	0.16	-0.07	5.00	0.24	0.00
Gl846	3848	0.02	7.20	0.19	-0.29	4.85	0.15	-0.12
Gl514	3727	-0.09	7.13	0.28	-0.25	4.65	0.21	-0.21
Gl382	3623	0.13	7.26	0.36	-0.34	4.82	0.21	-0.26
Gl15A	3603	-0.30	6.92	0.22	-0.25	4.47	0.22	-0.18
Gl436	3479	0.01	7.21	0.36	-0.27	4.69	0.20	-0.27
Gl876	3247	0.17	7.45	0.30	-0.19	4.60	0.47	-0.52
Gl699	3228	-0.40	6.71	0.52	-0.36	4.26	0.31	-0.29

4.3. Synthesis of line list and refinement

The next step was to examine each absorption line separately, by doing spectral synthesis of the whole line list for the M0 star Gl846, the M3 star Gl436, as well as the solar spectrum to see how the lines change as we move to the M-type stars. In this way, we could address the reasons behind the outlier lines, especially those appearing in more than half of the stars.

In order to do the spectral synthesis for each absorption line in our 56-line list, we downloaded from VALD all the elemental data, in a spectral region of 6 Å around each line of interest. These data along with the respective atomic numbers and dissociation numbers of several molecules (CN, OH, CH, NH, MgH, C_2, CO, TiO) were used as the input file "lines in" to the synthesis driver of MOOG. For each line, there are several parameters that are needed as input for MARCS model each time. Regarding the stellar atmospheric parameters, we used their reference values as adopted earlier in the input file "model in". Then, for each line we calculated and gave as input the full width half maximum (FWHM) value as λ/R, with R = 75000 which is the SPIRou resolution. The spectral resolution of a spectrometer is usually measured at the FWHM of a peak from a reference light source. Spectral resolution can be defined as R = $\lambda/\Delta\lambda$. Here, $\Delta\lambda$, meaning the minimum separation for two spectral lines to be considered as just resolved, is the FWHM and λ is the wavelength at which the measurement was taken. In addition, we gave as input each time the limb darkening coefficient values depending on $T_{\rm eff}$, $\log g$ and wavelength as derived by Al-Naimiy (1978). For M dwarfs, these values are equal to 0.52 at approximately 10000 Å and 0.48 at approximately 12000 Å, while for the Sun the respective values are equal to 0.37 and 0.34. We also set the input rotational velocity as $vsini$ = 3 km/s for synthesis of M dwarfs, since according to Jenkins et al. (2009) the distribution for samples of M dwarfs in the spectral range from M0 to M3.5 clearly peaks at $vsini$ values of around 3 km/s. For the Sun, the value was set as $vsini$ = 2 km/s (dos Santos et al., 2016). Regarding macroturbulence (v_{mac}), in the M dwarfs it is difficult to disentangle it from the other line-broadening process ($vsini$) and considering that it has typical values close to 0 for M dwarfs (Wende et al., 2009, Lindgren & Heiter, 2017), we kept it as 0 during synthesis. For the Sun, the value was set as v_{mac} = 3.2 km/s (dos Santos et al., 2016).

Other input parameters of the synthesis driver are the "synlimits" set for the beginning and ending wavelength synthesis, the atomic number of the line we synthesize, the "damping" set as 1 for the van der Waals line damping parameter, the "molecules" set as 2 to do the molecular equilibrium and output results, the ”lines” set as 1 which controls the output of the line data, the ”flux/int” set as 0 in order to perform integrated flux calculations, the ”units” set as 0 to specify the wavelength units in Å. For further technical details, one can read the pdf file describing the format of the code provided by MOOG*.

Regarding each line, firstly we synthesized the line itself for watching how similar is the synthetic line compared to the observed one, based on the input parameters. In addition, we synthesized all the lines in the region except the target line, in order to see what is the contamination of other elements to the actual absorption feature that we measure. Although we had selected by eye properly shaped lines for our line list, there could be part of absorption coming from other elements and being impossible to detect by visual inspection. Based on the synthesis of all lines and the measurements of their EWs in our sample of stars, we realized that lines with measured abundances far from the reference ones, are coming mostly from lines with EW > 150 mÅ because of expected poor Gaussian fitting to such wide shapes when measuring the EWs, and lines blended with other absorption features. As presented in Table B.1, at this stage we excluded from further investigation 19 lines with EWs greater than 150 mÅ in at least four out of seven M dwarfs in our sample, labelled as ”wide”. We also excluded 13 lines with blending, by labelling them with the note ”1st synthetic cut”. Such example of discarded line after synthesis, due to blending which could not be visually spotted in previous stage of line examination, is presented in Fig. 4.4.

In Appendix C, we present all the figures about synthesis of lines alone and surrounding regions alone, regarding the lines that we decided to keep for the next stages of our method. These figures include the lines we finally use in our method, labelled as ”applied”, as well as the lines that they are discarded later during the final stage of line-list refinement and they are labelled as ”2nd synthetic cut” in Table B.1.

Furthermore, as an attempt to constrain the gravity (expressed as $\log g$), since we cannot apply the ionization balance method due to the lack of well-shaped ionized lines, we explored whether any of our lines with wide wings are sensitive enough to changes of $\log g$. However, as presented in Fig. 4.5, the synthetic profiles of such lines with varying $\log g$ values (4.5, 4.8, 5.1) are not significantly different as to be used for that purpose, so we kept this parameter fixed to a common value of 4.8.

*http://www.as.utexas.edu/~chris/moog.html

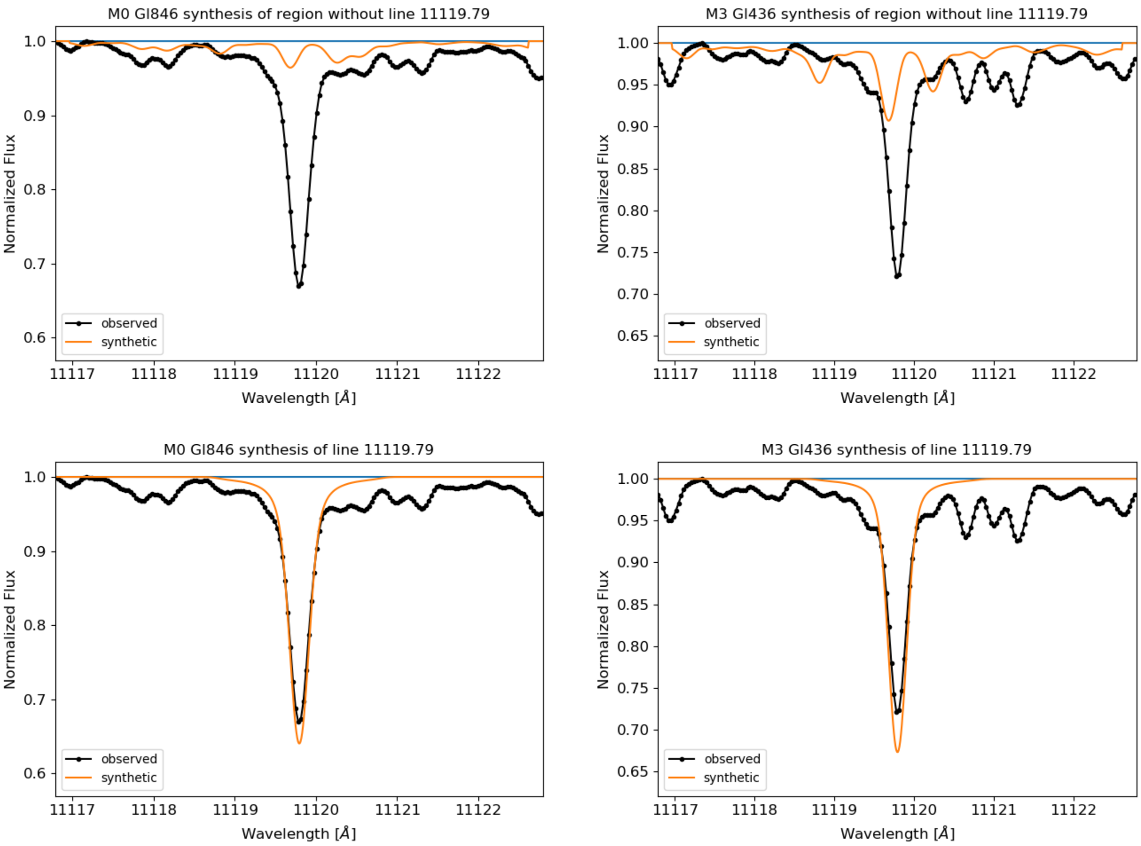

Figure 4.4: Example of discarded FeI line 11119.79 Å due to blending revealed by synthesis. Upper panels: Synthesis of region alone, without the target line, for the M0 dwarf Gl846 (left) and the M3 dwarf Gl436 (right). Lower panels: Synthesis of the target line alone for the M0 dwarf Gl846 (left) and the M3 dwarf Gl436 (right).

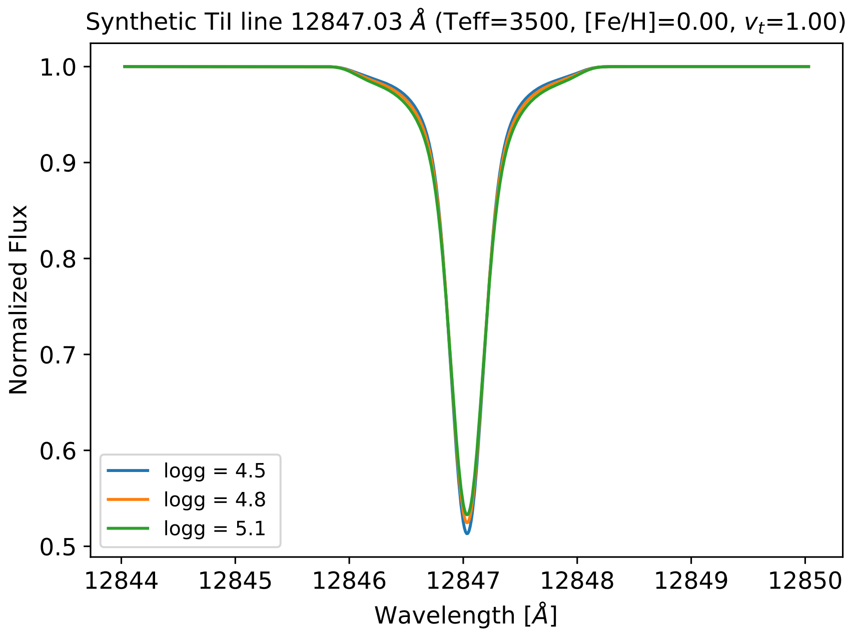

Figure 4.5: Example of line with wide wings, synthesized with different $\log g$ values.

4.4. Examination of EW measurements and abundances

At this point, after the 1st synthetic cut during which we excluded significantly blended and wide lines, we continued keeping 24 from the 56 lines. We calculated again the abundances of M dwarfs using ARES with the 24-line list. The [Fe/H] values were still underestimated for most M dwarfs, as it can be seen in Table 4.4. The mean underestimation of all M dwarfs was -0.21 dex, with the differences varying between -0.15 to -0.33 dex. This systematic underestimation of abundance was not visible based on the figures of comparison between the synthetic and observed lines. The dispersion (as standard deviation) for FeI and TiI abundances varied from 0.10 to 0.21 dex. Although there was a small improvement after discarding the wide and the mostly blended lines, as the mean underestimation was reduced from -0.28 dex to -0.21 dex, still the results could not be trusted.

At this point, the underestimation of resulting [Fe/H] led us to examine the EW values themselves that we give as input to MOOG computations. Therefore, we manually measured the EWs of M3 star Gl436 with an IRAF-like version of ARES* in three different ways and compared with the results of automatic ARES measurements.

Firstly, we tried to replicate the multiple line-fitting of ARES near the line of interest. Secondly, we fitted and measured the line of interest alone, placing the continuum to the level implied by the edges of the individual line. In the third way, we fitted and measured the line of interest, placing the continuum to the level implied by the surrounding spectral region. In Fig. 4.6, we show TiI line 11949.55 Å of Gl436 as an example for the different ways of EW measurements we examined in M dwarfs. Automatic ARES measured an EW value of 121 mÅ. Similarly, our way of replicating ARES with multi-line fitting measured an EW value of 122 mÅ. In the case of fitting and measuring the line of interest with a continuum implied by the line itself, the value was equal to 112 mÅ. Finally, when measuring the line of interest alone as a single line in the region, with the continuum at the level of the surrounding region, we got a value of 133 mÅ.

We compared the EW values overall and we concluded that in the first and second way, the EW values are similar to ARES with a resulting underestimation of the [Fe/H] assuming that the atomic data are correct. This is probably because of the small blending that occurs next to the line of interest and the eventual depression of the continuum, leading to constantly loose a part of the EW area for the line we measure. However, the third way of

*https://github.com/sousasag/ARES/tree/master/ares_cython measuring the EWs led to constantly higher values compared to automatic measurements and the other manual ways of measuring. So it was a strong indication to further test this method of setting manually the continuum to the proper place and make the fit for each line ourselves. In Fig. 4.7 we present the overall EW comparison between the automatic ARES results and our third-way manual results for EWs of the 24 lines in star Gl436. Most lines have constantly higher EW values when measured manually in this way.

Therefore, we calculated again the abundances of M dwarfs using our third manual way of measuring the EWs for the 24-line list as occurred after synthesis. As noticed in Table 4.5, eventually [Fe/H] appears to be compatible with the reference values for most stars, after the rough calculation with input parameters fixed. The [Fe/H] difference of the stars from their reference values is within 0.07 dex for them all, except the very metal-poor Gl15A. Moreover, the dispersions of FeI and TiI individual line abundances have significantly dropped below 0.10 dex for the early-M dwarfs.

Thus, having at this point an EW-measuring technique towards the correct direction of abundances, we proceeded to apply our code MPIRA for the actual determination of [Fe/H], $T_{\rm eff}$ and v_t.

Table 4.4: Attempt of abundance calculation with ARES+MOOG using the 24 lines. "STD" stands for standard deviation and "Diff." for difference compared to the reference value ("Ref."). The [Fe/H] values are slightly closer to the reference ones than with the 56-line list, but still significantly underestimated.

Star	Ref.$T_{\rm eff}$ [K]	Ref.[Fe/H] [dex]	Ab.FeI [dex]	STD FeI [dex]	FeI Diff. [dex]	Ab.TiI [dex]	STD TiI [dex]	TiI Diff. [dex]
HD189733	4969	-0.07	7.37	0.11	-0.03	4.99	0.27	-0.01
Gl846	3848	0.02	7.31	0.10	-0.18	4.88	0.10	-0.09
Gl514	3727	-0.09	7.23	0.10	-0.15	4.76	0.13	-0.10
Gl382	3623	0.13	7.32	0.19	-0.28	4.91	0.10	-0.17
Gl15A	3603	-0.30	6.92	0.12	-0.18	4.53	0.21	-0.12
Gl436	3479	0.01	7.29	0.08	-0.19	4.76	0.12	-0.20
Gl876	3247	0.17	7.48	0.15	-0.16	4.81	0.17	-0.31
Gl699	3228	-0.40	6.74	0.17	-0.33	4.34	0.18	-0.20

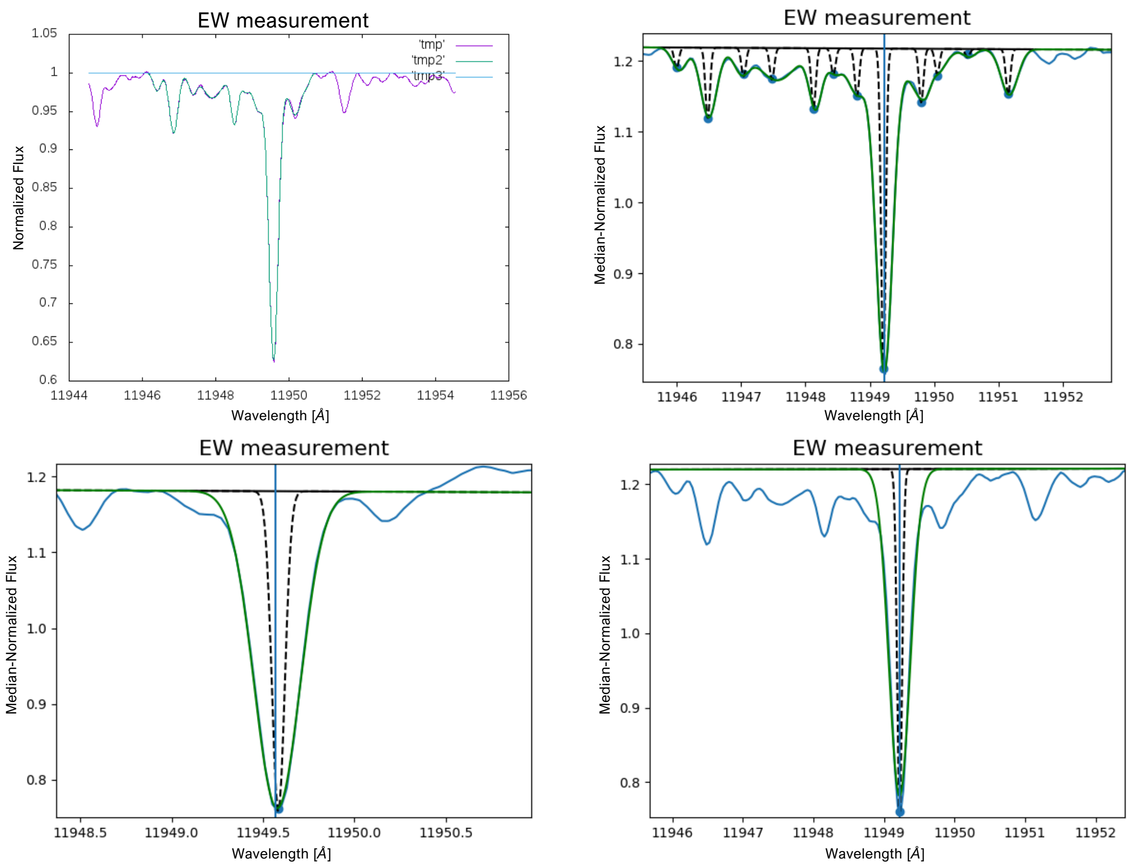

Figure 4.6: Examining ways of EW measurements in M dwarfs, with the example of TiI line at 11949.55 Å of Gl436. Upper left: Automatic fit by ARES (EW = 121 mÅ). Upper right: Manual multi-line fitting replicating ARES (EW = 122 mÅ). Lower left: Measurement by setting the continuum at the level indicated by the edges of the line (EW = 112 mÅ). Lower right: Measurement by setting the continuum at the level indicated by the surrounding region and fitting only the line of interest (EW = 133 mÅ). The y-axis of plots is the flux and the x-axis is the wavelength in Å.

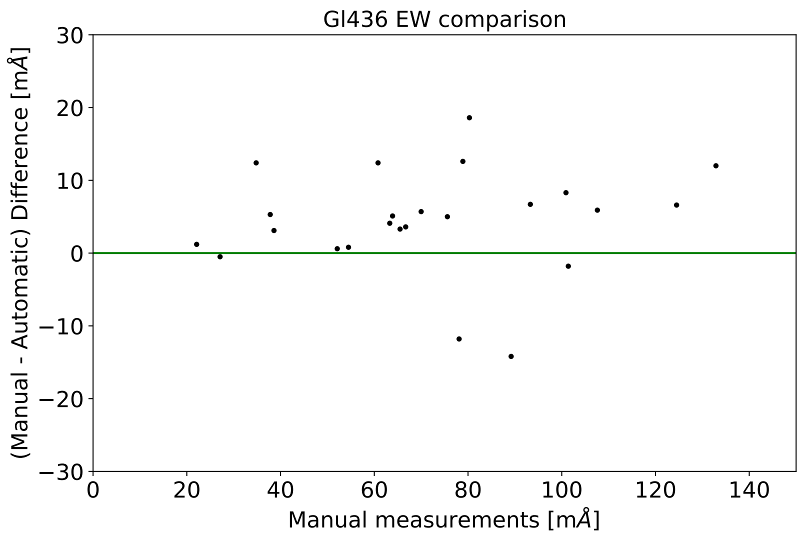

Figure 4.7: EW difference between automatic and manual measurements of our third way for Gl436. There is a trend of manual measurements giving higher EW values for most of the lines.

Table 4.5: Attempt of abundance calculation with manual version of ARES+MOOG using the 24 lines. Eventually, the [Fe/H] values of most stars have difference from their reference values and dispersion within reasonable range.

Star	Ref.$T_{\rm eff}$ [K]	Ref.[Fe/H] [dex]	Ab.FeI [dex]	STD FeI [dex]	FeI Diff. [dex]	Ab.TiI [dex]	STD TiI [dex]	TiI Diff. [dex]
Gl846	3848	0.02	7.42	0.05	-0.07	4.93	0.07	-0.04
Gl514	3727	-0.09	7.38	0.04	0.00	4.83	0.07	-0.03
Gl382	3623	0.13	7.56	0.08	-0.04	4.99	0.08	-0.09
Gl15A	3603	-0.30	7.00	0.10	-0.17	4.52	0.10	-0.13
Gl436	3479	0.01	7.41	0.10	-0.07	4.80	0.08	-0.16
Gl876	3247	0.17	7.61	0.13	-0.03	4.89	0.14	-0.23
Gl699	3228	-0.40	7.07	0.23	0.00	4.44	0.14	-0.11

4.5. MPIRA tool

"MPIRA.py" is the python code running the process. It is presented in Fig. 4.8 which shows the input, operations, and output in a concise manner.

At first, the input parameters are set for the star we want to analyze. The code, based on these values, runs the MARCS model interpolation and the MOOG computation of abundances for the selected list of FeI and TiI lines provided in the input. It reads the output average [Fe/H] and if it differs from the input value, it runs again the process of MARCS model and MOOG calculation with the new output value as input metallicity, until it reaches the point where the input value of the model and the output average value of FeI abundances are equal.

Then, it plots the abundance differences from their average FeI and TiI values, against the excitation-potential values. Based on the slope, we change the $T_{\rm eff}$ value, increasing it in case of positive slope or decreasing it in case of a negative slope. Similarly, it plots the abundance differences against the reduced EW values, expressed as $\log RW$. Based on the slope, we adjust the v_t value by increasing it if the slope is positive or decreasing it if the slope is negative. Based on this principle of balance, the process is iterated until we get the proper values of $T_{\rm eff}$ and v_t that lead to slopes equal or smaller than ±0.001, meaning that the individual abundances of FeI and TiI lines are not showing any trend compared to average abundance of the respective element, with which they should be equal in principal.

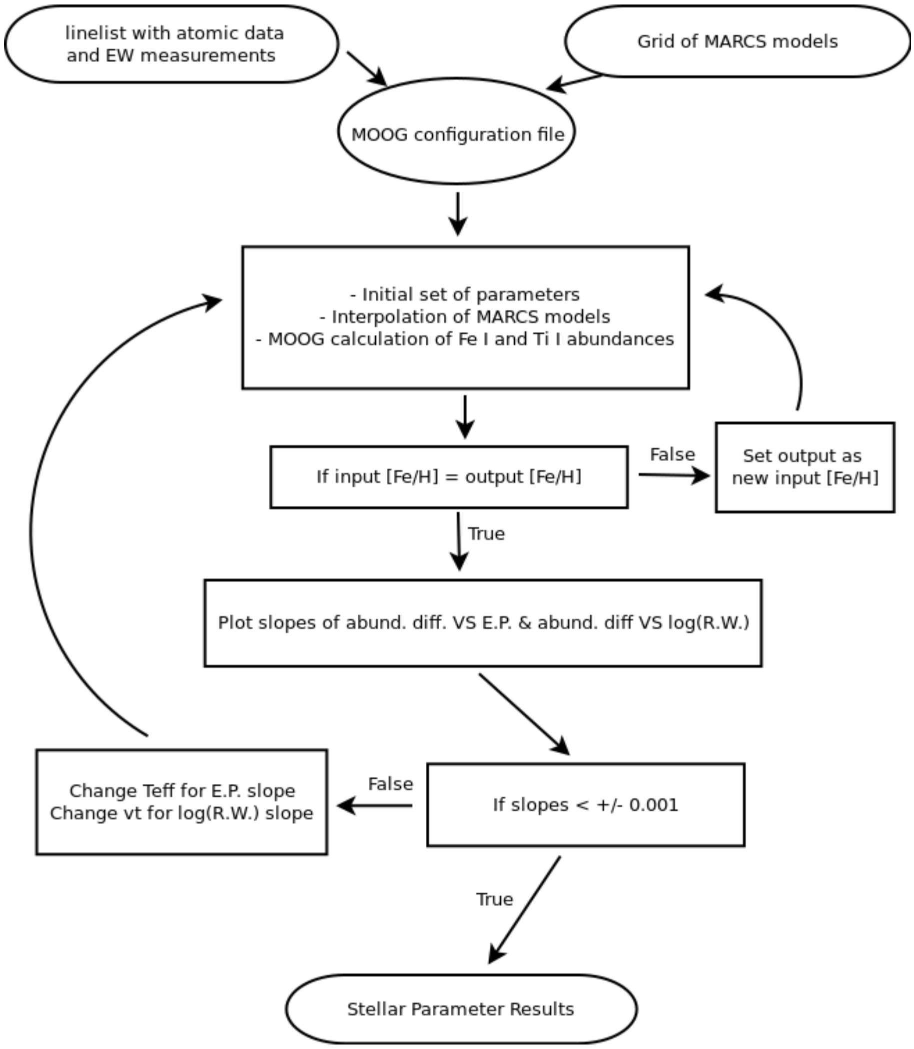

Figure 4.8: Workflow of MPIRA.py.

4.5.1 Application of MPIRA with 24-line list

According to the process described above, we derived [Fe/H], $T_{\rm eff}$ and v_t measuring manually the EWs of the 24 lines.

In Fig. 4.9, we present an example of plots for star Gl382. In the upper pair of panels, we present the abundance differences as occurred by the reference input [Fe/H] and $T_{\rm eff}$ by Mann et al. (2015) and reference v_t by Wende et al. (2009), Lindgren & Heiter (2017). The selected value for v_t is the expected one for M dwarf with its reference $T_{\rm eff}$ and adopted $\log g$, since these studies found that v_t decreases with lower $T_{\rm eff}$ and higher $\log g$. In the lower pair of panels, we present the abundance differences as occurred by the resulting parameters after convergence that lead to slopes equal to 0. The blue data points refer to FeI lines, while the green data points refer to TiI lines.

We applied MPIRA and summarize our results at this point for all seven M dwarfs up to type M4 in Table 4.6. We report as reference v_t for each star, the indicative v_t values for M dwarfs based on their reference T_{eff} and adopted $\log g$ (Wende et al., 2009, Lindgren & Heiter, 2017). It is noticed that after the iterations for convergence, the [Fe/H] results have differences within 0.12 dex compared to their reference values, except for Gl15A that its [Fe/H] results to a considerably lower value for this already metal-poor star. The resulting T_{eff} values have absolute differences compared to reference values that range from 38 to 242 K. Regarding v_t, in three out of seven stars, this parameter could not converge for a proper value, as even with zero values of v_t their respective slope was still negative. The standard deviation of FeI and TiI abundances among the stars had values from 0.03 to 0.11 dex.

Considering all the results above, we concluded that there was room for improvements, as the determinations of stellar parameters did not result to accurate values for all stars.

Table 4.6: Stellar parameters applying MPIRA with the 24-line list.

Star	T_{eff} [K]	T_{eff} Diff. [K]	[Fe/H] [dex]	[Fe/H] Diff. [dex]	STD FeI [dex]	STD TiI [dex]	ref.v_t [km/s]	v_t [km/s]
Gl846	3810	-38	0.02	0.00	0.05	0.06	0.45	0.63
Gl514	3613	-114	-0.15	-0.06	0.03	0.06	0.35	0.45
Gl382	3580	-53	0.20	0.07	0.07	0.07	0.35	0.46
Gl15A	3845	242	-0.70	-0.40	0.07	0.04	0.35	0.00
Gl436	3590	111	-0.10	-0.11	0.08	0.05	0.30	0.00
Gl876	3485	238	0.05	-0.12	0.09	0.11	0.25	0.00
Gl699	3395	167	-0.51	-0.11	0.10	0.10	0.25	0.70

4.5.2 Calibration of $\log(gf)$ values

In our attempt to achieve more accurate and precise determinations, we proceeded into calibrating the $\log(gf)$ values of the 24 lines in our current line list. The process of calibration was done by changing the $\log(gf)$ values of the calibrator star to such values that the individual abundance of every line, would be the equal to the overall reference abundance of the element, after setting the input stellar parameters to their reference values too.

We tested two stars as calibrators for $\log(gf)$ of lines. These stars were the M0 Gl846 and M2 Gl382, because those two had resulting T_{eff} and [Fe/H] closest to their reference

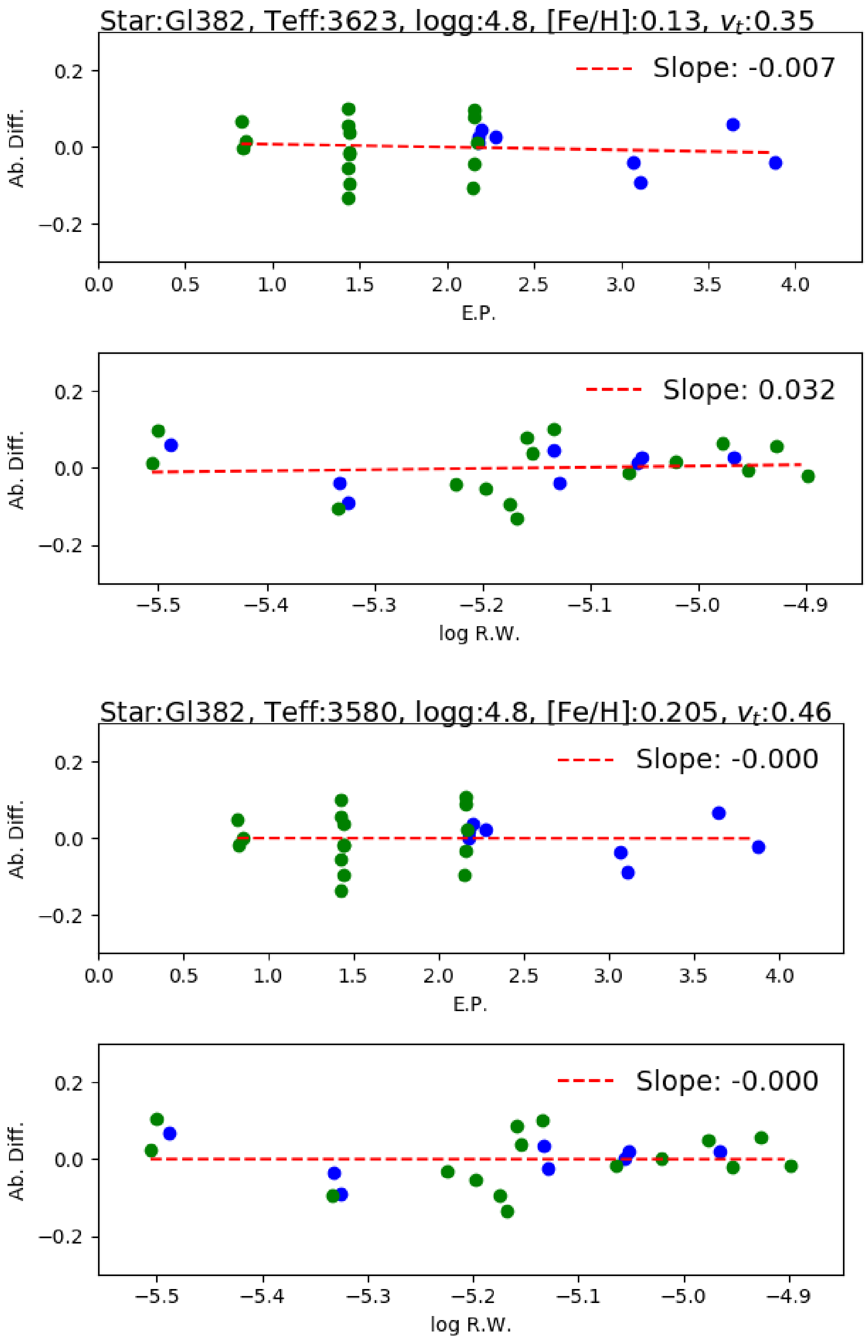

Figure 4.9: Example of applying MPIRA with the 24-line list to star Gl382. The blue datapoints refer to FeI lines, while the green ones to TiI lines. Upper pair of panels: The slopes of abundance differences when giving as input the reference parameters. Lower pair of panels: The slopes of abundance differences after convergence to the resulting parameters.

ones, as reported in Table 4.6, implying that our EW measurements were towards the correct direction to give accurate results.

However, by calculating the stellar parameters in other stars using the calibrated $\log(gf)$ values based on M0 Gl846, we noticed that all the other stars of later M types resulted in underestimated [Fe/H] and overestimated T_{eff} values. When we adjusted the $\log(gf)$ values using M2 Gl382 as calibrator star, the trend followed a similar pattern. Stars of later M types had results with [Fe/H] underestimated and T_{eff} overestimated, while the earlier M types gave opposite results, i.e. overestimated [Fe/H] and underestimated T_{eff}. Examples of the above are presented in Fig. 4.10.

Furthermore, we noticed that the abundances of the lines in other stars were reasonably following the trend of values being overestimated or underestimated, depending on earlier or later type compared to the calibrator star respectively. This trend can be seen in the example of line in Fig. 4.11, where for stars hotter than Gl382 (T_{eff} > 3623 K), the line abundances are overestimated, while for cooler stars (T_{eff} < 3623 K) the respective abundances are underestimated. This trend of abundance differences were noticed for most of the lines, both Fe and Ti ones.

Thus, it appears that as the blending in the spectral lines and the problem of a well-defined continuum become more significant towards later M types, calibrating the $\log(gf)$ values based on a specific M type creates a respective trend to other spectral types.

In general, we must keep in mind that we assume that our EW measurements for the calibrator star and the other stars are accurate. However, any overestimated or underestimated EWs for lines of our calibrator star, would affect their calibrated $\log(gf)$ values in a way that even if the EW measurements of other stars are correct, then their calculated abundances would end up overestimated or underestimated respectively. Similarly, if we measure correctly the EWs for our calibrator star, but then we overestimate or underestimate some lines for the other stars, then we will have again wrong results for those stars.

4.5.3 MPIRA with final 14-line list, results and uncertainties

Since our attempts of deriving more accurate stellar parameters were not fruitful by calibrating the $\log(gf)$ values of the 24 lines, eventually we returned to check again more strictly their figures of synthesis and we proceeded in excluding more lines that had minor

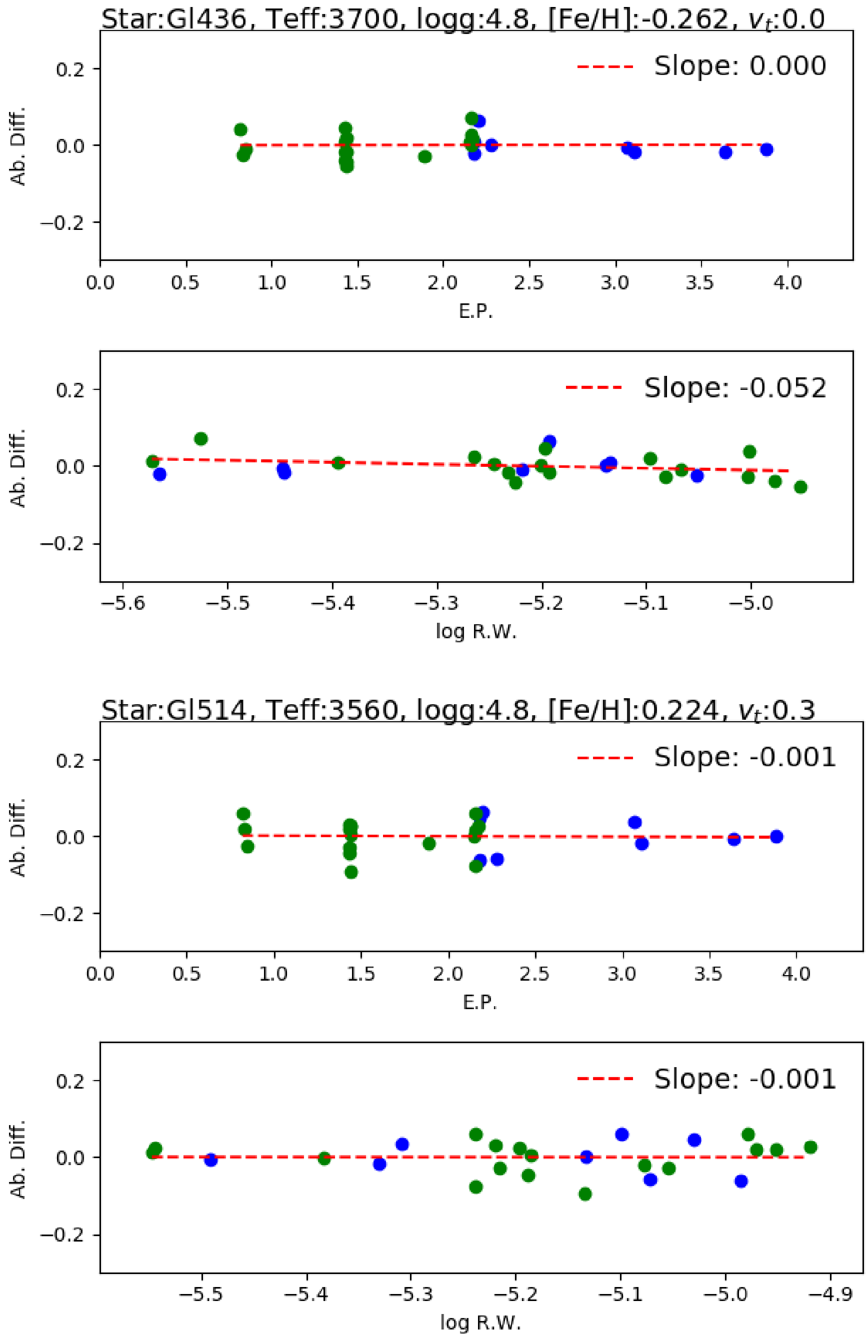

Figure 4.10: Example of overestimated and underestimated parameters due to $\log(gf)$ calibration using M2 Gl382 as calibrator. Upper pair of panels: The resulting parameters for M3 Gl436 which is of later type than the calibrator star (overestimated $T_{\rm eff}$ and underestimated [Fe/H]). Lower pair of panels: The resulting parameters for M1 Gl514 which is of earlier type than the calibrator star (underestimated $T_{\rm eff}$ and overestimated [Fe/H]).

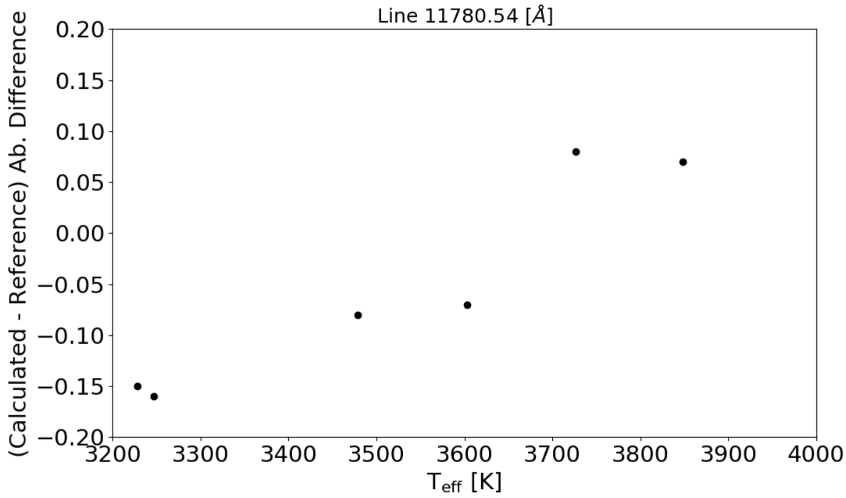

Figure 4.11: Example of abundance differences using $\log(gf)$ values calibrated based on M2 star Gl382, which has reference T_{eff} = 3623 K. Hotter stars have overestimated abundance compared to their reference values, while cooler stars have the same line with underestimated abundance, when $\log(gf)$ values are calibrated based on a star of different spectral type.

blends compared to those excluded at the first stage. These lines excluded at this final stage are labelled as ”2nd synth. cut” in Table B.1.

Thus, we restricted our line list to only 4 FeI and 10 TiI lines for which we trust sufficiently enough our manual measurements and used their $\log(gf)$ values from VALD, in order to avoid the emerging trends described above. Those lines finally used for the derivation of stellar parameters are labelled as ”applied” in Table B.1.

In Appendix D, we present our indicative manual way (referred as ”third way”) of measuring the selected lines applied in MPIRA. We present the measurements for the lines of M3 Gl436, since it was a star selected for synthesis too. In addition, its spectrum has more complicated features than the one of M0 Gl846 (also selected for synthesis), for which the measurements by a user should be more straight-forward because its continuum is better defined.

With this 14-line list we produced results for individual abundances and stellar atmospheric parameters with better accuracy and precision, as reported in Table 4.7. It is worth mentioning that eventually all the stars have reached convergence regarding v_t, having values between 0.14 and 0.95 km/s. We give an example of convergence to the final parameters for the star Gl514 in Fig. 4.12. The stars with the earliest M types, Gl846 and Gl514, have the closest agreement to their reference values of [Fe/H] and T_{eff}. In general, all stars (except the two very metal-poor ones) present T_{eff} differences between -62 and +62 K and [Fe/H] differences between -0.11 and +0.06 dex, as compared to their reference values adopted by Mann et al. (2015). On the other hand, regarding the greatest differences in [Fe/H] and T_{eff}, we notice that the two most metal-poor stars, Gl699 and Gl15A, are determined with significantly lower [Fe/H] values and greater T_{eff} values, as compared to their reference ones. The precision is greater than before, with the values of standard deviation for abundances varying between 0.02 and 0.09 dex and the dispersion increasing reasonably for the M4 star. In addition, we tested again the use of automatic ARES measurements for the EWs of our final line list, but the resulting parameters were once again wrong with severe underestimation of [Fe/H] and overestimation of T_{eff} values. So, we concluded that the use of manually measured EWs works optimally for our small line list in the NIR.

The comparison of our determinations with MPIRA to the reference values by Mann et al. (2015) are presented in Fig. 4.13. T_{eff} by MPIRA method has an average difference of 60 K and median difference of 51 K higher than values by Mann et al. (2015), with a standard deviation of 88 K. The average difference of [Fe/H] by MPIRA is -0.10 dex, but with a median difference of -0.05 dex and standard deviation of 0.14 dex, since the average one is significantly affected by the two metal-poor stars that MPIRA determines with considerably lower [Fe/H] values than Mann et al. (2015).

Finally, we constructed the error estimation process based on the method by Neuforge-Verheecke & Magain (1997). After we obtain the final parameters achieving convergence, we perturb v_t by 0.50 km/s. Based on the new set of parameters, the uncertainty of v_t is determined from the deviation in the slope of the least-squares fit of abundance differences versus the $\log RW$. Next, we perturb T_{eff} by 100 K and we calculate the new slope of abundance differences against excitation potential, taking into account also the contribution from the perturbation of v_t. The uncertainty of T_{eff} is determined from the deviation in the slope of the least-squares fit of abundance differences versus the excitation potential, in addition to the uncertainty in the slope due to the uncertainty of v_t. For the uncertainty of [Fe/H], we do the quadratic sum of the standard error of the mean (calculated as the standard deviation of [Fe/H] divided by the square root of the number of FeI lines), the contribution of the v_t error to [Fe/H] uncertainty and the contribution of the T_{eff} error to [Fe/H] uncertainty.

The uncertainties of final parameters are reported in Table 4.8. We notice that the uncertainties of [Fe/H] are between 0.07 and 0.13 dex, which are expected for M dwarfs in general. The uncertainties of T_{eff} are above 130 and below 200 K for most stars, with the exception of the two very metal-poor stars (Gl699 and Gl15A) which have T_{eff} errors of 303 and 215 K respectively. The uncertainties of v_t are between 0.20 and 0.55 km/s. Specifically, they vary from 0.20 to 0.35 km/s for the stars with spectral types from M0 to M2, while they grow around 0.50 km/s for the stars with spectral types from M3 to M4. The fact that we have very few lines that we can trust for measuring their EWs, makes our method sensitive when perturbing the parameters and thus the errors of T_{eff} and v_t grow considerably.

Table 4.7: Resulting stellar parameters and differences from reference values for M dwarfs in the NIR.

Star	T_{eff} [K]	T_{eff} Diff. [K]	[Fe/H] [dex]	[Fe/H] Diff. [dex]	v_t [km/s]	v_t Diff. [km/s]	STD FeI [dex]	STD TiI [dex]
Gl846	3848	0	0.00	-0.02	0.75	0.30	0.04	0.05
Gl514	3738	11	-0.06	0.03	0.87	0.52	0.02	0.03
Gl382	3685	62	0.02	-0.11	0.90	0.55	0.02	0.05
Gl15A	3830	227	-0.65	-0.35	0.41	0.06	0.02	0.05
Gl436	3530	51	-0.04	-0.05	0.14	-0.16	0.02	0.04
Gl876	3185	-62	0.23	0.06	0.18	-0.07	0.02	0.06
Gl699	3364	136	-0.67	-0.27	0.95	0.70	0.09	0.08

Table 4.8: Resulting stellar parameters with their calculated uncertainties for M dwarfs in the NIR.

Star	T_{eff} [K]	error T_{eff} [K]	[Fe/H] [dex]	error [Fe/H] [dex]	v_t [km/s]	error v_t [km/s]
Gl846	3848	$\pm$198	0.00	$\pm$0.13	0.75	$\pm$0.34
Gl514	3738	$\pm$131	-0.06	$\pm$0.07	0.87	$\pm$0.20
Gl382	3685	$\pm$134	0.02	$\pm$0.08	0.90	$\pm$0.25
Gl15A	3830	$\pm$215	-0.65	$\pm$0.08	0.41	$\pm$0.35
Gl436	3530	$\pm$157	-0.04	$\pm$0.08	0.14	$\pm$0.50
Gl876	3185	$\pm$184	0.23	$\pm$0.08	0.18	$\pm$0.51
Gl699	3364	$\pm$303	-0.67	$\pm$0.08	0.95	$\pm$0.55

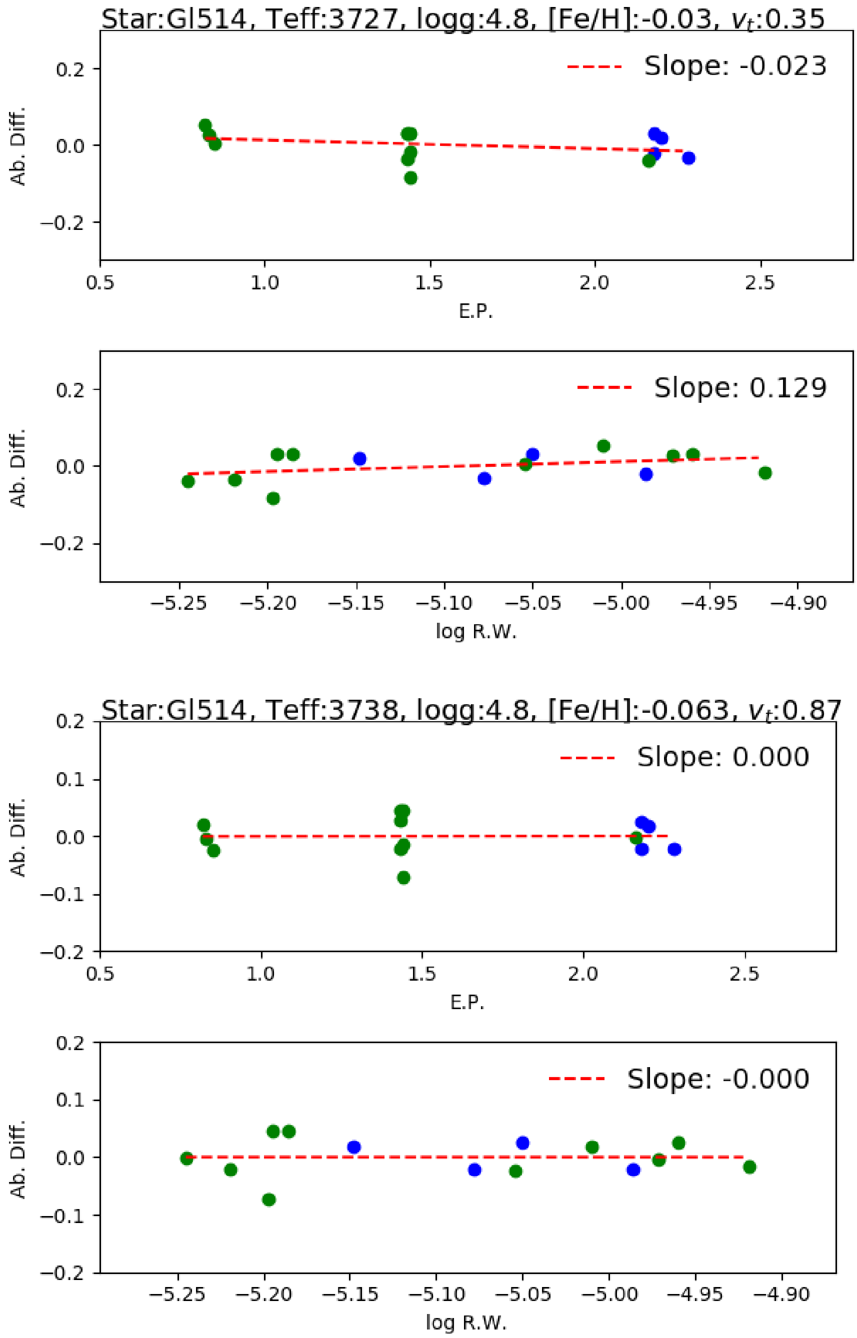

Figure 4.12: Example of applying MPIRA with the 14-line list to star Gl514. The blue datapoints refer to FeI lines, while the green ones to TiI lines. Upper pair of panels: The slopes of abundance differences when giving as input the reference parameters. Lower pair of panels: The slopes of abundance differences after convergence to the resulting parameters.

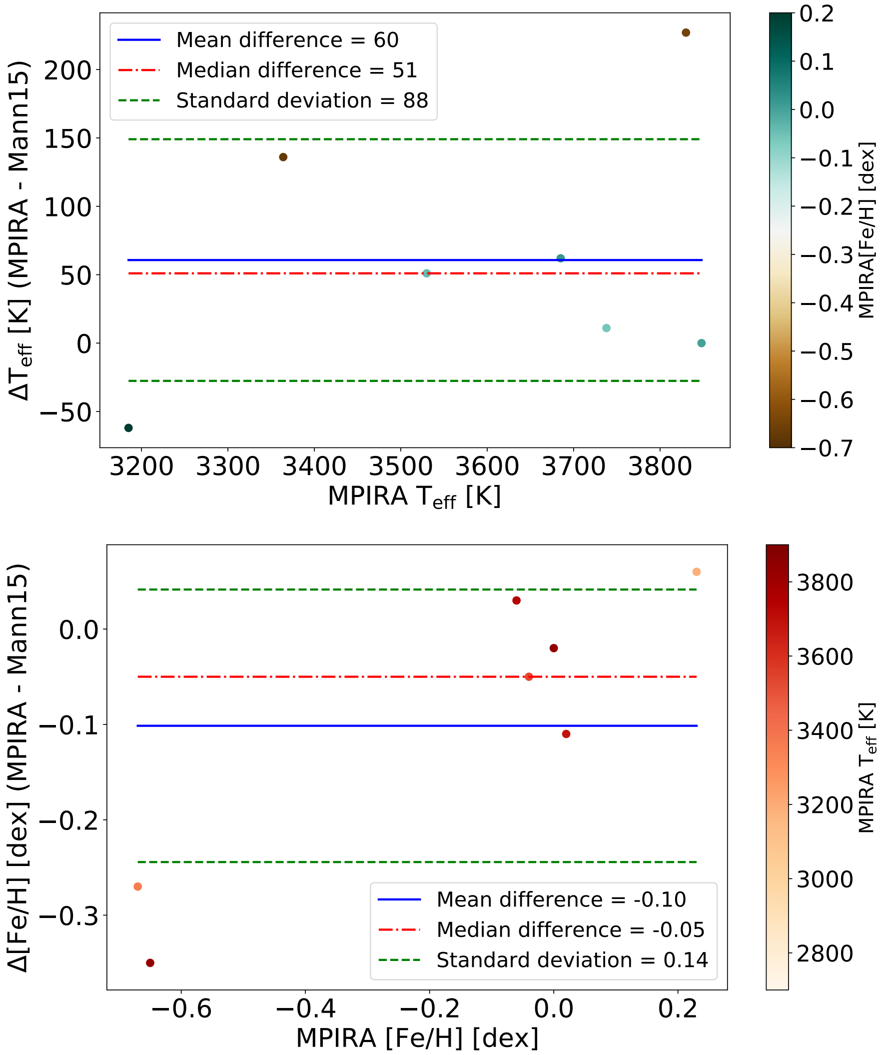

Figure 4.13: T_{eff} comparison (upper panel) and [Fe/H] comparison (lower panel) between between our results with MPIRA and Mann et al. (2015).

4.5.4 Comparison of results between MPIRA and ODUSSEAS

In Fig. 4.14 we compare our determinations applying MPIRA in the NIR to our determinations for the same stars applying ODUSSEAS in the optical. T_{eff} by MPIRA has average and median differences of 73 and 52 K respectively compared to the determinations by the new reference dataset of ODUSSEAS, with a standard deviation of 91 K. Regarding the uncertainties of the two methods, the lowest uncertainty of MPIRA is 131 K, which is higher than the highest typical uncertainties of ODUSSEAS.

The determinations of [Fe/H] are very close on average with a difference of 0.02 dex and a median difference of 0.04. However, the standard deviation is greater with a value of 0.11 dex. In the lower panel of Fig. 4.14, we notice the trend that MPIRA determines the metal-poor stars with even lower values than ODUSSEAS, while for the stars with determinations close to solar values and above, [Fe/H] results by MPIRA are quite higher than the results by ODUSSEAS. The uncertainties of MPIRA for [Fe/H] are between 0.07 and 0.13 dex, a range within which are also the total error budgets of ODUSSEAS. It seems that both methods underestimate [Fe/H], to an extent within typical uncertainties though, compared to studies in literature.

Overall, MPIRA seems to work considerably better for the earlier types of M dwarfs. This is reasonable, since we can measure more confidently the EWs of the lines, as they are less blended and the continuum can be defined with greater accuracy. In addition, it shows limitation in determining accurate results for stars with metallicity below -0.30 dex. The method could be tested further by making additional measurements and parameter determinations on a bigger sample of high-quality spectra in the NIR. Thus, we could select with more confidence the lines to be used, after examining them in more spectra.

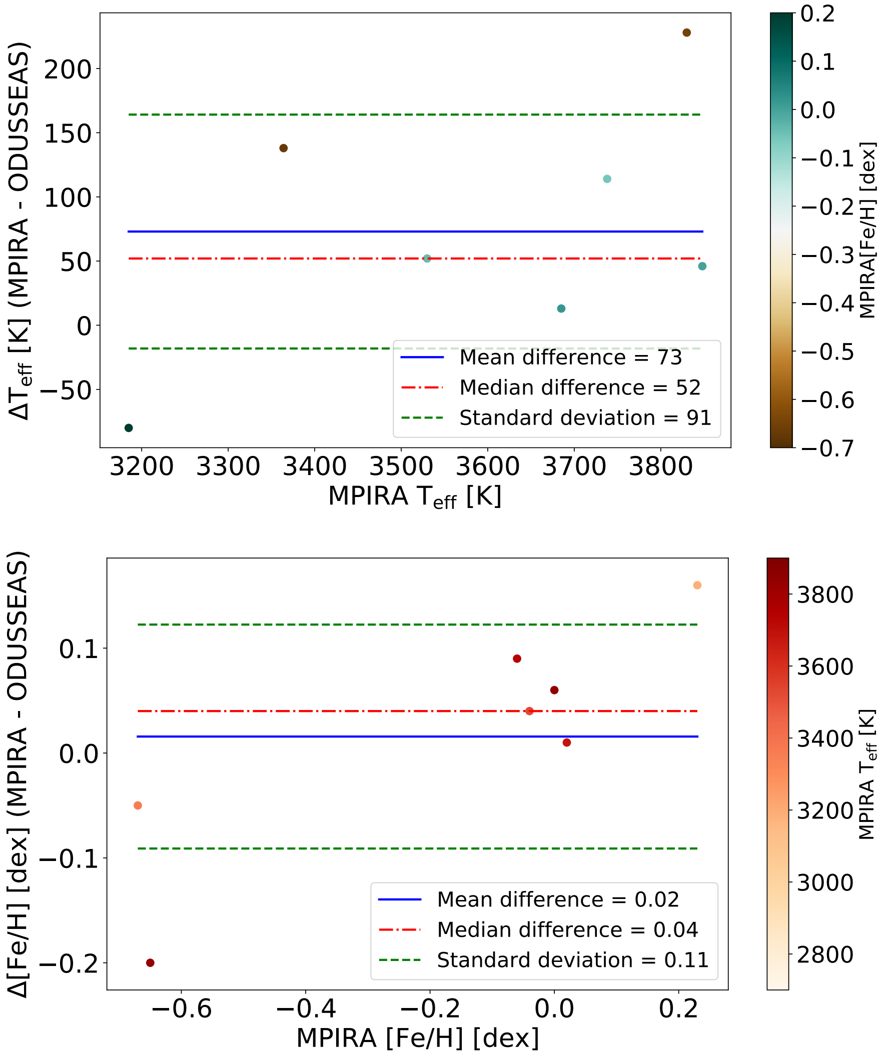

Figure 4.14: T_{eff} comparison (upper panel) and [Fe/H] comparison (lower panel) between our results with MPIRA and ODUSSEAS.

5. Conclusions

The motivation of the thesis was to develop methods of deriving stellar atmospheric parameters for M dwarf stars, given their importance in terms of being planetary hosts and of being the most abundant stars in the Galaxy. The main goal of the thesis was to create tools which can determine the parameters of M dwarfs in a consistent and accurate way, since current methods present parameters with disagreements among them.

Given the natural difficulties in the analysis of M-dwarf spectra, our goal was to explore the strong potential of machine learning, which offers techniques of advanced statistics in cases where current methods with traditional approaches present limits. Therefore, ODUSSEAS has been an innovative computational tool, available for stellar characterization in the optical, operating successfully for a variety of resolutions.

Regarding the near-infrared, our goal was to expand the EW method towards this wavelength domain that suffers less from line contamination compared to the optical one. Our goal, modifying the traditional approach and developing MPIRA accordingly for M dwarfs, was to examine its accuracy of determining stellar parameters using NIR spectra, that are becoming widely available to the community.

5.1. Work in optical

5.1.1 Summary of ODUSSEAS

We developed the machine learning tool ODUSSEAS for the derivation of T_{eff} and [Fe/H] in M dwarf stars, whose spectra are of varying resolution at wavelengths ranging between 530 and 690 nm. We provided a detailed explanation of how ODUSSEAS was built and how it works.

We created our own function to compute the pseudo EWs of lines and compared it to a similar method. We provided pre-computed reference datasets with pseudo EWs for different resolutions by applying convolution to our HARPS reference dataset.

We tested different regression methods of machine learning, in order to select the one that performs better in the case of M-dwarf spectra. We also tested different wavelength regions to examine with which part of the spectrum our tool has the highest efficiency. We presented the results of the tests we performed and we examined their accuracy and precision on spectra with resolutions that vary from 115000 down to 48000. We also measured spectra by degrading the S/N value and we conclude that they are required to have a S/N of above 20 for optimal predictions. Moreover, we validated our [Fe/H] determinations with measurements on binary systems.

In its original version, our tool operates with high machine learning scores of around 0.94 and achieves predictions of significantly high precision with mean absolute errors of $\sim$30 K for T_{eff} and $\sim$0.04 dex for [Fe/H]. Taking into consideration the intrinsic uncertainties of the reference parameters and injecting them accordingly, our models have maximum uncertainties of $\sim$65 K for T_{eff} and $\sim$0.10 dex for [Fe/H] when applied to the highest resolution, while $\sim$80 K for T_{eff} and $\sim$0.13 dex for [Fe/H] when applied to the lowest resolution, which are within the typical uncertainties for M dwarfs.

After the comparative study with other methods applied to the same set of spectra, we decided to create a new reference dataset for our tool, because our initial one was consistently underestimating T_{eff}. By upgrading our tool with the new reference dataset of T_{eff} based on interferometry and [Fe/H] based on updated parallaxes, we gain better accuracy in our results of T_{eff} as compared to literature, though the maximum model uncertainties are a bit higher than before ($\sim$90 K for T_{eff} and $\sim$0.11 dex for [Fe/H] when applied to the highest resolution, while $\sim$99 K for T_{eff} and $\sim$0.13 dex for [Fe/H] when applied to the lowest resolution), but still within the expected error range for M dwarfs.

Next, we proceeded to determine parameters for the planet-host M dwarfs reported in SWEET-Cat. Our parameters for stars with spectra from different instruments have consistent values among them, with standard deviation of 30 K for T_{eff} and 0.03 dex for [Fe/H] compared to the average of their results from the common spectra. We also compared our results with literature studies for stars in common, which follow different methods. We verified that our T_{eff} values are eventually compatible with the ones from other methods. Finally, we performed an analysis of the planetary mass distribution in relation with the stellar [Fe/H] for those planet hosts. We reported that the correlation of high-mass planets increasing at high stellar metallicity appears in M-dwarf systems too, in agreement with the core-accretion scenario of planet formation.

Our tool is valid for M dwarfs in the intervals 2700 to 4000 K for T_{eff} and -0.80 to 0.30 dex for [Fe/H], except from very active or young stars. ODUSSEAS can be used by downloading the files from `https://github.com/AlexandrosAntoniadis/ODUSSEAS`, after reading the README instructions for clarifying the technical details.

5.1.2 Further publications as co-author applying ODUSSEAS

As the developer of ODUSSEAS, apart from the publication of the tool (Antoniadis-Karnavas et al., 2020) and the work by Passegger et al. (2022) already discussed in Sect. 3.5.2, I have also participated in the following studies as co-author, applying the tool for stellar characterization.

Demangeon et al. (2021) reported the detection of the lowest-mass planet measured so far using radial velocities: L98-59 b, a rocky planet with half the mass of Venus. It is part of a system composed of a bright M dwarf (L98-59A) with three known transiting terrestrial planets. The discovery of a fourth non-transiting planet and indications for the presence of a fifth non-transiting terrestrial planet were reported. This system is destined to become a corner stone for comparative exoplanetology of terrestrial planets. It offers a unique opportunity to study the diversity of warm terrestrial planets without the unknowns associated with different host stars. I applied ODUSSEAS in its original version, as one of four methods, to the ESPRESSO spectrum of the star. I derived T_{eff} equal to 3280$\pm$65 K and [Fe/H] equal to -0.34$\pm$10 dex.

Cortés-Zuleta et al. (2023) characterized the magnetic field and stellar activity of the early, moderately active M dwarf Gl205 in the optical and NIR domains. High-precision quasi-simultaneous spectra were obtained in the optical and NIR with the SOPHIE spectrograph and SPIRou spectropolarimeter. The RV variations observed in Gl205 are due to stellar activity, with a complex evolution and different expressions in the optical and NIR revealed thanks to an extensive follow up. Spectropolarimetry remains the best technique to constrain the stellar rotation period over standard activity indicators, particularly for moderately active M dwarfs. In this study, I applied the new upgraded version of ODUSSEAS to analyze the SOPHIE spectrum of the star, reporting T_{eff} equal to 3878$\pm$81 K and [Fe/H] equal to 0.21$\pm$0.06 dex.

Castro-González et al. (2023) confirmed and characterized the TESS planet candidate TOI-244.01, which orbits the M2.5 M dwarf GJ1018 with an orbital period of 7.4 days. Markov Chain Monte Carlo methods were used to model 57 precise radial velocity measurements acquired by the ESPRESSO spectrograph together with TESS photometry and complementary HARPS data. TOI-244 b was found to be a super-Earth with a radius of 1.52$\pm$0.12 $R_{\oplus}$ and a mass of 2.68$\pm$0.30 $M_{\oplus}$. These values correspond to a density of 4.2$\pm$1.1 g/cm^3, which is below what would be expected for an Earth-like composition. I applied ODUSSEAS with its new version to the ESPRESSO spectrum of this star, serving as a second independent method of determination. I obtained T_{eff} equal to 3419±92 K and [Fe/H] equal to -0.03±0.11 dex.

5.1.3 Future Improvements of ODUSSEAS

ODUSSEAS has many advantages that make it a useful tool for the community. It can operate simultaneously for spectra obtained by different spectrographs, as it applies the reference datasets of the respective resolution to each of them. The process is highly automatic and it needs about one minute per star to provide the results. Moreover, it has increased the precision of the models compared to traditional methods of calibration applied to the same dataset.

However, the method is tied to any systematics of its reference datasets, since they affect via supervised machine learning the determinations on new spectra. As new techniques for parameter determination become more accurate and precise and as more spectra become available to us, their homogeneously derived parameters can be correlated with their pseudo EWs. Therefore, we take into account the potential creation of an even more improved reference dataset for our machine learning tool, that would consist of more reference stars, covering a wider parameter range and of reference stellar parameters derived with greater accuracy and precision.

5.2. Work in near-infrared

5.2.1 Summary of method MPIRA

We developed MPIRA tool for the determination of T_{eff}, [Fe/H] and v_t in M dwarfs at the NIR domain. We described the process that led to the creation of our method. MPIRA uses grid of MARCS model atmospheres and MOOG software for the computation of FeI and TiI abundances based on our EW measurements. We apply the principle of balance between abundance differences from average against excitation potential for T_{eff} and against $\log RW$ for v_t, while the input [Fe/H] being equal to the output [Fe/H].

As first step, we measured with ARES an initial line list, which was constructed based on K stars, in order to explore the possibility of using it towards M dwarfs. Since most lines were obviously blended for M dwarfs, we proceeded in downloading from VALD Fe and Ti lines present in M-dwarf spectra. We did a first examination by eye of those 260 lines in our spectra, in order to select those ones that did not have obvious blends that break their symmetric shape. Thus, we gathered 56 lines to calculate abundances in our M dwarf sample applying ARES+MOOG. There was severe underestimation of [Fe/H] values for most stars compared to the reference ones selected from literature (mean difference of -0.28 dex).

Consequently, we did synthesis of all 56 lines alone and their surrounding region separately, to identify blends in the lines not visible before, as well as to examine whether the observed lines match with the synthetic ones. We also discarded commonly wide lines, for which the Gaussian fitting is not a proper way to measure their EWs. After the first cut, we kept 24 lines and measured again the abundances with automatic ARES+MOOG process. Since the results had again a systematic mean underestimation of -0.21 dex for [Fe/H], we explored and compared ways of measuring the EWs manually. Thus, we concluded that measuring the line of interest alone with its continuum placed at the level implied by surrounding region, is the proper way to get abundances compatible with the reference values. However, we can not trust completely the results, because we might get higher abundances for the lines of interest by not considering all the lines below the surrounding continuum. On the other hand, when we did considered all the absorption lines in the region, the abundances of the lines of interest were consistently underestimated. So, the method has clear limitations, as only few lines in M dwarfs are really isolated from blends.

After having a preferable way to measure EWs and abundances that it agreed in general with the expected abundances, we applied MPIRA to determine T_{eff}, [Fe/H] and v_t parameters, while keeping the $\log g$ parameter fixed. Moreover, in our attempt to improve our results, we tested calibrated values of $\log(gf)$, but we noticed that the resulting parameters for other stars had overestimated or underestimated values depending on their spectral type. Finally, we shortened our line list to only 14 lines with the least blends by doing a more strict selection from our synthetic figures and applied their $\log(gf)$ values from VALD.

Our final determinations have differences within $\pm$62 K for T_{eff} and within $\pm$0.11 dex for [Fe/H], compared to reference values, for all stars except from the two very metal-poor ones. Those two stars (Gl15A and Gl699) give results with significantly overestimated T_{eff} and underestimated [Fe/H]. Regarding, v_t the results for all stars are between 0.14 and 0.95 km/s, which are within the expected range for M dwarfs. The derived uncertainties for [Fe/H] are between 0.07 and 0.13 dex, as our measurements for the 14 well-shaped lines are quite precise compared to the rest of the lines that we eventually discarded. However, the uncertainties for T_{eff} and v_t are above 130 K and 0.20 km/s respectively, due to the fact that our method is very sensitive to perturbations of the values since the measured lines are very few and the slopes get easily affected. Finally, we compared the determinations between MPIRA and ODUSSEAS. The standard deviation of the parameter differences is within the range of uncertainties that our methods have.

5.2.2 Future Improvements of MPIRA

MPIRA has the advantage that determines stellar parameters without the need of a reference dataset, that would propagate its systematics to the results, as it happens with methods based on several kinds of calibration.

However, it has shown the limited accuracy and precision of the EW measurements and the methods based on this concept, for the M dwarfs. It is limited by the fact that there are not many FeI and TiI lines that remain unaffected by blending of other elements, so the small number of applicable lines causes greater errors than similar methods for FGK stars. We reported though, that it is preferable to use a small line list with quite accurate EW measurements, rather than bigger line lists with uncertain measurements that cause random deviations from the true values. Another disadvantage of this method, is the level of subjectivity when measuring the EWs of the lines, even if a certain way is followed in principle. Although we provide examples of how we measure eventually the EWs in our method, it is doubtful that any user could reproduce the exact values for all the lines. The whole method could potentially improve significantly if we had FGK+M binaries available with NIR spectra. Thus, we could follow a process of selecting lines by already knowing the actual metallicity of the M dwarf and compare with the value we measure, because it should be the same as the FGK companion. There would be no need to use values directly derived for M dwarfs from literature as references, which can also suffer from systematics. Instead, results for FGK stars are much more in agreement between different methods so we could trust their values, in our attempt to find the proper line list for M dwarfs, so we can measure their EWs accurately in a consistent way. Furthermore, the atomic data provided by VALD are prone to errors. Better knowledge on those values would be a major upgrade for our method. Finally, the application of PHOENIX models would provide an interesting comparison in our search of deriving more accurate abundances for the coolest M dwarfs.

A. Reference datasets of ODUSSEAS

Here, we present the reference datasets which are available to be applied for training and testing the machine learning models of ODUSSEAS.

Table A.1 is the initial photometric reference dataset that was originally used in the tool. T_{eff} and [Fe/H] were determined by Casagrande et al. (2008) and Neves et al. (2012) respectively.

Table A.2 is the new reference dataset that was added in the new version of the tool. T_{eff} was derived based on interferometry. 43 stars were determined by Khata et al. (2021) and the last 4 stars at the bottom of the table were determined by Rabus et al. (2019). [Fe/H] was determined by applying the relation from Neves et al. (2012) with updated parallaxes.

Among the stars in common between the two reference datasets, the average difference between the new reference and the old reference scale is 151 K for T_{eff} and -0.01 dex for [Fe/H].

Table A.1: The original reference dataset of ODUSSEAS. T_{eff} and [Fe/H] were determined by Casagrande et al. (2008) and Neves et al. (2012) respectively.

Star	[Fe/H] [dex]	T_{eff} [K]
Gl1	-0.40	3528
Gl54.1	-0.40	2901
Gl87	-0.30	3565
Gl105B	-0.14	3054
HIP12961	-0.12	3904
LP771-95A	-0.51	3393
Gl163	0.00	3223
Gl176	0.02	3369
Gl179	0.14	3076
Gl191	-0.79	3679
Gl205	0.17	3497
Gl213	-0.19	3026
Gl229	-0.04	3586

continued

Star	[Fe/H] [dex]	T_{eff} [K]
HIP31293	-0.04	3312
HIP31292	-0.11	3158
Gl250B	-0.09	3369
Gl273	-0.05	3107
Gl300	0.09	2965
Gl2066	-0.09	3388
Gl317	0.22	3130
Gl341	-0.14	3633
Gl1125	-0.15	3162
Gl357	-0.30	3335
Gl358	0.01	3240
Gl367	-0.09	3452
Gl382	0.04	3429
Gl393	-0.13	3396
Gl3634	-0.02	3332
Gl413.1	-0.06	3373
Gl433	-0.13	3450
Gl436	0.01	3277
Gl438	-0.31	3536
Gl447	-0.23	2952
Gl465	-0.54	3382
Gl479	0.05	3238
Gl514	-0.13	3574
Gl526	-0.18	3545
Gl536	-0.13	3546
Gl555	0.13	2987
Gl569A	0.16	3235
Gl581	-0.18	3203
Gl588	0.07	3284
Gl618A	-0.05	3242
Gl628	-0.05	3107

continued

Star	[Fe/H] [dex]	T_{eff} [K]
Gl1214	0.03	2856
Gl667C	-0.47	3431
Gl674	-0.18	3284
Gl676A	0.10	3734
Gl678.1A	-0.10	3611
Gl680	-0.07	3395
Gl682	0.09	3002
Gl686	-0.29	3542
Gl693	-0.28	3188
Gl699	-0.59	3094
Gl701	-0.20	3535
Gl752A	0.04	3336
Gl832	-0.17	3450
Gl846	-0.08	3682
Gl849	0.24	3200
Gl876	0.14	3059
Gl877	-0.01	3266
Gl880	0.05	3488
Gl887	-0.20	3560
Gl908	-0.38	3587
LTT9759	0.17	3316

Table A.2: The new reference dataset of the upgraded ODUSSEAS version. T_{eff} was derived based on interferometry. 43 stars were determined by Khata et al. (2021) and the last 4 stars on the bottom of the table were determined by Rabus et al. (2019). [Fe/H] was determined by applying the relation from Neves et al. (2012) with updated parallaxes.

Star	[Fe/H] [dex]	T_{eff} [K]
Gl54.1	-0.42	2900
Gl87	-0.31	3604

continued

Star	[Fe/H] [dex]	T_{eff} [K]
Gl105B	-0.14	3251
Gl176	0.00	3590
Gl179	0.13	3382
Gl205	0.10	3813
Gl213	-0.24	3066
Gl229	-0.07	3796
Gl273	-0.07	3256
Gl300	0.09	3106
Gl2066	-0.12	3597
Gl1125	-0.15	3328
Gl357	-0.28	3395
Gl382	0.01	3672
Gl393	-0.14	3569
Gl436	-0.04	3401
Gl465	-0.56	3571
Gl514	-0.15	3671
Gl526	-0.15	3664
Gl536	-0.12	3674
Gl555	0.13	3258
Gl581	-0.20	3344
Gl628	-0.06	3362
Gl678.1A	-0.05	3704
Gl686	-0.30	3670
Gl699	-0.61	3256
Gl701	-0.22	3646
Gl752A	0.02	3538
Gl846	-0.07	3810
Gl849	0.19	3516
Gl876	0.13	3202
Gl880	0.03	3703
Gl908	-0.40	3475

continued

Star	[Fe/H] [dex]	T_{eff} [K]
Gl1129	0.00	3112
Gl1256	-0.05	2992
Gl1265	-0.21	3045
Gl203	-0.33	3227
Gl299	-0.65	3246
Gl402	0.02	3077
Gl480.1	-0.54	3373
Gl486	-0.01	3329
Gl643	-0.32	3243
LP816-60	-0.11	3071
Gl1	-0.42	3616
Gl674	-0.19	3409
Gl832	-0.21	3512
Gl887	-0.29	3692

B. NIR line list

The initial NIR line list that we constructed for the M Dwarf stars, consisting of 56 FeI and TiI lines, is presented in Table B.1. The lines which are finally used in the method for the determination of stellar parameters, are labelled as "applied". The lines that they have too wide wings, so that a Gaussian fit cannot properly measure the actual EW and thus lead to the correct abundance, having EWs above 150 mÅ for most of the stars examined, are labelled as "wide" and are excluded. The lines that suffer from blending and severe continuum contamination with other lines, are labelled as "1st synth. cut". Similarly, the lines that have blending that eventually prevents a safe calculation of their abundance are marked as "2nd synth. cut". Those lines are also excluded from the final selection.

Table B.1: The constructed NIR line list and final selection

Elem.	Wavelength(Å)	Excit.(eV)	$\log(gf)$	final selection
FeI	9738.57	4.99	0.150	1st synth. cut
FeI	10195.10	2.73	-3.580	1st synth. cut
FeI	10340.88	2.20	-3.577	applied
FeI	10395.79	2.18	-3.393	applied
FeI	10469.65	3.88	-1.184	2nd synth. cut
FeI	10783.05	3.11	-2.567	2nd synth. cut
FeI	10896.30	3.07	-2.694	2nd synth. cut
FeI	11119.79	2.85	-2.202	1st synth. cut
FeI	11374.08	2.18	-3.235	applied
FeI	11422.32	2.20	-2.700	wide
FeI	11439.12	2.84	-1.751	wide
FeI	11593.59	2.22	-2.448	wide
FeI	11783.26	2.83	-1.574	wide
FeI	11882.84	2.20	-1.668	1st synth. cut
FeI	12556.99	2.28	-3.626	1st synth. cut
FeI	12807.15	3.64	-2.452	2nd synth. cut
FeI	12879.76	2.28	-3.458	applied
FeI	16246.46	6.28	0.054	1st synth. cut

continued

Elem.	Wavelength(Å)	Excit.(eV)	$\log(gf)$	final selection
TiI	9688.87	0.81	-1.610	wide
TiI	9705.66	0.83	-1.009	wide
TiI	9718.96	1.50	-1.181	1st synth. cut
TiI	9728.40	0.82	-1.206	wide
TiI	9743.60	0.81	-1.306	wide
TiI	9770.30	0.85	-1.581	wide
TiI	9787.68	0.83	-1.444	wide
TiI	9832.14	1.89	-1.130	1st synth. cut
TiI	10003.08	2.16	-1.210	2nd synth. cut
TiI	10048.82	1.44	-1.930	2nd synth. cut
TiI	10057.73	2.17	-0.990	1st synth. cut
TiI	10059.90	1.43	-2.080	2nd synth. cut
TiI	10066.51	2.16	-1.850	2nd synth. cut
TiI	10120.89	2.17	-1.760	2nd synth. cut
TiI	10396.80	0.85	-1.539	wide
TiI	10496.11	0.84	-1.651	wide
TiI	10552.96	2.25	-1.573	1st synth. cut
TiI	10565.95	2.24	-1.777	1st synth. cut
TiI	10584.63	0.83	-1.775	wide
TiI	10607.71	0.85	-2.697	applied
TiI	10661.62	0.82	-1.915	wide
TiI	10732.86	0.83	-2.515	applied
TiI	10774.86	0.82	-2.666	applied
TiI	11780.54	1.44	-2.170	applied
TiI	11797.18	1.43	-2.280	applied
TiI	11892.87	1.43	-1.730	applied
TiI	11949.55	1.44	-1.570	applied
TiI	12600.28	1.44	-2.320	applied
TiI	12671.09	1.43	-2.360	applied
TiI	12811.48	2.16	-1.390	applied
TiI	12821.67	1.46	-1.190	wide

continued

Elem.	Wavelength(Å)	Excit.(eV)	$\log(gf)$	final selection
TiI	12831.44	1.43	-1.490	wide
TiI	12847.03	1.44	-1.330	wide
TiI	12919.90	2.15	-1.560	2nd synth. cut
TiI	13077.26	1.46	-2.220	1st synth. cut
TiI	15543.76	1.88	-1.080	wide
TiI	15715.57	1.87	-1.200	wide
TiI	16635.16	2.34	-1.582	1st synth. cut

C. Synthesis of NIR lines

In Fig. C.1 to Fig. C.14, we present the synthesis of the lines that we finally apply to our method.

In Fig. C.15 to Fig. C.24, we present the synthesis of the lines that we excluded at the ”2nd synth. cut” stage of refining the list.

Example of line that was discarded from the ”1st synth. cut” stage was given in the main text of Chapter 4.

All figures include panels with each line alone and the region without the target line, for stars M0 Gl846 and M3 Gl436.

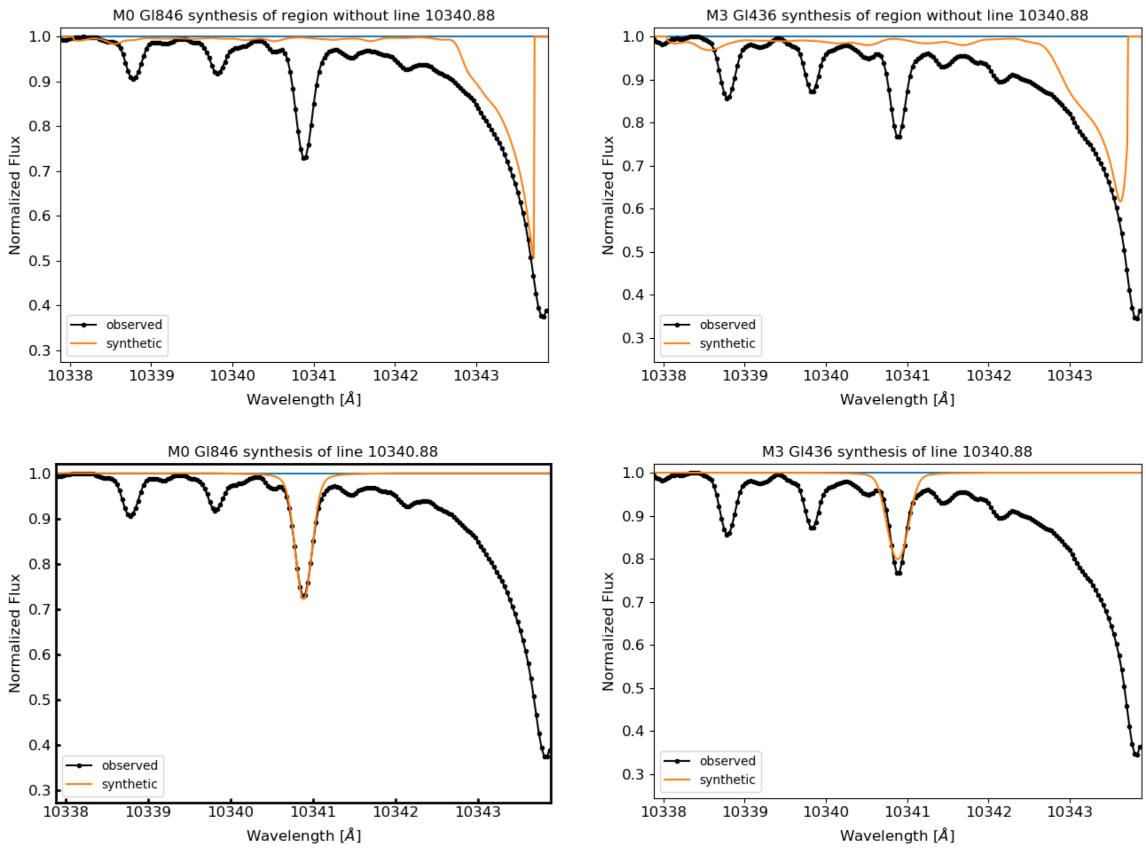

Figure C.1: Synthesis for applied Fe line 10340.88 Å.

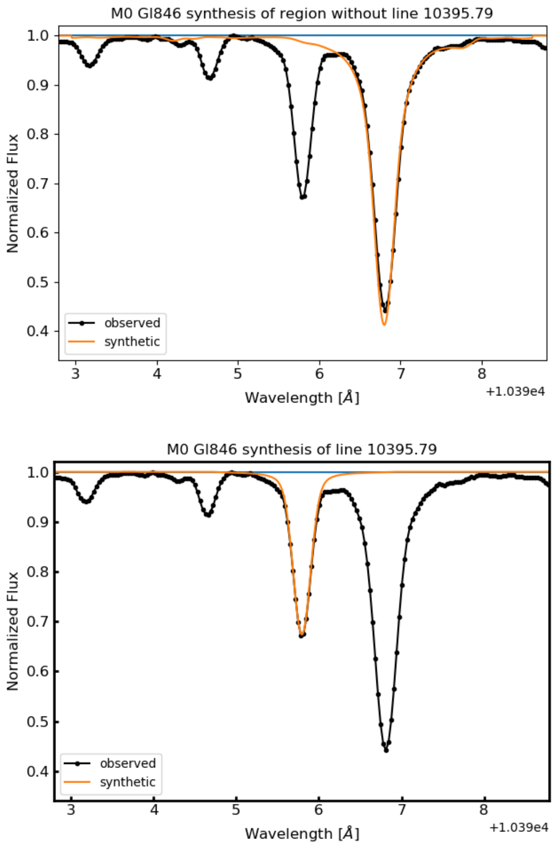

Figure C.2: Synthesis for applied Fe line 10395.79 Å.

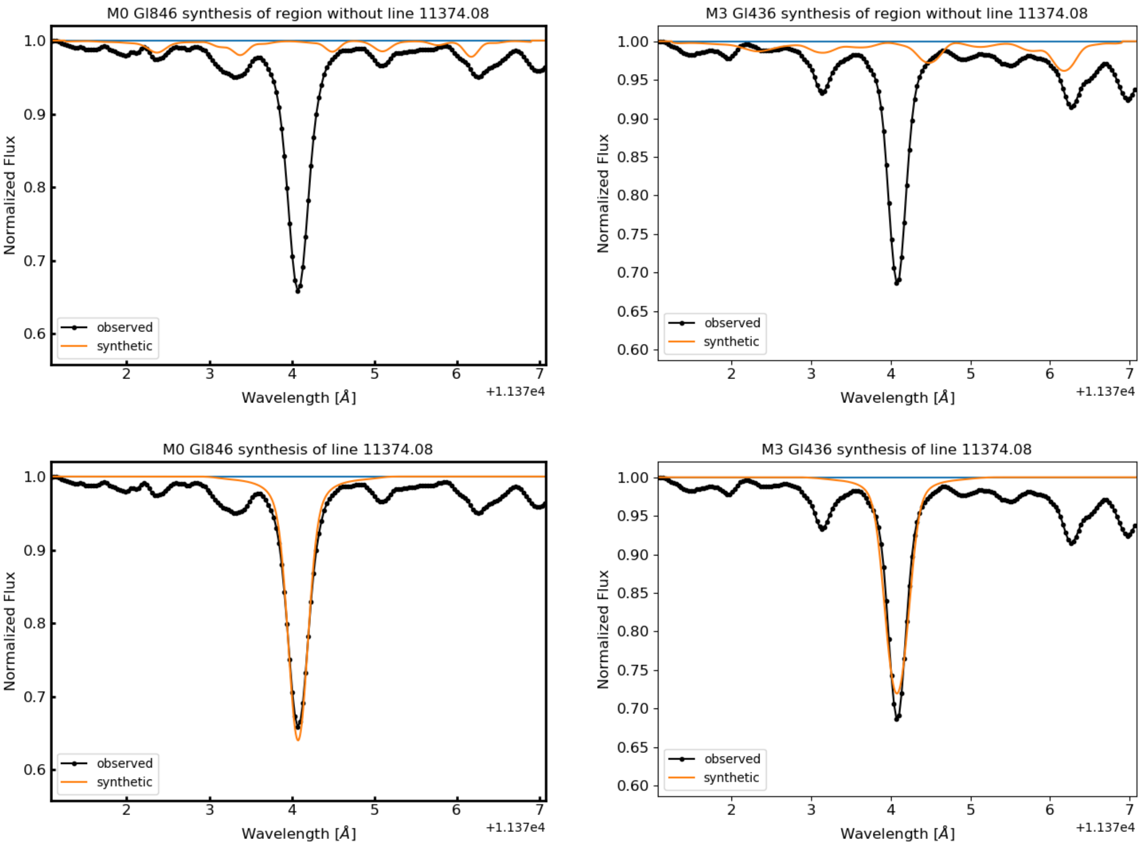

Figure C.3: Synthesis for applied Fe line 11374.08 Å.

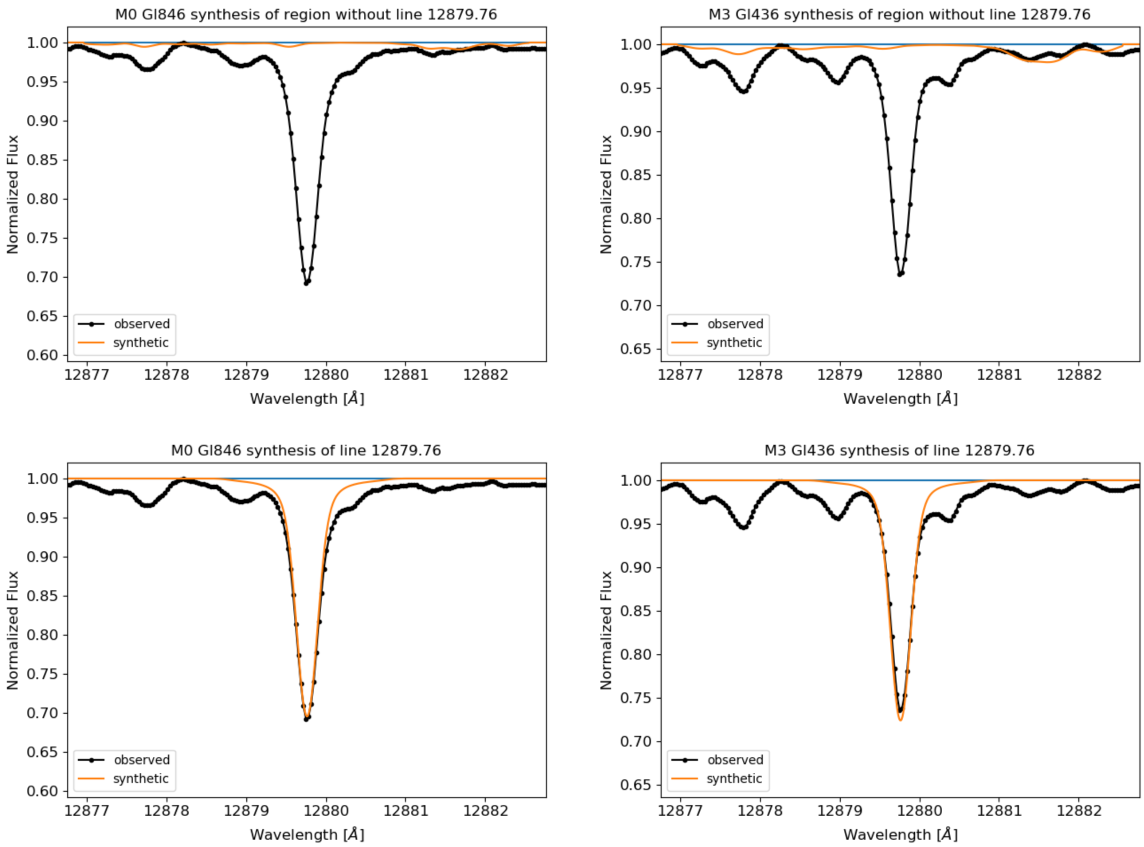

Figure C.4: Synthesis for applied Fe line 12879.76 Å.

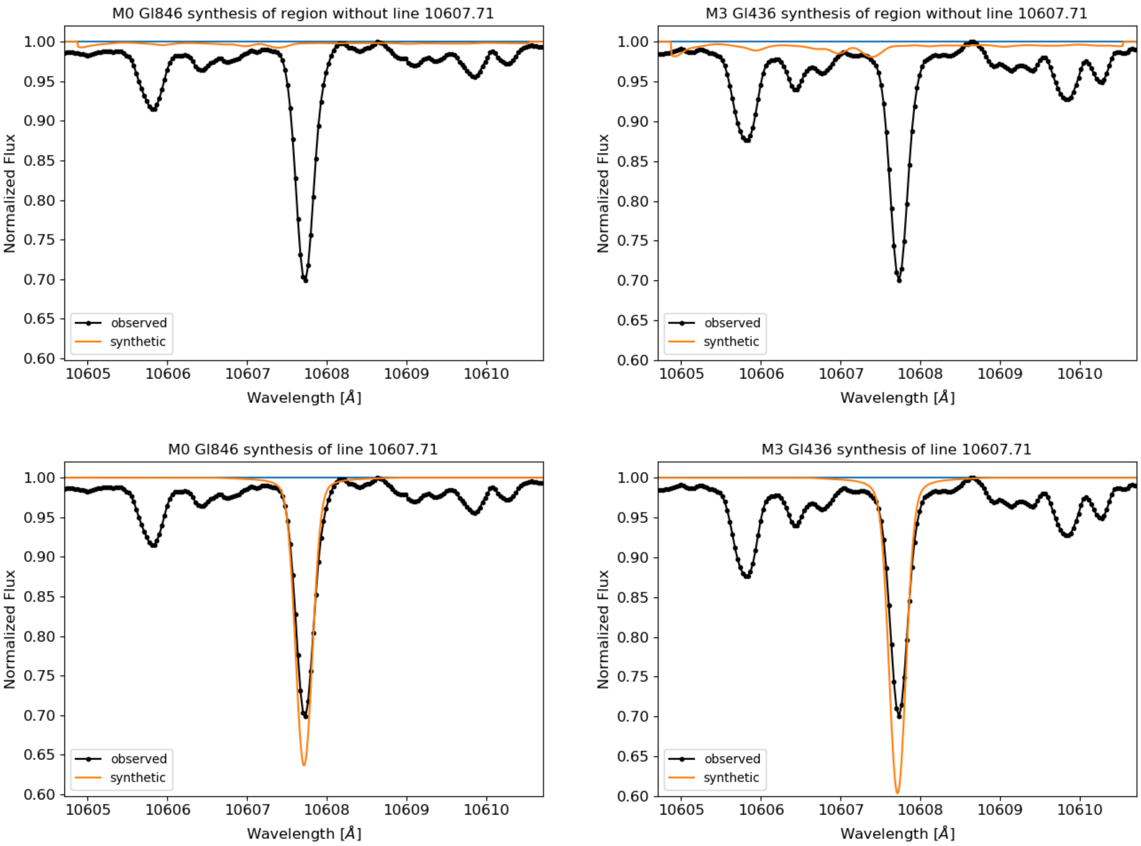

Figure C.5: Synthesis for applied Ti line 10607.71 Å.

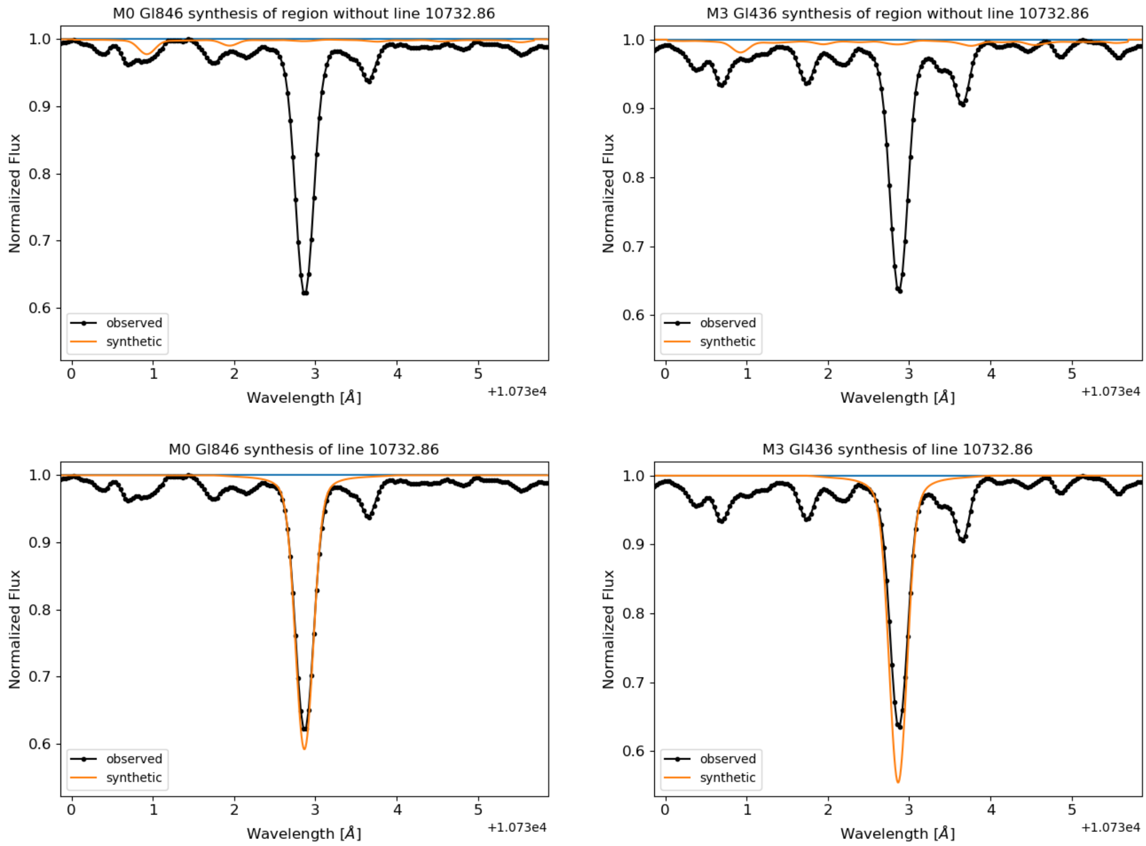

Figure C.6: Synthesis for applied Ti line 10732.86 Å.

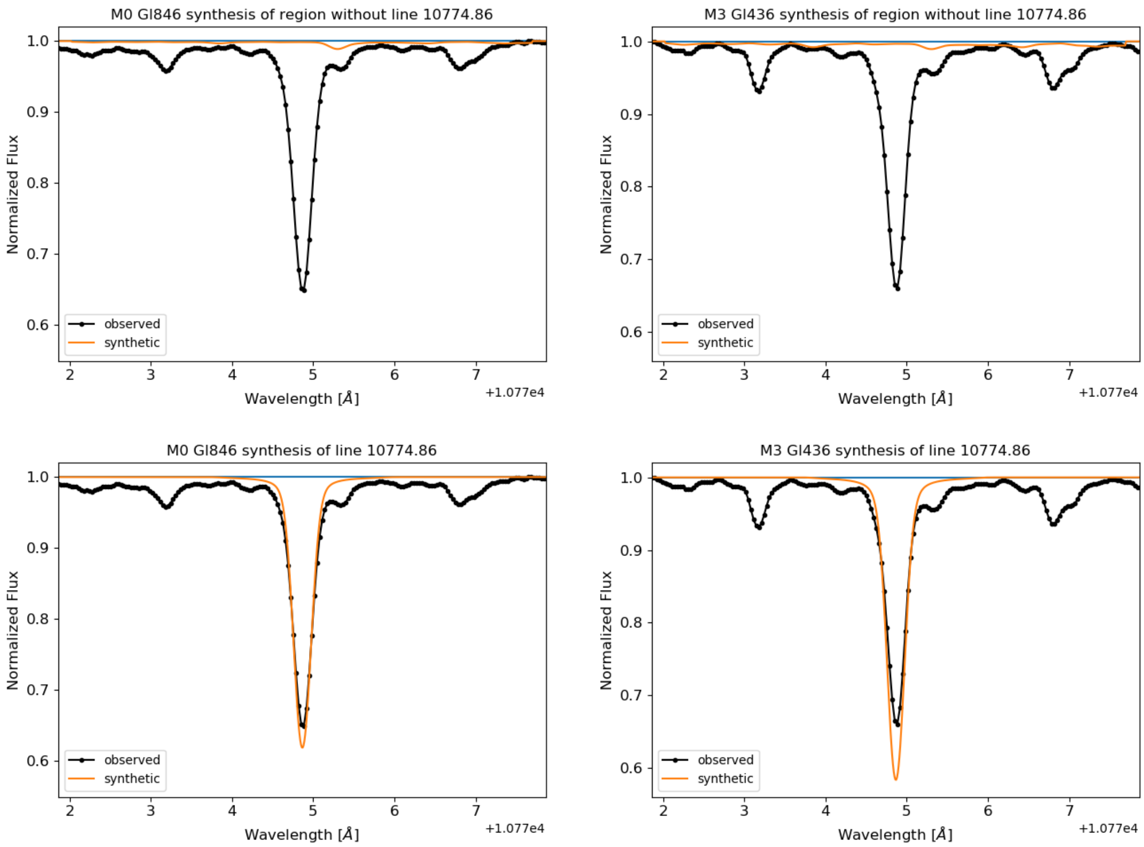

Figure C.7: Synthesis for applied Ti line 10774.86 Å.

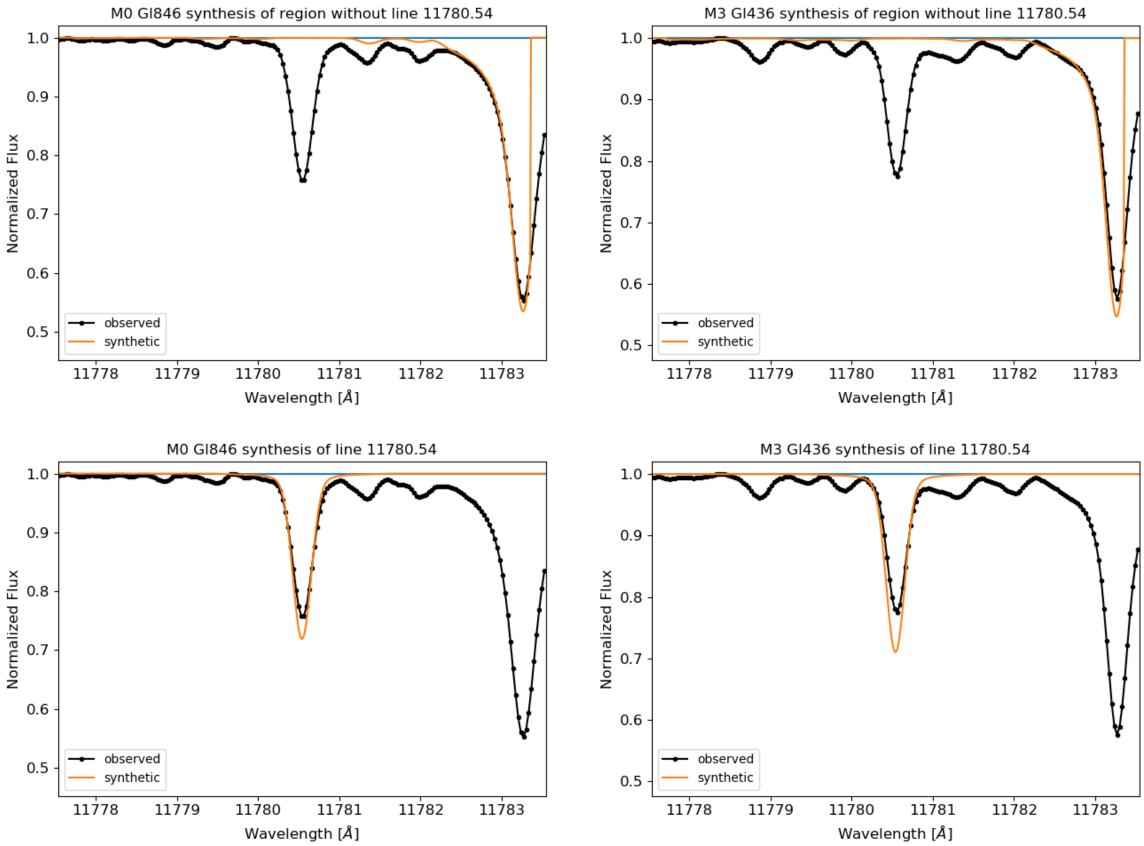

Figure C.8: Synthesis for applied Ti line 11780.54 Å.

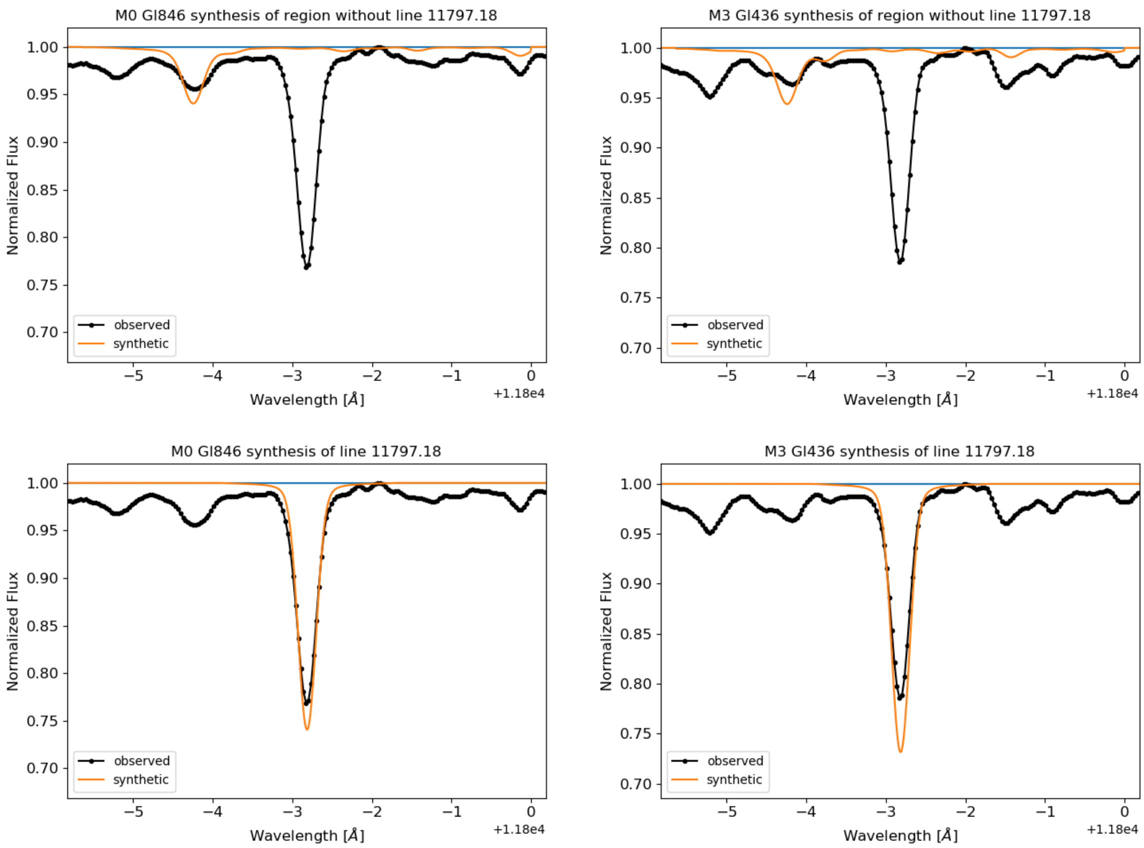

Figure C.9: Synthesis for applied Ti line 11797.18 Å.

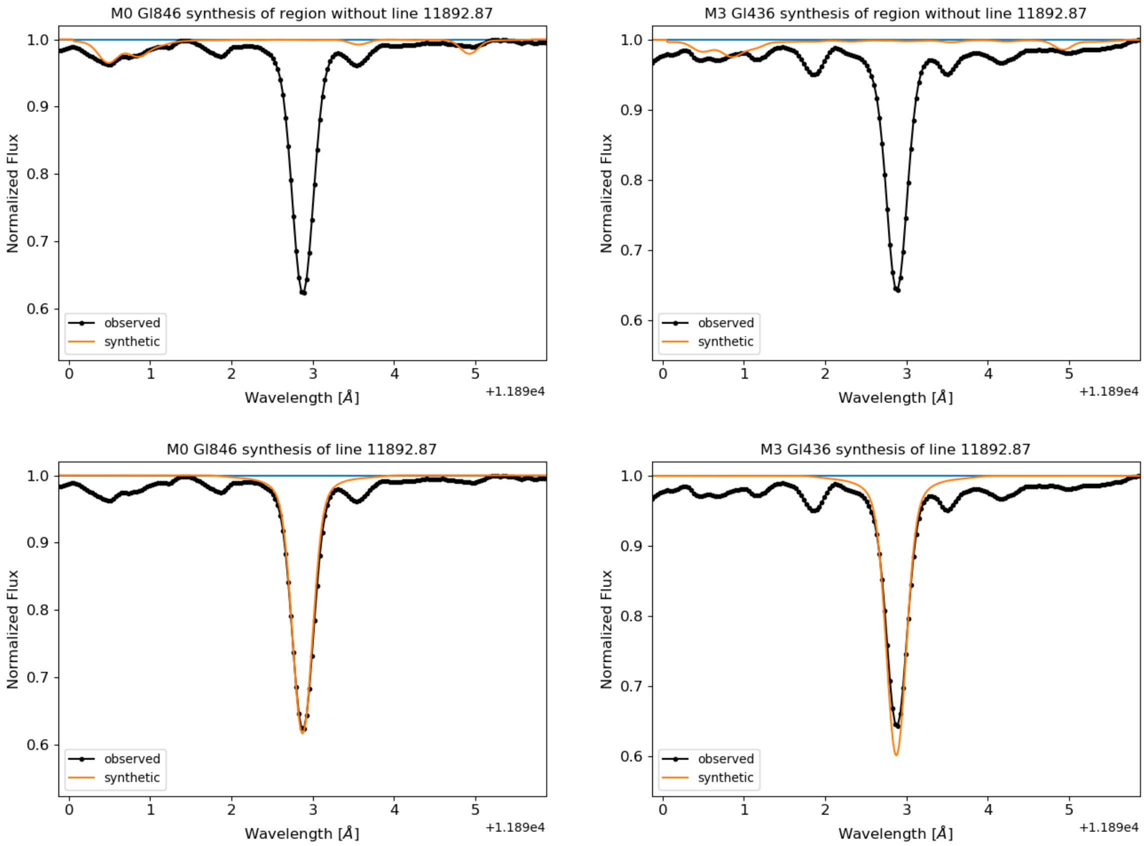

Figure C.10: Synthesis for applied Ti line 11892.87 Å.

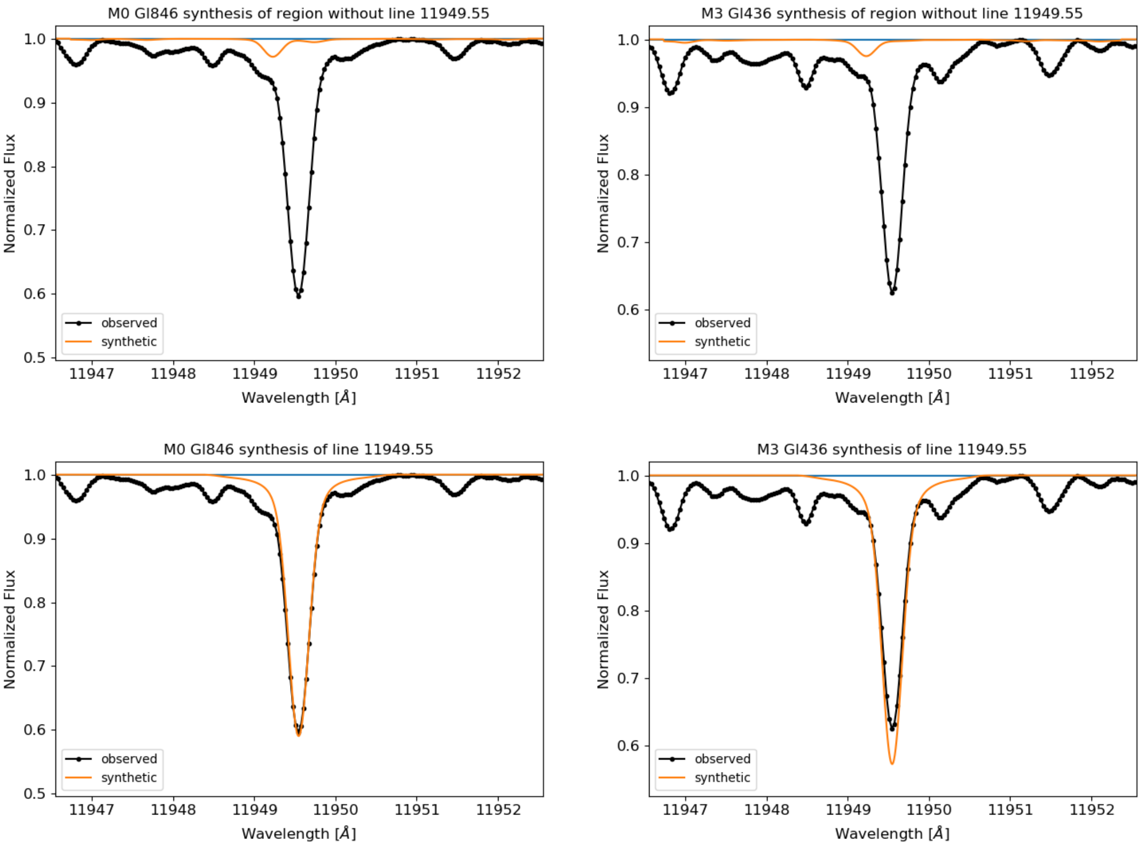

Figure C.11: Synthesis for applied Ti line 11949.55 Å.

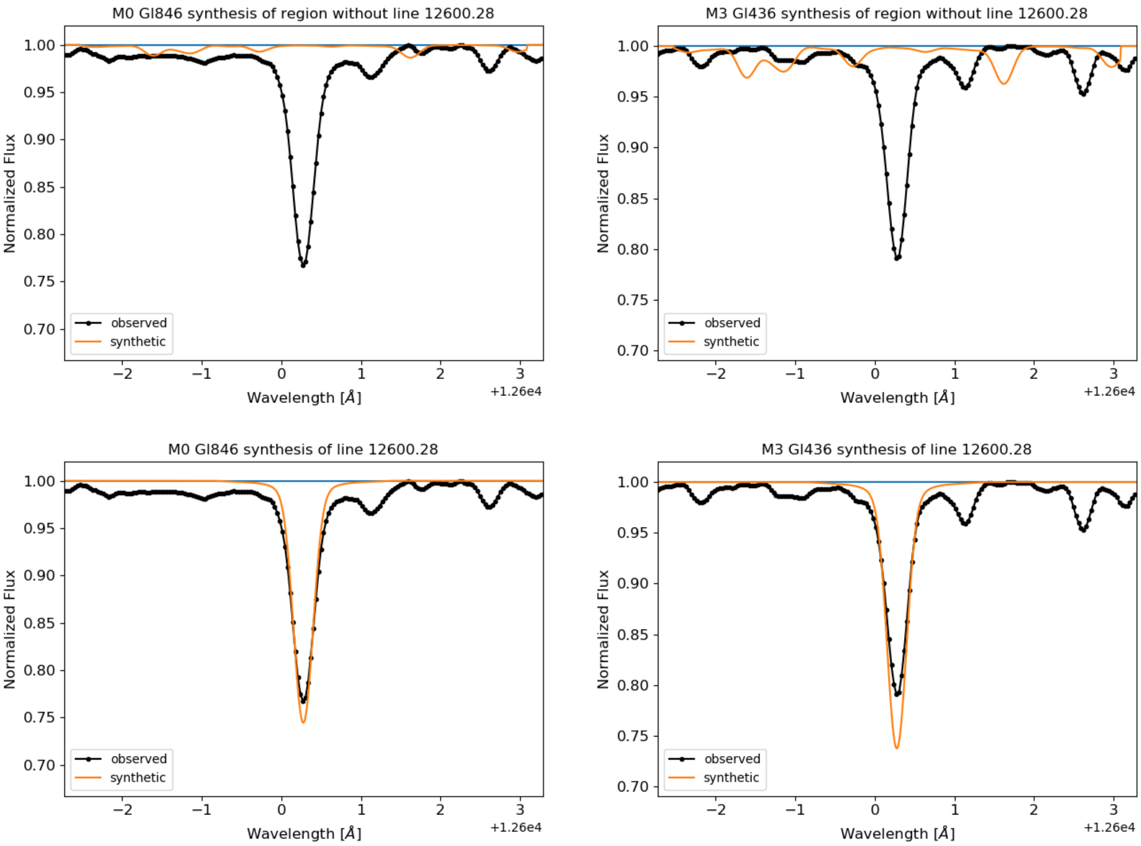

Figure C.12: Synthesis for applied Ti line 12600.28 Å.

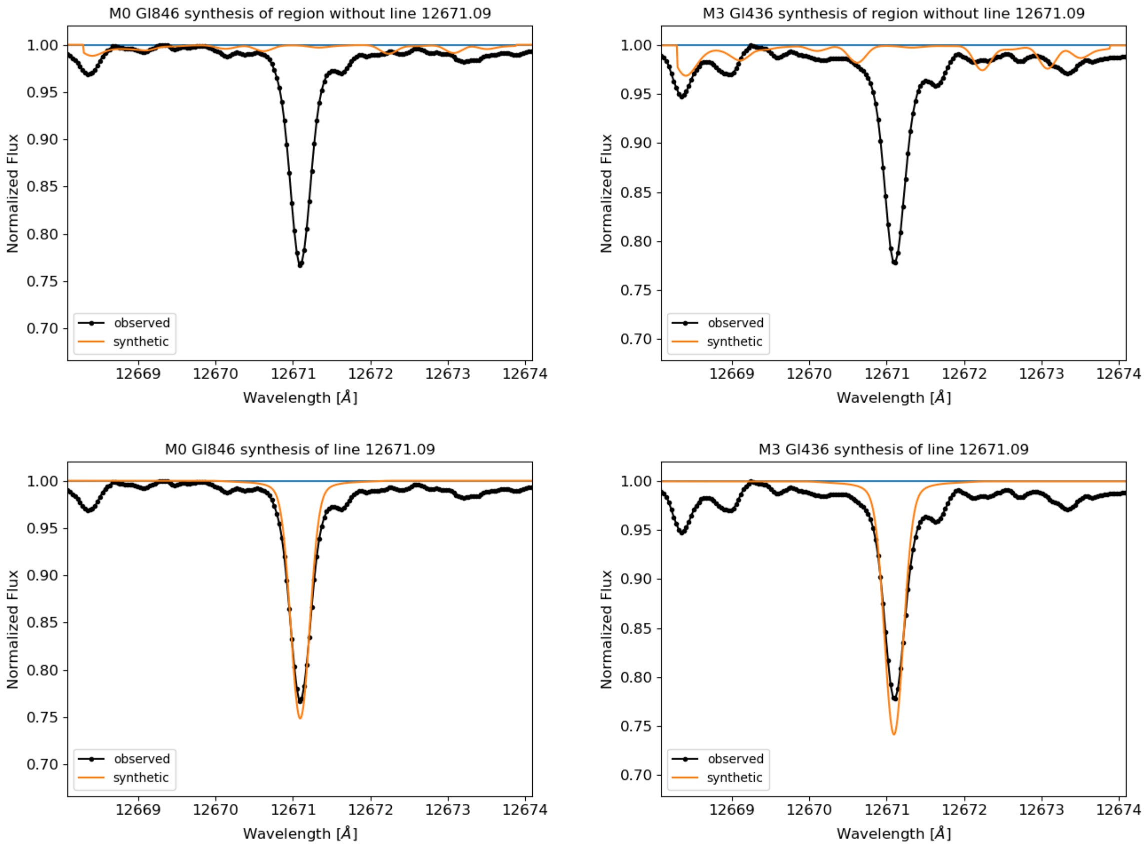

Figure C.13: Synthesis for applied Ti line 12671.09 Å.

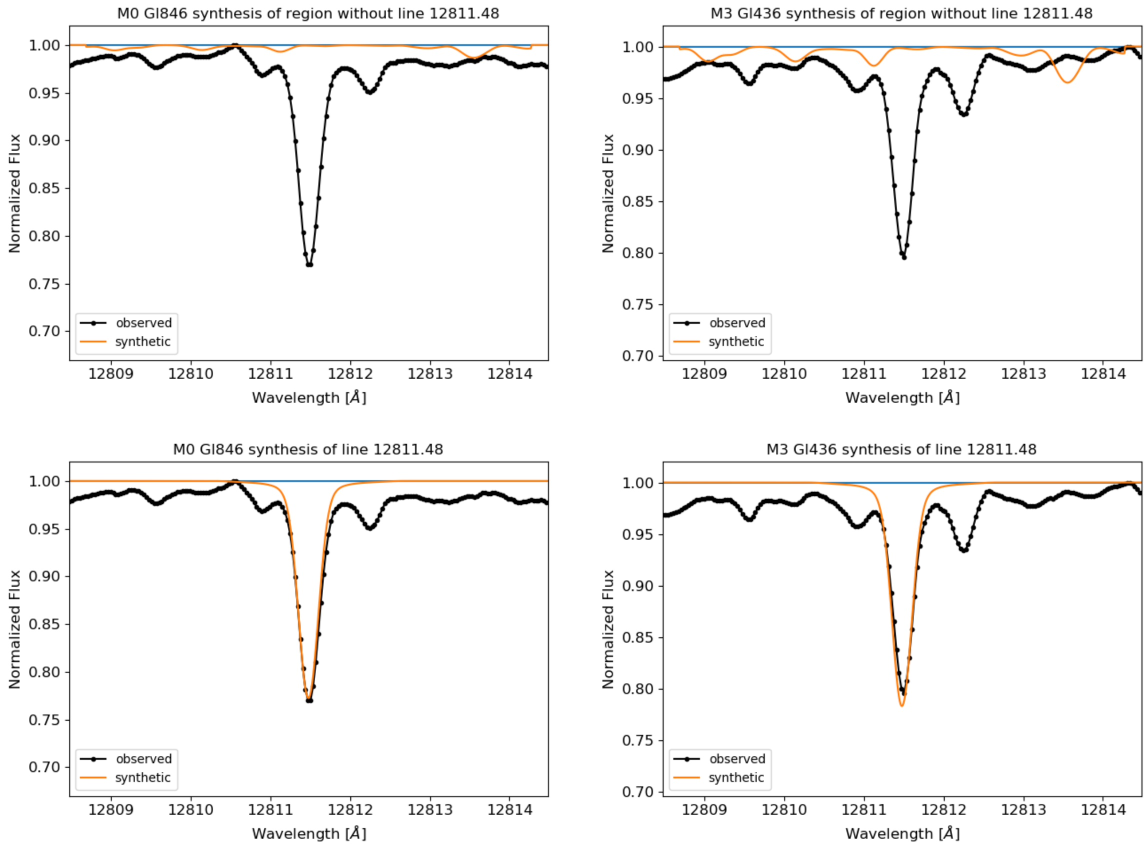

Figure C.14: Synthesis for applied Ti line 12811.48 Å.

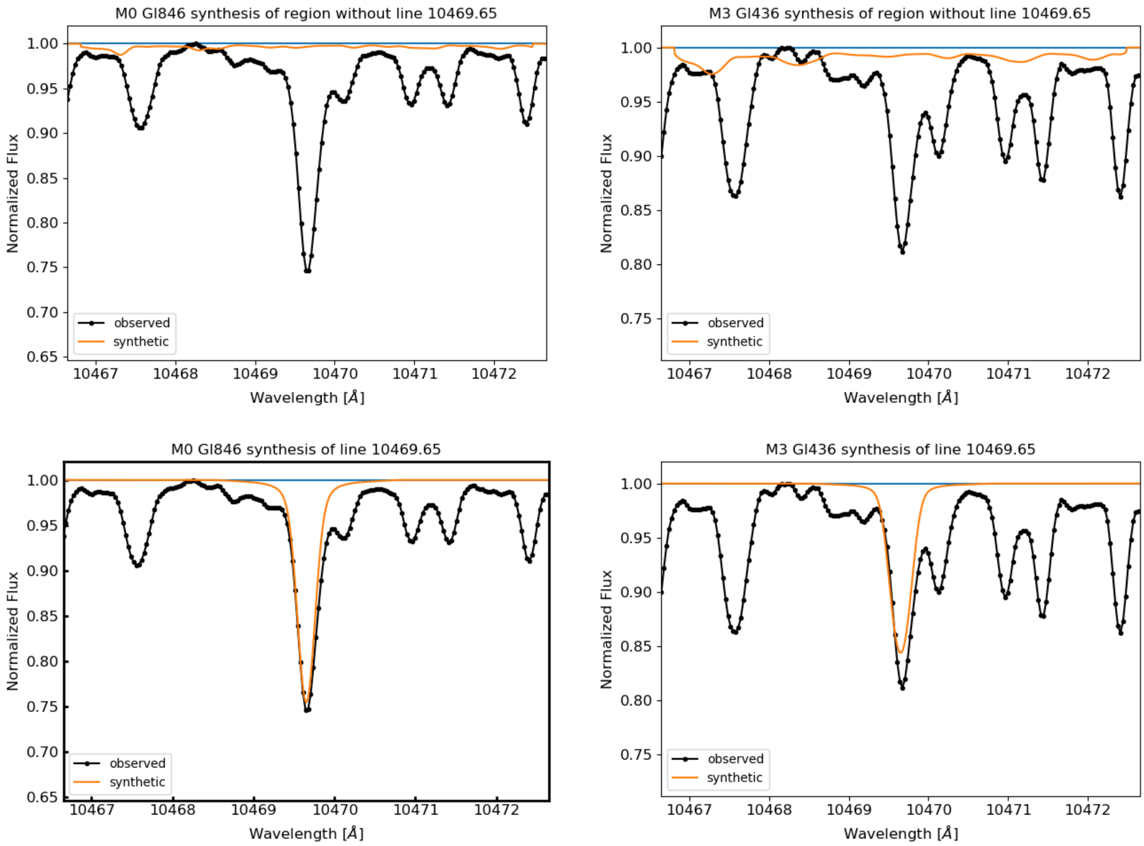

Figure C.15: Synthesis for ”2nd cut” Fe line 10469.65 Å.

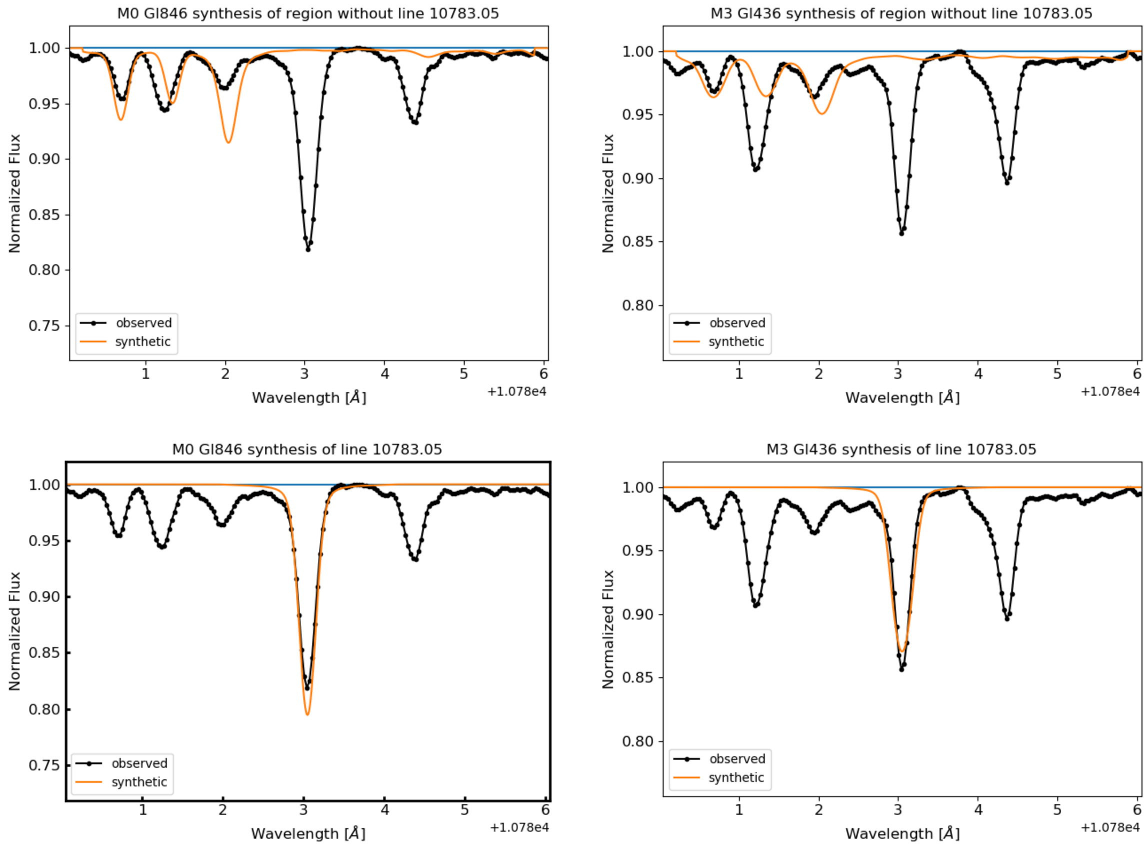

Figure C.16: Synthesis for "2nd cut" Fe line 10783.05 Å.

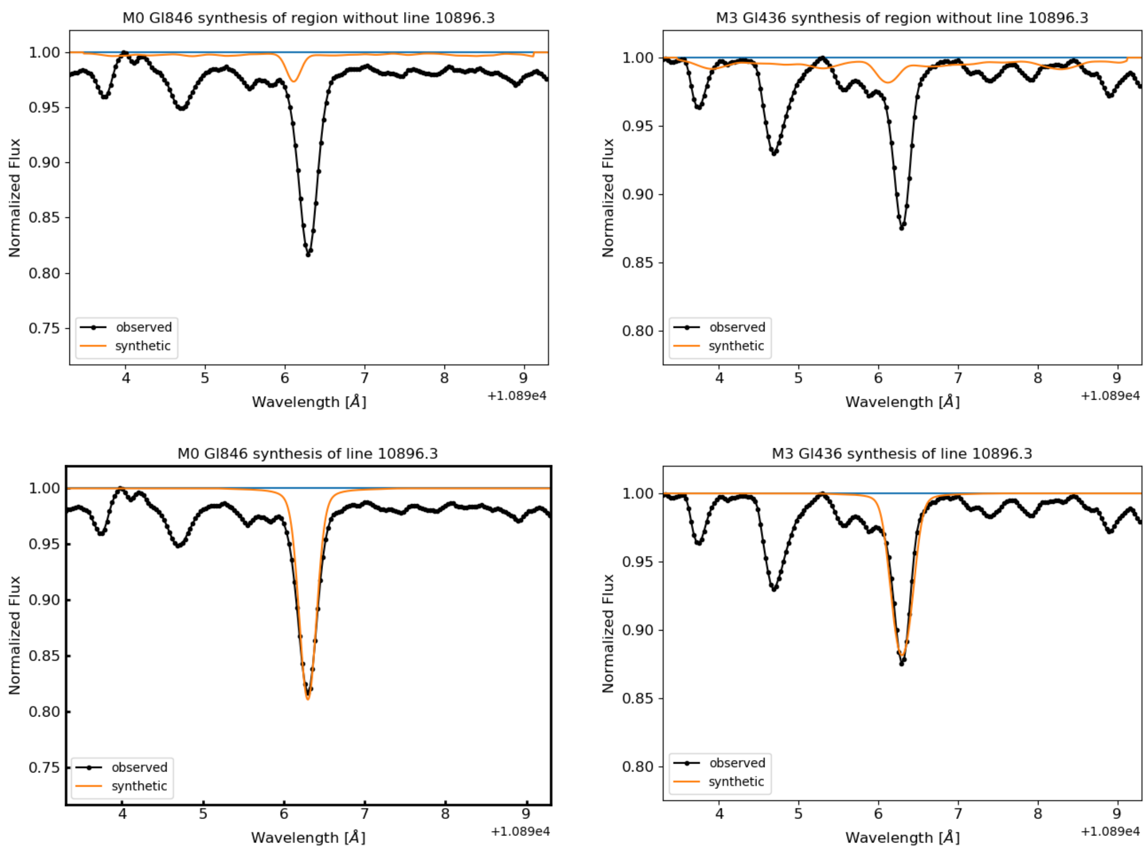

Figure C.17: Synthesis for ”2nd cut” Fe line 10896.30 Å.

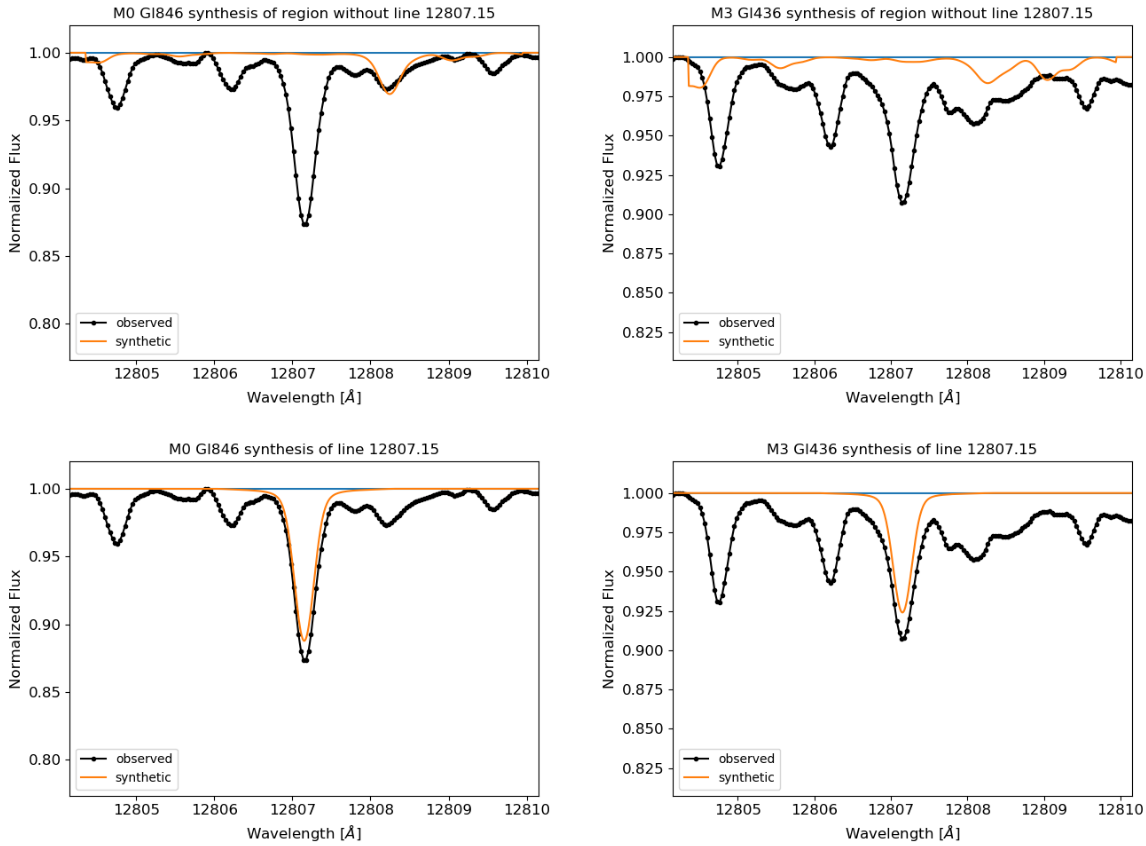

Figure C.18: Synthesis for ”2nd cut” Fe line 12807.15 Å.

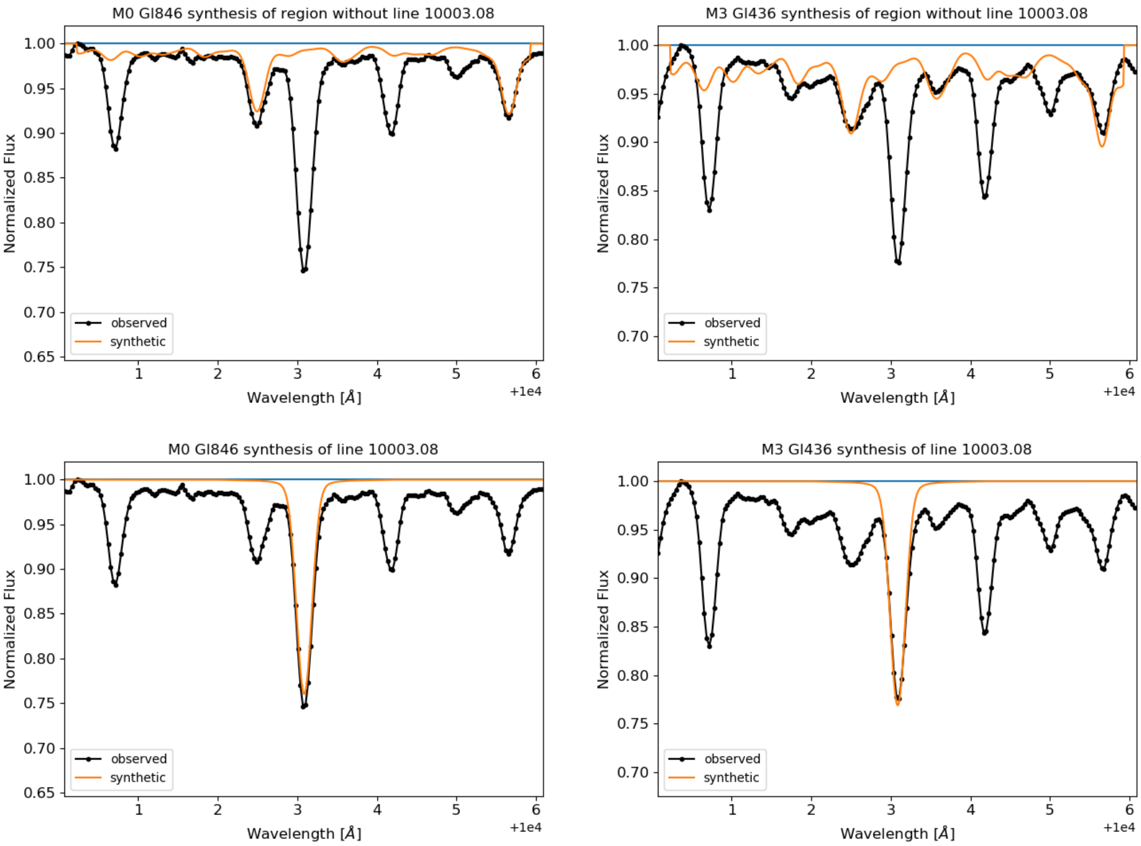

Figure C.19: Synthesis for ”2nd cut” Ti line 10003.08 Å.

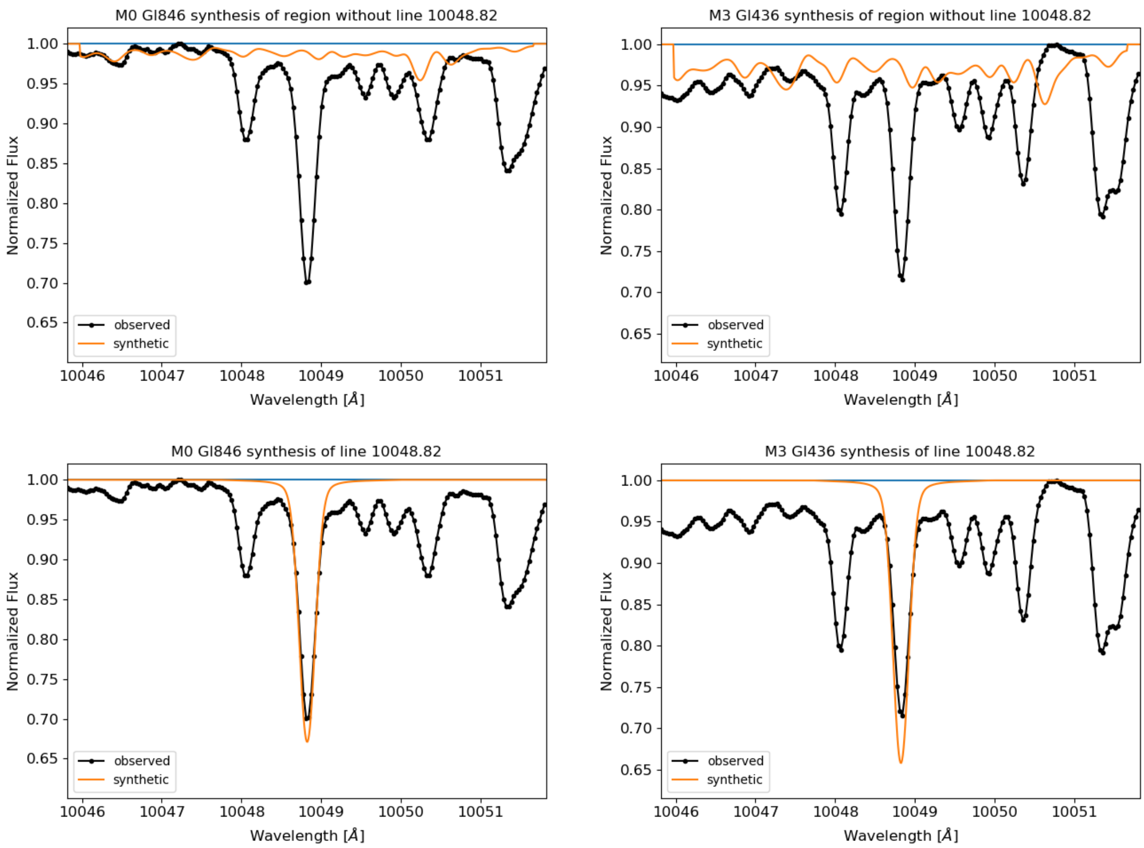

Figure C.20: Synthesis for ”2nd cut” Ti line 10048.82 Å.

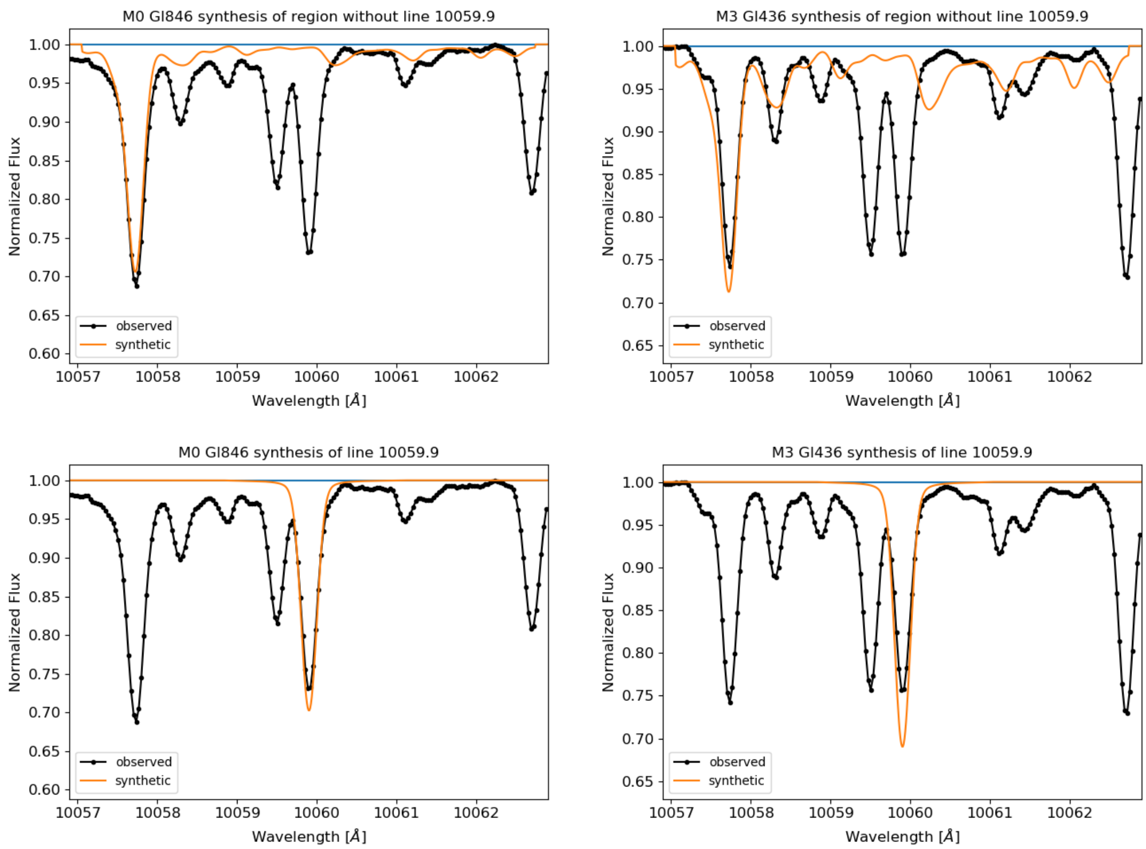

Figure C.21: Synthesis for ”2nd cut” Ti line 10059.90 Å.

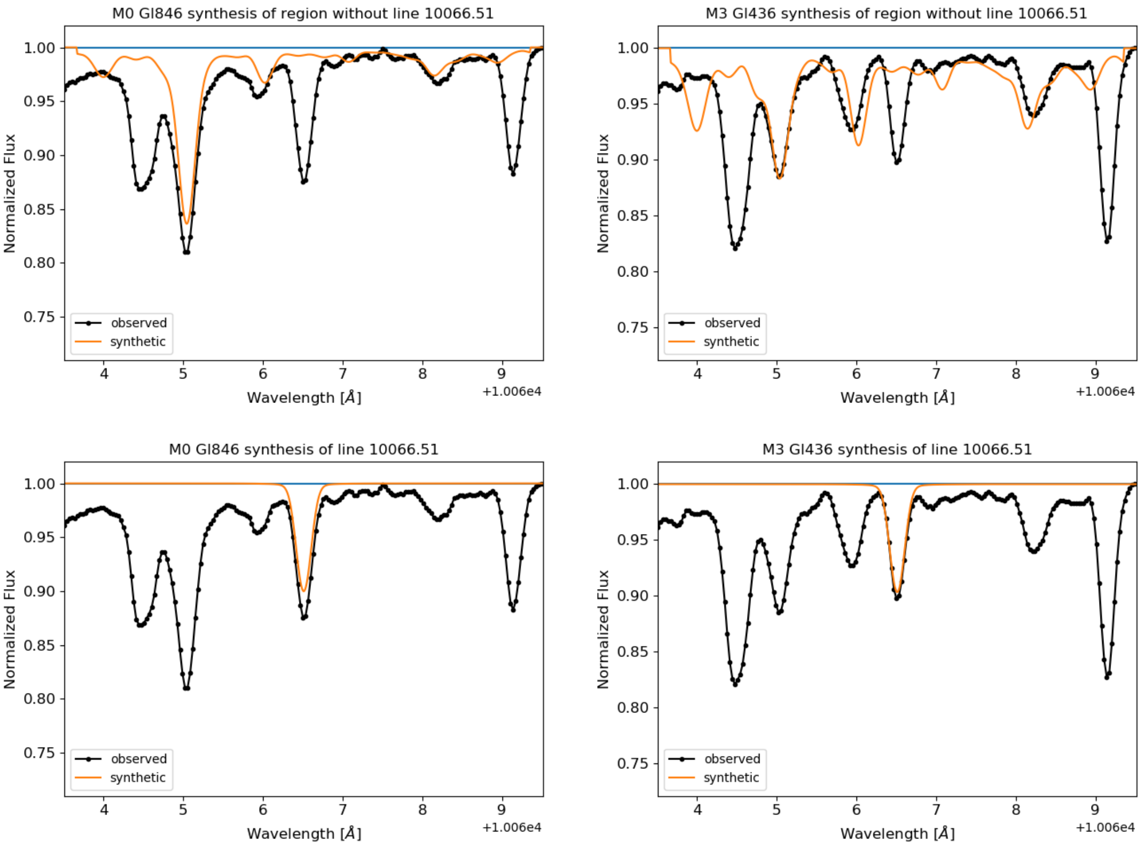

Figure C.22: Synthesis for "2nd cut" Ti line 10066.51 Å.

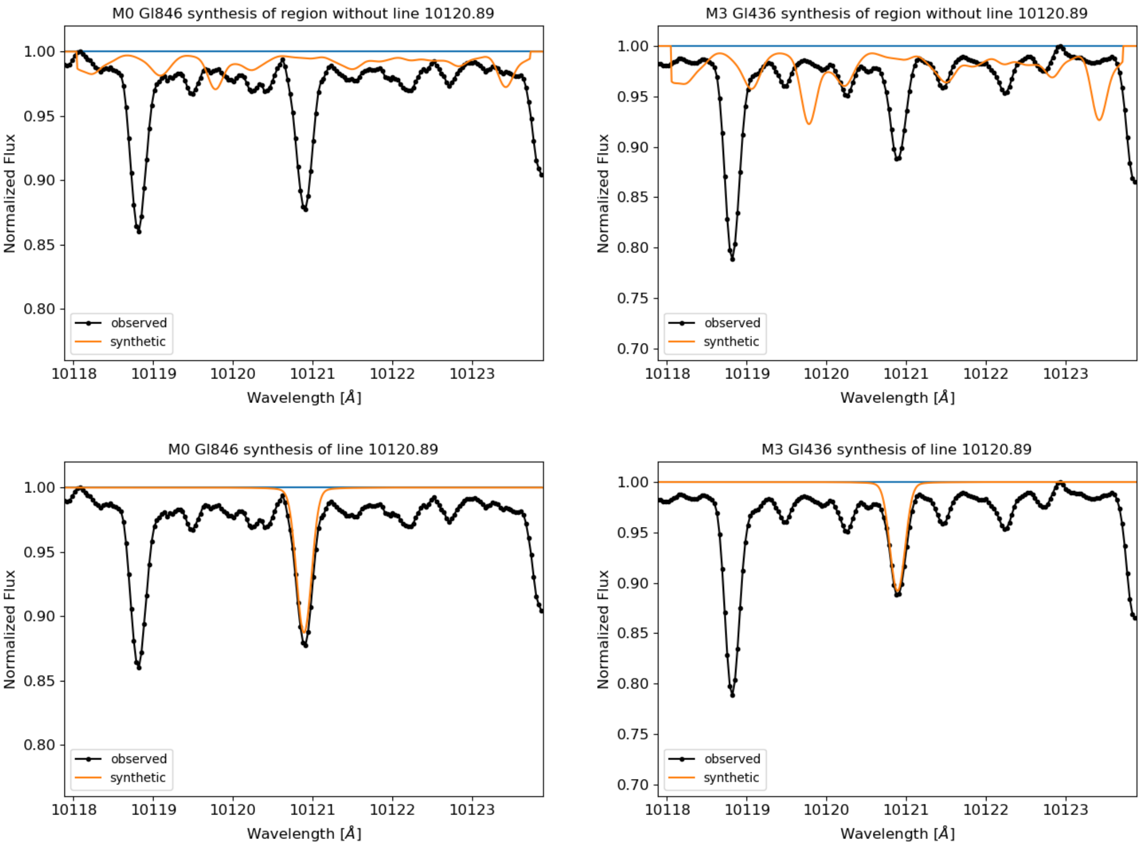

Figure C.23: Synthesis for ”2nd cut” Ti line 10120.89 Å.

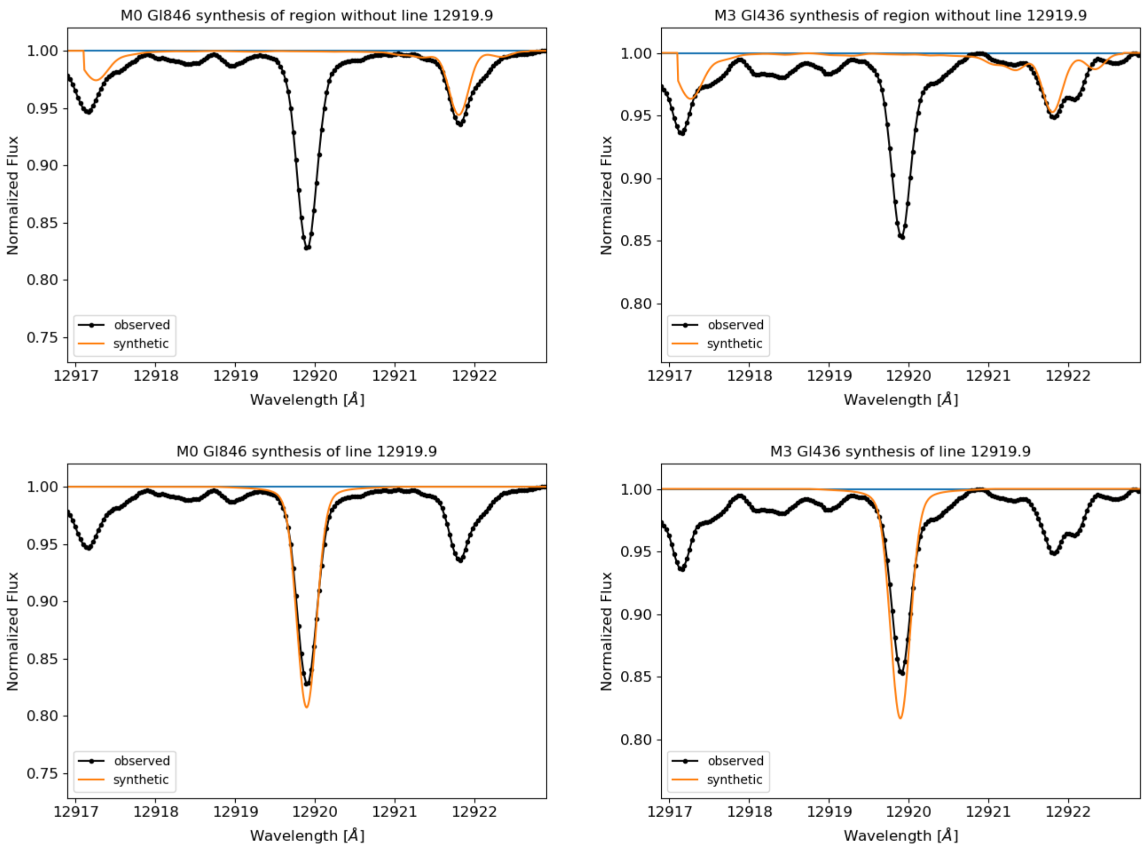

Figure C.24: Synthesis for ”2nd cut” Ti line 12919.90 Å.

D. Manual measurements of EWs for MPIRA

In Fig. D.1 to Fig. D.14, we present our indicative manual way (referred as ”third way”) of measuring the selected lines applied in MPIRA. We demonstrate the measurements for the lines of M3 Gl436, a star which was selected for synthesis too.

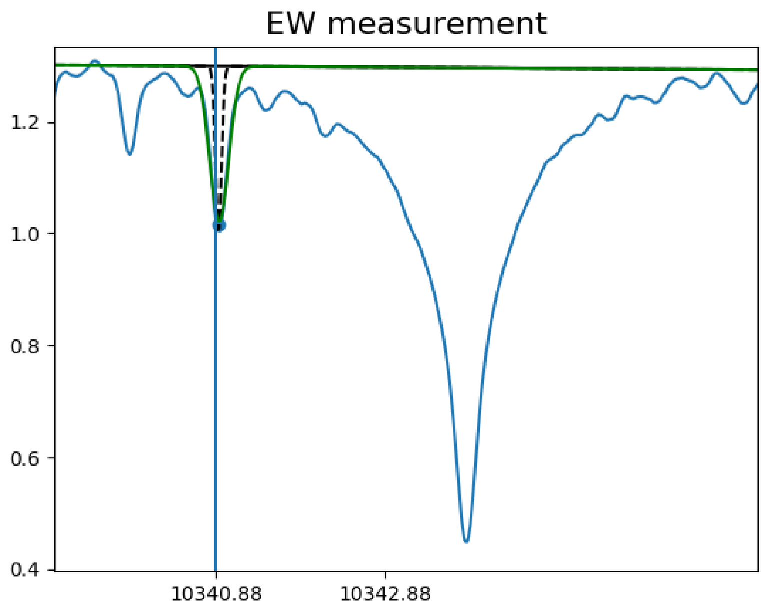

Figure D.1: Indicative manual EW measurement for applied Fe line 10340.88 Å of M3 Gl436. EW = 60.8 mÅ.

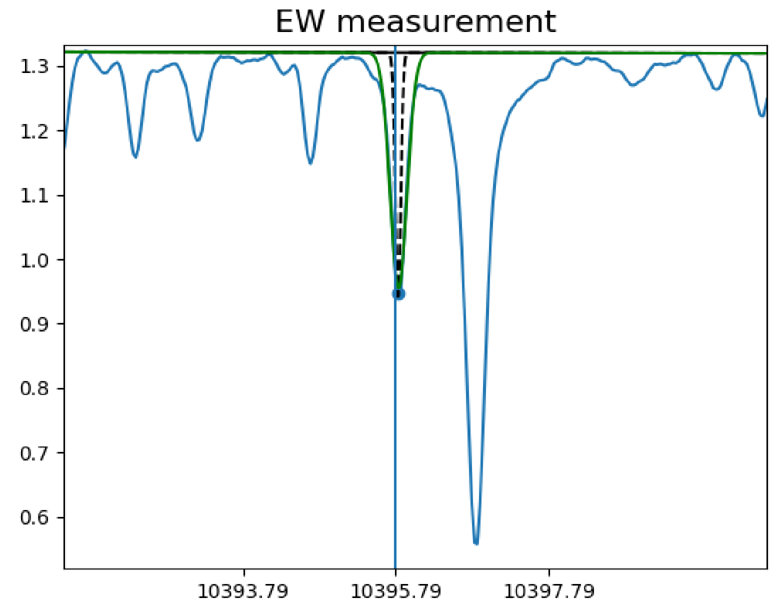

Figure D.2: Indicative manual EW measurement for applied Fe line 10395.79 Å of M3 Gl436. EW = 78.9 mÅ.

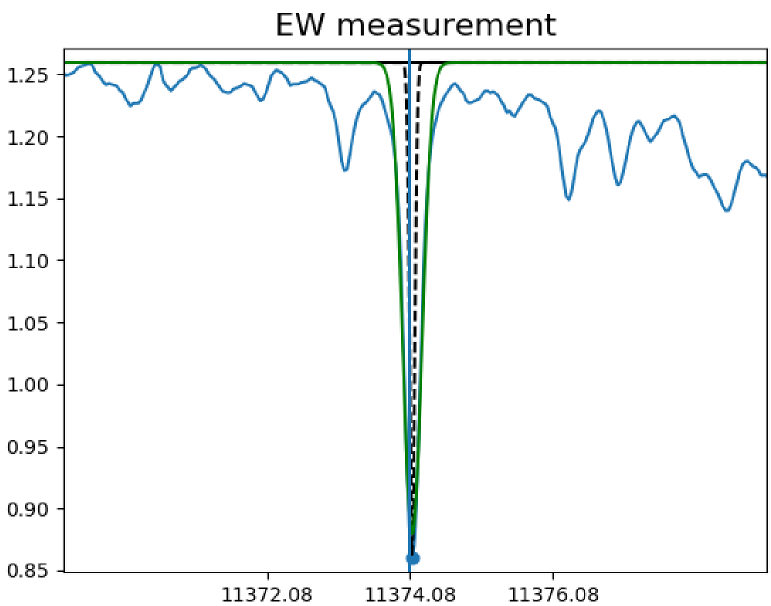

Figure D.3: Indicative manual EW measurement for applied Fe line 11374.08 Å of M3 Gl436. EW = 100.9 mÅ.

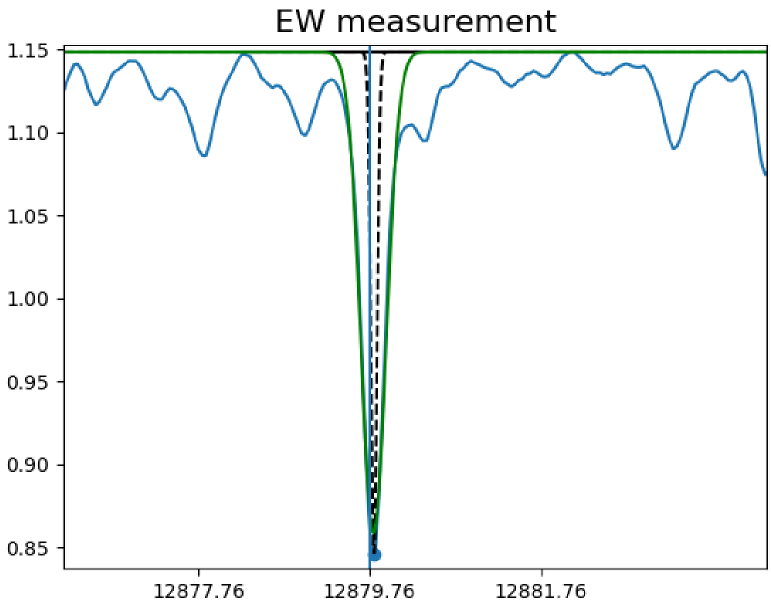

Figure D.4: Indicative manual EW measurement for applied Fe line 12879.76 Å of M3 Gl436. EW = 93.3 mÅ.

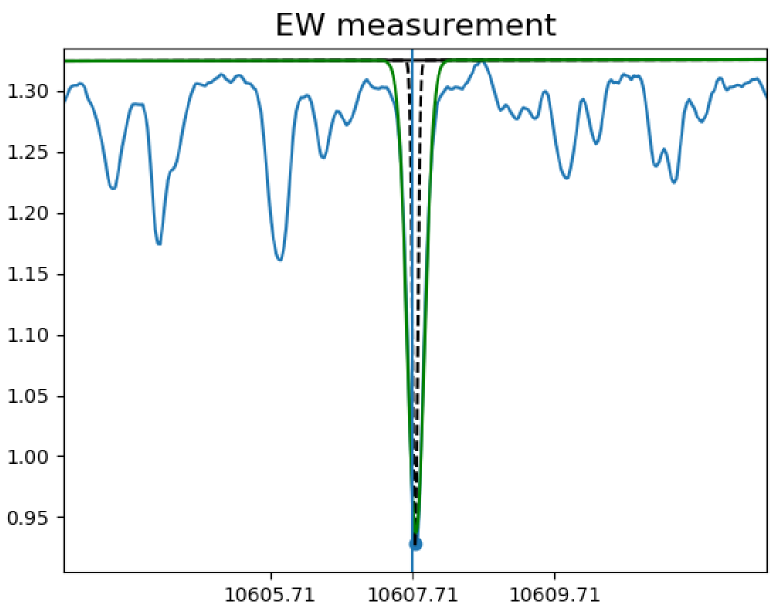

Figure D.5: Indicative manual EW measurement for applied Ti line 10607.71 Å of M3 Gl436. EW = 89.2 mÅ.

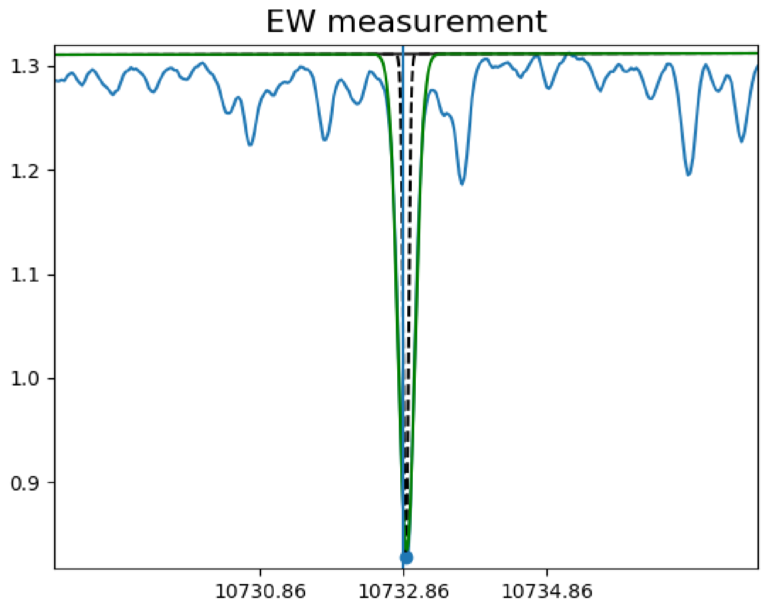

Figure D.6: Indicative manual EW measurement for applied Ti line 10732.86 Å of M3 Gl436. EW = 107.6 mÅ.

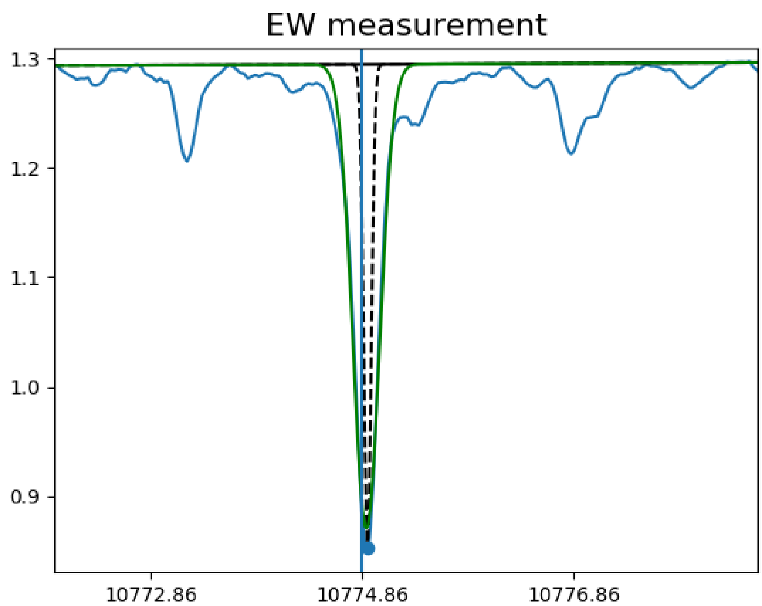

Figure D.7: Indicative manual EW measurement for applied Ti line 10774.86 Å of M3 Gl436. EW = 101.4 mÅ.

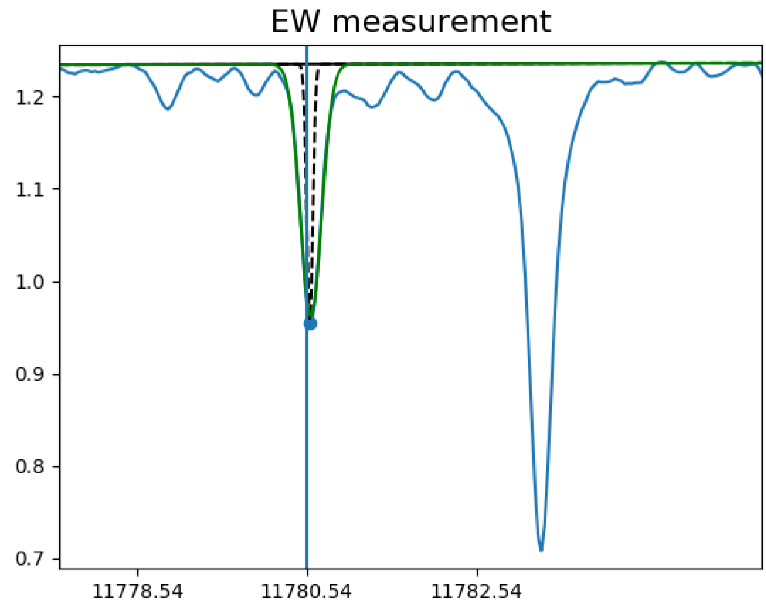

Figure D.8: Indicative manual EW measurement for applied Ti line 11780.54 Å of M3 Gl436. EW = 70.0 mÅ.

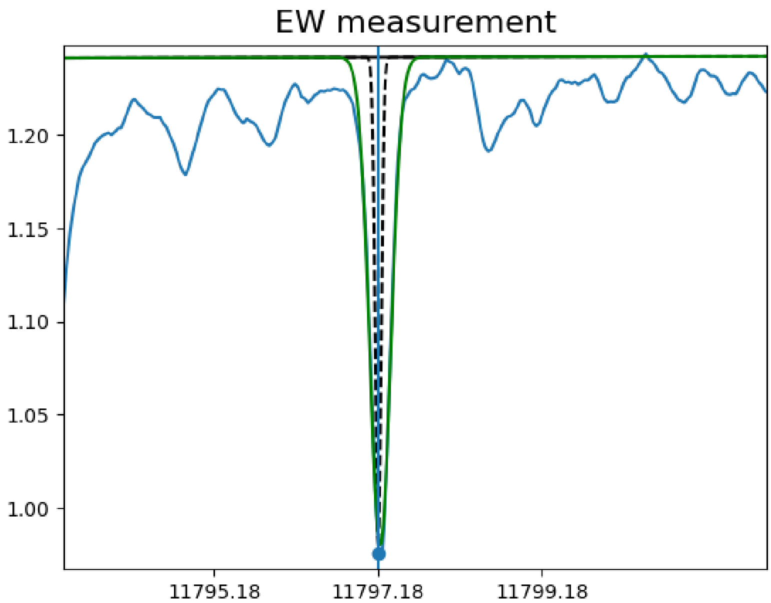

Figure D.9: Indicative manual EW measurement for applied Ti line 11797.18 Å of M3 Gl436. EW = 66.7 mÅ.

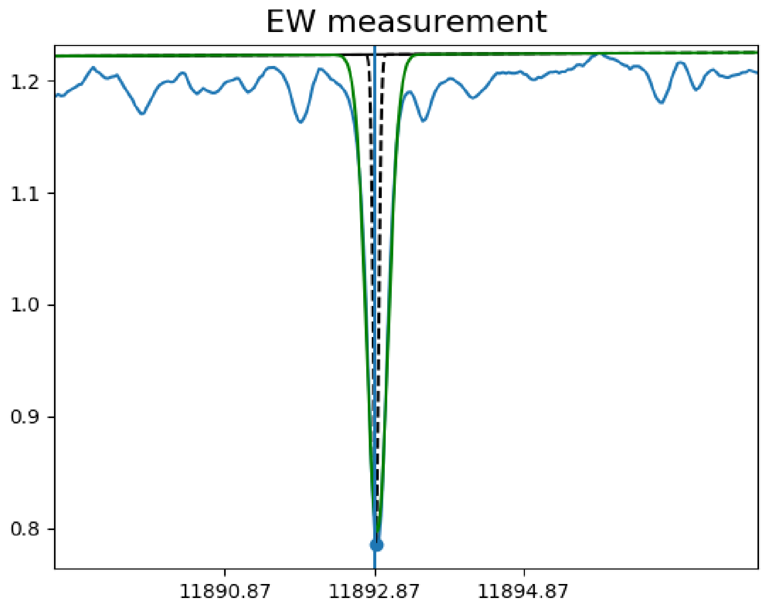

Figure D.10: Indicative manual EW measurement for applied Ti line 11892.87 Å of M3 Gl436. EW = 124.5 mÅ.

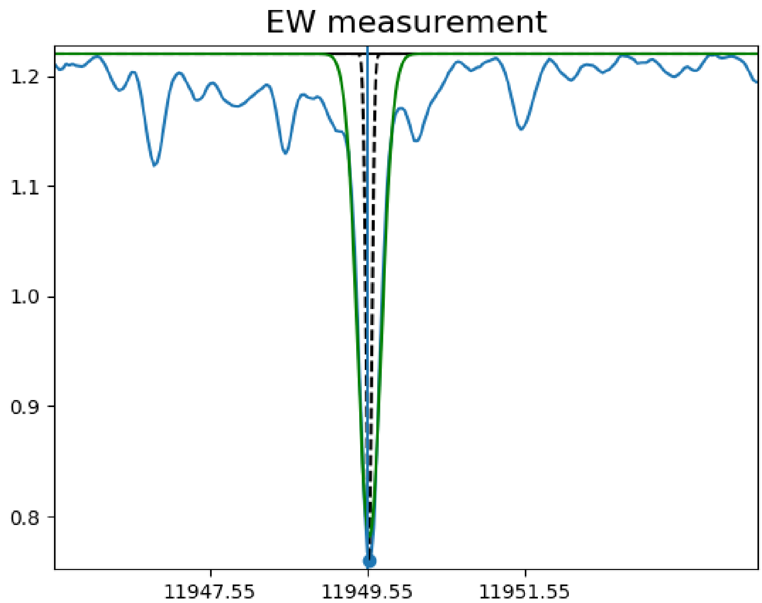

Figure D.11: Indicative manual EW measurement for applied Ti line 11949.55 Å of M3 Gl436. EW = 132.9 mÅ.

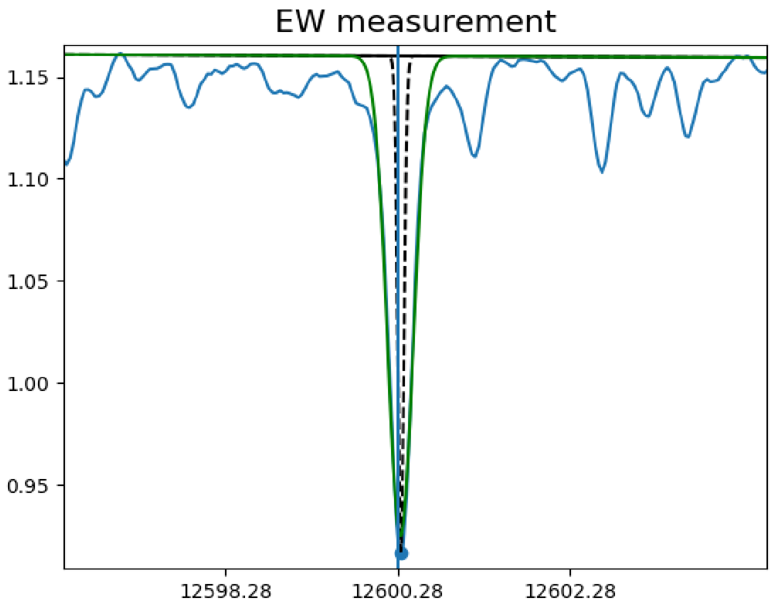

Figure D.12: Indicative manual EW measurement for applied Ti line 12600.28 Å of M3 Gl436. EW = 75.6 mÅ.

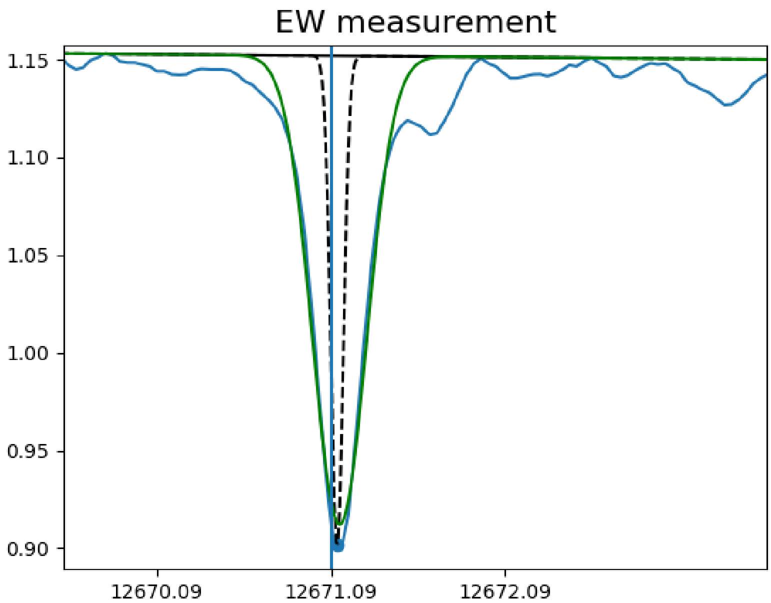

Figure D.13: Indicative manual EW measurement for applied Ti line 12671.09 Å of M3 Gl436. EW = 78.1 mÅ.

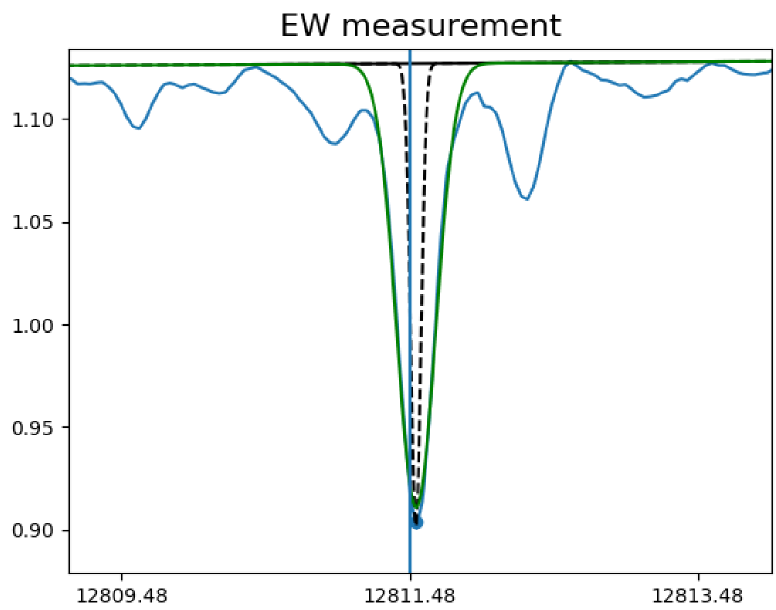

Figure D.14: Indicative manual EW measurement for applied Ti line 12811.48 Å of M3 Gl436. EW = 65.5 mÅ.

Bibliography

Abia, C., Tabernero, H. M., Korotin, S. A., et al. 2020, A&A, 642, A227 [Cited on page 22.]

Adibekyan, V. Z., Santos, N. C., Sousa, S. G., & Israelian, G. 2011, A&A, 535, L11 [Cited on page 22.]

Adibekyan, V. Z., Sousa, S. G., Santos, N. C., et al. 2012, A&A, 545, A32 [Cited on page 22.]

Agol, E., Steffen, J., Sari, R., & Clarkson, W. 2005, MNRAS, 359, 567 [Cited on page 16.]

Akras, S., Leal-Ferreira, M. L., Guzman-Ramirez, L., & Ramos-Larios, G. 2019, MNRAS, 483, 5077 [Cited on page 52.]

Al-Naimiy, H. M. 1978, Ap&SS, 53, 181 [Cited on page 127.]

Allard, F. & Hauschildt, P. H. 1995, ApJ, 445, 433 [Cited on pages 37 and 43.]

Allard, F., Homeier, D., Freytag, B., Schaffenberger, W., & Rajpurohit, A. S. 2013, Memorie della Societa Astronomica Italiana Supplementi, 24, 128 [Cited on pages 80, 83, and 101.]

Andreasen, D. T., Sousa, S. G., Delgado Mena, E., et al. 2016, A&A, 585, A143 [Cited on page 120.]

Antoniadis-Karnavas, A., Sousa, S. G., Delgado-Mena, E., et al. 2020, A&A, 636, A9 [Cited on pages 52 and 148.]

Artigau, É., Kouach, D., Donati, J.-F., et al. 2014, in Society of Photo-Optical Instrumentation Engineers (SPIE) Conference Series, Vol. 9147, Ground-based and Airborne Instrumentation for Astronomy V, ed. S. K. Ramsay, I. S. McLean, & H. Takami, 914715 [Cited on page 10.]

Astudillo-Defru, N., Forveille, T., Bonfils, X., et al. 2017, A&A, 602, A88 [Cited on page 5.]

Baade, W. 1944, ApJ, 100, 137 [Cited on page 21.]

Ball, N. M. & Brunner, R. J. 2010, International Journal of Modern Physics D, 19, 1049 [Cited on page 51.]

Baraffe, I. & Chabrier, G. 1996, ApJ, 461, L51 [Cited on page 4.]

Barclay, T., Rowe, J. F., Lissauer, J. J., et al. 2013, Nature, 494, 452 [Cited on page 7.]

Barklem, P. S. & O'Mara, B. J. 1998, MNRAS, 300, 863 [Cited on page 36.]

Baron, E., Chen, B., & Hauschildt, P. H. 2010, PHOENIX: A General-purpose State-of-the-art Stellar and Planetary Atmosphere Code, Astrophysics Source Code Library, record ascl:1010.056 [Cited on page 37.]

Bean, J. L., Benedict, G. F., & Endl, M. 2006a, ApJ, 653, L65 [Cited on page 43.]

Bean, J. L., Sneden, C., Hauschildt, P. H., Johns-Krull, C. M., & Benedict, G. F. 2006b, ApJ, 652, 1604 [Cited on page 42.]

Beaulieu, J. P., Bennett, D. P., Fouqué, P., et al. 2006, Nature, 439, 437 [Cited on pages 13 and 14.]

Berger, D. H., Gies, D. R., McAlister, H. A., et al. 2006, ApJ, 644, 475 [Cited on page 124.]

Berriman, G., Reid, N., & Leggett, S. K. 1992, ApJ, 392, L31 [Cited on page 38.]

Bessell, M. S. 1982, PASA, 4, 417 [Cited on page 43.]

Bessell, M. S. 1991, AJ, 101, 662 [Cited on page 4.]

Beuzit, J.-L., Feldt, M., Dohlen, K., et al. 2008, in Society of Photo-Optical Instrumentation Engineers (SPIE) Conference Series, Vol. 7014, Ground-based and Airborne Instrumentation for Astronomy II, ed. I. S. McLean & M. M. Casali, 701418 [Cited on page 13.]

Blanco-Cuaresma, S., Soubiran, C., Heiter, U., & Jofré, P. 2014, A&A, 569, A111 [Cited on page 49.]

Bok, P. F. 1941, PASP, 53, 168 [Cited on page 2.]

Bond, H. E. 1981, ApJ, 248, 606 [Cited on page 21.]

Bond, I. A., Udalski, A., Jaroszyński, M., et al. 2004, ApJ, 606, L155 [Cited on page 14.]

Bonfils, X., Delfosse, X., Udry, S., et al. 2013, A&A, 549, A109 [Cited on pages 6 and 54.]

Bonfils, X., Forveille, T., Delfosse, X., et al. 2005, A&A, 443, L15 [Cited on pages 24 and 39.]

Bonfils, X., Mayor, M., Delfosse, X., et al. 2007, A&A, 474, 293 [Cited on page 109.]

Borucki, W., Koch, D., Basri, G., et al. 2008, in Exoplanets: Detection, Formation and Dynamics, ed. Y.-S. Sun, S. Ferraz-Mello, & J.-L. Zhou, Vol. 249, 17–24 [Cited on page 7.]

Borucki, W. J., Koch, D., Basri, G., et al. 2010, in American Astronomical Society Meeting Abstracts, Vol. 215, American Astronomical Society Meeting Abstracts #215, 101.01 [Cited on pages 6 and 7.]

Borucki, W. J., Koch, D. G., Basri, G., et al. 2011, ApJ, 728, 117 [Cited on page 7.]

Boss, A. P. 2000, ApJ, 536, L101 [Cited on page 111.]

Boss, A. P. 2002, ApJ, 567, L149 [Cited on page 111.]

Boyajian, T. S., von Braun, K., van Belle, G., et al. 2012, ApJ, 757, 112 [Cited on pages 40, 44, 83, and 100.]

Broeg, C., Fortier, A., Ehrenreich, D., et al. 2013, in European Physical Journal Web of Conferences, Vol. 47, European Physical Journal Web of Conferences, 03005 [Cited on page 7.]

Brogi, M., de Kok, R. J., Birkby, J. L., Schwarz, H., & Snellen, I. A. G. 2014, A&A, 565, A124 [Cited on page 8.]

Buchhave, L. A., Latham, D. W., Johansen, A., et al. 2012, Nature, 486, 375 [Cited on page 109.]

Burrows, A., Guillot, T., Hubbard, W. B., et al. 2000, ApJ, 534, L97 [Cited on page 8.]

Butler, R. P., Marcy, G. W., Williams, E., Hauser, H., & Shirts, P. 1997, ApJ, 474, L115 [Cited on page 10.]

Carroll, B. W. & Ostlie, D. A. 1996, An Introduction to Modern Astrophysics [Cited on page 27.]

Casagrande, L., Flynn, C., & Bessell, M. 2008, MNRAS, 389, 585 [Cited on pages 24, 38, 44, 51, 52, 58, 60, 70, 79, 124, and 152.]

Casagrande, L., Portinari, L., & Flynn, C. 2006, MNRAS, 373, 13 [Cited on pages 38 and 80.]

Cassan, A., Kubas, D., Beaulieu, J. P., et al. 2012, Nature, 481, 167 [Cited on page 6.]

Castro-González, A., Demangeon, O. D. S., Lillo-Box, J., et al. 2023, A&A, 675, A52 [Cited on pages 79 and 148.]

Charbonneau, D., Brown, T. M., Latham, D. W., & Mayor, M. 2000, ApJ, 529, L45 [Cited on pages 7 and 10.]

Charbonneau, D., Brown, T. M., Noyes, R. W., & Gilliland, R. L. 2002, ApJ, 568, 377 [Cited on page 8.]

Chauvin, G., Lagrange, A. M., Dumas, C., et al. 2004, A&A, 425, L29 [Cited on page 12.]

Ciddor, P. E. 1996, Appl. Opt., 35, 1566 [Cited on page 123.]

Cortés-Zuleta, P., Boisse, I., Klein, B., et al. 2023, A&A, 673, A14 [Cited on page 148.]

Cosentino, R., Lovis, C., Pepe, F., et al. 2012, in Proc. SPIE, Vol. 8446, Ground-based and Airborne Instrumentation for Astronomy IV, 84461V [Cited on page 10.]

Cristofari, P. I., Donati, J. F., Masseron, T., et al. 2022, MNRAS, 516, 3802 [Cited on pages 24 and 50.]

Das, P. & Sanders, J. L. 2019, MNRAS, 484, 294 [Cited on page 52.]

Dekker, H., D'Odorico, S., Kaufer, A., Delabre, B., & Kotzlowski, H. 2000, in Society of Photo-Optical Instrumentation Engineers (SPIE) Conference Series, Vol. 4008, Optical and IR Telescope Instrumentation and Detectors, ed. M. Iye & A. F. Moorwood, 534–545 [Cited on page 59.]

Delfosse, X., Bonfils, X., Forveille, T., et al. 2013, A&A, 553, A8 [Cited on page 6.]

Delfosse, X., Forveille, T., Ségransan, D., et al. 2000, A&A, 364, 217 [Cited on pages 39 and 40.]

Delgado Mena, E., Tsantaki, M., Adibekyan, V. Z., et al. 2017, A&A, 606, A94 [Cited on page 22.]

Demangeon, O. D. S., Zapatero Osorio, M. R., Alibert, Y., et al. 2021, A&A, 653, A41 [Cited on pages 79 and 148.]

Dipierro, G., Price, D., Laibe, G., et al. 2015, MNRAS, 453, L73 [Cited on page 18.]

Dorn, C., Khan, A., Heng, K., et al. 2015, A&A, 577, A83 [Cited on page 5.]

dos Santos, L. A., Meléndez, J., do Nascimento, J.-D., et al. 2016, A&A, 592, A156 [Cited on page 127.]

Edlén, B. 1953, J. Opt. Soc. Am., 43, 339 [Cited on page 123.]

Esteves, L. J., De Mooij, E. J. W., & Jayawardhana, R. 2013, ApJ, 772, 51 [Cited on page 17.]

Fischer, D. A. & Valenti, J. 2005, ApJ, 622, 1102 [Cited on page 109.]

Fosbury, R. A. E., Villar-Martín, M., Humphrey, A., et al. 2003, ApJ, 596, 797 [Cited on page 22.]

Gaia Collaboration. 2020, VizieR Online Data Catalog, I/350 [Cited on page 53.]

Gaia Collaboration, Brown, A. G. A., Vallenari, A., et al. 2018, A&A, 616, A1 [Cited on page 15.]

Gaia Collaboration, Prusti, T., de Bruijne, J. H. J., et al. 2016, A&A, 595, A1 [Cited on pages 3 and 14.]

Gaidos, E., Mann, A. W., Lépine, S., et al. 2014, MNRAS, 443, 2561 [Cited on page 44.]

Gandolfi, D., Barragán, O., Livingston, J. H., et al. 2018, A&A, 619, L10 [Cited on page 7.]

Gizis, J. E., Reid, I. N., & Hawley, S. L. 2002, AJ, 123, 3356 [Cited on page 23.]

Gontcharov, G. A., Andronova, A. A., & Titov, O. A. 2000, A&A, 355, 1164 [Cited on page 15.]

Gonzalez, G., Laws, C., Tyagi, S., & Reddy, B. E. 2001, AJ, 121, 432 [Cited on page 109.]

Gray, D. F. 2005, The Observation and Analysis of Stellar Photospheres [Cited on pages 25, 28, 29, 30, 33, and 34.]

Greenstein, J. L., Neugebauer, G., & Becklin, E. E. 1970, ApJ, 161, 519 [Cited on page 38.]

Grevesse, N., Asplund, M., & Sauval, A. J. 2007, Space Sci. Rev., 130, 105 [Cited on page 37.]

Gustafsson, B. 1989, ARA&A, 27, 701 [Cited on page 4.]

Gustafsson, B., Bell, R. A., Eriksson, K., & Nordlund, A. 1975, A&A, 42, 407 [Cited on page 37.]

Gustafsson, B., Edvardsson, B., Eriksson, K., et al. 2008, A&A, 486, 951 [Cited on pages 37 and 117.]

Hauschildt, P. H., Allard, F., & Baron, E. 1999, ApJ, 512, 377 [Cited on pages 37 and 43.]

Hauschildt, P. H. & Baron, E. 2009, A&A, 498, 981 [Cited on page 37.]

Hawkins, M. R. S. & Bessell, M. S. 1988, MNRAS, 234, 177 [Cited on page 23.]

Heiter, U. & Eriksson, K. 2006, A&A, 452, 1039 [Cited on page 36.]

Henry, G. W., Marcy, G. W., Butler, R. P., & Vogt, S. S. 2000, ApJ, 529, L41 [Cited on page 7.]

Henry, T. J., Kirkpatrick, J. D., & Simons, D. A. 1994, AJ, 108, 1437 [Cited on page 4.]

Hobson, M. J., Jordán, A., Bryant, E. M., et al. 2023, ApJ, 946, L4 [Cited on page 79.]

Hoeijmakers, H. J., Ehrenreich, D., Heng, K., et al. 2018, Nature, 560, 453 [Cited on page 8.]

Holczer, T., Mazeh, T., Nachmani, G., et al. 2016, ApJS, 225, 9 [Cited on page 16.]

Holman, M. J. & Murray, N. W. 2005, Science, 307, 1288 [Cited on page 16.]

Howard, E. M. 2017, in Astronomical Society of the Pacific Conference Series, Vol. 512, Astronomical Data Analysis Software and Systems XXV, ed. N. P. F. Lorente, K. Shortridge, & R. Wayth, 245 [Cited on page 51.]

Huang, C. X., Burt, J., Vanderburg, A., et al. 2018, ApJ, 868, L39 [Cited on page 7.]

Husser, T. O., Wende-von Berg, S., Dreizler, S., et al. 2013, A&A, 553, A6 [Cited on pages 37, 81, 83, and 101.]

Ishikawa, H. T., Aoki, W., Hirano, T., et al. 2022, AJ, 163, 72 [Cited on page 22.]

Ivezić, Ž., Connolly, A. J., VanderPlas, J. T., & Gray, A. 2014, Statistics, Data Mining, and Machine Learning in Astronomy: A Practical Python Guide for the Analysis of Survey Data [Cited on page 51.]

Jenkins, J. S., Ramsey, L. W., Jones, H. R. A., et al. 2009, ApJ, 704, 975 [Cited on page 127.]

Jha, S., Charbonneau, D., Garnavich, P. M., et al. 2000, ApJ, 540, L45 [Cited on page 8.]

Johnson, J. A. & Apps, K. 2009, ApJ, 699, 933 [Cited on pages 24, 39, and 109.]

Kalas, P., Graham, J. R., Chiang, E., et al. 2008, Science, 322, 1345 [Cited on page 13.]

Kasting, J. F. 1997, Origins of Life and Evolution of the Biosphere, 27, 291 [Cited on page 21.]

Kasting, J. F., Whitmire, D. P., & Reynolds, R. T. 1993, Icarus, 101, 108 [Cited on page 21.]

Kaufer, A., Stahl, O., Tubbesing, S., et al. 1999, The Messenger, 95, 8 [Cited on page 59.]

Khata, D., Mondal, S., Das, R., & Baug, T. 2021, MNRAS, 507, 1869 [Cited on pages 46, 53, 60, 83, 84, 85, 152, and 154.]

Kirkpatrick, J. D., McGraw, J. T., Hess, T. R., Liebert, J., & McCarthy, Donald W., J. 1994, ApJS, 94, 749 [Cited on page 23.]

Klüter, J., Bastian, U., Demleitner, M., & Wambsganss, J. 2018, A&A, 620, A175 [Cited on page 14.]

Kochukhov, O. P. 2007, in Physics of Magnetic Stars, ed. I. I. Romanyuk, D. O. Kudryavtsev, O. M. Neizvestnaya, & V. M. Shapoval, 109–118 [Cited on page 35.]

Kokubo, E. & Ida, S. 2002, ApJ, 581, 666 [Cited on page 111.]

Koll, D. D. B. & Abbot, D. S. 2016, ApJ, 825, 99 [Cited on page 17.]

Kopparapu, R. K., Ramirez, R., Kasting, J. F., et al. 2013, ApJ, 765, 131 [Cited on page 21.]

Kurucz, R. 1993, ATLAS9 Stellar Atmosphere Programs and 2 km/s grid. Kurucz CD-ROM No. 13. Cambridge, 13 [Cited on page 76.]

Kurucz, R. L. 1970, SAO Special Report, 309 [Cited on pages 35 and 36.]

Kurucz, R. L. 2005, Memorie della Societa Astronomica Italiana Supplementi, 8, 14 [Cited on page 36.]

Lada, C. J. 2006, ApJ, 640, L63 [Cited on page 5.]

Laughlin, G. 2000, ApJ, 545, 1064 [Cited on page 109.]

Laughlin, G., Bodenheimer, P., & Adams, F. C. 1997, ApJ, 482, 420 [Cited on page 21.]

Lépine, S., Rich, R. M., & Shara, M. M. 2007, ApJ, 669, 1235 [Cited on pages 21 and 43.]

Lillo-Box, J., Figueira, P., Leleu, A., et al. 2020, A&A, 642, A121 [Cited on page 79.]

Lindgren, S. & Heiter, U. 2017, A&A, 604, A97 [Cited on pages 48, 126, 127, 134, and 135.]

Lindgren, S., Heiter, U., & Seifahrt, A. 2016, A&A, 586, A100 [Cited on pages 24 and 48.]

Lissauer, J. J., Marcy, G. W., Rowe, J. F., et al. 2012, ApJ, 750, 112 [Cited on page 16.]

Long, F., Pinilla, P., Herczeg, G. J., et al. 2018, ApJ, 869, 17 [Cited on page 18.]

Macintosh, B. A., Graham, J. R., Palmer, D. W., et al. 2008, in Society of Photo-Optical Instrumentation Engineers (SPIE) Conference Series, Vol. 7015, Adaptive Optics Systems, ed. N. Hubin, C. E. Max, & P. L. Wizinowich, 701518 [Cited on page 13.]

Madhusudhan, N. & Burrows, A. 2012, ApJ, 747, 25 [Cited on page 17.]

Maldonado, J., Affer, L., Micela, G., et al. 2015, A&A, 577, A132 [Cited on pages xii, 44, 100, 101, and 102.]

Maldonado, J., Micela, G., Baratella, M., et al. 2020, A&A, 644, A68 [Cited on page 109.]

Mann, A. W., Brewer, J. M., Gaidos, E., Lépine, S., & Hilton, E. J. 2013a, AJ, 145, 52 [Cited on pages 24, 47, and 101.]

Mann, A. W., Deacon, N. R., Gaidos, E., et al. 2014, AJ, 147, 160 [Cited on page 101.]

Mann, A. W., Dupuy, T., Kraus, A. L., et al. 2019, ApJ, 871, 63 [Cited on page 4.]

Mann, A. W., Feiden, G. A., Gaidos, E., Boyajian, T., & von Braun, K. 2015, ApJ, 804, 64 [Cited on pages vii, ix, xii, xiii, 40, 79, 80, 81, 82, 83, 100, 101, 105, 125, 134, 140, and 143.]

Mann, A. W., Gaidos, E., & Ansdell, M. 2013b, ApJ, 779, 188 [Cited on pages 80 and 83.]

Marfil, E., Tabernero, H. M., Montes, D., et al. 2021, A&A, 656, A162 [Cited on pages 24 and 49.]

Marois, C., Doyon, R., Racine, R., et al. 2005, JRASC, 99, 130 [Cited on page 13.]

Marois, C., Macintosh, B., Barman, T., et al. 2008, Science, 322, 1348 [Cited on page 13.]

Marois, C., Zuckerman, B., Konopacky, Q. M., Macintosh, B., & Barman, T. 2010, Nature, 468, 1080 [Cited on page 13.]

Martins, J. H. C., Santos, N. C., Figueira, P., et al. 2015, A&A, 576, A134 [Cited on page 17.]

Mayor, M., Marmier, M., Lovis, C., et al. 2011, arXiv e-prints, arXiv:1109.2497 [Cited on page 109.]

Mayor, M., Pepe, F., Queloz, D., et al. 2003, The Messenger, 114, 20 [Cited on pages 10 and 59.]

Mayor, M. & Queloz, D. 1995, A Jupiter-mass companion to a solar-type star [Cited on pages 10 and 19.]

Mould, J. R. 1976, A&A, 48, 443 [Cited on pages 36 and 43.]

Mould, J. R. & Wyckoff, S. 1978, MNRAS, 182, 63 [Cited on page 36.]

Murdin, P. 2000, in Encyclopedia of Astronomy and Astrophysics, ed. P. Murdin, 3624 [Cited on page 1.]

Neuforge-Verheecke, C. & Magain, P. 1997, A&A, 328, 261 [Cited on page 140.]

Neves, V., Bonfils, X., Santos, N. C., et al. 2012, A&A, 538, A25 [Cited on pages 24, 39, 44, 51, 52, 53, 58, 60, 70, 79, 80, 83, 84, 85, 88, 100, 101, 152, and 154.]

Neves, V., Bonfils, X., Santos, N. C., et al. 2013, A&A, 551, A36 [Cited on page 109.]

Neves, V., Bonfils, X., Santos, N. C., et al. 2014, A&A, 568, A121 [Cited on pages vii, ix, xi, 44, 51, 54, 55, 56, 58, 70, 71, 73, 74, and 75.]

Newton, E. R., Charbonneau, D., Irwin, J., & Mann, A. W. 2015, ApJ, 800, 85 [Cited on page 83.]

Olander, T., Heiter, U., & Kochukhov, O. 2021, A&A, 649, A103 [Cited on page 50.]

Önehag, A., Heiter, U., Gustafsson, B., et al. 2012, A&A, 542, A33 [Cited on pages 4, 5, 24, 47, and 117.]

Oreshenko, M., Heng, K., & Demory, B.-O. 2016, MNRAS, 457, 3420 [Cited on page 17.]

Panahi, A., Zucker, S., Clementini, G., et al. 2022, A&A, 663, A101 [Cited on page 15.]

Passegger, V. M., Bello-García, A., Ordieres-Meré, J., et al. 2022, A&A, 658, A194 [Cited on pages 81, 87, and 148.]

Passegger, V. M., Bello-García, A., Ordieres-Meré, J., et al. 2020, A&A, 642, A22 [Cited on pages 52 and 82.]

Passegger, V. M., Reiners, A., Jeffers, S. V., et al. 2018, A&A, 615, A6 [Cited on pages xii, 45, 81, 100, 101, and 104.]

Passegger, V. M., Schweitzer, A., Shulyak, D., et al. 2019, A&A, 627, A161 [Cited on pages 24, 45, and 81.]

Passegger, V. M., Wende-von Berg, S., & Reiners, A. 2016, A&A, 587, A19 [Cited on pages 44, 45, and 101.]

Pecaut, M. J. & Mamajek, E. E. 2013, ApJS, 208, 9 [Cited on pages 9 and 11.]

Pepe, F., Cristiani, S., Rebolo, R., et al. 2021, A&A, 645, A96 [Cited on pages 10 and 77.]

Pepe, F., Molaro, P., Cristiani, S., et al. 2014, Astronomische Nachrichten, 335, 8 [Cited on page 10.]

Perez, S., Dunhill, A., Casassus, S., et al. 2015, ApJ, 811, L5 [Cited on page 18.]

Perruchot, S., Kohler, D., Bouchy, F., et al. 2008, in Society of Photo-Optical Instrumentation Engineers (SPIE) Conference Series, Vol. 7014, Ground-based and Airborne Instrumentation for Astronomy II, ed. I. S. McLean & M. M. Casali, 70140J [Cited on page 59.]

Perryman, M., Hartman, J., Bakos, G. Á., & Lindegren, L. 2014, ApJ, 797, 14 [Cited on page 14.]

Pinte, C., Price, D. J., Ménard, F., et al. 2018, ApJ, 860, L13 [Cited on page 18.]

Pinte, C., van der Plas, G., Ménard, F., et al. 2019, Nature Astronomy, 3, 1109 [Cited on page 18.]

Piskunov, N. & Valenti, J. A. 2017, A&A, 597, A16 [Cited on page 35.]

Piskunov, N. E., Kupka, F., Ryabchikova, T. A., Weiss, W. W., & Jeffery, C. S. 1995, A&AS, 112, 525 [Cited on page 41.]

Plez, B. 2012, Turbospectrum: Code for spectral synthesis, Astrophysics Source Code Library, record ascl:1205.004 [Cited on page 36.]

Pollacco, D. L., Skillen, I., Collier Cameron, A., et al. 2006, PASP, 118, 1407 [Cited on page 8.]

Pollack, J. B., Hubickyj, O., Bodenheimer, P., et al. 1996, Icarus, 124, 62 [Cited on page 111.]

Quirrenbach, A., Amado, P. J., Caballero, J. A., et al. 2016, in Society of Photo-Optical Instrumentation Engineers (SPIE) Conference Series, Vol. 9908, Ground-based and Airborne Instrumentation for Astronomy VI, ed. C. J. Evans, L. Simard, & H. Takami, 990812 [Cited on pages 10 and 59.]

Rabus, M., Lachaume, R., Jordán, A., et al. 2019, MNRAS, 484, 2674 [Cited on pages 40, 53, 60, 83, 152, and 154.]

Rajpurohit, A. S., Allard, F., Rajpurohit, S., et al. 2018, A&A, 620, A180 [Cited on pages 24, 42, 45, and 124.]

Rau, M. M., Koposov, S. E., Trac, H., & Mandelbaum, R. 2019, MNRAS, 484, 409 [Cited on page 52.]

Rauer, H., Catala, C., Aerts, C., et al. 2014, Experimental Astronomy, 38, 249 [Cited on pages 6 and 7.]

Reetz, J. 1991 [Cited on page 35.]

Reid, I. N., Gizis, J. E., Cohen, J. G., et al. 1997, PASP, 109, 559 [Cited on page 23.]

Reid, I. N. & Hawley, S. L. 2005, New light on dark stars : red dwarfs, low-mass stars, brown dwarfs [Cited on page 4.]

Reid, N. & Gilmore, G. 1984, MNRAS, 206, 19 [Cited on page 38.]

Ricker, G. R., Winn, J. N., Vanderspek, R., et al. 2015, Journal of Astronomical Telescopes, Instruments, and Systems, 1, 014003 [Cited on pages 6 and 7.]

Rodríguez, J.-V., Rodríguez-Rodríguez, I., & Woo, W. L. 2022, WIREs Data Mining and Knowledge Discovery, 12, e1476 [Cited on page 51.]

Rojas-Ayala, B., Covey, K. R., Muirhead, P. S., & Lloyd, J. P. 2010, ApJ, 720, L113 [Cited on pages 24 and 46.]

Rojas-Ayala, B., Covey, K. R., Muirhead, P. S., & Lloyd, J. P. 2012, ApJ, 748, 93 [Cited on pages xii, 24, 46, 100, 103, and 109.]

Sahlmann, J., Ségransan, D., Queloz, D., et al. 2011, A&A, 525, A95 [Cited on page 15.]

Santerne, A., Díaz, R. F., Moutou, C., et al. 2012, A&A, 545, A76 [Cited on page 8.]

Santos, N. C., Israelian, G., & Mayor, M. 2004, A&A, 415, 1153 [Cited on pages 39, 41, and 109.]

Santos, N. C., Israelian, G., Mayor, M., Rebolo, R., & Udry, S. 2003, A&A, 398, 363 [Cited on page 109.]

Santos, N. C., Sousa, S. G., Mortier, A., et al. 2013, A&A, 556, A150 [Cited on pages 76 and 86.]

Sarmento, P., Rojas-Ayala, B., Delgado Mena, E., & Blanco-Cuaresma, S. 2021, A&A, 649, A147 [Cited on pages 49, 118, and 124.]

Sbordone, L., Bonifacio, P., Castelli, F., & Kurucz, R. L. 2004, Memorie della Societa Astronomica Italiana Supplementi, 5, 93 [Cited on page 35.]

Schlaufman, K. C. & Laughlin, G. 2010, A&A, 519, A105 [Cited on pages 39 and 109.]

Sirbu, D., Thomas, S., Belikov, R., & Bendek, E. 2017, ApJ, 849, 142 [Cited on page 13.]

Sneden, C., Bean, J., Ivans, I., Lucatello, S., & Sobeck, J. 2012, MOOG: LTE line analysis and spectrum synthesis, Astrophysics Source Code Library, record ascl:1202.009 [Cited on page 34.]

Sneden, C. A. 1973, PhD thesis, University of Texas, Austin [Cited on pages 34, 76, and 117.]

Sousa, S. G., Adibekyan, V., Delgado-Mena, E., et al. 2018, A&A, 620, A58 [Cited on page 125.]

Sousa, S. G., Adibekyan, V., Delgado-Mena, E., et al. 2021, A&A, 656, A53 [Cited on page 86.]

Sousa, S. G., Santos, N. C., Adibekyan, V., Delgado-Mena, E., & Israelian, G. 2015, A&A, 577, A67 [Cited on pages 51, 120, and 125.]

Sousa, S. G., Santos, N. C., Israelian, G., et al. 2011, A&A, 526, A99 [Cited on page 109.]

Sousa, S. G., Santos, N. C., Mayor, M., et al. 2008, A&A, 487, 373 [Cited on pages 51, 76, and 109.]

Souto, D., Cunha, K., García-Hernández, D. A., et al. 2017, ApJ, 835, 239 [Cited on page 49.]

Souto, D., Cunha, K., Smith, V. V., et al. 2020, ApJ, 890, 133 [Cited on pages 24 and 49.]

Souto, D., Cunha, K., Smith, V. V., et al. 2022, ApJ, 927, 123 [Cited on page 22.]

Souto, D., Unterborn, C. T., Smith, V. V., et al. 2018, ApJ, 860, L15 [Cited on page 49.]

Stauffer, J. R. & Hartmann, L. W. 1986, ApJS, 61, 531 [Cited on page 43.]

Tabernero, H. M., Marfil, E., Montes, D., & González Hernández, J. I. 2022, A&A, 657, A66 [Cited on pages 49 and 82.]

Terrien, R. C., Mahadevan, S., Bender, C. F., et al. 2012, ApJ, 747, L38 [Cited on page 109.]

Terrien, R. C., Mahadevan, S., Deshpande, R., & Bender, C. F. 2015, ApJS, 220, 16 [Cited on page 48.]

Thiabaud, A., Marboeuf, U., Alibert, Y., et al. 2014, A&A, 562, A27 [Cited on page 5.]

Tinetti, G., Vidal-Madjar, A., Liang, M.-C., et al. 2007, Nature, 448, 169 [Cited on page 8.]

Tinney, C. G., Mould, J. R., & Reid, I. N. 1993, AJ, 105, 1045 [Cited on page 38.]

Ucci, G., Ferrara, A., Gallerani, S., et al. 2019, MNRAS, 483, 1295 [Cited on page 52.]

Udry, S., Mayor, M., Benz, W., et al. 2006, A&A, 447, 361 [Cited on page 109.]

Valenti, J. A. & Piskunov, N. 1996, A&AS, 118, 595 [Cited on page 35.]

Veyette, M. J., Muirhead, P. S., Mann, A. W., et al. 2017, ApJ, 851, 26 [Cited on page 48.]

Wang, J. & Fischer, D. A. 2015, AJ, 149, 14 [Cited on page 109.]

Wehrhahn, A., Piskunov, N., & Ryabchikova, T. 2023, A&A, 671, A171 [Cited on page 35.]

Wende, S., Reiners, A., & Ludwig, H. G. 2009, A&A, 508, 1429 [Cited on pages 126, 127, 134, and 135.]

West, A. A., Bochanski, J. J., Hawley, S. L., et al. 2006, AJ, 132, 2507 [Cited on page 23.]

Wildi, F., Blind, N., Reshetov, V., et al. 2017, in Society of Photo-Optical Instrumentation Engineers (SPIE) Conference Series, Vol. 10400, Society of Photo-Optical Instrumentation Engineers (SPIE) Conference Series, 1040018 [Cited on page 11.]

Winn, J. N. 2010, in Exoplanets, ed. S. Seager, 55–77 [Cited on pages 17 and 18.]

Wolszczan, A. & Frail, D. A. 1992, Nature, 355, 145 [Cited on page 5.]

Woolf, V. M., Lépine, S., & Wallerstein, G. 2009, PASP, 121, 117 [Cited on page 44.]

Woolf, V. M. & Wallerstein, G. 2005, MNRAS, 356, 963 [Cited on pages 23, 39, and 43.]